Density Functional Theory Approach towards Electronic Structures, Formation of High Valent Metal Species and Metal Mediated C-H/O-H Bond Activation

Thesis Submitted to the Central University of Haryana
for the partial fulfillment of the Degree of

Doctor of Philosophy

in

Chemistry

By

Monika

Department of Chemistry
Central University of Haryana
Mahendergarh-123031
Haryana, India

January 2022

Dedicated

to

My Family and Friends

DECLARATION

(*As required under clause I2 of Ordinance IIA of the Central University of Haryana*)

This is to certify that the material embodied in the present work, entitled **"Density Functional Theory Approach towards Electronic Structures, Formation of High Valent Metal Species and Metal Mediated C-H/O-H Bond Activation"**, is based on my original research work. The research work was carried out under the supervision of **Dr. Azaj Ansari (Supervisor)**, Central University of Haryana. This work has not been submitted, in part or full, for any other diploma or degree of any University/Institution Deemed to be University and College/Institution of National Importance. References from other works have been duly cited at the relevant places.

Monika
Candidate
(Roll No. - 10816)

Dr. Azaj Ansari
(Supervisior)
Department of Chemistry
Central University of Haryana
Mahendergarh-123031
Haryana, India

Prof. Vinod Kumar
Head, Department of Chemistry
Central University of Haryana
Mahendergarh-123031
Haryana, India

Abstract

Thesis entitled **"Density Functional Theory Approach towards Electronic Structures, Formation of High Valent Metal Species and Metal Mediated C-H/O-H Bond Activation"** is devoted to study on modeling structures, energetics of vanadium, chromium, manganese, iron, cobalt, nickel, and copper complexes containing amino ligands by using Density Functional Theory (DFT) methods. The C-H bond activation by metal-superoxo complexes has been investigated in detail using density functional theory (DFT). Mechanistic pathways studies for the catalytic reactions mediated by these transient species. Studies on different systems is presented in this thesis to (i) support/verify experimental findings, (ii) improve our understanding of the above-mentioned systems, and also (iii) make predictions to improve the efficiency, selectivity, and robustness of the existing catalysts. The results of this thesis are divided into four sections. In the first section, we have discussed electronic structures of iron TAML species, and their derivates. In second section, we have studied the mechanistic study for selective C-H/O-H bond activation in the allylic system by using iron(V)-oxo TAML species. In the third section, we have studied the electronic structures of metal-superoxo species (where, M = V(III), Cr(III), Mn(III), Fe(III), and Co(III)) and also studied the effect of TMC-ring size on electronic structures and their comparative reactivity towards C-H bond activation. Our results reveal that ring size plays an important role in C-H bond activation. In the fourth section, we have discussed the formation of metal-oxo species with metal (Cr, Mn, Fe, Co, Ni, and Cu). Our findings suggest that the formation of earlier transition metal-oxo species have a smaller barrier than the late transition metal-oxo species.

Acknowledgments

Here is the place and time to say “thank you” to everybody who, in one way or another, contributed to my life during my years in CUH. Some of you helped me by simply being my friends, and some even took part in my research and, of course, all of you made it possible for me come to “the finish”.

First of all, I would like to express my gratitude to my supervisor **Dr. Azaj Ansari** allowed me to make my Ph.D. here at CUH. It is an honor to be your student, Thank you very much. For your scientific guidance, invariable support and patience, continuous support of my motivation, enthusiasm, and invaluable guidance, he showed me until the successful end of my thesis. To achieve goals that were beyond my capabilities and helped me to realize what all I can do. As his first Ph.D. student ever, he teaches me almost everything from the basics of density functional theory to the writing of the scientific paper. His supervision is unmatchable and I am with great luck to be his first Ph.D. student which will be treasured forever, and would also like to thank him for his great mentorship and his willingness to let me work freely and to take my project in the direction I found most interesting. I honestly thank God for giving you as my supervisor. I think I can’t express my gratitude in words but one thing I want to say is if anyone has a supervisor like him, this journey which demands a lot of patience, sacrifice, and hard work can become smooth. He always boosted my confidence whenever I was a little down. I want to thank him again for this marvelous journey and kind support.

I am also thankful to *prof. Vinod Kumar, Head of Department of Chemistry, CUH,* and *Dr. Prakash Kanoo, Dr. Manoj Kumar* (Department of Statistics), *Dr. Manoj Kumar Gupta,* members of the advisory committee for monitoring the research progress and offering their insightful comments, ingenious suggestions, and active support.

I wish to express my sincere gratitude to:

 Prof. A. J. Varma, former Head, Department of Chemistry, Central University of Haryana for his encouragement and sharing research experience during the initial days of my Ph.D.

 Prof. Deepak Pant, former Head, Department of Chemistry, Central University of Haryana for his encouragement and sharing research experience during my Ph.D.

 Prof. Harish Kumar, and Dr. Rajiv S. Menon, Department of Chemistry, Central University of Haryana for giving invaluable suggestions and creating a stimulating working environment.

 Prof. Gopalan Rajaraman, Department of Chemistry, Indian Institute of Bombay for providing computing facility during the initial days of my Ph.D.

I pay special thanks to all lab members and senior fellows for their loving attitude towards me and guiding me and making a positive and enjoyable working environment. My fellows were always present with me in all discussions, sharing all moments during this long journey. You guys made this journey very beautiful. I want to thank Mrs. Oval Yadav, Mr. Manjeet Kumar, and Mr. Mukhtar Ahmed, and all other research scholars from the Department of Chemistry, Central University of Haryana for their immense support at every moment.

Everybody confines in the family. For me, this journey was not only of me. Each and every member of my family has this journey with me. I want to thank them for believing in me so religiously. My grandmother *Smt. Shanti Devi* and grandfather *Shri Chhtar Pal* have the greatest role in shaping my life in the right direction.

My parents *Shri Shripal* and *Smt. Maya Devi* played a great role in every step of my life. I learned from them how to be hard-working and consistent in my work. My sister-in-law *Mrs. Pooja* and my brother *Mr. Gagan Pal* who were always there to support me mentally deserve a special place in my research work.

I am fortunate to have a family which is always behind me regardless of whatever happened. I thank my beloved parents and my lovely brother. I dedicate this thesis to my family; especially my loving parents.

Abbervations

HF	Hartree-Fock
DFT	Density Functional Theory
WFT	Wave Function theory
K S	Kohn-Sham
SCF	Self Consistent Field
V_{xc}	Exchange Correlation Potential
E_{xc}	Exchange Correlation Functional
LDA	Local Density Approximation
LSDA	Local Spin-Density Approximation
VWN	Vosko-Wilk-Nusair Correlation
GGA	Generalized Gradient Approximation
MGGA	Meta Generalized Gradient Approximation
LYP	Lee Yang Parr
BLYP	Becke Lee Yang Parr
BP86	Becke Perdew 86
LCAO	Linear combination of atomic orbitals
STO	Slater Type Orbital
GTO	Gaussian Type Orbital
CGTO	Contracted Gaussian Type Orbital
TZV	Triple zeta valance
VDZ	Valence double zeta
VTZP	Valence triple zeta polarisation
ECP	Effective core potential
NAO	Natural Atomic orbitals
NBO	Natural Bond Orbital
NHO	Natural Hybrid Orbital
SCRF	Self-Consistent Reaction Field
PCM	Polarized Continuum Model
TD-DFT	Time dependent density functional theory
HOMO	Highest occupied molecular orbital
LUMO	Lowest occupied molecular orbital
SNO	Spin Natural Orbital
HS	High spin
IS	Intermediate spin
LS	Low spin
BS	Broken symmetry
J	Magnetic exchange
JF	Ferromagnetic interaction
JAF	Antiferromagnetic interaction
TSR	Two State Reactivity
TS	Transition state
IRC	Intrinsic Reaction Coordinate
TST	Transition State Theory
Å	Angstrom (10-10 m)
^{o}	Degree
ca.	calculated

Contents

Chapter 1

A General Introduction to Bioinspired High Valent Metal Complexes

1.1 Introduction

In nature, metalloenzymes carry out a wide range of biological and chemical reactions such as oxygen transport, radical formation, redox reactions, rearrangements, signal transduction proteins, storage and transport of proteins.[1] Metalloenzyme such as oxalate oxidase, catalase, superoxide dismutase, cytochrome P450, Rieske dioxygenases involves manganese/iron-peroxo.[2–7] While isopenicillin, cysteine dioxygenases, peptidylglycine-α-amidating monooxygenase, and dopamine β-monooxygenase have iron/copper-superoxo[8–13] as reactive intermediates, by the help of these intermediates many reactions are carried out such as hydroxylation, epoxidation, halogenation, and N-dealkylation.[14] High valent metal-oxo species are involved in oxidation reactions occurring in heme and non-heme iron systems and also in water oxidation in photosystem-II.[14-28]

Metalloenzymes are involved in dioxygen activation to form metal-oxygen intermediates, and these act as a reactive intermediate in metal-mediated catalytic transformation in biological and industrial processes.[14,29–32] Cytochrome P450 is a heme enzyme; it plays an important role in natural product biosynthesis, degradation of xenobiotics, steroid biosynthesis, and drug metabolism. In the liver of the human body, cytochrome P450 is involved in metabolism of xenobiotics and also involved in synthesis of estrogen and other hormones.[15-20] It is an important biocatalyst in nature because of substrate structure and it catalyzes many regio and stereo selective reactions such as hydroxylation, epoxidation, nitration, C-C bond coupling, or cleavage.[33,34] Side-on manganese(III)-peroxo intermediate is involved in catalytic cycles of a biological system such as photosystem-II and superoxide dismutase.[35–37] In photosystem-II manganese(III)-peroxo catalyze photolysis of water and produce molecular oxygen and in SOD these are involved in the biodegradation of toxic superoxide and lead to the formation of hydrogen peroxide and water. In a catalytic cycle of Rieske dioxygenase, a non-heme iron(V)-oxo intermediate is also an important reactive intermediate, and catalyzes many

reactions such as *cis*-dihydroxylations, O/N-demethylations, and C-C bond formation.[31,38–41] Binuclear, non-heme iron enzymes carry out many reactions by dioxygen activation, most-studied enzymes such as RNR1[42] (ribonucleotide reductase) which initiates radical chemistry to generate DNA building blocks, methane monooxygenase[43] and helps in the hydroxylation of methane to methanol. Desaturase[44] inserts a double bond into fatty acids to produce lipid precursors. Many metal ions such as Mg, Mn, Fe, Co, Ni, Cu, and Zn are involved as a reactive intermediate in the hydrolysis process, radical-based rearrangement, electron transfer reactions, oxidation-reduction process, and DNA processing.[8,33,35]

These intermediates are short-lived and experimental evidence are available for their existence. For understanding the catalytic mechanism of these enzymes there is a requirement for the development of synthetic model complexes that mimic their catalytic activity and also investigate electronic structures, and mechanistic pathways.[45-61] In biological studies, bioinorganic chemists are dedicated to develope biomimetic model complexes which mimic the reactivity of many catalytic reactions. All these provide a deeper insight into structures and mechanistic details of metalloenzymes under analysis.

1.2 Biomimetic Catalysts

Chemical catalysis that mimics certain key characteristics of enzymatic systems are known as "biomimetic catalysis".[62] In bioinorganic chemistry, structure of active sites, reactive intermediates, mechanism of dioxygen activation, oxygenation reactions occurring at the active site, and factors that affect catalytic transformation reactions are studied.[14,63] Natural phenomena and reactive nature of intermediates involved in reactions such as water splitting, biosynthesis of DNA, organic hydroperoxides[64,65] cyt P450 and Rieske dioxygenase enzymes[66,67] have inspired scientist to develop synthetic biomimetic models which help us in understanding the nature of active sites and mechanism of catalytic intermediates of these

important enzymes and proteins. The catalytic mechanism of these enzymes can be investigated by the development of a synthetic biomimetic model studying the structural, electronic, and mechanistic pathways.[43-59] Several attempts have been undertaken towards the development of synthetic complexes.[50-57]

Fortunately, several biomimetic complexes have been synthesized and characterized. Some of the representative ligands which are functional models of mononuclear non-heme enzymes are given in Scheme 1.1. "Biomimetic catalysis" refers to chemical catalysis that mimics the main key features of enzymatic systems.[68–72] Theoretical studies help to understand the electronic structures of biomimetic complex and mechanism of metal-mediated catalytic transformation reactions and can tune the reactivity and product selectivity of dioxygen activation which can be governed by the interaction between metal and substrate. Understanding the mechanism of C-H/O-H bond activation remains a key consideration, and computational modeling provides insight into the process. Computational modeling of mechanism pathway provides characteristics of the transition state (TS) and intermediate on potential energy surface. It provides the assessment of energy barrier ($E^{\#}$) and activation barriers ($G^{\#}$). Transition state determination provides a better understanding of the reaction mechanism and suggests rate-limiting steps and provides insight into the reaction mechanism. Many reaction cycles have been proposed based on transition state and understanding of mechanism provides helps to generate new reaction conditions and reagents. The electronic structure of transition states facilitates the characterization of reaction mechanisms in terms of bonds that are broken and which are formed.

Understanding of the biomimetic system not only enhances scientific knowledge but also broadens the scope of cheap, efficient, selective, and environment friendly oxygenation catalysts.

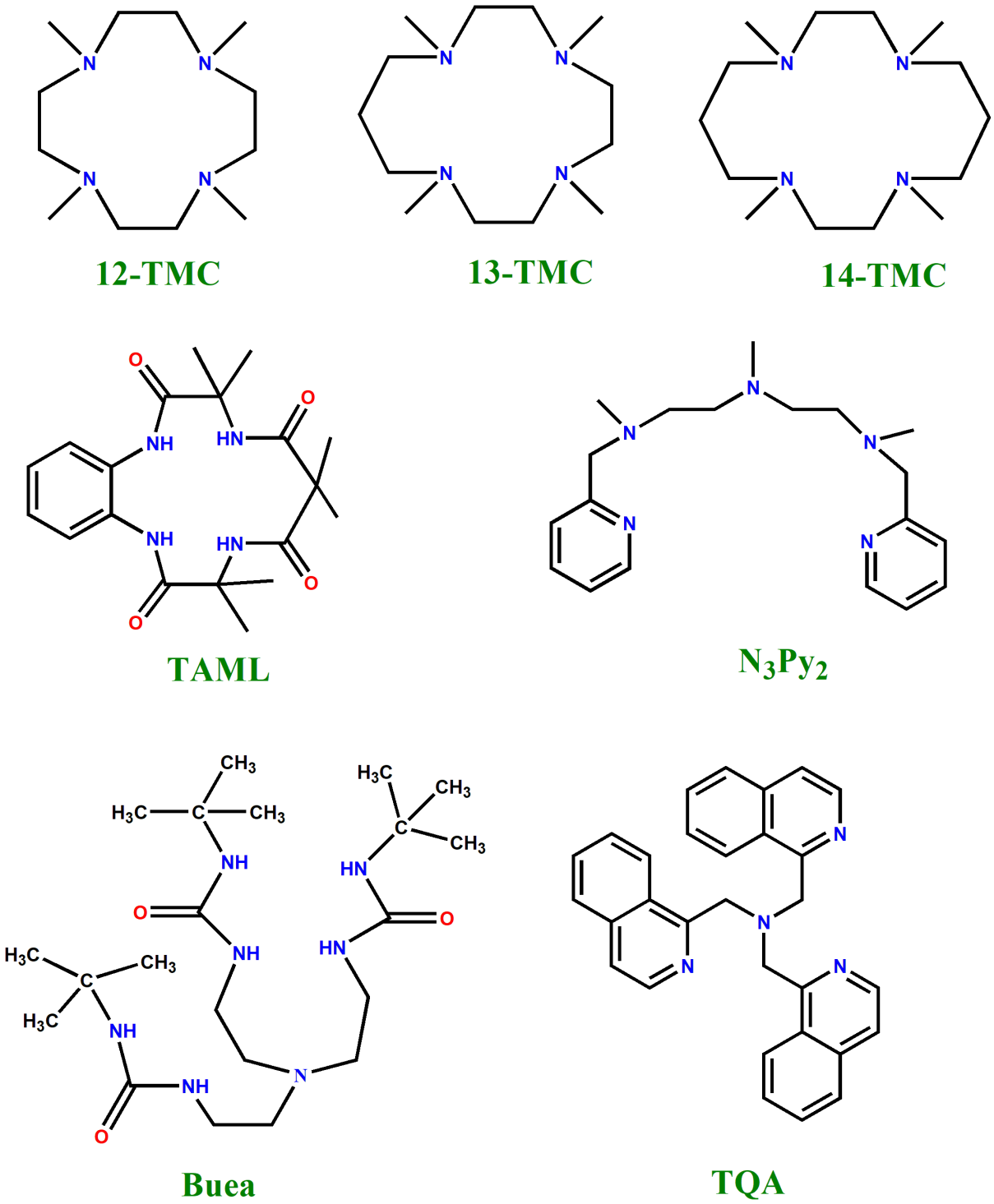

Scheme 1.1. Representative examples of ligands employed in biomimetic non-heme model complexes.

Where, 12-TMC= 1,4,7,10-tetramethyl-1,4,7,10-tetraazacyclododecane, 13-TMC= 1,4,7,10-tetramethyl-1,4,7,10-tetraazacyclotridecane; 14-TMC=1,4,8,11-tetramethyl-1,4,8,11-tetraazacyclotetradecane, TAML= tetramidomacrocyclic ligand, N_3Py_2= N,N′-dimethyl-N-(2-(methyl(pyridin-2-ylmethyl)-amino)ethyl)-N′-(pyridin-2-ylmethyl-)ethane-1,2-diamine,

buea=tris[(N'-tert-butylureayl)-N-ethyl]-(6-pivalamido-2-pyridylmethyl)aminato], TQA=tris(2-quinolylmethyl)amine.

Biomimetic chemistry covers the synthesis and study of artificial enzymes. Metal-superoxo/peroxo/hydroperoxo/oxo species have been synthesized and these acts as, a reactive intermediate in metal-mediated catalytic transformation and industrial processes.

1.3 Metal-Superoxo

Metal-superoxo/peroxo are involved as an important intermediate in dioxygen (O_2) activation by enzymes and metal-containing proteins, and dioxygen formation by photosystem-II.[9,31,54] In Rieske dioxygenases iron-peroxo is proposed as an active intermediate, which carries *cis*-dihydroxylation of aromatic compound whereas manganese-peroxo helps water oxidation in photosystem-II.[39,40,60,73] Metal-superoxo species are also reactive intermediates in enzymatic reactions, like non-heme iron enzymes such as isopenicillin N synthase, 2,3-dioxygenase, myo-inositol oxygenase, homoprotocatechuate, and cysteine dioxygenase along with copper-containing enzymes peptidylglycine-α-amidating monooxygenase and dopamine β-monooxygenase.[8–12,74] Iron(III)-hydroperoxo species is involved as a key intermediate and involved in the catalytic cycle of bleomycin and Rieske dioxygenase.[75–79] Metal-superoxo species have gained more attention as iron(III)/copper(II)-superoxo, are active oxidants in hydrogen atom abstraction reactions.[8,10-12,74] Dioxygen binding metal-complexes such as superoxo (η^1; end on) and peroxo (η^2; side on) have been synthesized with the help of X-ray crystallography and several spectroscopic techniques binding nature of dioxygen and nature of metal ions have been intensively investigated.[39,60,80–85] Metal-superoxo species carried out wide range of chemical reactions which play an important role in pharmaceutical industries and environmental applications.[60,82,86-100] Non-heme iron(III)-superoxo species, is also a

precursor of iron-oxo which is an oxidant in enzymatic reactions.[8,9,14,101] Both iron-oxo and iron-superoxo complexes are biologically important.[10-12] Many iron containing heme mononuclear enzymes use high-spin iron(II) ions and react with dioxygen (O_2) and form the iron(III)-superoxo species and they are converted to iron(III)-peroxo by one-electron reduction. In heme system, iron(III)-superoxo complexes were well characterized and their crystal structure was also studied.[102,103] Nam *et al.*[97,104,105] proposed iron(III)-superoxo as a short-lived 'putative' intermediate during dioxygen activation by non-heme iron(II) complexes, while Goldberg *et al.*[105] proposed that iron(III)-superoxo species formation is ease by sulfur ligand at the axial position of iron(II) complex. Evidence for the existence of side-on manganese(III)-peroxo species are also found as a reactive intermediate in biological catalytic cycle for example in photosystem-II and superoxide dismutase.[35–37]

Inspired by these natural processes, for understanding the catalytic intermediates involved in proteins and enzymes, synthetic biomimetic models have been developed. Iron(III)-superoxo complex with TAML (tetramido macrocyclic ligand) is reported, and it is characterized as side on (η^2) iron(III)-superoxo complex, both structurally and spectroscopically,[106] $[(TAML)Fe^{III}(O_2)]^{2-}$. Bakac and co-workers reported mononuclear chromium(III)-superoxo complex as chemical models in dioxygen activating metalloenzymes and acts as a reactive intermediate in the oxidation of substrates.[107,108] Chromium(III)-superoxo complex, $[Cr^{III}(O_2)(TMC)(Cl)]^+$ has been reported and characterized by X-ray and spectroscopic studies along with C-H bond activation.[109-111] A rare thiolate-ligated cobalt-superoxo species $Co(O_2)$ has been synthesized and characterized by spectroscopic techniques.[112] Cu(II)-superoxo is also synthesized and also participitate in C-H/O-H bond activation.[94,113–115] Formation of nickel(III)-peroxo is characterized by UV-vis, electrospray ionization mass spectrometry, resonance Raman, electron paramagnetic resonance and X-ray analysis.[116] In literature studies, it is found that supporting ligands also play an important role in tuning the

geometric and electronic structures, stabilities, and reactivities of oxygen-coordinating metal complexes. One notable example among such types of ligands is N-tetramethylated cyclam (TMC) and its derivatives.[117] It has been proved as an accomplished ligand in the biomimetic chemistry of dioxygen activation by metal complexes.

First row-transition metal-peroxo/superoxo (TMC) complexes have been synthesized and they are involved in many oxidation reactions.[109,118–128] It is also found that the nature of metal ions and the size of the TMC ring alter the electronic structure of $[M(n\text{-}TMC)(O_2)]^{n+}$ complexes.

1.4 Effect of Ligands

Dioxygen reacts with the metal to form either metal-superoxo or metal-peroxo species. From the literature studies, it is found that some metals form superoxo species or some forms peroxo species. As $[Cr^{II}(14\text{-}TMC)(Cl)]^+$ reacts with dioxygen (O_2) or H_2O_2 in the presence of a base such as triethylamine (TEA) or tetramethylammonium hydroxide (TMAH) to form $[Cr^{III}(14\text{-}TMC)(O_2)(Cl)]^+$ species and it is characterized by spectroscopic methods. Single crystal structure of $[Cr^{III}(14\text{-}TMC)(O_2)(Cl)]^+$ revealed that mononuclear end-on chromium-superoxo complex is distorted octahedral geometry, in which N-methyl groups of 14-TMC are oriented anti to the superoxo moiety and syn to chlorine ligand.[109-111] By substiting methylamino at pyridine ring of PDP ligand (2-((R)-2-[(R)-1-(pyridine-2-ylmethyl)pyrrolidin-2-yl]pyrrolidin-1-ylmethyl) pyridine) the catalytic reactivity, enantioselectivity towards asymmetric epoxidation increases.[129]

Spin state of complex is affected by ligand, for it consider octahedral iron(IV)-oxo complex, where spin state of complex is determined by the energy gap between orbitals d_{xy} and $d_{x^2-y^2}$.[130] This energy gap is larger than the spin-pairing energy, then S=1 complex is formed, and

if the equatorial ligand is weak then it will give S=2 complex.[131] From ortho hydroxylation of aromatic compounds with $[Fe^{II}(BPMEN)(CH_3CN)_2]^{2+}$ and $[Fe^{II}(TPA)(CH_3CN)_2]^{2+}$ (where TPA = tris(2-pyridylmethyl)amine and BPMEN = N,N'-dimethyl-N,N'-bis(2-pyridylmethyl)ethane-1,2-diamine), it is found that complex $[Fe^{II}(BPMEN)(CH_3CN)_2]^{2+}$ is more reactive than the $[Fe^{II}(TPA)(CH_3CN)_2]^{2+}$, and it because of ligand design as in complex $[Fe^{II}(TPA)(CH_3CN)_2]^{2+}$ pyridine ring is parallel to Fe(V)=O bond that is formed during reaction by which it mix with the $\pi_{Fedxy\text{-}Opy}$ which in turn reduces the electrophilicity of ferryl oxygen atom, whereas in $[Fe^{II}(BPMEN)(CH_3CN)_2]^{2+}$ pyridine ring is perpendicular to the Fe(V)=O bond.[132] For adopting the trigonal bipyramidal geometry d_{xy} and $d_{x^2\text{-}y^2}$ orbital will be degenerate. Reactivity of cobalt(III)-nitrosyl complexes bearing TMC ligands are studied in NO-transfer and deoxygenation reactions are significantly influenced by the spin state of cobalt(II) center, caused by ring size of TMC ligands.[124,133-135] From earlier studies, it is also found that non-heme iron(IV)-oxo complexes with smaller TMC ligand it is more reactive in both the HAT and OAT reactions.[136]

1.5 Formation of High Valent Metal-oxo Species

Transition metals in higher oxidation states either co-ordinates to oxygen or nitrogen by multiple bonds to form high valent metal-oxo or imido complexes. Metal-oxo are involved as active intermediates in the catalytic cycles of enzymes and biomimetic compounds to carry out oxidation reactions of organic substrates and water.[14,22,66,137–139] These also help in C-H/N-H/O-H bond activation and oxygen atom transfer reactions, mediated by a biological and chemical catalysts[14,32,43,60,140–153] and also play a very important role in pharmaceutical industries. Studies of high valent metal centers have been a subject of great interest because of their biological relevance and help to understand the structural and spectroscopic properties of metal-containing enzymes. Modeling active sites of enzymatic systems and

developing biomimetic alkane hydroxylation catalysts have become important and emerged as a vast area.[146-153]

Mononuclear heme and non-heme enzymes have metal ions at active sites. Metal ions bind with dioxygen, to produce metal-superoxo species, and by one-electron reduction, it gets converted to metal-peroxo species, and protonation of peroxo species results in the formation of hydroperoxo species. Alternatively, superoxo species can be directly converted to hydroperoxo species by abstracting hydrogen atoms. This direct conversion occurs only in non-heme iron enzymes. Heterolytic O---O bond cleavage in hydroperoxo species produce metal(V)-oxo species[66] whereas homolytic O---O bond cleavage produces high valent metal(IV)-oxo species. In the non-heme system metal(III)-hydroperoxo species gets converted to metal(II)-hydroperoxo species by one-electron reduction and then via heterolytic O---O bond cleavage it gets converted to metal(IV)-oxo species.[9,88,154]

From the last decades, in biomimetic complexes, high valent metal-oxo species have been intensively studied and synthetic terminal high valent iron-oxo and manganese-oxo complexes have been reported.[155,156] Heme and non-heme iron enzymes, terminal as well as bridging high-valent iron-oxo are found as important oxidizing intermediates in activation of molecular oxygen and these have spectroscopically characterized and found to be responsible for a wide number of oxidative transformations such as, in catalytic cycles of monooxygenase heme enzymes e.g. cytochrome P450, catalase,[14,66,137] and peroxidase high valent iron(IV)-oxo π-cationic radical intermediate is involved is supported by spectroscopic evidence by UV-vis, EPR, and M*ö*ssbauer.[157] Iron(IV)-oxo carries aliphatic hydroxylation, substrate epoxidation, aromatic hydroxylation, desaturation, and heteroatom transfers such as sulfoxidation reactions.[158,159] The capacity of iron to exist in multiple redox states and its availability in abundance makes it one of the common transition metals acting as a key

intermediate in many biotransformation reactions, occurring via C-H/O-H bond activation, including biological O_2 activation.[32-37] The chief interest in high valent iron chemistry is due to its ubiquitous nature, low toxicity, inexpensive, and its ability to carry out green catalytic oxidations.[38-40] The first, biomimetic metalloporphyrins catalysts, high valent iron(IV)-oxo porphyrin π-radical intermediate was synthesized and characterized by Groves and co-workers in 1981.[144] [(TMP)Fe^{III}(Cl)] (TMP = meso-tetramesityl porphinate dianion) reacts *m*-chloroperbenzoic acid at -78˚C in a dichloromethane-methanol mixture, to produce a green colored species, which was spectroscopically characterized as iron(IV)-oxo coordinated with a porphyrin-π radical, $[(TMP)Fe^{IV}(O)(CH_3OH)]^+$. These species have the characteristic features of cpdI present in P450, and found that it is an olefin epoxidation and alkane hydroxylation.[142,143,145] After that many iron(IV)-oxo porphyrin π radicals having electron-rich and electron-deficient porphyrins with different axial ligands have been reported to make understanding of the effect of electronic effects of porphyrin and axial ligands. The first time, non-heme iron(IV)-oxo intermediate was reported in 2000, during the reaction of $[Fe^{III}$(cyclam-acetato)$(CF_3SO_3)]^+$ and O_3 in acetone and water at -80˚C, spectroscopically detected by Wieghardt and co-workers. M*ö*ssbauer analysis characterized it as an intermediate-spin Fe(IV)-oxo (S=1).[160] The First, well-characterized mononuclear $[Fe^{IV}(O)(TMC)(NCCH_3)]^{2+}$ was reported in 2003. It is characterized by many spectroscopic methods such as and features a short Fe=O bond distance of 1.646(3) Å.[161–163] Most of the synthetic non-heme iron(IV)-oxo complexes have a triplet spin state (S=1) as the ground state while a small number of complex have quintet spin state (S=2) as a ground state.[164-166] Along with Fe^{IV}=O species, Fe^{V}=O species also acts as a reactive intermediate in many biological reactions. First, iron(V)-oxo complex was reported with TAML ligand. First time, TAML ligand was characterized by the collines group in 2002. TAML systems have gained importance as green catalysts because the chemistry mimicking these system performances is

comparatively greener than the current technological chemistry based upon environment degrading chemicals.[43] Capacity of TAML to stabilize diverse iron-oxo species in the high valent state such as: iron(IV) complex in the high spin state (S=2), iron(IV) complexes in the intermediate spin state (S=1), diiron(IV) dimers having an oxo-bridge and iron(III) (TAML-radical-cation) complex in a singlet state (S=0) and Fe(V)-oxo has been reported.[50] Synthetic Fe(V)-oxo complex with the tetra-amido ligand is well characterized by spectroscopic techniques e.g. electronic, magnetic circular dichroism, Raman, electron paramagnetic resonance (EPR), and Mössbauer spectroscopy. It also acts as a reactive intermediate in selective hydroxylation of aliphatic compounds, and carries reactions such as C-H and C=C oxidation reactions. Many iron complexes carry out regio-selective hydroxylation reactions.[167] The first example, published by Que and co-workers is $[Fe^{II}(TPA)(CH3CN)_2]^{2+}$ (TPA = tris(2-pyridylmethyl)amine) and it is capable of performing stereoselective C-H bond hydroxylation.[51] Reactivity of alkane hydroxylation and olefin epoxidation are greatly affected by several factors, such as by nature of supporting and axial ligands, spin states of metal ions.[23,28,63,143,156,168–174]

Along with, high valent iron-oxo, manganese-oxo complexes have also investigated and spectroscopically characterized[14,66,137] and these are involved in various oxidation reactions, such as C-H bond activation, oxygen atom transfer (OAT), and electron-transfer (ET) reactions.[173-174] Terminal manganese-oxo complex with buea (tris(N'-tert-butylureaylato)-N-ethylene) aminato) ligand in a tetragonal environment is stabilized by hydrogen bonding with it is notable for its elegant and concise design.[27,175–179] Terminal or bridging manganese-oxo is transient but not separable is supposed to be involved in a critical part of the energy demanding O-O bond formation step. Terminal vanadium/chromium-oxo complexes have also been synthesized to provide an additional chemical basis to understand the reaction mechanism of metalloenzymes and also help to develop artificial oxidation catalysts.[119] For a

long time, many metal-oxo and imido complexes of the 7,8 group have isolated and characterized.[119,121,180–208] High valent metal-oxo of earlier transition metal series are well known, but in late transition series, a few are known. This is related to the "Oxo Wall" concept proposed by Wray and Wrinkler. According to which "The high valent metal-oxo of late transition series are not supported in tetragonal geometry". Whereas, a few metal-oxo species of late transition series are reported in other geometries. High valent metal-oxo species of late transition series, mainly the cobalt-oxo is a reactive transit species involved in the C-H bond activation and O-O bond formation.[209–211] Cobalt(IV)-oxo species are proposed as the reactive intermediate in many cobalt-mediated oxidation reactions.[186–190,192,193] Catalytic oxidation of water to give molecular oxygen, remain a topic of intensive research in developing artificial photosynthesis and water-efficient splitting catalyst (EPR), X-ray absorption, and time resolved Fourier-transform infrared spectroscopic methods provides the evidence for the involvement of terminal and bridging cobalt(IV)-oxo species as a key intermediate in water oxidation reactions. Proposed cobalt(IV)-oxo intermediates are short-lived and highly reactive it makes their chemical and physical properties in catalytic cycles of cobalt-based oxidation catalysts. Even though these are considered more reactive than iron-oxo species because of the weak bond between metal and oxygen,[153,212] reactivity of metal-oxo complexes is governed by the electronic environment about the metal center. Inspired by enzymes such as NOD (nickel oxide dismutase), and its potential towards the activation of small molecules such as H_2O_2,[213–216] mCPBA,[210,217] and NaOCl.[218–220] Synthetic nickel complexes have gained attention but these are less explored as compared to Fe/Mn-oxo intermediates. There, many high valent Ni(III),[213–215,221], and Ni(IV)[221,222] intermediates have been characterized spectroscopically, but the formation of Ni(III), Ni(IV) oxido complexes is controversial to Oxowall premise.[223,224] Although a few high valent Ni(II) and

Ni(III) oxido complexes formed with O_2 and H_2O_2 have been characterized at low temperature.[80,225–228]

1.6 Dinuclear Metal Complexes

Apart from mononuclear species, Fe, Mn, and Cu dinuclear species which are bridged via oxygen as {M-μ(O)-M} are found in enzymes such as tyrosinase, catechol oxidase, methane monooxygenase and play an important role in the biological system.[229] These enzymes use dinuclear metal centers for catalyzing biological transformations. Dinuclear μ-bridged complexes play a very important role in biological systems such as binuclear, non-heme iron enzymes carry out many reactions by dioxygen activation. In non-heme diiron enzymes such as methane monooxygenase (MMO) and ribonucleotide reductase (RNR) high valent non-heme intermediates are reported.[229–233] MMO catalyzes the hydroxylation of methane to methanol via diiron(IV) intermediate and the RNR catalyzes the conversion of ribonucleotides to deoxyribonucleotides to produce a via Fe(III)Fe(IV) intermediate and initiates radical chemistry to generate DNA building blocks. Dinuclear iron-oxo species acts as an active species in hydroxylating and dehydrogenating enzymes.[227] From last few years, many model complexes having dimeric μ-oxo bridged metal ions coordinated with ligands are investigated.

The coordination chemistry of Mn(II) complexes is also very important because Mn is involved in many metalloenzymes such as manganese peroxidase (MnP), manganese thiosulphate oxidase,[234] manganese catalase,[150] ribonucleotide reductase,[235] acid phosphase[236], and superoxide dismutase (MnSOD).[237] Along with manganese many dinuclear cobalt, nickel, and copper complexes, have been explored to mimic the various biological metalloenzyme.[238–244] From literature, the design, construction, and characterization of

dinuclear transition metal complexes has become important because of their intriguing structure and wide applications in magnetism, optics, electronics, catalysis, and fluorescence.[245–252] There has been also a great interest in polynuclear manganese and copper complexes because of their wide application in the field of bioinorganic chemistry and material science.

1.7 C-H/O-H Bond Activation

C-H/O-H bond activation in alkanes offers insertion of a functional group into a relatively inert hydrocarbon in a cost-effective manner and these have a wide application in industry.[60,63,240,253,254] Metal-oxo/superoxo/peroxo species play an important role in hydroxylation, epoxidation, halogenation etc. Understanding the mechanism of C-H/O-H bond activation remains a key consideration, and computational modeling provides insight into the process.[255]

From the last several decades, many affords have been made for the selective transformation of the C-H bond in other functional groups that have many practical implications. As the prosperity of C-H bond functionalization has a very great impact in the industry for the manufacturing of chemicals. Selective C-H bond activation affects the synthesis of chemicals, natural products, polymers, and agrochemicals and these have boosted the economy and efficiency.[256] The direct C-H bond activation can thoroughly shorten the possible routes in natural product synthesis by disconnecting the unknown steps and have the potential for smooth schemes, by eliminating the need for preparation and separation. Two factors regulate selective C-H bond activation one is inert and another one is selectivity control. Challenge in C-H bond cleaving is due to its strong, unpolar, and unreactive nature. The saturated alkanes are formed by C-C and C-H bonds, due to which neither empty orbital of low energy nor filled orbital of higher energy are present to participate in the chemical

reaction. This is different with alkenes, alkynes, and aromatics which provide π and π* orbitals for reactions.[257] Their underutilization in chemical synthesis is may be because of the higher thermodynamic stability of most of the C-H bonds. To overcome this thermodynamic barrier, one has to use the regents that are oxidizing, nonselective, and also incompatible with other functional groups. Some oxidants may have costly and toxic metal ions, their expensiveness and environment incompatibilities makes limit their use. Thus the development of new reagents which are efficient, environment friendly and easily accessible towards the specific C-H bond is an important area in chemical science.

There are two possible approaches for cleaving the C-H bond to attack iron-oxo either may attack from the top of the equatorial position. Both the possibilities have different electronic structures and have different pathways. From, the orbital occupancy evolution diagram, in triplet channel C-H bond electron, is transferred to d_{xz} orbital (π mechanism), for maximum orbital overlap in between electron donor and acceptor orbitals, the substrate may take a horizontal approach to iron-oxo reactive center. This orbital overlap and Pauli repulsion lead to the transition states having bent Fe-O-H angle. In the quintet state pathway, electron of the substrate is shifted to d_z^2 orbital (σ-mechanism). To, the upwards pointing lobe of the Op_z orbital, for overlapping there should be a vertical approach of the substrate; thus transition state has nearly collinear Fe-O-H-C arrangement (see Scheme 1.2).

C-H bond activation mechanism can occur in two possible ways, either by H-atom transfer (HAT) or proton-coupled electron transfer (PCET), these are the fundamental process in the biological and chemical process.[181,226,258] HAT reactions take place via a two-step mechanism, either proton transfer followed by electron transfer or electron transfer is followed by proton transfer, while in PCET proton and electron are transferred simultaneously such as in lipooxygenase and cytochrome P450 enzymes.[259–263]

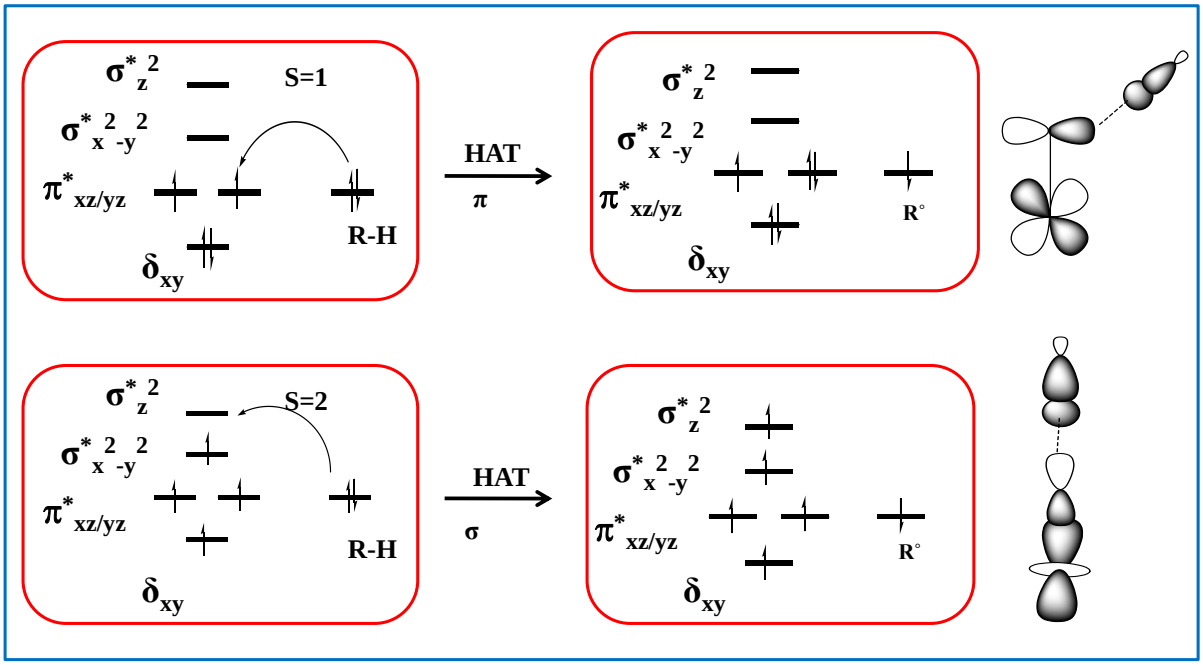

Scheme 1.2. Schematic summary of the electronic structure changes along with the reaction Pathway in the triplet and quintet state of mononuclear non-heme iron(IV)-oxo complexes.

Sason Shaik has led the proponent notion of exchange-enhanced reactivity, where exchange stabilization favors the pathway in which at a metal center number of an unpaired electron during transition state increases.[264–267]As the reactivity of Fe^{IV}=O complexes towards C-H bond, is found that S=2 state is more reactive than the S=1 spin state. While Solomon favors the frontier molecular orbital (FMO) approach that states stereo electronic factors can affect the C-H bond approach towards the Fe=O unit, it depends upon that whether the target C-H bond interacts with σ* FMO or π* FMO of Fe=O unit.[264-267] The reaction may proceed via single state or multi-state reactivity. The fundamental characteristic of TSR/MSR is that the reaction proceeds at least on two potential energy surfaces with different spin multiplicity, either they may cross each other or they may have approximate energy, and different spin states produce different products.

Apart from C-H bond activation, O-H bond also play an important role. Diiron complex (*μ*-oxo)bis(m-carboxylato)) was proposed to cleave the strong O-H bonds of methanol and *t*-

butanol. Reactivity of methanol is studied by this complex, and found that it occurs at spin state of S=2, arised from the triplet state at individual iron center. Antiferromagnetic coupling spin state is the ground state but during the transition state it shows ferromagnetic coupling. It is due to enhance exchanged reactivity. It occurs via σ-π/π-π pathway through proton coupled electron transfer mechanism.

1.8 Importance of Present Thesis Work

The main motto of this thesis is to study the electronic structures and reaction mechanisms occurring during catalytic transformation reactions carried out by biomimetic model complexes using computational tools. For understanding the reaction mechanism, it is very important to study the structure and chemical bonding of the catalytic site. Rate of reactions are affected by the electronic and steric factor, therefore it is essential/important to study how these factors affect the rate of similar reactions. It is difficult to control the relative height of the activation energy barrier to tune their catalytic selectivity experimentally, but computationally it can be achieved. The computational study provides many ideas to understand the important biological process that occurs in nature with the help of high valent metal-oxo species. Additionally, it also helps the experimentalists to design new environment friendly and cheap catalysts.

1.9 Aim of Current Thesis

Metalloenzymes are involved in a wide number of reactions. Many model complexes are purposed that mimic the biological activity of metalloenzymes. The main aim is that these model complex help to understand the reactivity of enzymes and get a catalyst with very high efficiency, selectivity. In this context many heme and non-heme biomimetic models have

been reported, where several catalytic reactions, electronic structures, mechanistic study and reactivity pattern.

The second chapter presents an introduction to the methodology used in our investigations. This assists in understanding the basic computational approaches in calculations. Transition state theory provides a fundamental role in the analysis of chemical reactivity. In our third chapter, we have focused on the electronic structures of TAML ligated mono/dinuclear complexes. Mononuclear and dinuclear iron complexes are found as key intermediates in many synthetic and bio-catalytic reactions. By computing all the possible spin states for these species, we have predicted the ground state, structure-function relationships in their ground states, and analyzed the bonding aspects of these species by employing MO analysis. We have also discussed the shifting of iron centers out of the plane and magnetic coupling between iron and iron/oxygen centers. In our fourth chapter, we have studied the mechanistic study on allylic oxidation of aliphatic compounds cyclohex-2-enol to cyclohex-2-enone by tetraamido iron(V)-oxo. Metal catalyzed allylic oxidations of aliphatic compounds are attractive intermediates and these are very useful in pharmaceutical industries. We have reported electronic structures and also a first-time mechanistic detail of selective allylic oxidation of the cyclohex-2-enol by an oxidant non-heme iron-oxo species. The reaction can be feasible via O-H (***pathway a***) and C-H (***pathway b***) bond activation. We have found that the C-H bond activation is relatively preferable over the O-H and oxygen attack. Additionally, we have also performed the epoxidation of cyclohex-2-enol by iron(V)-oxo species.

In the fifth chapter, we have studied the metal-superoxo species, as it is of great interest because plays an important role in carrying many metal-mediated catalytic transformation reactions. Such catalytic reactivity is affected by many factors such as by nature of metal ions and the ring size of ligands. We have reported the electronic structures of a series of metal-

superoxo species (M=V, Cr, Mn, Fe, and Co) with two different ring size ligands i.e. 13-TMC/14-TMC, and a detailed mechanistic study of C-H bond activation of cyclohexa-1,4-diene followed by the effect of ring size of ligands. Our DFT results show that the electron density at distal oxygen plays an important role in C-H bond activation. Computing energetics of C-H bond activation and mapping potential energy surface, it is found that initial hydrogen abstraction is the rate-determining step, with both the TMC rings with all studied metal-superoxo species. A significant electron density at cyclohex-1,4-diene carbon indicates that the reaction proceeds via a proton-coupled electron transfer mechanism. Here, we have performed first and foremost theoretical studies on ring size, and found that TMC is more reactive towards C-H bond activation and is also supported by structural correlation.

In the sixth chapter, we have studied the formation of high valent metal-oxo species. High valent terminal metal-oxo species containing iron and manganese are involved in biological and catalytic reactions. Terminal metal-oxo of earlier transition metals are well known, whereas metal-oxo of late transition series are rare. This is related to the concept of the "Oxo wall". According to "Oxo Wall" late transition metals cannot support a terminal oxo ligand. Here, we have undertaken the first and foremost theoretical initiative for the formation of metal-oxo from metal hydroperoxo with 3*d* transition metal series (Metal= Cr, Mn, Fe, Co, Ni, Cu) by calculations of the transition state barrier height of O-O bond cleavage with two different octahedral and trigonal bipyramidal geometries. Our calculations show that the barrier height for the cobalt/nickel/copper-oxo is higher than the corresponding chromium, manganese and iron-oxo species, which is also supported by the concept of the "Oxo Wall".

1.10 References

(1) Chin, D.; Means, A. R. *Trends Cell Biol.* **2000**, *10*, 322-328.

(2) Grove, L. E.; Brunold, T. C. *Comments Inorg. Chem.* **2008**, *29*, 134-168.

(3) Opaleye, O.; Rose, R.-S.; Whittaker, M. M.; Woo, E.-J.; Whittaker, J. W.; Pickersgill, R. W. *J. Biol. Chem.* **2006**, *281*, 6428-6433.

(4) Borowski, T.; Bassan, A.; Richards, N. G. J.; Siegbahn, P. E. M. *J. Chem. Theory Comput.* **2005**, *1*, 686-693.

(5) Bull, C.; Niederhoffer, E. C.; Yoshida, T.; Fee, J. A. *J. Am. Chem. Soc.* **1991**, *113*, 4069-4076.

(6) Hearn, A. S.; Tu, C.; Nick, H. S.; Silverman, D. N. *J. Biol. Chem.* **1999**, *274*, 24457-24460.

(7) Hearn, A. S.; Stroupe, M. E.; Cabelli, D. E.; Lepock, J. R.; Tainer, J. A.; Nick, H. S.; Silverman, D. N. *Biochemistry* **2001**, *40*, 12051-12058.

(8) Bollinger, J. M.; Krebs, C. *Curr. Opin. Chem. Biol.* **2007**, *11*, 151-158.

(9) van der Donk, W. A.; Krebs, C.; Bollinger, J. M. *Curr. Opin. Struct. Biol.* **2010**, *20*, 673-683.

(10) Prigge, S. T. *Science* **2004**, *304*, 864-867.

(11) Klinman, J. P. *J. Biol. Chem.* **2006**, *281*, 3013-3016.

(12) Rolff, M.; Tuczek, F. *Angew. Chem., Int. Ed.* **2008**, *47*, 2344-2347.

(13) Ansari, A.; Ansari, M.; Singha, A.; Rajaraman, G. *Chem. -Eur. J.* **2017**, *23*, 10110-10125.

(14) Nam, W. *Acc. Chem. Res.* **2007**, *40*, 465-634.

(15) Suga, M.; Akita, F.; Hirata, K.; Ueno, G.; Murakami, H.; Nakajima, Y.; Shimizu, T.; Yamashita, K.; Yamamoto, M.; Ago, H.; Shen, J.-R. *Nature* **2014**, *517*, 99-103.

(16) Cox, N.; Pantazis, D. A.; Neese, F.; Lubitz, W. *Acc. Chem. Res.* **2013**, *46*, 1588-1596.

(17) Young, K. J.; Brennan, B. J.; Tagore, R.; Brudvig, G. W. *Acc. Chem. Res.* **2015**, *48*, 567-574.

(18) Concepcion, J. J.; Jurss, J. W.; Brennaman, M. K.; Hoertz, P. G.; Patrocinio, A. O. T.; Murakami Iha, N. Y.; Templeton, J. L.; Meyer, T. J. *Acc. Chem. Res.* **2009**, *42*, 1954-1965.

(19) Li, H.; Li, F.; Zhang, B.; Zhou, X.; Yu, F.; Sun, L. *J. Am. Chem. Soc.* **2015**, *137*, 4332-4335.

(20) Du, P.; Eisenberg, R. *Energy Environ. Sci.* **2012**, *5*, 6012-6021.

(21) Joya, K. S.; Joya, Y. F.; Ocakoglu, K.; van de Krol, R. *Angew. Chem., Int. Ed.* **2013**, *52*, 10426-10437.

(22) Kärkäs, M. D.; Verho, O.; Johnston, E. V; Åkermark, B. *Chem. Rev.* **2014**, *114*, 11863-12001.

(23) Nam, W.; Lee, Y.-M.; Fukuzumi, S. *Acc. Chem. Res.* **2014**, *47*, 1146-1154.

(24) Fukuzumi, S.; Ohkubo, K.; Lee, Y.-M.; Nam, W. *Chem. -Eur. J.* **2015**, *21*, 17548-17559.

(25) Engelmann, X.; Monte-Pérez, I.; Ray, K. *Angew. Chem., Int. Ed.* **2016**, *55*, 7632-7649.

(26) Hong, S.; Lee, Y.-M.; Ray, K.; Nam, W. *Coord. Chem. Rev.* **2017**, *334*, 25-42.

(27) Neu, H. M.; Baglia, R. A.; Goldberg, D. P. *Acc. Chem. Res.* **2015**, *48*, 2754-2764.

(28) Puri, M.; Que, L., Jr. *Acc. Chem. Res.* **2015**, *48*, 2443-2452.

(29) Baik, M.-H.; Newcomb, M.; Friesner, R. A.; Lippard, S. J. *Chem. Rev.* **2003**, *103*, 2385-2420.

(30) Holm, R. H.; Solomon, E. I. *Chem. Rev.* **2014**, *114*, 3367-3368.

(31) Kovaleva, E. G.; Lipscomb, J. D. *Nat. Chem. Biol.* **2008**, *4*, 186-193.

(32) Krebs, C.; Galonić Fujimori, D.; Walsh, C. T.; Bollinger, J. M. *Acc. Chem. Res.* **2007**, *40*, 484-492.

(33) Zhang, X.; Li, S. *Nat. Prod. Rep.* **2017**, *34*, 1061-1089.

(34) Guengerich, F. P.; Munro, A. W. *J. Biol. Chem.* **2013**, *288*, 17065-17073.

(35) Jackson, T. A.; Brunold, T. C. *Acc. Chem. Res.* **2004**, *37*, 461-470.

(36) Streit, B. R.; Blanc, B.; Lukat-Rodgers, G. S.; Rodgers, K. R.; DuBois, J. L. *J. Am. Chem. Soc.* **2010**, *132*, 5711-5724.

(37) Siegbahn, P. E. M. *Chem. -Eur. J.* **2008**, *14* , 8290-8302.

(38) Ferraro, D. J.; Gakhar, L.; Ramaswamy, S. *Biochem. Biophys. Res. Commun.* **2005**, *338*, 175-190.

(39) Wolfe, M. D.; Parales, J. V; Gibson, D. T.; Lipscomb, J. D. *J. Biol. Chem.* **2001**, *276*, 1945-1953.

(40) Wolfe, M. D.; Lipscomb, J. D. *J. Biol. Chem.* **2003**, *278*, 829-835.

(41) Barry, S. M.; Challis, G. L. *ACS Catal.* **2013**, *3*, 2362-2370.

(42) Nordlund, P.; Reichard, P. *Annu. Rev. Biochem.* **2006**, *75*, 681-706.

(43) Tinberg, C. E.; Lippard, S. J. *Acc. Chem. Res.* **2011**, *44*, 280-288.

(44) Fox, B. G.; Lyle, K. S.; Rogge, C. E. *Acc. Chem. Res.* **2004**, *37*, 421-429.

(45) Hirao, H.; Kumar, D.; Thiel, W.; Shaik, S. *J. Am. Chem. Soc.* **2005**, *127*, 13007-13018.

(46) Costas, M.; Tipton, A. K.; Chen, K.; Jo, D.-H.; Que, L., Jr. *J. Am. Chem. Soc.* **2001**, *123*, 6722-6723.

(47) de Visser, S. P.; Tahsini, L.; Nam, W. *Chem. -Eur. J.* **2009**, *15*, 5577-5587.

(48) Olsson, E.; Martinez, A.; Teigen, K.; Jensen, V. R. *Inorg. Chem.* **2011**, *2011*, 2720-2732.

(49) Fish, R. H.; Konings, M. S.; Oberhausen, K. J.; Fong, R. H.; Yu, W. M.; Christou, G.; Vincent, J. B.; Coggin, D. K.; Buchanan, R. M. *Inorg. Chem.* **1991**, *30*, 3002-3006.

(50) Hirao, H.; Que, L.; Nam, W.; Shaik, S. *Chem. Eur. J.* **2008**, *14*, 1740-1756.

(51) Jensen, M. P.; Lange, S. J.; Mehn, M. P.; Que, E. L.; Que, L., Jr. *J. Am. Chem. Soc.*

2003, *125*, 2113-2128.

(52) Costas, M.; Mehn, M. P.; Jensen, M. P.; Que, L., Jr. *Chem. Rev.* **2004**, *104*, 939-986.

(53) Que, L., Jr. *Dalton Trans.* **1997**, 21, 3933-3940.

(54) Tahsini, L.; Bagherzadeh, M.; Nam, W.; de Visser, S. P. *Inorg. Chem.* **2009**, *48*, 6661-6669.

(55) Bassan, A.; Blomberg, M. R. A.; Siegbahn, P. E. M.; Que, L., Jr. *Angew. Chem., Int. Ed.* **2005**, *44*, 2939-2941.

(56) Bassan, A.; Blomberg, M. R. A.; Siegbahn, P. E. M.; Que, L., Jr. *J. Am. Chem. Soc.* **2002**, *124*, 11056-11063.

(57) de Visser, S. P. *J. Am. Chem. Soc.* **2009**, *132*, 1087-1097.

(58) de Visser, S. P. *Angew. Chem., Int. Ed.* **2006**, *45*, 1790-1793.

(59) de Visser, S. P.; Kumar, D.; Cohen, S.; Shacham, R.; Shaik, S. *J. Am. Chem. Soc.* **2004**, *126*, 8362-8363.

(60) de Visser, S. P.; Oh, K.; Han, A.-R.; Nam, W. *Inorg. Chem.* **2007**, *46*, 4632-4641.

(61) de Visser, S. P.; Rohde, J.-U.; Lee, Y.-M.; Cho, J.; Nam, W. *Coord. Chem. Rev.* **2013**, *257*, 381-393.

(62) Marchetti, L.; Levine, M. Biomimetic Catalysis. *ACS Catal.* **2011**, *1*, 1090-1118.

(63) Nam, W. *Acc. Chem. Res.* **2007**, *40*, 522-531.

(64) Sheng, Y.; Abreu, I. A.; Cabelli, D. E.; Maroney, M. J.; Miller, A.-F.; Teixeira, M.; Valentine, J. S. *Chem. Rev.* **2014**, *114*, 3854-3918.

(65) Yano, J.; Yachandra, V. *Chem. Rev.* **2014**, *114*, 4175-4205.

(66) Ortiz de Montellano, P. R. *Chem. Rev.* **2010**, *110*, 932-948.

(67) Wackett, L. P. *Enzyme Microb. Technol.* **2002**, *31*, 577-587.

(68) Breslow, R. *J. Biol. Chem.* **2009**, *284*, 1337-1342.

(69) Breslow, R. *Chem. Soc. Rev.* **1972**, *1*, 553-580.

(70) Leete, E. *Chem. Commun.* **1972**, *19*, 1091a-1091a.

(71) Burke, D. E.; le Quesne, P. W. *Chem. Commun.* **1972**, 11, 678-678.

(72) Breslow, R.; Dong, S. D. *Chem. Rev.* **1998**, *98*, 1997-2012.

(73) Bassan, A.; Blomberg, M. R. A.; Siegbahn, P. E. M. *J. Biol. Inorg. Chem.* **2004**, *9*, 439-452.

(74) Chen, P.; Solomon, E. I. *Proc. Natl. Acad. Sci.* **2004**, *101*, 13105-13110.

(75) Chow, M. S.; Liu, L. V; Solomon, E. I. *Proc. Natl. Acad. Sci.* **2008**, *105*, 13241-13245.

(76) Decker, A.; Chow, M. S.; Kemsley, J. N.; Lehnert, N.; Solomon, E. I. *J. Am. Chem. Soc.* **2006**, *128*, 4719-4733.

(77) Liu, L. V; Bell, C. B.; Wong, S. D.; Wilson, S. A.; Kwak, Y.; Chow, M. S.; Zhao, J.; Hodgson, K. O.; Hedman, B.; Solomon, E. I. *Proc. Natl. Acad. Sci.* **2010**, *107*, 22419-22424.

(78) Neibergall, M. B.; Stubna, A.; Mekmouche, Y.; Münck, E.; Lipscomb, J. D. *Biochemistry* **2007**, *46*, 8004-8016.

(79) Karlsson, A. *Science* **2003**, *299*, 1039-1042.

(80) Yao, S.; Driess, M. *Acc. Chem. Res.* **2011**, *45*, 276-287.

(81) Bakac, A. *Coord. Chem. Rev.* **2006**, *250*, 2046-2058.

(82) Solomon, E. I.; Brunold, T. C.; Davis, M. I.; Kemsley, J. N.; Lee, S.-K.; Lehnert, N.; Neese, F.; Skulan, A. J.; Yang, Y.-S.; Zhou, J. *Chem. Rev.* **2000**, *100*, 235-350.

(83) Klotz, I. M.; Kurtz, D. M. *Chem. Rev.* **1994**, *94*, 567-568.

(84) Cramer, C. J.; Tolman, W. B.; Theopold, K. H.; Rheingold, A. L. *Proc. Natl. Acad. Sci. U. S. A.* **2003**, *100*, 3635-3640.

(85) Cramer, C. J.; Tolman, W. B. *Acc. Chem. Res.* **2007**, *40*, 601-608.

(86) Kunishita, A.; Kubo, M.; Sugimoto, H.; Ogura, T.; Sato, K.; Takui, T.; Itoh, S. *J. Am.*

Chem. Soc. **2009**, *131*, 2788-2789.

(87) Schax, F.; Suhr, S.; Bill, E.; Braun, B.; Herwig, C.; Limberg, C. *Angew. Chem., Int. Ed.* **2014**, *54*, 1352-1356.

(88) Chiang, C.-W.; Kleespies, S. T.; Stout, H. D.; Meier, K. K.; Li, P.-Y.; Bominaar, E. L.; Que, L.; Münck, E.; Lee, W.-Z. *J. Am. Chem. Soc.* **2014**, *136*, 10846-10849.

(89) Chen, H.; Cho, K.-B.; Lai, W.; Nam, W.; Shaik, S. *J. Chem. Theory Comput.* **2012**, *8*, 915-926.

(90) Lee, Y.-M.; Hong, S.; Morimoto, Y.; Shin, W.; Fukuzumi, S.; Nam, W. *J. Am. Chem. Soc.* **2010**, *132*, 10668-10670.

(91) Mukherjee, A.; Cranswick, M. A.; Chakrabarti, M.; Paine, T. K.; Fujisawa, K.; Mu□nck, E.; Que, L., Jr. *Inorg. Chem.* **2010**, *49*, 3618-3628.

(92) Cho, K. Bin; Chen, H.; Janardanan, D.; de Visser, S. P.; Shaik, S.; Nam, W. *Chem. Commun.* **2012**, *48*, 2189-2191.

(93) Neidig, M. L.; Solomon, E. I. *Chem. Commun.* **2005**, *47*, 5843-5863.

(94) Solomon, E. I.; Wong, S. D.; Liu, L. V; Decker, A.; Chow, M. S. *Curr. Opin. Chem. Biol.* **2009**, *13*, 99-113.

(95) Abu-Omar, M. M.; Loaiza, A.; Hontzeas, N. *Chem. Rev.* **2005**, *105*, 2227-2252.

(96) Itoh, S. *Acc. Chem. Res.* **2015**, *48*, 2066-2074.

(97) Lee, J. Y.; Karlin, K. D. *Curr. Opin. Chem. Biol.* **2015**, *25*, 184-193.

(98) Pirovano, P.; Magherusan, A. M.; McGlynn, C.; Ure, A.; Lynes, A.; McDonald, A. R. *Angew. Chem., Int. Ed.* **2014**, *53*, 5946-5950.

(99) Lee, J. Y.; Peterson, R. L.; Ohkubo, K.; Garcia-Bosch, I.; Himes, R. A.; Woertink, J.; Moore, C. D.; Solomon, E. I.; Fukuzumi, S.; Karlin, K. D. *J. Am. Chem. Soc.* **2014**, *136*, 9925-9937.

(100) Peterson, R. L.; Himes, R. A.; Kotani, H.; Suenobu, T.; Tian, L.; Siegler, M. A.;

Solomon, E. I.; Fukuzumi, S.; Karlin, K. D. *J. Am. Chem. Soc.* **2011**, *133*, 1702-1705.

(101) Bruijnincx, P. C. A.; van Koten, G.; Klein Gebbink, R. J. M. *Chem. Soc. Rev.* **2008**, *37* , 2716-2744.

(102) Phillips, S. E. V. *Nature* **1978**, *273*, 247-248.

(103) Collman, J. P.; Gagne, R. R.; Reed, C. A.; Robinson, W. T.; Rodley, G. A. *Proc. Natl. Acad. Sci.* **1974**, *71*, 1326-1329.

(104) Hong, S.; Lee, Y.-M.; Shin, W.; Fukuzumi, S.; Nam, W. *J. Am. Chem. Soc.* **2009**, *131*, 13910-13911.

(105) Badiei, Y. M.; Siegler, M. A.; Goldberg, D. P. *J. Am. Chem. Soc.* **2011**, *133*, 1274-1277.

(106) Hong, S.; Sutherlin, K. D.; Park, J.; Kwon, E.; Siegler, M. A.; Solomon, E. I.; Nam, W. *Nat. Commun.* **2014**, *5*, 5440-5447.

(107) Bakac, A.; Scott, S. L.; Espenson, J. H.; Rodgers, K. R. *J. Am. Chem. Soc.* **1995**, *117*, 6483-6488.

(108) Bakac, A. *J. Am. Chem. Soc.* **1997**, *119*, 10726-10731.

(109) Cho, J.; Woo, J.; Nam, W. *J. Am. Chem. Soc.* **2010**, *132*, 5958-5959.

(110) Cho, J.; Woo, J.; Eun Han, J.; Kubo, M.; Ogura, T.; Nam, W. *Chem. Sci.* **2011**, *2*, 2057-2062.

(111) Ansari, A.; Rajaraman, G. *Dataset Pap. Sci.* **2014**, *2014*, 1-7.

(112) Gordon, J. B.; Vilbert, A. C.; Siegler, M. A.; Lancaster, K. M.; Moënne-Loccoz, P.; Goldberg, D. P. *J. Am. Chem. Soc.* **2019**, *141*, 3641-3653.

(113) Maiti, D.; Fry, H. C.; Woertink, J. S.; Vance, M. A.; Solomon, E. I.; Karlin, K. D. *J. Am. Chem. Soc.* **2007**, *129*, 264-265.

(114) Fujii, T.; Yamaguchi, S.; Hirota, S.; Masuda, H. *Dalton Trans.* **2008**, *1*, 164-170.

(115) Maiti, D.; Lee, D.-H.; Gaoutchenova, K.; Würtele, C.; Holthausen, M. C.; Narducci

Sarjeant, A. A.; Sundermeyer, J.; Schindler, S.; Karlin, K. D. *Angew. Chem., Int. Ed.* **2008**, *47*, 82-85.

(116) Kim, J.; Shin, B.; Kim, H.; Lee, J.; Kang, J.; Yanagisawa, S.; Ogura, T.; Masuda, H.; Ozawa, T.; Cho, J. *Inorg. Chem.* **2015**, *54*, 6176-6183.

(117) McDonald, A. R.; Que, L. *Coord. Chem. Rev.* **2013**, *257*, 414-428.

(118) Kent Barefield, E. *Coord. Chem. Rev.* **2010**, *254*, 1607-1627.

(119) van Eldik, R. *Coord. Chem. Rev.* **2007**, *251*, 1649-1662.

(120) Himes, R. A.; Karlin, K. D. *Curr. Opin. Chem. Biol.* **2009**, *13*, 119-131.

(121) Gunay, A.; Theopold, K. H. *Chem. Rev.* **2010**, *110*, 1060-1081.

(122) Cho, J.; Sarangi, R.; Nam, W. *Acc. Chem. Res.* **2012**, *45*, 1321-1330.

(123) de Visser, S. P.; Rohde, J. U.; Lee, Y. M.; Cho, J.; Nam, W. *Coord. Chem. Rev.* **2013**, *257*, 381-393.

(124) Yokoyama, A.; Han, J. E.; Cho, J.; Kubo, M.; Ogura, T.; Siegler, M. A.; Karlin, K. D.; Nam, W. *J. Am. Chem. Soc.* **2012**, *134*, 15269-15272.

(125) Cho, J.; Sarangi, R.; Nam, W. *Acc. Chem. Res.* **2012**, *45*, 1321-1330.

(126) Cho, J.; Jeon, S.; Wilson, S. A.; Liu, L. V; Kang, E. A.; Braymer, J. J.; Lim, M. H.; Hedman, B.; Hodgson, K. O.; Valentine, J. S.; Solomon, E. I.; Nam, W. *Nature* **2011**, *478*, 502-505.

(127) Cho, J.; Sarangi, R.; Annaraj, J.; Kim, S. Y.; Kubo, M.; Ogura, T.; Solomon, E. I.; Nam, W. *Nat. Chem.* **2009**, *1*, 568-572.

(128) Cho, J.; Woo, J.; Nam, W. *J. Am. Chem. Soc.* **2012**, *134*, 11112-11115.

(129) Wang, F.; Sun, W.; Xia, C.; Wang, Y. *J. Biol. Inorg. Chem.* **2017**, *22*, 987-998.

(130) Decker, A.; Rohde, J.-U.; Klinker, E. J.; Wong, S. D.; Que, L., Jr.; Solomon, E. I. *J. Am. Chem. Soc.* **2007**, *129*, 15983-15996.

(131) Pestovsky, O.; Stoian, S.; Bominaar, E. L.; Shan, X.; Munck, E.; Que, L., Jr., Bakac,

A. *Angew. Chem., Int. Ed.* **2005**, *44*, 6871-6874.

(132) Ansari, A.; Rajaraman, G. *Phys. Chem. Chem. Phys.* **2014**, *16*, 14601-14613.

(133) Kieber-Emmons, M. T.; Annaraj, J.; Seo, M. S.; Van Heuvelen, K. M.; Tosha, T.; Kitagawa, T.; Brunold, T. C.; Nam, W.; Riordan, C. G. *J. Am. Chem. Soc.* **2006**, *128*, 14230-14231.

(134) Sarangi, R.; Cho, J.; Nam, W.; Solomon, E. I. *Inorg. Chem.* **2010**, *50*, 614-620.

(135) Garcia-Bosch, I.; Cowley, R. E.; Díaz, D. E.; Siegler, M. A.; Nam, W.; Solomon, E. I.; Karlin, K. D. *Chem. -Eur. J.* **2016**, *22*, 5133-5137.

(136) Hong, S.; So, H.; Yoon, H.; Cho, K.-B.; Lee, Y.-M.; Fukuzumi, S.; Nam, W. *Dalton Trans.* **2013**, *42*, 7842-7845.

(137) Krest, C. M.; Onderko, E. L.; Yosca, T. H.; Calixto, J. C.; Karp, R. F.; Livada, J.; Rittle, J.; Green, M. T. *J. Biol. Chem.* **2013**, *288*, 17074-17081.

(138) Nocera, D. G. *Acc. Chem. Res.* **2012**, *45*, 767-776.

(139) Blakemore, J. D.; Crabtree, R. H.; Brudvig, G. W. *Chem. Rev.* **2015**, *115*, 12974-13005.

(140) Svastits, E. W.; Dawson, J. H.; Breslow, R.; Gellman, S. H. *J. Am. Chem. Soc.* **1985**, *107*, 6427-6428.

(141) Lancaster, K. M.; Roemelt, M.; Ettenhuber, P.; Hu, Y.; Ribbe, M. W.; Neese, F.; Bergmann, U.; DeBeer, S. *Science* **2011**, *334*, 974-977.

(142) Thorneley, R. N. F.; Lowe, D. J. *Biochem. J.* **1984**, *224*, 903-909.

(143) Thorneley, R. N. F.; Lowe, D. J. *Biochem. J.* **1984**, *224*, 887-894.

(144) Lowe, D. J.; Thorneley, R. N. *Biochem. J.* **1984**, *224*, 877-886.

(145) Lowe, D. J.; Thorneley, R. N. F. *Biochem. J.* **1984**, *224*, 895-901.

(146) Ertl, G. *Angew. Chem., Int. Ed.* **1990**, *29*, 1219-1227.

(147) Pierpont, A. W.; Cundari, T. R. *Inorg. Chem.* **2009**, *49*, 2038-2046.

(148) Chakrabarty, S.; Austin, R. N.; Deng, D.; Groves, J. T.; Lipscomb, J. D. *J. Am. Chem. Soc.* **2007**, *129*, 3514-3515.

(149) Friedle, S.; Reisner, E.; Lippard, S. J. *Chem. Soc. Rev.* **2010**, *39*, 2768-2779.

(150) Fujii, H. *Coord. Chem. Rev.* **2002**, *226*, 51-60.

(151) Groves, J. T. *J. Inorg. Biochem.* **2006**, *100*, 434-447.

(152) Groves, J. T.; Haushalter, R. C.; Nakamura, M.; Nemo, T. E.; Evans, B. J. *J. Am. Chem. Soc.* **1981**, *103*, 2884-2886.

(153) Jung, C. *Biochim. Biophys. Acta - Proteins Proteomics* **2011**, *1814*, 46-57.

(154) Baldwin, J. E.; Bradley, M. *Chem. Rev.* **1990**, *90*, 1079-1088.

(155) Kleespies, S. T.; Oloo, W. N.; Mukherjee, A.; Que, L., Jr. *Inorg. Chem.* **2015**, *54*, 5053-5064.

(156) Chen, Z.; Yin, G. *Chem. Soc. Rev.* **2015**, *44*, 1083-1100.

(157) Rittle, J.; Green, M. T. *Science* **2010**, *330*, 933-937.

(158) Sono, M.; Roach, M. P.; Coulter, E. D.; Dawson, J. H. *Chem. Rev.* **1996**, *96*, 2841-2888.

(159) Meunier, B.; de Visser, S. P.; Shaik, S. *Chem. Rev.* **2004**, *104*, 3947-3980.

(160) Grapperhaus, C. A.; Mienert, B.; Bill, E.; Weyhermüller, T.; Wieghardt, K. *Inorg. Chem.* **2000**, *39*, 5306-5317.

(161) Rohde, J. U.; In, J. H.; Lim, M. H.; Brennessel, W. W.; Bukowski, M. R.; Stubna, A.; Münck, E.; Nam, W.; Que, L., Jr. *Science* **2003**, *299*, 1037-1039.

(162) Sastri, C. V; Park, M. J.; Ohta, T.; Jackson, T. A.; Stubna, A.; Seo, M. S.; Lee, J.; Kim, J.; Kitagawa, T.; Münck, E.; Que Lawrence; Nam, W. *J. Am. Chem. Soc.* **2005**, *127*, 12494-12495.

(163) Decker, A.; Rohde, J.-U.; Que Lawrence; Solomon, E. I. *J. Am. Chem. Soc.* **2004**, *126*, 5378-5379.

(164) Pestovsky, O.; Stoian, S.; Bominaar, E. L.; Shan, X.; Münck, E.; Que, L.; Bakac, A. *Angew. Chem., Int. Ed.* **2005**, *44*, 6871-6874.

(165) MacBeth, C. E.; Golombek, A. P.; Young, V. G.; Yang, C.; Kuczera, K.; Hendrich, M. P.; Borovik, A. S. *Science* **2000**, *289*, 938-941.

(166) Lacy, D. C.; Gupta, R.; Stone, K. L.; Greaves, J.; Ziller, J. W.; Hendrich, M. P.; Borovik, A. S. *J. Am. Chem. Soc.* **2010**, *132*, 12188-12190.

(167) Makhlynets, O.; Das, P.; Taktak, S.; Flook, M.; Mas-Balleste, R.; Rybak-Akimova, E.; Que, L., Jr. *Chem. -Eur. J.* **2009**, *15*, 13171-13180.

(168) Cook, S. A.; Borovik, A. S. *Acc. Chem. Res.* **2015**, *48*, 2407-2414.

(169) Denisov, I. G.; Makris, T. M.; Sligar, S. G.; Schlichting, I. *Chem. Rev.* **2005**, *105*, 2253-2278.

(170) Yin, G. *Acc. Chem. Res.* **2012**, *46*, 483-492.

(171) Ray, K.; Pfaff, F. F.; Wang, B.; Nam, W. *J. Am. Chem. Soc.* **2014**, *136*, 13942-13958.

(172) Ray, K.; Heims, F.; Schwalbe, M.; Nam, W. *Curr. Opin. Chem. Biol.* **2015**, *25*, 159-171.

(173) Nam, W. *Acc. Chem. Res*. **2015**, *48*, 2415-2423.

(174) Cook, S. A.; Hill, E. A.; Borovik, A. S. *Biochemistry* **2015**, *54*, 4167-4180.

(175) Song, W. J.; Seo, M. S.; DeBeer George, S.; Ohta, T.; Song, R.; Kang, M.-J.; Tosha, T.; Kitagawa, T.; Solomon, E. I.; Nam, W. *J. Am. Chem. Soc.* **2007**, *129*, 1268-1277.

(176) Liu, W.; Groves, J. T. *Acc. Chem. Res.* **2015**, *48*, 1727-1735.

(177) Taguchi, T.; Gupta, R.; Lassalle-Kaiser, B.; Boyce, D. W.; Yachandra, V. K.; Tolman, W. B.; Yano, J.; Hendrich, M. P.; Borovik, A. S. *J. Am. Chem. Soc.* **2012**, *134*, 1996-1999.

(178) Taguchi, T.; Stone, K. L.; Gupta, R.; Kaiser-Lassalle, B.; Yano, J.; Hendrich, M. P.; Borovik, A. S. *Chem. Sci.* **2014**, *5*, 3064-3071.

(179) Hong, S.; Lee, Y.-M.; Sankaralingam, M.; Vardhaman, A. K.; Park, Y. J.; Cho, K.-B.; Ogura, T.; Sarangi, R.; Fukuzumi, S.; Nam, W. *J. Am. Chem. Soc.* **2016**, *138*, 8523-8532.

(180) Oloo, W. N.; Que, L., Jr. *Acc. Chem. Res.* **2015**, *48*, 2612-2621.

(181) Parsell, T. H.; Yang, M.-Y.; Borovik, A. S. *J. Am. Chem. Soc.* **2009**, *131*, 2762-2763.

(182) Gupta, R.; Borovik, A. S. *J. Am. Chem. Soc.* **2003**, *125*, 13234-13242.

(183) Gupta, R.; MacBeth, C. E.; Young Victor G.; Borovik, A. S. *J. Am. Chem. Soc.* **2002**, *124*, 1136-1137.

(184) Shirin, Z.; Hammes, B. S.; Young Victor G.; Borovik, A. S. *J. Am. Chem. Soc.* **2000**, *122*, 1836-1837.

(185) Lyashenko, G.; Herbst-Irmer, R.; Jancik, V.; Pal, A.; Mösch-Zanetti, N. C. *Inorg. Chem.* **2007**, *47*, 113-120.

(186) Lu, E.; Chu, J.; Chen, Y.; Borzov, M. V; Li, G. *Chem. Commun.* **2011**, *47*, 743-745.

(187) Lu, E.; Li, Y.; Chen, Y. *Chem. Commun.* **2010**, *46*, 4469-4471.

(188) Hersleth, H.-P.; Ryde, U.; Rydberg, P.; Görbitz, C. H.; Andersson, K. K. *J. Inorg. Biochem.* **2006**, *100*, 460-476.

(189) Que, L., Jr. *Acc. Chem. Res.* **2007**, *40*, 493-500.

(190) Berry, J. F. *Comments Inorg. Chem.* **2009**, *30*, 28-66.

(191) Eikey, R. *Coord. Chem. Rev.* **2003**, *243*, 83-124.

(192) Fukuzumi, S. *Coord. Chem. Rev.* **2013**, *257*, 1564-1575.

(193) Borovik, A. S. *Chem. Soc. Rev.* **2011**, *40*, 1870-1874.

(194) Shi, S.; Wang, Y.; Xu, A.; Wang, H.; Zhu, D.; Roy, S. B.; Jackson, T. A.; Busch, D. H.; Yin, G. *Angew. Chem., Int. Ed.* **2011**, *50*, 7321-7324.

(195) Betley, T. A.; Wu, Q.; Van Voorhis, T.; Nocera, D. G. *Inorg. Chem.* **2008**, *47*, 1849-1861.

(196) Berry, J. F.; DeBeer George, S.; Neese, F. *Phys. Chem. Chem. Phys.* **2008**, *10*, 4361-4374.

(197) Berry, J. F.; Bill, E.; Bothe, E.; George, S. D.; Mienert, B.; Neese, F.; Wieghardt, K. *Science* **2006**, *312*, 1937-1941.

(198) Chen, J.; Lee, Y.-M.; Davis, K. M.; Wu, X.; Seo, M. S.; Cho, K.-B.; Yoon, H.; Park, Y. J.; Fukuzumi, S.; Pushkar, Y. N.; Nam, W. *J. Am. Chem. Soc.* **2013**, *135*, 6388-6391.

(199) Fukuzumi, S.; Morimoto, Y.; Kotani, H.; Naumov, P.; Lee, Y.-M.; Nam, W. *Nat. Chem.* **2010**, *2*, 756-759.

(200) Mehn, M. P.; Peters, J. C. *J. Inorg. Biochem.* **2006**, *100*, 634-643.

(201) Eikey, R. A.; Khan, S. I.; Abu-Omar, M. M. *Angew. Chem., Int. Ed.* **2002**, *41*, 3591-3595.

(202) Danopoulos, A. A.; Green, J. C.; Hursthouse, M. B. *J. Organomet. Chem.* **1999**, *591*, 36-44.

(203) Cho, J.; Woo, J.; Eun Han, J.; Kubo, M.; Ogura, T.; Nam, W. *Chem. Sci.* **2011**, *2*, 2057-2062.

(204) Groysman, S.; Villagrán, D.; Nocera, D. G. *Inorg. Chem.* **2010**, *49*, 10759-10761.

(205) Janas, Z.; Sobota, P. *Coord. Chem. Rev.* **2005**, *249*, 2144-2155.

(206) Waidmann, C. R.; DiPasquale, A. G.; Mayer, J. M. *Inorg. Chem.* **2010**, *49*, 2383-2391.

(207) Sousa, S. C. A.; Cabrita, I.; Fernandes, A. C. *Chem. Soc. Rev.* **2012**, *41*, 5641-5653.

(208) Mösch-Zanetti, N. C.; Wurm, D.; Volpe, M.; Lyashenko, G.; Harum, B.; Belaj, F.; *Inorg. Chem.* **2010**, *49*, 8914-8921.

(209) Fukuzumi, S.; Mandal, S.; Mase, K.; Ohkubo, K.; Park, H.; Benet-Buchholz, J.; Nam, W.; Llobet, A. *J. Am. Chem. Soc.* **2012**, *134*, 9906-9909.

(210) Pfaff, F. F.; Heims, F.; Kundu, S.; Mebs, S.; Ray, K. *Chem. Commun.* **2012**, *48*, 3730-

3732.

(211) Zhang, M.; de Respinis, M.; Frei, H. *Nat. Chem.* **2014**, *6*, 362-367.

(212) Limberg, C. *Angew. Chem., Int. Ed.* **2009**, *121*, 2305-2308.

(213) Cho, J.; Kang, H. Y.; Liu, L. V.; Sarangi, R.; Solomon, E. I.; Nam, W. *Chem. Sci.* **2013**, *4*, 1502-1508.

(214) Honda, K.; Cho, J.; Matsumoto, T.; Roh, J.; Furutachi, H.; Tosha, T.; Kubo, M.; Fujinami, S.; Ogura, T.; Kitagawa, T.; Suzuki, M. *Angew. Chem., Int. Ed.* **2009**, *48*, 3304-3307.

(215) Tano, T.; Doi, Y.; Inosako, M.; Kunishita, A.; Kubo, M.; Ishimaru, H.; Ogura, T.; Sugimoto, H.; Itoh, S. *Bull. Chem. Soc. Jpn.* **2010**, *83*, 530-538.

(216) Morimoto, Y.; Bunno, S.; Fujieda, N.; Sugimoto, H.; Itoh, S. *J. Am. Chem. Soc.* **2015**, *137*, 5867-5870.

(217) Corona, T.; Pfaff, F. F.; Acuña-Parés, F.; Draksharapu, A.; Whiteoak, C. J.; Martin-Diaconescu, V.; Lloret-Fillol, J.; Browne, W. R.; Ray, K.; Company, A. *Chem. -Eur. J.* **2015**, *21*, 15029-15038.

(218) Draksharapu, A.; Codolà, Z.; Gómez, L.; Lloret-Fillol, J.; Browne, W. R.; Costas, M. *Inorg. Chem.* **2015**, *54*, 10656-10666.

(219) Pirovano, P.; Farquhar, E. R.; Swart, M.; McDonald, A. R. *J. Am. Chem. Soc.* **2016**, *138*, 14362-14370.

(220) Corona, T.; Draksharapu, A.; Padamati, S. K.; Gamba, I.; Martin-Diaconescu, V.; Acuna-Parés, F.; Browne, W. R.; Company, A. *J. Am. Chem. Soc.* **2016**, *138*, 12987-12996.

(221) Corona, T.; Company, A. *Chem. -Eur. J.* **2016**, *22*, 13422-13429.

(222) Corona, T.; Draksharapu, A.; Padamati, S. K.; Gamba, I.; Martin-Diaconescu, V.; Acuña-Parés, F.; Browne, W. R.; Company, A. *J. Am. Chem. Soc.* **2016**, *138*, 12987-

12996.

(223) Gray, H. B.; Hare, C. R. *Inorg. Chem.* **1962**, *1*, 363-368.

(224) O'Halloran, K. P.; Zhao, C.; Ando, N. S.; Schultz, A. J.; Koetzle, T. F.; Piccoli, P. M. B.; Hedman, B.; Hodgson, K. O.; Bobyr, E.; Kirk, M. L.; Knottenbelt, S.; Depperman, E. C.; Stein, B.; Anderson, T. M.; Cao, R.; Geletii, Y. V; Hardcastle, K. I.; Musaev, D. G.; Neiwert, W. A.; Fang, X.; Morokuma, K.; Wu, S.; Kögerler, P.; Hill, C. L. *Inorg. Chem.* **2012**, *51*, 7025-7031.

(225) Mandimutsira, B. S.; Yamarik, J. L.; Brunold, T. C.; Gu, W.; Cramer, S. P.; Riordan, C. G. *J. Am. Chem. Soc.* **2001**, *123*, 9194-9195.

(226) Weinberg, D. R.; Gagliardi, C. J.; Hull, J. F.; Murphy, C. F.; Kent, C. A.; Westlake, B. C.; Paul, A.; Ess, D. H.; McCafferty, D. G.; Meyer, T. J. *Chem. Rev.* **2012**, *112*, 4016-4093.

(227) Solans-Monfort, X.; Fierro, J. L. G.; Hermosilla, L.; Sieiro, C.; Sodupe, M.; Mas-Ballesté, *Dalton Trans.* **2011**, *40*, 6868-6876.

(228) Balamurugan, M.; Mayilmurugan, R.; Suresh, E.; Palaniandavar, M. *Dalton Trans.* **2011**, *40*, 9413-9424.

(229) Wallar, B. J.; Lipscomb, J. D. *Chem. Rev.* **1996**, *96*, 2625-2658.

(230) Bollinger, J. M.; Edmondson, D. E.; Huynh, B. H.; Filley, J.; Norton, J. R.; Stubbe, J. *Science.* **1991**, *253*, 292-298.

(231) Ravi, N.; Bollinger, J. M.; Huynh, B. H.; Stubbe, J.; Edmondson, D. E. *J. Am. Chem. Soc.* **1994**, *116*, 8007-8014.

(232) Sturgeon, B. E.; Burdi, D.; Chen, S.; Huynh, B.-H.; Edmondson, D. E.; Stubbe, J.; Hoffman, B. M. *J. Am. Chem. Soc.* **1996**, *118*, 7551-7557.

(233) Ansari, A.; Ansari, M.; Singha, A.; Rajaraman, G. *Chem. -Eur. J.* **2017**, *23*, 10110-10125.

(234) Cammack, R.; Chapman, A.; Lu, W.-P.; Karagouni, A.; Kelly, D. P. *FEBS Lett.* **1989**, *253*, 239-243.

(235) Nordlund, P.; Sjöberg, B.-M.; Eklund, H. *Nature* **1990**, *345*, 593-598.

(236) Sugiura, Y.; Kawabe, H.; Tanaka, H.; Fujimoto, S.; Ohara, A. *J. Biol. Chem.* **1981**, *256*, 10664-10670.

(237) Mathieu, E.; Bernard, A.-S.; Delsuc, N.; Quévrain, E.; Gazzah, G.; Lai, B.; Chain, F.; Langella, P.; Bachelet, M.; Masliah, J.; Seksik, P.; Policar, C. A *Inorg. Chem.* **2017**, *56*, 2545-2555.

(238) Singh, Y. P.; Patel, R. N.; Singh, Y.; Choquesillo-Lazarte, D.; Butcher, R. J. *Dalton Trans.* **2017**, *46*, 2803-2820.

(239) Jana, M.; Majumdar, A. *Inorg. Chem.* **2018**, *57*, 617-632.

(240) Solomon, E. I.; Sundaram, U. M.; Machonkin, T. E. *Chem. Rev.* **1996**, *96*, 2563-2606.

(241) Cho, K.-B.; Cho, J.; Shaik, S.; Nam, W. *J. Phys. Chem. Lett.* **2014**, *5*, 2437-2442.

(242) Chakraborty, P.; Majumder, I.; Kara, H.; Chattopadhyay, S. K.; Zangrando, E.; Das, D. *Inorganica Chim. Acta* **2015**, *436*, 139-145.

(243) Das, K.; Datta, A.; Roy, S.; Clegg, J. K.; Garribba, E.; Sinha, C.; Kara, H. *Polyhedron* **2014**, *78*, 62-71.

(244) Rompel, A.; Fischer, H.; Büldt-Karentzopoulos, K.; Meiwes, D.; Zippel, F.; Nolting, H.-F.; Hermes, C.; Krebs, B.; Witzel, H. *J. Inorg. Biochem.* **1995**, *59*, 715-719.

(245) Gatteschi, D.; Sessoli, R. *Angew. Chem., Int. Ed.* **2003**, *42*, 268-297.

(246) Taguchi, T.; Wernsdorfer, W.; Abboud, K. A.; Christou, G. *Inorg. Chem.* **2009**, *49*, 199-208.

(247) Gamer, M. T.; Lan, Y.; Roesky, P. W.; Powell, A. K.; Clérac, R. *Inorg. Chem.* **2008**, *47*, 6581-6583.

(248) Albores, P.; Rentschler, E. *Angew. Chem., Int. Ed.* **2009**, *48*, 9366-9370.

(249) Zhang, S.-H.; Tang, M.-F.; Ge, C.-M. *Allg. Chemie* **2009**, *635*, 1442-1446.

(250) Ma, L.-F.; Wang, L.-Y.; Huo, X.-K.; Wang, Y.-Y.; Fan, Y.-T.; Wang, J.-G.; Chen, S.-H. *Cryst. Growth Des.* **2008**, *8*, 620-628.

(251) Zhang, S.-H.; Zhou, Y.-L.; Sun, X.-J.; Wei, L.-Q.; Zeng, M.-H.; Liang, H. *J. Solid State Chem.* **2009**, *182*, 2991-2996.

(252) Zhang, S.-H.; Song, Y.; Liang, H.; Zeng, M.-H. *Cryst. Eng. Comm.* **2009**, *11*, 865-872.

(253) Punniyamurthy, T.; Velusamy, S.; Iqbal, J. *Chem. Rev.* **2005**, *105*, 2329-2364.

(254) Shaik, S.; Lai, W.; Chen, H.; Wang, Y. *Acc. Chem. Res.* **2010**, *43*, 1154-1165.

(255) Balcells, D.; Clot, E.; Eisenstein, O. *Chem. Rev.* **2010**, *110*, 749-823.

(256) Bergman, R. G. *Nature* **2007**, *446*, 391-393.

(257) Labinger, J. A.; Bercaw, J. E. *Nature* **2002**, *417*, 507-514.

(258) Warren, J. J.; Tronic, T. A.; Mayer, J. M. *Chem. Rev.* **2010**, *110*, 6961-7001.

(259) Roth, J. P.; Mayer, J. M. *Inorg. Chem.* **1999**, *38*, 2760-2761.

(260) Wang, Y.; Chen, H.; Makino, M.; Shiro, Y.; Nagano, S.; Asamizu, S.; Onaka, H.; Shaik, S. *J. Am. Chem. Soc.* **2009**, *131*, 6748-6762.

(261) Wang, Y.; Hirao, H.; Chen, H.; Onaka, H.; Nagano, S.; Shaik, S. *J. Am. Chem. Soc.* **2008**, *130*, 7170-7171.

(262) Tishchenko, O.; Truhlar, D. G.; Ceulemans, A.; Nguyen, M. T. *J. Am. Chem. Soc.* **2008**, *130*, 7000-7010.

(263) Hammes-Schiffer, S.; Soudackov, A. V. *J. Phys. Chem. B* **2008**, *112*, 14108-14123.

(264) Decker, A.; Clay, M. D.; Solomon, E. I. *J. Inorg. Biochem.* **2006**, *100*, 697-706.

(265) Decker, A.; Rohde, J.-U.; Klinker, E. J.; Wong, S. D.; Que, L., Jr.; Solomon, E. I. *J. Am. Chem. Soc.* **2007**, *129*, 15983-15996.

(266) Hirao, H.; Kumar, D.; Que, L.; Shaik, S. *J. Am. Chem. Soc.* **2006**, *128*, 8590-8606.

(267) Shaik, S.; Chen, H.; Janardanan, D. *Nat. Chem.* **2011**, *3*, 19-27.

Chapter 2

Theoretical Background and Methods

2.1 Introduction

Theoretical chemistry uses mathematical methods which are related to the physics fundamental laws and study the chemical relevance. By the theoretical chemistry, we can calculate the many properties such as a stable geometrical arrangement of the nuclei, their relative energies, rate, polarizability, dipole moment etc. In earlier times theoretical chemistry was not a vast area but due to the increase of technology, theoretical chemistry has become a very broad area nowadays. It deals with many areas of chemistry such as atmospheric, physical, inorganic, organic, bioinorganic chemistry. Along with chemistry it is also used in physical, mathematical, biological, and computer science, etc. and provides an idea to solve electronic properties and provide connections between all these branches of science.

Quantum chemistry deals, fundamentally, with the motion of electrons under the influence of the electromagnetic force exerted by nuclear charges. To understand the electronic structure, and rate of reaction quantum chemistry is used, which is based on the Schrödinger equation (time-independent and time-dependent). In the present thesis, ground-state chemical reactions have been studied, that's why it is sufficient to use the time-independent Schrödinger equation.[3,4] However, one-electron system equations can be solved by it, but it is very complicated for the many-electron system. For which many approximations are taken. It is extensively used in the design of new drugs and materials. It can be also used to find out the molecular geometry, energies of molecules, transition states, chemical reactivity, IR, UV, and NMR spectra. It can also be used to study the interaction of a substrate with an enzyme and the physical properties of substances etc. The development of DFT gives a very big achievement in computational chemistry. DFT is based mainly on electron density. DFT method has been used for modeling electronic structure and mechanism in this thesis.

Quantum mechanics is mainly divided into three parts

1. Hartree-Fock Theory
2. Semi-emipirical methods
3. Density Functional Theory

2.2 Hartree-Fock Theory (HF)

The most important and primary function of computational methods is to obtain the wave function of the system which gives all the information about the quantum mechanical behavior of the system. The main paradigm is to find out the energy of the molecular system.[5-8]

The time-independent Schrödinger equation[9] is shown in equation 2.1.

$$\hat{H}\psi = E\psi \tag{2.1}$$

Where Ψ is wave function associated with the system, E is the energy eigenvalue of Hamiltonian operator contains kinetic energy and potential energy terms.

Schrödinger's equation cannot be solved exactly for more than one electron. Therefore, there are several approximations for solving the Schrödinger equation for molecules with more than one electron system. First, an approximation is a Born-Oppenheimer approximation, it considers that the mass of nuclei is very large as compared to electron, thus we may consider that nuclei are stationary and it also neglects the relativistic effects, and they reduce the many-electron problem to one-electron problem. Then, the Schrödinger equation for the electronic motion is given by

$$\hat{H}_{elect}\psi_{elect} = E_{elect}\psi_{elect} \tag{2.2}$$

Where, $\hat{H}_{elect}$ is the pure electronic Hamiltonian

$$\widehat{H}_{elect} = -\sum_{i=1}^{n} \frac{h^2}{4\pi m_e} \nabla_i^2 - \frac{1}{4\pi\varepsilon_\circ}\left(\sum_{i=1}^{n}\sum_{\alpha=1}^{M} \frac{Z_\alpha e^2}{r_{i\alpha}} - \sum_{i=1}^{n}\sum_{j>i}^{N} \frac{e^2}{r_{ij}}\right) \quad (2.3)$$

Where m_e is the mass of each electron and M is the number of nuclei. The α-th nucleus has mass M_α and charges $Z_{\alpha e}$ where e is the electronic charge. Electronic coordinates are written as r_i's. Unfortunately, the Born-Oppenheimer approximation is not sufficient to solve the Schrödinger equation for many-electron systems. The basic wave function method is known as Hartree-Fock method, which is based upon an independent molecular orbital model. In the HF method, each electron is described by an orbital; total wave function is given by the product of orbitals, where wave function is considered by the approximation. The wave function is solved by the time-independent Schrödinger equation and the relativistic motion is not taken into consideration.

According to it Schrödinger equation of a molecule may be divided into electronic and nuclear energy. These quantum chemical models differ in the nature of approximations employed and spanned over a wide range both in terms of their capability and reliability. It is an *ab initio* type calculation, in which columbic electron-electron repulsion is taken into account, and it gives the average effect, it does not include explicit repulsions. This is a variational calculation; in which calculated average energy is always equal to or greater than the exact value. In many-electron system Schrödinger equation is broken down in the single electron approximation, and the wave function is the linear combination of atomic orbitals (Gaussian type Orbital (GTO)). The limitation of the approximation is that it does not take into account the corre Hartree-Fock uses single Slater type determinant.[10] Single Slater determinant gives the accurate description of the system. HF considers the interaction of each electron with mean-field of electrons, instead of considering the individual electron-electron interaction separately. The energy calculated with HF is too high, and increase in energy due to this error is referred correlation energy i.e. it calculates the probability of finding an

electron around an atom by taking the distance from the nucleus which does not take into account the distance of an electron from other electrons. The HF energy after adding correlational energy will give the exact solution to the Schrödinger equation. By increasing the quality of basis sets, the calculated energy can approach the exact solution. HF theory only takes into account the average electron-electron interaction and neglects the electron correlation. Due to which it lacks a certain amount of electronic energy. This missing energy only represents a small percentage of total energy while it is essential to solve the chemical problems and to evaluate the relative energy.

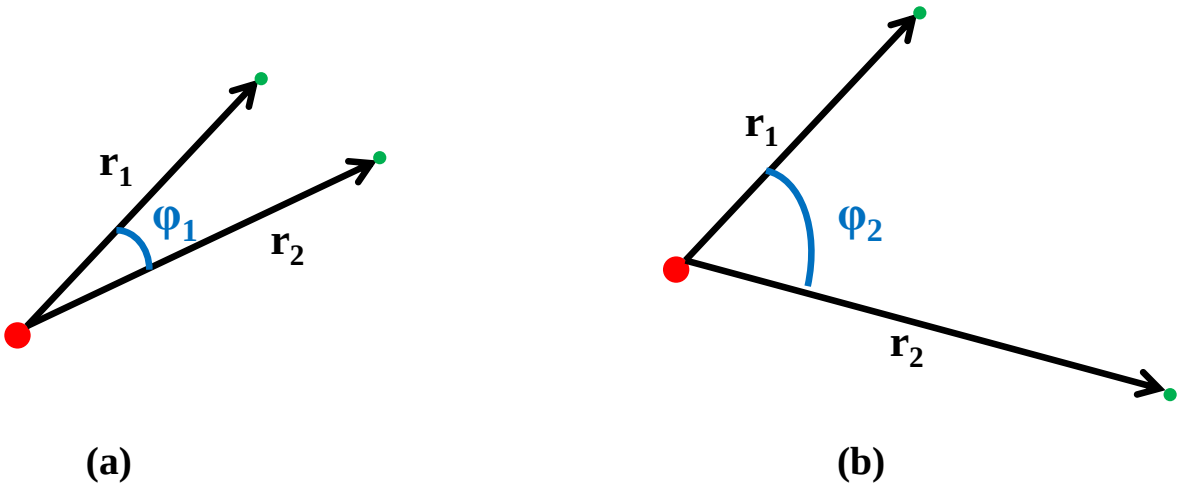

Figure 2.1. Two different arrangements of electrons in atom around the nucleus have same probability within HF theory, but not in correlated calculations.

To improve the accuracy beyond the HF method, explicit electronic correlations to be include. To include the electron correlation, multi-determinant wave function is used which is beyond Hartree-Fock. Some of these are Möller-Plesset perturbation methods (e.g. MP2 and MP4), configuration interaction method (e.g. CISD), multi-configurational self-consistent field (MCSCF), configurational interaction (CI), and coupled-cluster methods (e.g. CCSD (T)). These methods are multi determinants and optimize both their orbitals and coefficients. NEVPT2 (N-electron valence state perturbation theory) is the multireference method using perturbation theory, it improves the results significantly. Computed molecular geometry and

energies are more accurate that includes correlation. However, these theories require a large computational facility and are expensive. Thus, it can be applied to small systems, while for the large system we have to use alternative methods. An alternative to the wave function-based method is density functional theory (DFT), which is used for understanding chemical problems.

2.3 Semi-empirical Method

Semi-empirical calculations are performed by taking the structure of the HF i.e. Hamiltonian and wave function, where some information is approximated or completely omitted. The core electrons are not included in the calculation. Parameterizations are used to predict the omitted parameters and are calculated either by experiments or by *ab initio* calculations. For example, Hückel, Pariser-Parr-Pople (PPP), complete neglect of differential overlap (CNDO), modified intermediate neglect of differential overlap (MINDO), Intermediate neglect of differential overlap (INDO), and Austin Model 1 (AM1). These methods are faster than the *ab initio* calculations. The disadvantage of these methods is that these results depend upon the parameterization, if the computed molecule is similar to that is used to parameterize the method then the results are good otherwise not.

2.4 Density Functional Theory (DFT)

According to DFT, energy is calculated by the electron density, not by the wave function. Here, "*electronic energy is functional of electron density which is a function of space and time*".[11-13] DFT theory was developed by the theorem proposed by Hohenberg and Kohn. In this theory, the determinant is formed by the electron density. DFT is classified into many classes that include the electron exchange, not the correlation. Density functional theory is

based on electron density instead of the wave function. DFT is based on two Hohenberg-Kohn theorem.[14,15]

The first, Hohenberg-Kohn theorem, states that "*any ground state property of a molecule is a functional of the ground-state electron density function*".

$$E_o = F[\rho_o] = E[\rho_o] \tag{2.4}$$

This theorem assures that many molecular properties can be calculated from the electron density, and approximate functional will give at least approximate answers. The second Hohenberg-Kohn theorem is the DFT analog of the wave function variation theorem that has connection with the *ab initio* method. It states that "*any trial electron density function will give energy higher than (or equal to, if it were exactly the true electron density function) the true ground state energy*".

$$E_v[\rho_t] \geq E_o[\rho_o] \tag{2.5}$$

DFT methods give more accurate structures and vibrational energies for the transition metals than the Hartree-Fock methods and their results are similar to the post-HF method. DFT calculations are computationally less expensive and become the routine choice of method for transition metal compounds.[16-23] The approximate functional employed by current DFT methods partition the electronic energy into several terms:

$$E = E_T + E_V + E_J + E_{Exc} \tag{2.6}$$

Where, E_T = kinetic energy arising from the motion of electrons,

E_V = potential energy of the nuclear-electron attraction and the repulsion between pairs of nuclei

E_J = Coulomb self-interaction of electron-electron

E_{Exc} = exchange-correlation energy term

2.4.1 Exchange correlation functional (E_{xc})

The E_{xc} function not only defines the difference in kinetic energy of an interacting and non-interacting system but also deals with the difference between classical and quantum mechanical electron repulsion.

$$E_{xc} = E_x + E_c \tag{2.7}$$

For the total energy calculation there is a requirement to make the approximation for the exchange-correlation energy, and the DFT method's accuracy depend upon how well the approximations have been made. Beyond, the pure electrostatic interactions exchange-correlation potential describes Pauli's principle effects coulomb potential.

Classification of density functional theory has been proposed and some of them are discussed here.

(a) Local density approximation (LDA)

Local density approximation (LDA) is applicable on uniform electron gas i.e. electron density varies very slowly with the position.[24,25] In LDA, functional depends on the electron density at each point in space. The term local is used because at any point only the conditions at that point are considered, while in nonlocal methods at each point a gradient, which considers the region a bit beyond the point is used. These calculations are performed for the study of band structure; its results are not good for the calculation of molecular structure where errors of both qualitative and quantitative results are incorporated. The exchange-correlation energy[15] is written as;

$$E_{xc}^{LD} = \int d^3r n(r) E_{xc}^{unif} n(r) \tag{2.8}$$

Where, $E_{xc}^{unif} n(r)$ = exchange-correlation energy of uniform electron gas

Better results than LDA can be obtained by elaborating LDA, that alpha (α) and beta (β) electrons have different orbitals say, $\psi_\alpha = \psi_\beta$, by which they have different electron densities ρ^α and ρ^β. This "unrestricted" LDA method is known as local spin density approximation. The advantage of LSDA is that it can handle systems like radicals, which are having one or more unpaired electrons, and the systems in which electrons are going to get unpaired. In LSD approximation, the exchange functional is given by

$$E_{xc}^{LSD}[n_\uparrow][n_\downarrow] = \int d^3r\, n(r) E_{xc}^{unif}(n_\uparrow(r), n_\downarrow(r)) \tag{2.9}$$

Where, $E_{xc}^{unif}(n_\uparrow(r), n_\downarrow(r))$ is exchange-correlation energy of each particle of a uniform electron gas with spin densities $n_\uparrow(r)$, and $n_\downarrow(r)$. Ground state properties such as lattice constant, bulk, etc. are described in LDA, and the dielectric constant is 10-40 % overestimated in LDA as compared to the experiment. This overestimation is due to the neglect of a polarization-dependent exchange-correlation in LDA as compared to LSDA. It can be improved by including the gradient of density in functional. The generalized gradient approximation (GGA) is an example of this type of approach.

(b) Generalized-gradient approximation (GGA)

The electron density in an atom or molecule varies greatly from place to place, so it is not surprising that the uniform electron gas model has serious shortcomings. It assumes non-uniform electron gas. It takes the exchange and correlation energy. These depend not only on electron density but also depend on its gradient (first derivatives of density with respect to position). These functional are called *gradient corrected*, or said to use the *generalized gradient approximation* (GGA). They are also called *nonlocal* functional or "*semi local*". GGA functional proposed for the correlation energy. The general formula for GGA functional is:

$$E_{xc}^{GGA}[n_{\uparrow}, n_{\downarrow}] = \int d^3r n(r) E_{xc}^{GGA}(n_{\uparrow}, n_{\downarrow} \Delta n_{\uparrow}, \Delta n_{\downarrow}) \quad (2.10)$$

One popular functional was proposed by A.D. Becke (B or B88)[26]

$$\varepsilon_x^{B88} = \varepsilon_x^{LDA} + \Delta\varepsilon_x^{B88}$$

$$\varepsilon_x^{B88} = -\beta\rho^{1/3}\frac{x^2}{1 + 6\beta x \sinh^{-1} x}$$

$$x = \frac{|\nabla\rho|}{\rho^{4/3}}$$

One popular GGA functional is *Lee*, *Yang*, and *Parr* (LYP),[27,28] the LYP functional does not include parallel spin correlation when all the spins are aligned (e.g. the LYP correlation energy for ^{3}He is zero). The LYP correlation functional is often combined with the B88 or OPTX exchange functional to produce the BLYP and OLYP acronyms. DFT calculations with functional incorporating gradient corrections, and the HF exchange term (hybrid functional), can be speeded up with only a little loss in accuracy by a so-called perturbation method.

(c) Meta generalized-gradient approximation (MGGA)

It is an extension of GGA methods and it allows the exchange and correlation functional to depend on higher-order derivatives of the electron density. Inclusion of either the Laplacian or orbital kinetic energy density as a variable leads to the so-called *meta-GGA* functionals[29-31] Calculation of the orbital kinetic energy density is numerically more stable than a calculation of the Laplacian of the density. Results have more accuracy than the earlier approximations. The normal form of the meta-GGA functional is

$$E_{xc}^{mGGA}[n_{\uparrow}, n_{\downarrow}] = \int d^3r n(r) E_{xc}^{mGGA}(n_{\uparrow}, n_{\downarrow} \Delta n_{\uparrow}, \Delta n_{\downarrow}, \Delta_{n_{\uparrow}}^2, \Delta_{n_{\downarrow}}^2, \tau_{\uparrow}, \tau_{\downarrow}) \quad (2.11)$$

The most popular GGA functionals are TPSSh, M06-L, etc.

(d) Hybrid density functional methods

Hybrid Density Functional methods are also known as the *Adiabatic Connection Model* (ACM).[32-34] Correlation energy may similarly be taken as the LSDA formula plus a gradient correction term. There is an exact connection between the non-interacting density functional to the fully interacting many-body systems which allow for calculating the exact exchange-correlation functional. It is the combination of Hartree-Fock exchange-correlation and density functional. This generally has a linear combination of HF exact exchange functional.

$$E_{xc} = (1 - a)_{Ex}^{DFT} + aE_x^{HF} \tag{2.12}$$

Models that include exact exchange are often denoted as hybrid methods and Becker 3 parameter functional (B3) methods are examples of such hybrid models, B3LYP is one of the most widely employed hybrid functional. It is a combination of the three parameters such as exchange-correlation, LSDA and gradient corrected term. It was developed by Becke in 1993, modified by Stevens *et al.* in 1994 by the introduction of correlation-energy functional LYP 1988. It is used for calculating the atomization energies, ionization potentials, proton affinities, and total atomic energies of small molecules. For improving the exchange-correlation functional a portion of HF theory is added to it, the resulting functional is called hybrid functional. It is given by

$$E_{XC}^{B3LYP} = (1 - a_o - a_x)E_x^{LSDA} + a_o E_x^{HF} + a_x E_x^{B88} + (1 - a_c)E_c^{VWN} + a_c E_c^{LYP} \tag{2.13}$$

Where, E_x^{LSDA} is 'pure DFT' LSDA non-gradient-corrected exchange functional, E_x^{HF} is the KS-orbital-based HF exchange energy functional, E_x^{B88} is the Becke exchange functional, E_c^{VWN} is the Vosko, Wilk, Nusair function, E_c^{LYP} is the LYP correlation functional. The parameters a_o, a_x and a_c are those that give the best fit of the calculated energy to molecular atomization energies. The general form of the functional is given below,

$$E_{XC}^{HF} = E_{XC}^{LSDA} + 0.2(E_X^{HF} - E_X^{LSDA}) + 0.72\Delta E_X^{B88} + 0.81\Delta E_c^{PW91} \tag{2.14}$$

Here, ΔE_X^{B88} and ΔE_c^{PW91} are the GGA corrections that are widely used to LSDA exchange and correlation energies respectively.[35-36]

(e) Density functional theory including dispersion corrections

At the fifth level of Jacob's ladder classification, the full information of the KS orbitals is employed, i.e. not only the occupied but also the virtual orbitals are included. The formalism here becomes similar to those used in the random phase approximation, but a little work has appeared on such methods. Inclusion of the virtual orbitals is expected to significantly improve, for example, dispersion (such as Vander Waals) interactions, which is a significant problem for several functionals. The optimized effective potential (OEP) method can be considered in this category.[4]

By using DFT, many properties such as spectroscopic including IR, UV, and NMR spectra can be studied, along with these properties such as dipole moments, bond orders, charges, ionization energies, electron affinity, electronegativity, harder and softer properties can be studied. DFT functionals are not capable of describing the weak forces of attraction like Vander Waal forces and non-covalent interactions. B3LYP functional is named as B3LYP-D/D2/D3 functional after the addition of dispersion correction term.[37-39] Some functionals like M06[40] suite and B97D[41] are present in which dispersion correction term is already included in their functional form. To predict the performance of a functional in DFT, one must have to try on a variety of molecules and properties to assess its performance. DFT is mainly the ground state theory; researchers are working to extend it to the excited state.

For this, an alternative approach is used i.e. time-dependent Schrodinger equation to calculate the absorption of energy from light by calculating effect of the time-dependent electric field on the molecule.

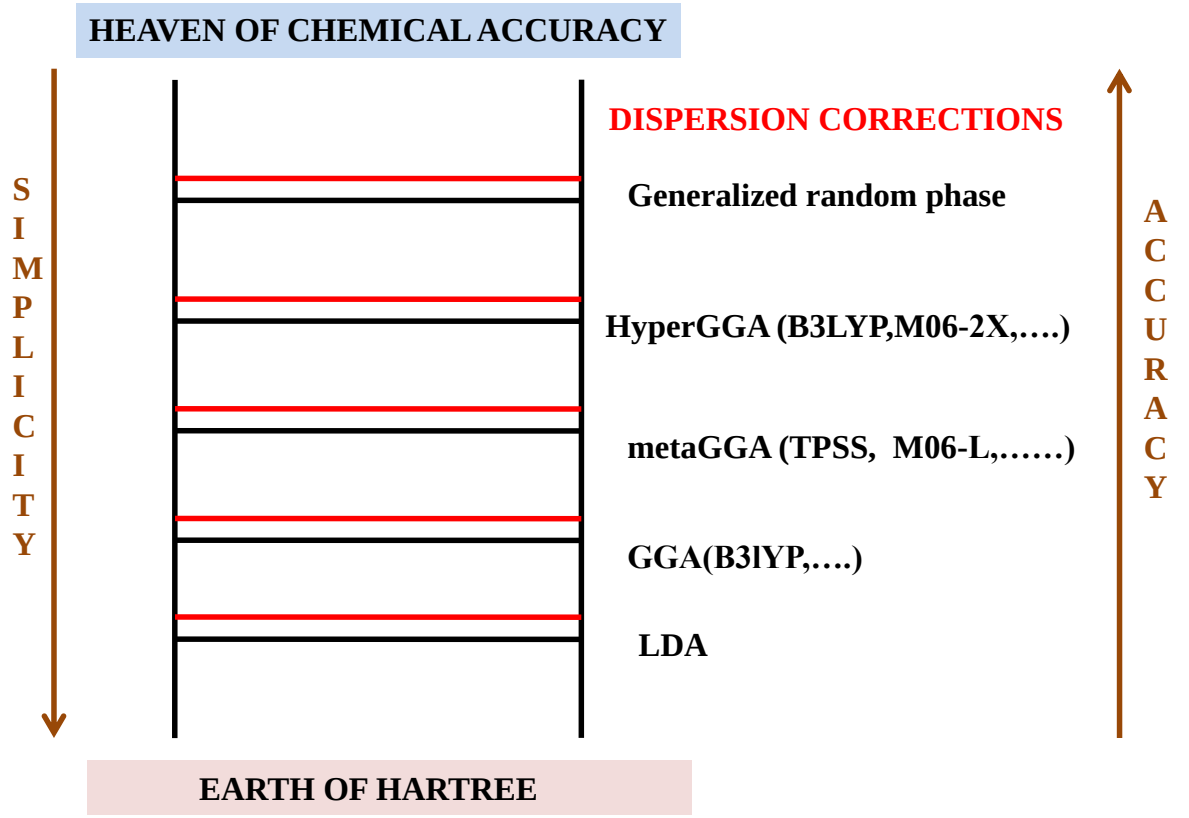

Figure 2.2. Classification of XC functionals by Jacob's ladder.

It is an alternative development of time-dependent quantum mechanics, in which density is the fundamental variable instead of many-body wave function. Time-dependent density is calculated by solving the non-interacting Schrodinger equation.[46]

Theorem of TDDFT confirms the one-to-one correspondence between electronic density n(r,t) and the external (time-dependent) potential, V_{ext} (r,t), for many-body systems evolving from a fixed initial state.[46] First time, TDDFT calculation was performed by Ando to predict the inter sub-band transition in heterostructure of semiconductor.[47] Zangwill and Soven[48] performed the first calculations for finite systems.

For, the more accurate TDDFT results, Casida and Salahub stated that these two criteria should follow: (i) Excited energy should be smaller as compared to molecular ionization potential. (ii) Excitations should not be in orbitals having positive KS eigenvalues. For many

absorptions results, organosulphur compounds B3LYP, TDDFT and INDO/S results were compared by the Fabian.[49] It was found that the performance of TDDFT is good.

2.5 Basis Sets

"Basis set is a group of mathematical functions used to describe the shape of the orbitals in a molecule".[50] Molecular orbitals are the linear combination of basis function and angular function. It gives a mathematical description of atomic orbitals. There are two types of atomic orbitals; one is Slater type and the other is Gaussian type orbital. It was Slater who proposed atomic orbitals first time, which correspond to a set of functions in which distance from the nuclei decays exponentially ($e^{-\xi r}$).[51] The expression for the Slater type orbital is

$$G_{\xi,n,l,m}(r,\theta,\varphi) = NY_{l,m}(\theta,\varphi)r^{n-1}e^{-\xi r} \tag{2.15}$$

Slater-type orbitals are used for the atoms having many electrons whose analytical solution is difficult and computational studies are expensive. Alternative for the slater type orbital is the linear combination of Gaussian type orbitals (GTO). In Gaussian type orbitals the distance from nuclei decay as $e^{-\xi r^2}$.

$$G_{\xi,n,l,m}(r,\theta,\varphi) = NY_{l,m}(\theta,\varphi)r^{2n-2-l}e^{-\xi r^2} \tag{2.16}$$

The exact solution of the Schrodinger equation for the hydrogen atom is the Slater type orbital. GTO requires more primitive than the STO to describe the wave function. However, the numeric integral over GTO can be computed analytically much faster than the STO that's why a given accuracy can be obtained quickly using the GTO.

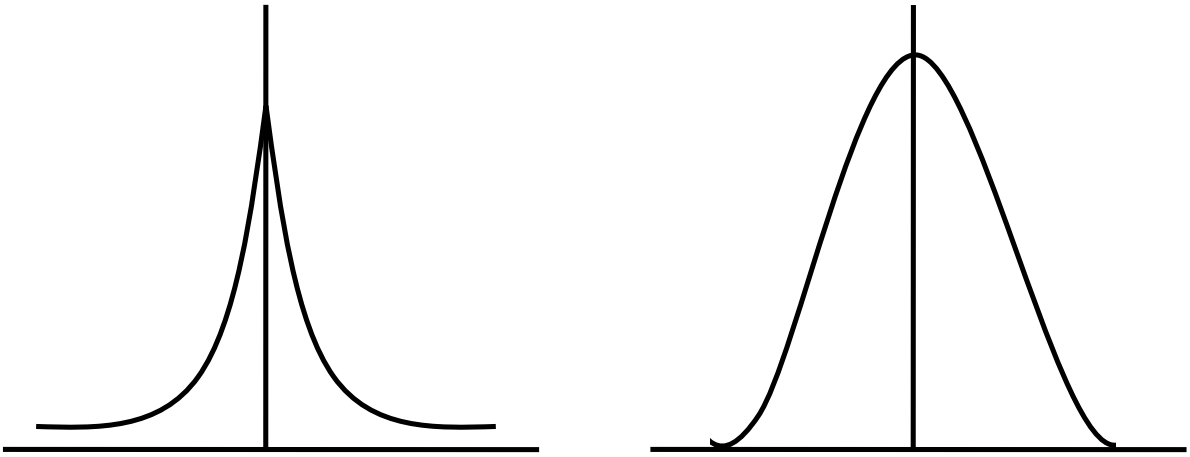

Figure 2.3. Slater type orbital (STO) and Gaussian type orbital (GTO).

The normalized Gaussian type orbital in Cartesian coordinates is given by

$$\varphi(x,y,z;i,j,k) = \left(\frac{2\alpha}{\pi}\right)^{3/4} \left[\frac{(8\alpha)^{i+j+k} i!j!k!}{(2i)!(2j)!(2k)!}\right]^{1/2} x^i y^j z^k e^{-\alpha(x^2+y^2+z^2)} \quad (2.17)$$

Where,

Exponent α, and *i*, *j*, and *k* = non-negative integer and these define the nature of orbital in a Cartesian type.

If all the three indices (*i*, *j*, and *k*) are zero, then the GTO has spherical symmetry is called an s-type GTO. When only one index (*i*, *j*, *k*) have value one, then it has axial symmetry about a single Cartesian axis is called *p*-type GTO. When the sum of *i*, *j*, and *k* is one, then it is called *p*-type GTOs have three functions named as p_x, p_y, and p_z orbitals and when the sum of indices is equal to two, then it is *d*-type GTO. A complication arises for basic functions with *d* orbitals or higher symmetry orbitals. Five *d* real orbitals are xy, xz, yz, x^2-y^2, and d_z^2, where z^2 is $2z^2$-x^2-y^2. For the fast integral, evaluation is to use the six Cartesian orbitals, which are xy, xz, yz, x^2, y^2, and z^2. These six orbitals are equivalent to 5 pure *d* orbitals and one additional spherically symmetric function $x^2+y^2+z^2$. Calculations using the 6*d* orbitals have lower energy than the calculations performed with 5*d* orbitals because of the additional

function. Some *ab intio* programs have the option to use 5*d* (pure-*d*) or 6*d* (Cartesian). Similarly, with *f* orbital 7*f* (pure-*f*) and 10*f* (Cartesian).

Choosing a standard GTO basis set means that the wave function is defined by a finite number of functions. This created the approximation in calculations. To describe the wave function exactly infinite numbers of GTO functions are needed. Differences in results due to the quality of the basis set *vs.* another are known as basis set effects. To avoid the basis set effects, some high-accuracy work is done with a numeric basis set. Cubic spline set is an example of such a basis set. The choice of basis set affects the CPU time required to perform the calculation. The amount of CPU time for Hartree-Fock calculations scales N^4. For example, we have to twice the calculation then it will take the time 2^4 (16) times longer.

2.5.1 Classification of basis sets

Minimal basis set:

When the minimum number of basis functions are used to represent each orbital in an atom, is known as a minimal basis set, for example, STO-G, STO-6G, etc.[52-54]

e.g. One s function for H (1s); and 5 basis function for N (1s, 2s, $2p_x$, $2p_y$, $2p_z$).

Double/triple zeta basis set:

Doubling all the basis functions gives rise to the double zeta function. e.g: two s functions for H (1s and 1s′), and 10 basis functions for N (1s, 1s′, 2s, 2s′, $2p_x$, $2p_y$, $2p_z$, $2p_{x'}$, $2p_{y'}$ and $2p_{z'}$)

Split valence basis set:

As the separate basis functions are used singly for core and multiple for valence orbital it gives split valence basis set[55] and these can be Valence Double/Triple/Quadruple Zeta function. When the double basis function is used for valence orbital and then it is the valence

double zeta (VDZ) when the triple basis function is used then it gives valence triple zeta (VTZ) basis set.

N = (1s, 2s, 2s′, $2p_x$, $2p_y$, $2p_z$, $2p_{x'}$, $2p_{y'}$ and $2p_{z'}$) Valence double zeta

N = (1s, 2s, 2s′, 3s’, $2p_x$, $2p_y$, $2p_z$, $2p_{x'}$, $2p_{y'}$ and $2p_{z'}$, $3p_{x''}$, $3p_{y''}$, $3p_{z''}$) Valence triple zeta

Split valence basis set is represented as *k-nlmG* in **Pople notation**.

Where,

k = number of primitive Gaussians (PGTOs)

nlm = number of Gaussian functions for the valence orbitals that are split into the PGTOs for a specific basis set

Two values (*nl*) indicate double split valence while three values (*nlm*) indicate a triple split valence basis. e.g. 6-31G, 6-311G

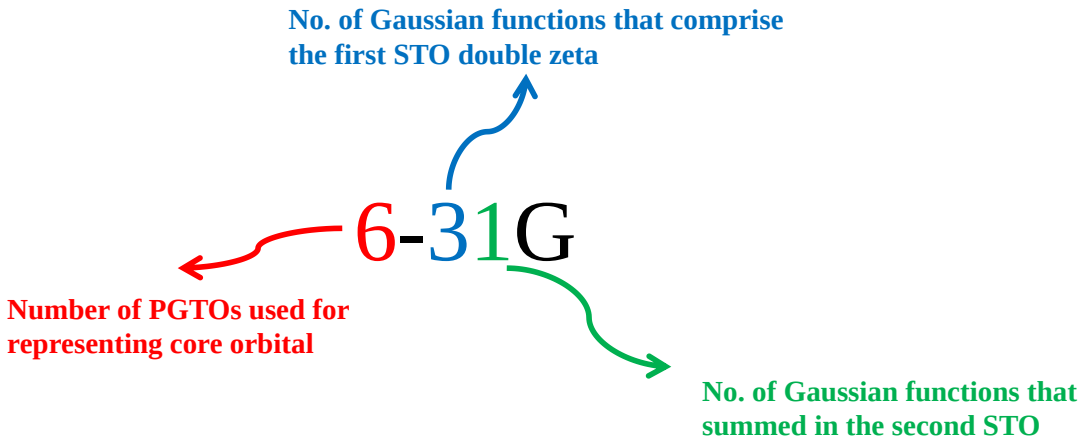

Figure 2.4. Basis set notation.

Polarization/diffusion basis set:

When polarization (angular momentum) function included then it is known as the polarization basis set.[56] It is denoted by an asterisk (*, **). A single asterisk (*) denotes that the *d* polarization function has been added to each atom except hydrogen and helium atoms. Two asterisks (**), indicates that a polarization *p* basis function is also added to hydrogen and helium atom. Polarization functions are represented after G with a separate designation for heavy and hydrogen atoms. The 6-31G* basis is identical to 6-31G (*d*), and 6-31G** is identical to 6-31G (*d*, *p*). In general, to polarize a basis function with angular momentum (*l*), mix it with the functions of angular momentum (*l*+1), e.g. polarized basis set adds *d* functions to a carbon atom and *f* function to transition metals.[14] These are functions of higher angular momentum and help to describe anisotropic charge distributions around the nuclei. Polarized functions are important for accurate description of bonding between atoms because the presence of other atoms distorts the environment of electrons and removes its spherical symmetry. These give more accurate computed geometries and vibrational frequencies. The basis set 3-21* shows the exceptionality that the *d* functions are added to 2nd row atoms. To indicate this difference, this basis set is given the notation 3-21(*).

Diffuse functions are added when there is electron density found far from the nuclei.[57] It is denoted by a plus sign (+). Single '+' denotes that diffuse function is added to all atoms except hydrogen and helium. While the Double ('++') indicates that diffuse function is also added to atoms along with hydrogen and helium. Diffuse functions are represented before the G, for example, 6-31++G. Diffuse functions are used for anions and for describing interactions at long distances, such as Vander Waals interactions. These basis functions are essential for the description of weak interactions such as hydrogen bonding and molecules having lone pairs. Diffuse functions change the relative energies of the various geometries associated with these systems.

Many basis sets are identified by the author's surname such as Huzinaga, Dunning, and Duijneveldt basis set, and along with surname, the number of primitive is also used such as D95 is the basis set created by Dunning with nine *s* primitives and 5*p* primitives. Semi-empirical methods are formulated to neglect the core electrons while the *ab initio* method represents. The elements in the lower part of the periodic table have a large number of core electrons, and core electrons are not involved in chemical transformation, but it is necessary to use a large number of basis functions to expand it, otherwise, the valence orbitals will not be described properly. There is the lower part of periodic table relativistic effects are also important. Further, to reduce the heavy computation necessity for the heavy elements. This is done by modeling the core electrons by a suitable function and treating the valence electrons explicitly.

Effective core potential

By replacing core electrons and their basis functions in the wave function with a potential term in Hamiltonian. This is called core potential, effective core potentials (ECP), or the relativistic effective core potentials (RECP) in the chemical community, while in the physics community it is known as pseudopotential. [58-60] Core potentials must be used along with a valence basis set that was created to accompany them. To reduce the computation time, relativistic mass defect and spin coupling term are significant near the nuclei of heavy atoms. To generate the pseudopotential, and LSD atomic calculation was performed using the method of Troullier and Martins. For example, LanL1MB and LanL2DZ (Los Alamos National Laboratory 2 Double-Zeta).

A limitation with the pseudopotential method is that it does not describe the properties which depend directly on core electrons such as X-ray photoelectron spectroscopy and the electron density near to nucleus i.e. NMR shielding and coupling constants. One common thing of

pseudopotential is that the parameters depend on the employed method, i.e. potential derived e.g. Local spin density approximation (LSDA) functional is different from that derived from a generalized gradient functional such as (PBE) Perdew-Burke-Ernzerh. In practice, the difference is small and pseudopotential optimized for one functional is used with other functional without re-optimization.

2.5.2 Basis set superposition errors

Most of the basis set's molecular applications are centered on the nuclei. A complete basis set cannot be used in practice, M_{basis}^{4} increases computational effort limits for practical calculations to hundreds or a few thousand basis functions at best. The absolute errors in energy from basis set are quite large, may be several au or kJ/mol. There is usually interest in relative energies; to make errors as constant as possible. Thus, it is important to select a "balanced" basis set. Same basis set must be used for comparing energies, for example, for comparing energies of two isomers, 6-31G basis set is used for one, and DH basis set for other isomer is meaningless, although both basis sets are of double zeta quality.

For comparing energies at different geometries, nuclear-fixed basis set introduces an error. This is because the quality of basis set is not same at all geometries, since electron density around one nucleus may be described by functions centered at another nucleus. This is especially troublesome when calculating small effects, such as energies of Vander Waals complexes and hydrogen-bonds.

It is also observed that CP (Car and Parrinello) corrections for methods including electron correlation are larger and more sensitive to the size of the basis set than at the HF level. The HF wave function converges much faster concerning the size of the basis set than correlated wave functions.

Chemical Hamiltonian Approach (CHA), methods are not commonly used yet. For intramolecular cases, it is difficult to define a unique procedure for estimating the BSSE (basis set superposition error). Performance of functional is not same for two sets of results. A minor part of this difference is due to the difference in basis sets, and remaining difference is due to the difference in data sets.

2.6 Magnetic Exchange

The net spin state of metal ion that interacts with the nearby spin and gives a particular type of electronic exchange (ferromagnetic or antiferromagnetic) interaction is mentioned as Heisenberg magnetic exchange (*J*). Hoffmann and Kahn's model's[61] are the active electron approximation, in which only unpaired electrons are considered, core electrons are neglected. In these models, spin-orbit interactions are considered, the minimal basis set under *semi-empirical* methods to evaluate the integrals. As a result, these models give a poor estimate of *J* value compared to experiments, though these models are widely used to interpret the magnetic properties. Magnetic exchange interactions are calculated in two different spin state centers in metal or in between the metal center and radical. These are calculated by employing the following spin Hamiltonian,

$$\widehat{\boldsymbol{H}} = -\boldsymbol{J}\,\mathbf{S_1}.\mathbf{S_2} \qquad (2.18)$$

Where, S_1 and S_2 denote the total spin of the individual center, and *J* is the magnetic exchange coupling constant.

The magnetic exchange is calculated by energy of the high spin (intermediate spin and low spin) state and their corresponding broken symmetry.[62] Ruiz *et al.* provide a very good methodology for the estimation of *J* values.[63-64] Positive and negative *J* value, indicates ferromagnetic and antiferromagnetic interaction.

2.7 Natural Bond Orbital (NBO) Analysis

The natural bond orbital analysis uses the many bonds wave functions in terms of localized electron pairs.[65] NBO is the name of a whole set of analysis techniques. It determines the natural atomic orbitals (NAO), natural bond orbitals (NBO), natural localized molecular orbitals (NLMO) and uses these to analyze natural population analysis (NPA), NBO energetic analysis of wave function properties, natural resonance theory (NRO) and natural chemical shielding (NCS) analysis.

One of these is the natural population analysis (NPA) for obtaining occupancies and charges.

NBO uses the natural orbitals instead of molecular orbitals directly. Natural orbital is the eigenfunctions of the first-order reduced density matrix. The eigenfunctions of the second-order density matrix are called Natural Germinals. For single-determinant RHF wave function, in which natural orbitals have the occupation number exactly either 0 or 2. While for the multi-determinant wave function and UHF, the occupation number is fractional in between 0 and 2. The natural orbital provides the fastest convergence. Natural atomic orbital (NAO) and Natural Bond Orbital (NBO) analysis was developed by Weinhold and coworkers and these use the one-electron density matrix for defining the atomic orbitals in the molecular environment and derive the molecular bond by electron density between them. These are localized for achieving well-defined division of the electrons, the orbitals should be orthogonalized.

NBO analysis is based on a method of transformation of a given wave function into localized form, corresponding to one-center (lone pair) and two-center (bond) elements of Lewis structure.

The order of transformations of the input atomic orbital basis set.[66-68]

$$AOs \rightarrow NAOs \rightarrow NHOs \rightarrow NBOs \rightarrow NLMOs$$

Based on the magnitude of occupation number the natural atomic orbital may be divided into a “natural minimal basis” (having occupation number significantly different from zero) and “Rydberg” (having occupation number close to zero) orbitals. Analysis of basis function allows classifying the transformed orbitals as bonding, antibonding, core, and Rydberg orbitals. There is also a procedure for the resonant system which predicts the π bonding in such systems.

Second-order perturbative estimates the donor-acceptor (bond-antibond) interaction on NBO basis. For this analysis, all the possible interactions between “filled” Lewis-type NBOs (donor, L) and “unfilled” (acceptor, NL) non-Lewis type NBOs are examined. These interactions lead to loss of occupancy from idealized Lewis structure localized NBO to empty non-Lewis orbital; this is known as “delocalization” correction to zeroth-order natural Lewis structure. Donor-acceptor stabilization E(2) from donor NBO (i) to acceptor NBO (j) is given by

$$E(2) = \Delta E_{ij(2)} = \frac{q_i F(i,j)}{(E_j - E_i)} \tag{2.19}$$

Where, q_i is the donor orbital occupancy (2 for closed-shell, 1 for open-shell) E_i and E_j are diagonal elements (orbital energies), and F(i,j) is the off-diagonal NBO Fock matrix element. This is a popular technique that is available in many software packages and is easy to understand. It is a convenient method to classify the type of orbital.

2.8 Solvation

In quantum chemistry, basis calculations are performed in gas-phase, assuming that the interaction between the model complex and surrounding medium is negligible. However, most natural and laboratory reactions do not occur in a vacuum, the reaction occurs in the solution that means interaction between solute and solvent particles exist. The solute

properties such as structure, stability, spectra, and reactivity depend on the solvent, particularly a polar one. Computational chemistry also evaluates the environment, of solvent. Methods for evaluating solvent effects are mainly two types: One describes the individual solvent molecules and the other treats the solvent as a continuous medium.[69-71] Combinations of these two are also possible, for example considering explicit first shell and remaining as a continuum model. Solvent effects are mainly of two types one is long-range (non-specific) and the other is short-range (specific) effect. Solvent polarization and orientation of dipole are long-range effects whereas hydrogen bonds, Vander Waals interaction, solvent-solute dynamics, charge transfer effects and hydrophobic effects are short-range solvation effects. Methods, in which solvent molecules are explicitly described, required a sampling of phase space. These methods are computationally expensive, thus there is strong interest to develop methods, in which solvent is modeled in gentle fashion.

Langevin dynamics method takes into account the average solute-solvent dynamics. By considering the solvent as a homogenous medium having a dielectric constant, the solvation non-specific effects can be modeled.

Continuum Solvation Models

Continuum models[72] consider the solvent as a uniform polarizable medium with a dielectric constant(ε). The dielectric constant is the characteristic property of a solvent. For a given medium value of the dielectric constant is fixed. While in dynamic phenomena it is taken as dependent on frequency.[73] Solvent having the same dielectric constant value are treated equally. For example acetone (ε = 20.7) and propan-1-ol (ε = 20.1), or benzene (ε = 2.28) and carbon tetrachloride (ε = 2.24) are nearly equal. But, in reality, the hydrogen bonding capability of propan-1-ol is different from acetone while the dynamics of spherical carbon tetrachloride is different from that of planar benzene.

The self-consistent reaction field (SCRF)[74-76] is a solvation model which is based on Onsager's reaction field theory.[77] In this model, solvent containing the solute molecule turns a cavity into a polarized form. The main drawback of this model is that the solvent effect will not be observed for the system having zero dipole moment.

The polarized continuum method (PCM) is the most popular self-consistent reaction field (SCRF) method, developed by Tomasi and coworkers. In the PCM method, a spherical cavity around each atom is used, and numerical integration over the solute charge density is used. Several variations use the nonspherical cavity. This method is widely used because of its good results in a cost-effective manner and applies to the arbitrary solute. However, it is sensitive towards the basis set used.

The conductor-like screening model (COSMO) is a continuum method based on solvent-accessible surface and it is fast. It can be used with a variety of semi-empirical, *ab initio,* and DFT methods. Cavity construction differs in different COSMO implementations and it is constructed as an assembly of atom-centered spheres with radii having 20% greater than the Vander Waal interaction. In real calculations, the cavity surface is approximated by segments, e.g., hexagons, pentagons, or triangles. By determining the charge distribution of the molecule, and the solvent charge, the interaction energy between solute and solvent can be calculated.

2.9 Reaction Mechanism

Transformation of one species to another takes place in elementary steps and this is called reaction mechanism.[78] Reaction mechanism is the description; step to step that occurs during the reaction at every stage of the reaction. It also describes the reactive intermediates, and the transition states. Reactive intermediate is a stable geometry and exists at the minimum of the energy occurring during the reaction and has a lifetime in order of 10^{-13} and 10^{-14} sec and

these are often radicals or ions.[79] Transition states are the unstable molecular entities involved during the reaction and these have an unstable number of bonds and unstable geometry. These correspond to the maxima on the reaction coordinates.

The rate of a reaction depends upon the concentration of the reactant. The bimolecular reaction between *a* moles of A and *b* moles of B is given below;

$$aA \quad + \quad bB \quad \rightarrow \quad products \tag{2.20}$$

The rate expression for the above reaction can be given by;

$$r = k[A]^a[B]^b \tag{2.21}$$

Where, k is rate constant, it is independent of the concentration of reactant, it depends only on the reaction temperature, and by the Arrhenius equation rate constant k is given by

$$k = Ae^{-E_a/RT} \tag{2.22}$$

Where, E_a is the activation energy and A is called the pre-exponential factor.

As the higher value of k, indicates faster will be the reaction, lower the value of k slower be reaction and for the intermediate value of k moderate will be the reaction rate. It is necessary to know the factors affecting reaction rate for understanding the reaction mechanism.

2.9.1 Transition state theory

Eyring, Polanyi, and Evans in 1935 developed the Transition state theory (TST). It is also known as absolute reaction rate theory (ARRT) and activated complex theory (ACT) and this is used to calculate the reaction rate of a chemical reaction and describe how a reaction can occurs.

TST is based on many mathematical assumptions. It assumes that Maxwell-Boltzmann statistics predict that how many molecular collisions have energy equal to or greater than the activation energy i.e. the molecules at transition structure are in equilibrium with the reactant,

it is known as quasi-equilibrium. It also assumes that at the transition state molecules react irreversibly. Consider a reaction

$$A + B \underset{}{\overset{K^{\#}}{\rightleftharpoons}} R \longleftrightarrow TS \xrightarrow{k'} C + D \rightleftharpoons P \qquad (2.23)$$

$$K^{\#} = \frac{[TS]}{[R]} \qquad (2.24)$$

$$[TS] = K^{\#}[R] \qquad (2.25)$$

$K^{\#}$ is the equilibrium constant between the reactant and the transition state.

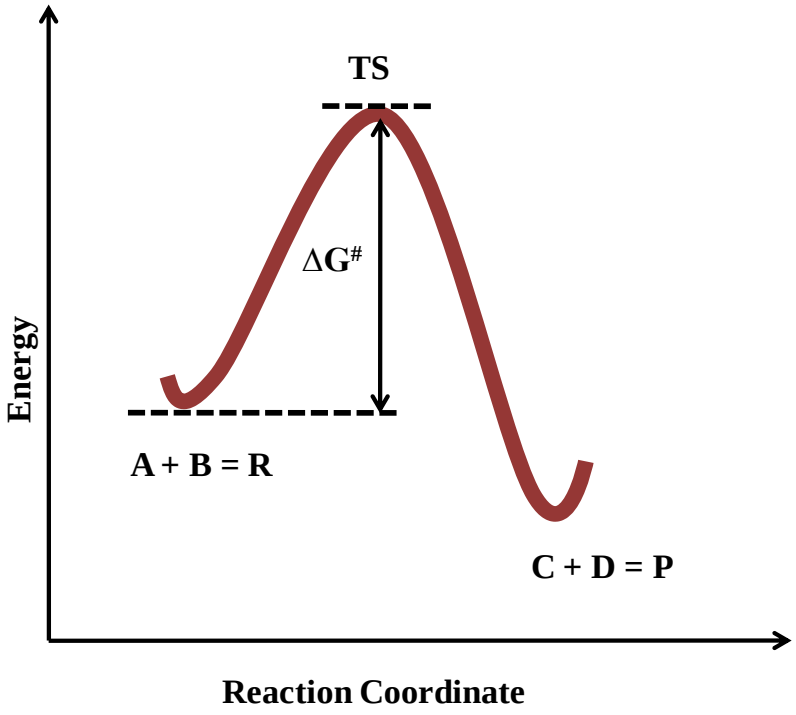

Figure 2.5. The chart showing the PES of an elementary single-step bimoleculer reaction.

From the classical mechanics, the energy of vibration is given by RT/N_A whereas from quantum mechanics it is given by $h\upsilon$. Thus,

$$h\upsilon = \frac{RT}{N_A} \qquad (2.26)$$

$$\upsilon = k_B T/h \qquad \text{Where, } R = k_B N_A \qquad (2.27)$$

The vibrational frequency υ is the rate at which the activated complex molecules move across the energy barrier. Thus, the rate constant k_2 can be identified by υ.

The reaction rate is given by,

$$-\frac{d[A]}{dt} = kk'[TS] \quad (2.28)$$

$$-\frac{d[A]}{dt} = k\left(\frac{K_B T}{h}\right)[TS] \quad (2.29)$$

Where k, is the transmission coefficient, which is a measure of the probability that a molecule, passes over the barrier, will keep on going ahead and do not return. It can be omitted from rate expression as its value is taken as unity.

$$-\frac{d[A]}{dt} = \left(\frac{K_B T}{h}\right) K^{\#}[R] \quad (2.30)$$

Rate constant k' can be expressed as

$$k' = \left(\frac{K_B T}{h}\right) K^{\#} \quad (2.31)$$

The equilibrium constant $K^{\#}$ can be expressed in terms of $(G^{\circ})^{\#}$, called the standard Gibbs free energy of activation. Since, for the activated complex, we can write

$$(G^{\circ})^{\#} = -RTlnK^{\#} \quad (2.32)$$

$$K^{\#} = e^{-(G^{\circ})^{\#}/RT} \quad (2.33)$$

Rate constant can be given by

$$k_{rate} = \left(\frac{K_B T}{h}\right) e^{-(G^{\circ})^{\#}/RT} \quad (2.34)$$

Where,

Boltzmann constant (K_B) = 1.38×10^{-23} J/K

Planck`s constant (h) = 6.63×10^{-34} Js

Gas constant (R) = 8.314 J K^{-1} mol^{-1}

Temperature (T) = in Kelvin

$(G^{\circ})^{\#}$ = difference in Gibbs free energy between reactant and the transition state theory is characterized by one imaginary frequency

$\Delta G^{\#}$ = calculated at the saddle point of Born-Oppenheimer free energy surface

2.10 Gaussian

The most widely used program in computational chemistry is Gaussian. It was released by John Pople in 1970. This name is given because Pople's use the Gaussian orbitals to speed up the calculations of molecular structure. It is a suite of programs with *ab initio*, density functional theory, semi-empirical, molecular mechanics, and various hybrid methods for predicting many properties of the atom, molecule, and reactive systems including molecular energies, structures, transition states, vibrational frequencies, IR, Raman spectra, thermochemical properties, reaction pathways, molecular orbitals, atomic charges, multipole moments, NMR shielding, magnetic susceptibilities, vibrational circular dichroism intensities, electron affinities, ionization potentials, polarizabilities and hyperpolarizabilities, electrostatic potentials and electron densities.

2.11 References

1. Shavitt, I. *In Modern Theoretical Chemistry,* Schaefer III, H. F. Ed.; Plenum New York, 1997.
2. Szabo, A.; Ostlund, N. S. *Modren Quantum Chemistry Introduction to Advanced Electronic Structure Theory,* McGraw-Hill New York, 1989.
3. Koch, W.; Holthausen, M. C. *A Chemist's Guide to Density Functional Theory,* Wiley-VCH, 2001.
4. Jensen, F. *Introduction to Computational Chemistry,* Wiley, 2006.
5. Leach, A. R. *Molecular Modelling, Principles and Applications,* Longmann, 1996.
6. Atkins, P. W.; Friedman, R. S. *Molecular Quantum Mechanics,* Third Edition, Oxford, 1997.
7. Szabo, S.; Ostlund, N. S. *Modern Quantum Chemistry, Introduction to Advanced Electronic Structure Theory,* Dover, 1996.
8. Levine, I. N. *Quantum Chemistry,* Fourth Edition, Prentice-Hall, 1991.
9. Schrödinger, E. *Phys. Rev.* **1926**, *28*, 1049-1070.
10. Slater, J. C. *Phys. Rev.* **1930**, *35*, 210-211.
11. Dreizler, R. M.; Gross, E. K. V. *Density Functional Theory*, Springer, Berlin, 1990.
12. Ziegler, T. *Chem. Rev.* **1991**, *91*, 651-667.
13. Parr, R. G.; Yang, W. *Density-Functional Theory of Atoms and Molecules,* Oxford University Press: New York, 1989.
14. Hohenburg, P.; Kohn, W. *Phys. Rev.* **1964**, *136*, 864-871.
15. Kohn, W.; Sham, L. J. *Phys. Rev* **1965**, *140*, 1133-1139.
16. Deeth, R. J. *Struct. Bond.* **1995**, *82*, 1-42.
17. Anderson, W. I; Cundari, T. R.; Drago, R. S.; Zerner, M. C. *Inorg. Chem.* **1980**, *29*, 1-3.

18. Zerner, M. C. In: *Reviews in Computational Chemistry;* Lipkowitz K. B. Boyd, D. B. Eds.; VCH: New York 2000.

19. Jensen, F. *Introduction to Computational Chemistry*, Wiley: New York, 1991.

20. Hoffman, R. *Science* **1981**, *211*, 995-1002.

21. Hall, M. B.; Fenske, R. F. *Inorg. Chem.* **1972**, *11*, 768-779.

22. Koch, W.; Holthausen, M. C. *A Chemist's Guide to Density Functional 5 Theory;* Wiley-VCH: Weinheim, 2000.

23. Parr, R. G.; Yang, W. *Density Functional Theory of Atoms and Molecules;* Oxford Universtity.

24. Ceperley, D. M. Alder, B. J. *Phys. Rev. Lett.* **1980**, *45*, 566-569.

25. Vosko, S. H.; Wilk, L.; Nusair, M. *Can. J. Phys.* **1980**, *58*, 1200-1211.

26. Becke, A. D. *Phys. Rev. A* **1988**, *38*, 3098-3100.

27. Lee, C.; Yang, W.; Parr, R. G. *Phys. Rev. B* **1988**, *37*, 785-789.

28. Miehlich, B.; Savin, A.; Stoll, H.; Preuss, H. *Chem. Phys. Lett.* **1989**, *157*, 200-206.

29. Tschinke, V.; Zieglar, T. *Can. J. Chem.* **1989**, *67*, 460-472.

30. Neumann, R.; Handy, N. C. *Chem. Phys. Lett.* **1997**, *266*, 16-22.

31. Perdew, J. P.; Kurth, S.; Zupan, A.; Blaha, P. *Phys. Rev. Lett.* **1999**, *82*, 2544-2547.

32. Pines, D.; Nozières, P. *The Theory of Quantum Liquids*, Benjamin, New York, 1966.

33. Harris, J.; Jones, R. O. *J. Phys. F*. **1974**, *4*, 1170-1186.

34. Becke, A. D. *J. Chem. Phys.* **1993**, *98*, 1372-1377.

35. Becke, A. D. *J. Chem. Phys.* **1993**, *98*, 5648-5652.

36. Becke, A. D. *J. Chem. Phys.* **1988**, *88*, 1053-1062.

37. Grimme, S. *J. Comput. Chem.* **2006**, *27*, 1787-1799.

38. Grimme, S.; Antony, J.; Ehrlich, S.; Krieg, H. *J. Chem. Phys.* **2010**, *132*, 154101-154104.

39. Grimme, S.; Muck-Lichtenfeld, C.; Antony, J. *Phys. Chem. Chem. Phys.* **2008**, *10*, 3327-3334.

40. Zhao, Y.; Truhlar, D. G. *Theor. Chem. Acc.* **2008**, *120*, 215-241.

41. Reed, A. E.; Weinhold, F. J. *J. Chem. Phys.* **1983**, *78*, 4066-4073.

42. Levine, I. N. "*Quantum Chemistry*" 5th Ed., Prentice Hall, Upper Saddle River, New Jersey, 2000.

43. Friesner, R. A.; Murphy, R. B.; Beachy, M. D.; Ringnalda, M. N.; Pollard, W. T.; Dunietz, B. D.; Cao, Y. *J. Phys. Chem. A.* **1999**, *103*, 1913-1928.

44. Kohn, W.; Becke, A. D.; Parr, R. G. *J. Phys. Chem.* **1996**, *100*, 12974-12980.

45. Parr, R. G.; Yang, W. *Annu. Rev. Phys. Chem.* **1995**, *46*, 701-728.

46. Marques, M. A. L.; Gross, E. K. U. *Annu. Rev. Phys. Chem.* **2004**, *55*, 427-455.

47. Ando, T. Z. *Phys. B.* **1977**, *26*, 263-268.

48. Zangwill, A.; Soven, P. *Phys. Rev. A.* **1980**, *21*, 1561-1572.

49. Cramer, C. J. *Essentials of Computational Chemistry: Theories and Models* John Wiley & Sons, Ltd, 2001.

50. Foresman, J. B.; Frisch, A. *Exploring Chemistry with Electronic Structure Method; Gaussian,* Inc. Pittsburg, 1993.

51. Slater, J. C. *Phys. Rev.* **1930**, *36*, 57-64.

52. Hehre, W. J.; Stewart, R. F.; Pople, J. A. *J. Chem. Phys.* **1969**, *51*, 2657-2664.

53. Hehre, W. J.; Ditchfie, R.; Stewart, R. F.; Pople, J. A. *J. Chem. Phys.* **1970**, *52*, 2769-2773.

54. Pietro, W. J.; Levi, B. A.; Hehre, W. J.; Stewart, R. F. *Inorg. Chem.* **1980**, *19*, 2225-2229.

55. Hehre, W. J.; Radom, L.; Schleyer, P. v. R.; Pople, J. A. *ab initio molecular orbital theory,* John Wiley, New York, 1986.

56. Carlsen, N. R. *Chem. Phys. Lett.* **1977**, *51*, 192-195.

57. Clark, T.; Chandrasekar, J.; Spitznagel, G. W.; Schleyer, P. V. R. *J. Comp. Chem.* **1983**, *4*, 294-301.

58. Frenking, G.; Antes, I.; Böhme, M.; Dapprich, S.; Ehlers, A.W.; Jonas, V.; Nauhaus, A.; Otto, M.; Stegmann, R.; Veldkamp, A.; Vyboishchikov, S. F. *Rev. Comp. Chem.* **1996**, *8*, 63-143.

59. Cundari, T. R.; Benson, M. T.; Lutz, M. L.; Sommerer, S. O. *Rev. Comp. Chem.* **1996**, *8*, 145-202.

60. Payne, M. C.; Teter, M. P.; Allan, D. C.; Arias, T. A.; Joannopoulos, J. D. *Rev. Mod. Phys.* **1992**, *64*, 1045-1097.

61. Cramer, C. J. *Essentials of Computational Chemistry: Theories and Models*, John Wiley & Sons, Ltd, 2001.

62. Ruiz, E.; Alvarez, S.; Rodriguez-Fortea, A.; Alemany, P.; Pouillon Y.; Massobiro, C. *Magnetism: Molecules to Materials,*, (Ed.: J. S. Miller, M.Drillon), Wiley-VCH, Weinheim, 2001.

63. Noodleman, L. *J. Chem. Phys.* **1981**, *74*, 5737-5743.

64. Noodleman, L.; Davidson, E. R. *Chem. Phys.* **1986**, *109*, 131-143.

65. Weinhold, F. *In Encyclopedia of Computational Chemistry;* Schleyer, P. V. R.; Allinger, N. L.; Kollman, P. A.; Clark, T.; Schaefer, H. F.; Gasteiger, J.; Scheiner, P. R., Eds.; John Wiley & Sons, 1999; Vol. 3.

66. Foster, J. P.; Weinhold, F. *J. Am. Chem. Soc.* **1980**, *102*, 7211-7218.

67. Reed, A. E.; Curtiss, L. A.; Weinhold, F. *Chem. Rev.* **1988**, *88*, 899-926.

68. Reed, A. E.; Weinhold, F. J. *J. Chem. Phys.* **1983**, *78*, 4066-4073.

69. Mikkelsen, K. V.; Ågren, H. *J. Mol. Struct. (Theochem)* **1991**, *234*, 425-467.

70. Cramer, C. J.; Truhlar, D. G. *Chem. Rev*. **1999**, *99*, 2161-2200.

71. Smith, P. E.; Pettitt, B. M. *J. Phys. Chem.* **1994**, *98*, 9700-9711.

72. Roux, B.; Simonson, T. *Biophys. Chem.* **1999**, *78*, 43-68.

73. Mikkelsen, K.V.; Sylvester-Hvid, K. O. *J. Phys. Chem.* **1996**, *100*, 9116-9126.

74. Tapia, O.; Goscinki, O. *Mol. Phys.* **1975**, *29*, 1653-1661.

75. Wong, M. W.; Frisch, M. J.; Wiberg, K. B. *J. Am. Chem. Soc.* **1991**, *113*, 4776-4782.

76. Wong, M. W.; Wiberg, K. B.; Frisch, M. J. *J. Chem. Soc.* **1991**, *95*, 8991-8998.

77. Onsagar, L. *J. Am. Chem. Soc.* **1936**, *58*, 1486-1493.

78. Denbigh, K. *The Principles of Chemical Equilibrium;* Cambridge University Press: Cambridge, 1991.

79. Lowry, T. H.; Richardson, K. S. *Mechanism and Theory in Organic Chemistry* Harper Collins: Cambridge, 1987.

Chapter 3

Electronic Structures and Energetics of Tetraamido Macrocyclic Ligated Iron Complexes

3.1 Introduction

Non-heme mononuclear and dinuclear complexes are involved in many catalytic reactions such as C-H activation, oxygen transfer, alcohol oxidation, deformylation reactions.[1-7] C-H bond activation in hydrocarbons is highly inert and biomimetic species can provide a direct way to introduce functional groups, cost-effectively, and has high industrial applications.[8-10] C-H bond activation is inspired by models of Cyt P450 and Rieske dioxygenase, and these hydroxylate unactivated C-H bonds with higher selectivity at fast rates.[11-12] Selective functionalization of C-H bond in organic compounds is a "grand challenge" in catalysis science.[13-18] To carry out selective C-H bond activation, many heme,[19-21] and non-heme[22-29] iron-containing complexes have been used with dioxygen as an oxidant. Dioxygen (O_2) is an ideal oxidant due to several reasons as it is abundant in nature, a renewable chemical oxidant, water as a byproduct, non-toxic at most of the conditions, and its reduction potential are more than sufficient to carry many chemical transformations.[30-35] Non-heme complexes with tetradentate N-atom donor ligand having *cis* labile sites (FeN_4) show great promise for selective C-H bond activation.[36-39] As iron is ubiquitous, has low toxicity and can exist in multiple redox states make its chemistry interseting and acts as a key intermediate in many biotransformation reactions, occurring via C-H, O-H activation, including biological O_2 activation, etc.[40-45]

Tetraamido macrocyclic ligand (TAML) activator is widely used in chemical and biological agents such as petroleum refining, water treatment, textiles, cleaning, etc.[46] TAML activators have about 10000 turnovers per hour in many applications.[47] The TAML coordinated metal species being environment friendly have been tested.[48] To investigate the catalytic properties, many experimental and theoretical studies such as Mossbauer, EPR, density functional theory (DFT), transient and steady-state kinetics have been used.[39,49-50] Last two decades,

tetradentate TAML ligated iron species becomes a popular oxidant to achieve an effective small biomimetic molecule of oxidizing enzymes for green oxidation chemistry.[30,51] It has biological elements like C, H, N, O, and Fe, and is devoid of toxic functionalities.[52] There are several Fe-TAML complexes such as mononuclear iron oxo/peroxo/superoxo/hydroperoxo as well as oxygen bridged dinuclear species that are observed in previous literature.[50,53-56] Some of the species are also well characterized by X-rays and spectroscopic parameters.[49,50,57] These species are also important intermediates generated during various metal-mediated catalytic transformation reactions such as alkane hydroxylation, olefin epoxidation, and sulfoxidation[58-74] occurring via C-H bond activation. These reactions are also important in synthetic pharmaceutical[75] and biological processes such as medicine, photosystem-II, naphthalene dioxygenase, etc.[76-77]

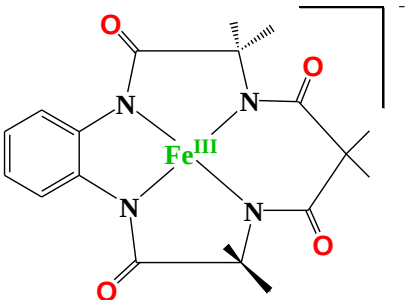

Scheme 3.1. A schematic diagram of tetraamido macrocyclic ligand coordinated iron $[Fe^{III}(TAML)]^-$ species.[39,50]

The growing interest in TAML ligated iron species motivated us to explore structures and spin-state energetics of mononuclear oxo/peroxo/superoxo/hydroperoxo and oxygen bridged dinuclear species as a possible oxidant in many catalytic transformation reactions. Here, we would like to underpin and compare electronic structures, bonding, magnetic interactions, and spin-state energetic aspects of Fe(III/IV/V)-O/O_2 and Fe(IV)-μ-O_1/O_2-Fe(IV)-species. By a study of structures and bonding of the species, we also like to comment on their reactivity.

3.2 Computational Details

All calculations are carried out by using Gaussian09 programs.[78] In earlier work, DFT calculations have performed on iron species employing B3LYP, B3LYP-D2, wB97XD, B97D, M06-2X, OLYP, TPPSh, and MP2 methods.[71,73] Among the tested functional, B3LYP incorporating dispersion correction (B3LYP-D2 functional) was found to be superior in predicting the correct spin ground state of iron species.[71,73] So here, we have restricted geometry optimizations using only B3LYP-D2 functional.[79] The LACVP basis set comprising the LanL2DZ-Los Alamos effective core potential for the iron[80-82] and a 6-31G[83] basis set for the other atoms (C, H, N, and O) have been employed for geometry optimization. To identify the geometry is located at the lowest point on the potential energy surface is made by frequency calculations which are performed on optimized geometry and confirmed by the absence of imaginary frequencies, free energy corrections are also found by frequency calculation. Single point energy calculations are made by using a TZVP[76,84-85] basis set on all-atoms of the optimized geometries. For computing the solvation energies using acetonitrile as a solvent, PCM solvation model is used. The quoted DFT energies are B3LYP-D2 solvation including free-energy corrections with TZVP basis set at the temperature of 298.15 K. From the optimized geometries, structural parameters, vibrational wavenumbers, and other molecular properties like HOMO-LUMO and NBO are analyzed. The vibrational energy distribution analysis (VEDA) program is used to calculate the partial energy distribution (PED),[86] by using PED fundamental vibrational modes are characterized. Theoretical and valuable information about intra and intermolecular charge transfer (ICT), conjugation and hyperconjugation of the molecular system[87-88] are provided by natural bonding orbital (NBO) analysis. Using the Mulliken population analysis (MPA) method with B3LYP-D2 functional charges on the atoms of complexes are calculated. In the Gaussian09 fragment approach available which is employed to aid smooth convergence. In the diiron species, the magnetic

exchange between both the iron centers is calculated by employing the following spin Hamiltonian,

$$\widehat{H} = -J\,\mathbf{S_1}.\mathbf{S_2}$$

Where *J* is the magnetic exchange coupling constant, the positive *J* value shows the ferromagnetic coupling while negative *J* values show the antiferromagnetic coupling. Noodleman's broken symmetry is used to compute the magnetic exchange coupling (*J*) constant.[89-90] Common notation of $^{mult}A_{spin\ state}$ is used throughout where the mult, A, and spin state denote the total multiplicity, the species, and the possible spin states respectively.

3.3 Results and Discussion

Here, we will thoroughly discuss electronic structures, bonding nature and spin state energetics of biomimetic $[Fe^{III}(TAML)]^{-}$ (species I) and its possible mononuclear derivatives end on $[(TAML)Fe^{IV}\text{-}\eta^{1}\text{-}O_2]^{\bullet-}$ (species II), side on $[(TAML)Fe^{IV}\text{-}(\eta^{2}\text{-}O_2)]^{2-}$ (species IIIa), $[(TAML)Fe^{III}\text{-}(\eta^{2}\text{-}O_2)]^{3-}$ (species IIIb), $[(TAML)Fe^{IV}\text{-}OOH]^{-}$ (species IV), $[(TAML)Fe^{IV}\text{-}O]^{2-}$ species (V), $[(TAML)Fe^{V}\text{-}O]^{-}$ species (VI), and dinuclear derivaties $[(TAML)Fe^{IV}\text{-}\mu O\text{-}(TAML)Fe^{IV}]^{2-}$ (species VII) and $[(TAML)Fe^{IV}\text{-}\mu O_2\text{-}Fe^{IV}(TAML)]^{2-}$ (species VIII) followed by comparative study.

3.3.1 Electronic structure and energetics of $[Fe^{III}(TAML)]^{-}$ (species I)

It is a tetraamido macrocyclic species containing iron ions, is a very efficient and selective catalyst.[22-29] In species I, iron is surrounded by four deprotonated N-amido ligands and is almost square planar species.[39] This is well characterized by X-ray, UV-vis, EPR, and EXAFS.[39] We have optimized species I on the surfaces of S=5/2 (sextet; $^{6}I_{hs}$) and S=3/2

(quartet; $^4I_{is}$), and our DFT calculations reveal that the quartet state is computed to be the ground state, and the sextet state lies at 89.0 kJ/mol higher in energy (see Figure 3.1).

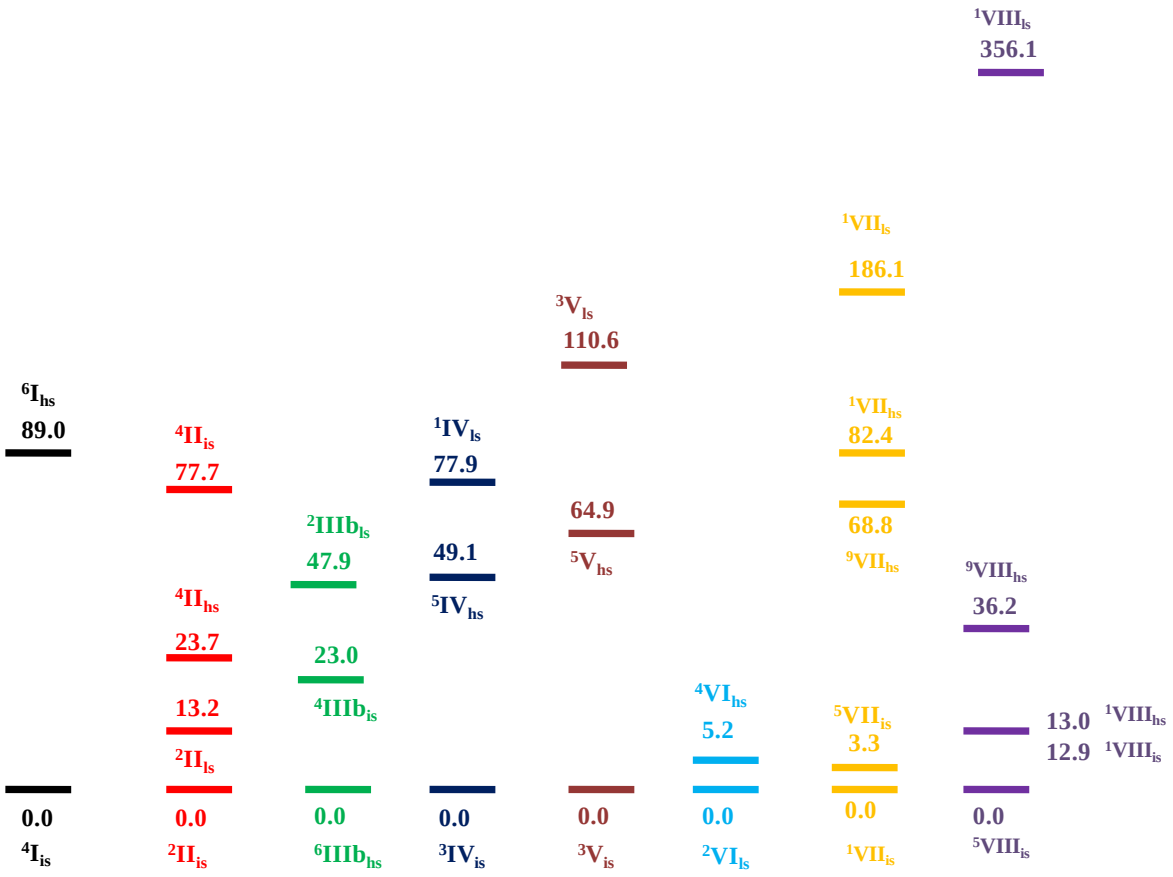

Figure 3.1. B3LYP-D2 computed relative energies (in kJ/mol) of species I-VIII.

This ground state is also supported by the experimental report.[39] The computed Fe-N_{avg} bond length of the ground state is found to be 1.865 Å and this is in good agreement with the X-ray structure (see Table 3.1).[39] A spin density of ρ = 2.663 is located at the iron center (see Table 3.2). The optimized structure of ground state and the corresponding spin density plot is shown in Figure 3.2(a,b). The electronic configuration at the metal center is found to be $(d_{yz})^2$, $(d_{xz})^1$, $(d_z^2)^1$, $(d_{xy})^1$ and $(d_{x^2-y^2})^0$ (see Figure 3.3).

Table 3.1. B3LYP-D2 computed selective structural parameters of species I-VIII.

	Bond length (Å)									Bond angle (°)				
Spin States	Fe-N_1	Fe-N_2	Fe-N_3	Fe-N_4	Fe1-N_{av}	Fe1-N_{av}	Fe-O1	Fe-O2	O1-O2	N_1-Fe-N_3	N_4-Fe-N_1	Fe-O1-O2	Fe_2-O_2-O_1	Fe1-O1-Fe2
$^6I_{hs}$	1.984	1.983	1.924	1.924	1.953	-	-	-	-	159.7	159.7	-	-	-
$^4I_{is}$	1.864	1.864	1.867	1.867	1.865	-	-	-	-	171.9	171.9	-	-	-
Exp.[39]	1.881	1.876	1.892	1.889	1.884									
$^4II_{hs}$	1.876	1.876	1.881	1.881	1.878	-	2.121	-	1.321	162.1	162.1	117.3	-	-
$^4II_{is}$	1.873	1.873	1.872	1.871	1.872	-	2.001	-	1.325	160.9	160.9	119.1	-	-
$^2II_{is}$	1.877	1.877	1.877	1.877	1.877	-	2.173	-	1.296	162.7	162.7	118.5	-	-
$^2II_{ls}$	1.877	1.877	1.883	1.882	1.879	-	1.963	-	1.321	160.2	160.2	121.7	-	-
$^6III_{hs}$	2.127	2.058	2.093	2.096	2.093	-	1.994	2.009	1.537	128.8	133.5	-	-	-
$^4III_{is}$	2.176	2.119	1.990	2.053	2.084	-	1.953	1.973	1.508	127.1	132.9	-	-	-
$^2III_{ls}$	1.980	1.978	1.988	1.985	1.983	-	1.954	1.952	1.516	129.2	150.8	-	-	-
Exp.[56]							1.927							
$^5IV_{hs}$	1.887	1.915	1.906	1.883	1.898	-	2.028	-	1.482	159.4	158.1	113.9	-	-
$^3IV_{is}$	1.881	1.875	1.884	1.889	1.882	-	1.889	-	1.486	156.4	155.3	112.5	-	-
$^1IV_{ls}$	1.876	1.893	1.866	1.878	1.878	-	1.756	-	1.522	154.0	156.5	115.1	-	-
$^5V_{hs}$	1.953	1.986	1.981	2.066	1.996	-	1.680	-	-	148.3	134.8	-	-	-
$^3V_{is}$	1.912	1.912	1.911	1.911	1.911	-	1.653	-	-	152.9	152.9	-	-	-
$^1V_{ls}$	1.943	1.874	1.944	1.866	1.906	-	1.657	-	-	159.3	144.5			
Exp.[29]					1.86		1.64							
$^4VI_{hs}$	1.914	1.914	1.878	1.878	1.896	-	1.664	-	-	155.7	155.8	-	-	-
$^2VI_{hs}$	1.898	1.898	1.887	1.886	1.892	-	1.630	-	-	152.2	152.1	-	-	-

Exp.[50]					1.87		1.59							
$^{9}VII_{hs}$	-	-	-	-	1.917	1.917	1.860	1.860	-	-	-	-	-	169.8
$^{I}VII_{hs}$	-	-	-	-	1.913	1.895	1.834	1.711	-	-	-	-	-	160.5
$^{5}VII_{is}$	-	-	-	-	1.904	1.903	1.800	1.801	-	-	-	-	-	167.6
$^{1}VII_{is}$	-	-	-	-	1.913	1.895	1.835	1.711	-	-	-	-	-	160.5
$^{1}VII_{ls}$	-	-	-	-	1.891	1.885	1.704	1.744	-	-	-	-	-	149.4
Exp.[55]					1.89		1.74							
$^{9}VIII_{hs}$	-	-	-	-	1.882	1.886	2.261	2.256	1.330	-	-	118.3	118.1	
$^{I}VIII_{hs}$	-	-	-	-	1.890	1.884	2.115	2.078	1.370	-	-	113.1	112.7	
$^{5}VIII_{is}$	-	-	-	-	1.882	1.883	2.124	2.127	1.334	-	-	116.4	116.3	
$^{1}VIII_{is}$	-	-	-	-	1.891	1.884	2.078	2.115	1.370	-	-	113.1	112.7	
$^{1}VIII_{ls}$	-	-	-	-	1.879	1.878	1.756	1.759	1.472	-	-	113.9	115.1	

Table 3.2. B3LYP-D2 computed spin density values of the species I-VIII.

Spin states	Fe1	Fe2	O`1	O2
$^{6}I_{hs}$	3.914	-	-	-
$^{4}I_{is}$	2.663	-	-	-
$^{2}I_{ls}$	1.187	-	-	-
$^{4}II_{is}$	0.984	-	0.548	0.771
$^{2}II_{is}$	2.586	-	-0.703	-0.881
$^{2}II_{ls}$	-1.029	-	0.591	0.771
$^{6}IIIb_{hs}$	3.887	-	0.315	0.338
$^{4}IIIb_{is}$	3.018	-	-0.443	-0.327
$^{2}IIIb_{ls}$	1.089	-	-0.060	-0.057
$^{5}IV_{hs}$	2.591		0.446	0.101
$^{3}IV_{is}$	2.109		-0.104	-0.026
$^{1}IV_{ls}$	0		0	0
$^{5}V_{hs}$	3.087	-	0.576	-
$^{3}V_{is}$	1.347	-	0.584	-
$^{1}V_{ls}$	0	-	0	-
$^{4}VI_{hs}$	1.279	-	0.757	-
$^{2}VI_{ls}$	1.061	-	0.585	-
$^{9}VII_{hs}$	3.208	3.208	0.876	-
$^{I}VII_{hs}$	1.524	-2.351	0.125	-
$^{5}VII_{is}$	2.207	2.202	0.261	-
$^{1}VII_{is}$	2.351	-1.524	-0.125	-
$^{1}VII_{ls}$	0	0	0	-
$^{9}VIII_{hs}$	2.662	2.663	0.739	0.738
$^{I}VIII_{hs}$	2.512	-2.639	0.498	0.427
$^{5}VIII_{is}$	2.593	2.593	-0.584	-0.583
$^{1}VIII_{is}$	2.639	-2.511	-0.498	-0.426
$^{1}VIII_{ls}$	0	0	0	0

The HOMO-LUMO gap of the ground state is found to be 4.446 eV (see Figure 3.2c). By reaction of $[Fe^{III}(TAML)]^{-}$ species with dioxygen can form mononuclear end-on $\{[(TAML)Fe^{IV}\text{-}\eta^{1}\text{-}O_2]^{\bullet-}\}$/side-on species $\{[(TAML)Fe^{III/IV}\text{-}\eta^{2}\text{-}O_2]^{3/2-}\}$ or dinuclear μ-oxo$\{[(TAMLFe^{IV})_2(\mu\text{-oxo})]^{2-}\}$/peroxo $\{[(TAMLFe^{IV})_2(peroxo(O_2)]^{2-}\}$bridged species which can also consequently form iron(IV/V)-oxo species.[55] After reactions of species I with

dioxygen, the iron metal center is no longer in the plane but it gets out of the plane due to repulsion between charges of the coordinated nitrogen atoms and the axial ligands, that forces the iron atom out of the plane. The distance of the shift of iron metal out of the plane depends upon the elastic force that drives the iron metal back into the plane is balanced.[39]

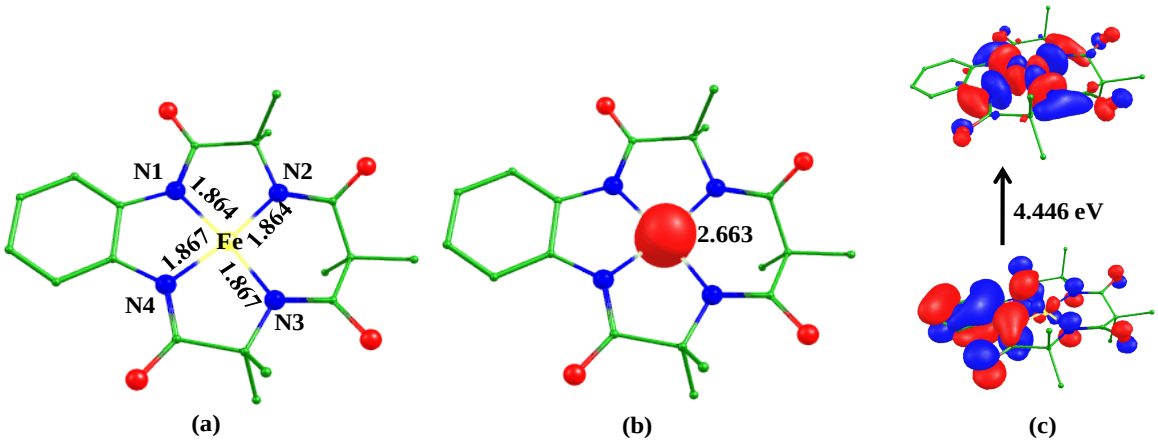

Figure 3.2. Computed Eigen-value plot incorporating energies computed for *d*-based orbitals for alpha and beta spin corresponding to the ground state ($^4I_{is}$) (energies are given in eV).

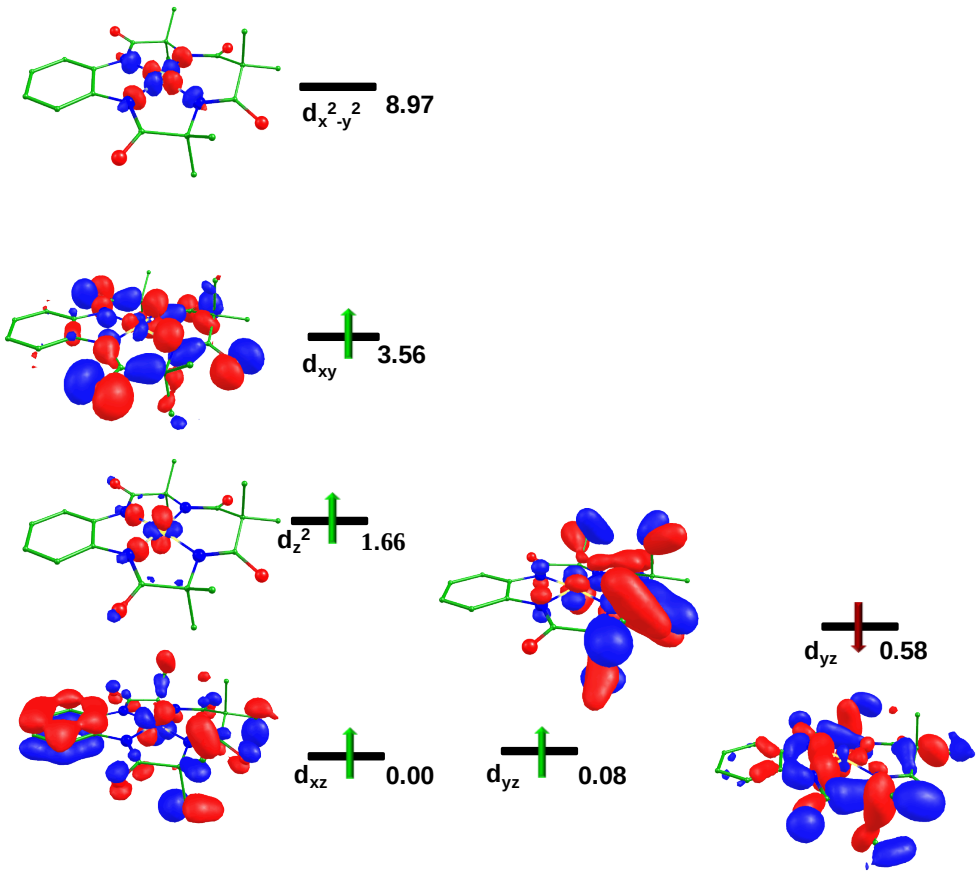

Figure 3.3. B3LYP-D2 a) optimized structure of $^4I_{is}$ (bond length in Å), b) its spin density plot, and c) HOMO-LUMO frontier molecular orbitals of $^4I_{is.}$

3.3.2 Electronic structure and energetics of end-on [(TAML)Fe^{IV}-η ^{1}-O$_2$] $^{\bullet-}$ (species II)

When the binding mode of oxygen is η ^{1} can generate end on iron-superoxo species.[91-92] Five spin interactions can be possible due to the presence of four unpaired electrons at the iron center and one unpaired electron at distal oxygen. We have optimized all spin states of this species except $^6II_{hs}$ (due to the spin convergence issue). The antiferromagnetically coupled intermediate spin state ($^2II_{is}$) is found to be the ground state with the $^4II_{hs}$, $^4II_{is,}$ and $^2II_{is}$ lie at 23.8, 77.7, and 13.2 kJ/mol, respectively (see Table 3.3), and the ground state is also inconsistent with similar species in the previous report.[56] The optimized structure and spin density plot of the ground state are shown in Figure 3.4. The average Fe-N_{avg} bond of species II is larger than species I by 0.013 Å.

Table 3.3. Possible electronic configuration for superoxo species II.

	Electronic configuration		
Spin state	**Fe(IV)**	**$O_2^{\bullet-}$**	**Relative energy(kJ/mol)**
$^6II_{hs}$	$\pi^*_{xz}{}^{\uparrow}\ \pi^*_{yz}{}^{\uparrow}\ \delta_{xy}{}^{\uparrow}\ \sigma^*_{z^2}{}^{\uparrow}\ \delta_{x^2-y^2}$	$\Phi^{\uparrow}$	-
$^4II_{hs}$	$\pi^*_{xz}{}^{\uparrow}\ \pi^*_{yz}{}^{\uparrow}\ \delta_{xy}{}^{\uparrow}\ \sigma^*_{z^2}{}^{\uparrow}\ \delta_{x^2-y^2}$	$\Phi^{\downarrow}$	23.7
$^4II_{is}$	$\pi^*_{xz}{}^{\uparrow\downarrow}\ \pi^*_{yz}{}^{\uparrow}\ \delta_{xy}{}^{\uparrow}\ \sigma^*_{z^2}\ \delta_{x^2-y^2}$	$\Phi^{\uparrow}$	77.7
$^2II_{is}$	$\pi^*_{xz}{}^{\uparrow\downarrow}\ \pi^*_{yz}{}^{\uparrow}\ \delta_{xy}{}^{\uparrow}\ \sigma^*_{z^2}\ \delta_{x^2-y^2}$	$\Phi^{\downarrow}$	0
$^2II_{ls}$	$\pi^*_{xz}{}^{\uparrow\downarrow}\ \pi^*_{yz}{}^{\uparrow\downarrow}\ \delta_{xy}\ \sigma^*_{z^2}\ \delta_{x^2-y^2}$	$\Phi^{\uparrow}$	13.2

The Fe-O1 and O1- O2 bond lengths are computed to be 2.173 Å and 1.296 Å. The O1-O2 bond length is in agreement with the other metal-superoxo species that are ca. 1-2-1.3 Å.[92-97]

The stretching frequencies of the Fe-O and O-O bonds are computed to be *v*314 cm^{-1} and *v*1200 cm^{-1} that are also agreed with calculated stretching frequency with other superoxide species.[92-96] The iron center of this species is found to be shifted by 0.08 Å (see Table 3.4) above the plane along with the axial bond concerning species I and this is due to repulsion between charges of equatorial ligated nitrogen atoms and axial superoxo ligands, that forces the iron metal out of the plane, and suggested species II is relatively less planar.

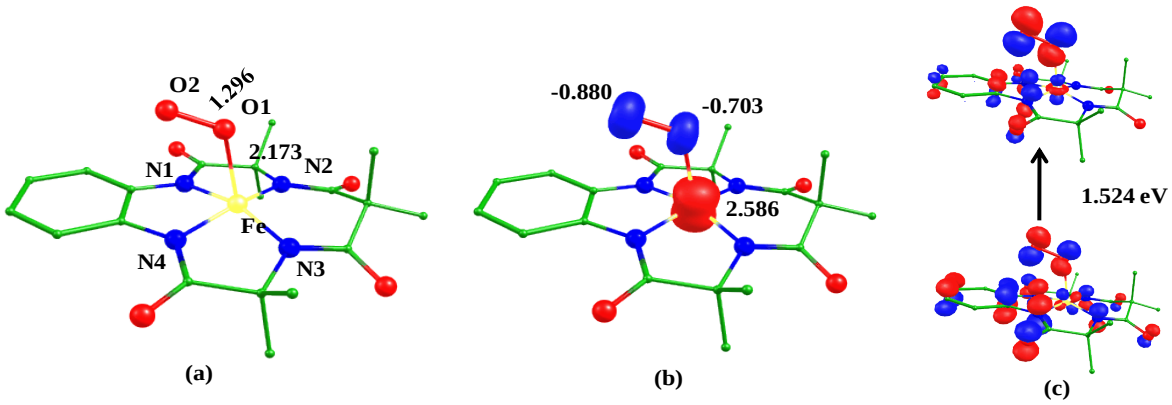

Figure 3.4. B3LYP-D2 a) optimized structure (bond length in Å) of $^{2}II_{is}$, b) its spin density plot and c) The HOMO-LUMO frontier molecular orbitals of $^{2}II_{is}$.

Table 3.4. B3LYP-D2 computed displacement in Z-axis species II-VIII.

Species	Displacement in Z-axis (Å)
$^{2}II_{is}$	0.08
$^{6}IIIb_{hs}$	0.72
$^{3}IV_{is}$	0.19
$^{3}V_{is}$	0.35
$^{2}VI_{ls}$	0.40
$^{1}VII_{is}$	-0.41, 0.42
$^{5}VIII_{is}$	0.04, -0.07

The HOMO-LUMO gap of species II is found to be 1.524 eV (see Figure 3.4c) and the gap is smaller than the species I. The eigenvalue plot of the ground state is shown in Figure 3.5, and

the electronic configuration at the metal center is found to be $(d_{xz})^2$, $(d_{yz})^1$, $(d_{xy})^1$, $(d_z^2)^0$ and $(d_{x^2-y^2})^0$. The spin density values at iron and distal oxygen centers are computed to be 2.586 and -0.881 suggest the presence of antiferromagnetic coupling between them and a significant spin density at distal oxygen can activate C-H and O-H bond.[56,61,97]

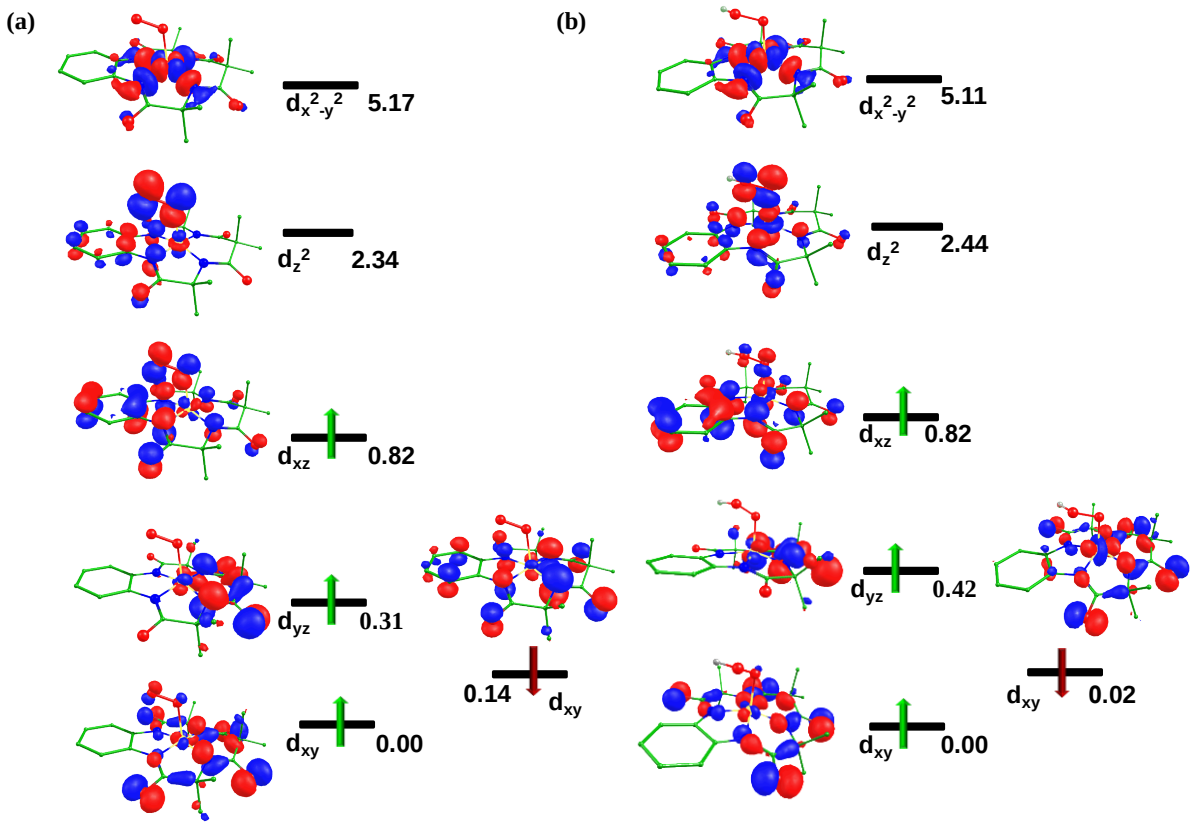

Figure 3.5. Computed eigenvalue plot incorporating energies computed for *d*-based orbitals for alpha and beta spin corresponding to the ground state a) ($^2II_{is}$) b) ($^3IV_{is}$) (energies are given in eV).

3.3.3 Electronic structure and energetics of side-on $[(TAML)Fe^{IV}\text{-}(\eta^2\text{-}O_2)]^{2-}$ (species IIIa) and $[(TAML)Fe^{III}\text{-}(\eta^2\text{-}O_2)]^{3-}$ (species IIIb)

When the binding mode of oxygen is η^2, the side-on species can be formed.[96-97] Similar to species II, we have tried to optimize all three possible spin surfaces (such as $^5IIIa_{hs}$, $^3IIIa_{is}$, and $^1IIIa_{ls}$) of species III but here we have got optimization only at one spin state i.e. the low

spin surface (^{1}IIIa$_{ls}$), and other spin surfaces have found bond cleavage between iron and oxygen atoms. The optimized structure for the low spin is shown in Figure 3.6a, and spin density on the iron center is found to be zero as (S=0). The Fe-N$_{avg}$ bond elongates to 1.904 Å and this is lower than species IIIb and higher than species II (see Table 1). The computed Fe-O1, Fe-O2, and O1-O2 bond lengths are found to be 1.908 Å, 1.906 Å, and 1.478 Å, these are also found to be similar to Mn(III)-peroxo species.[6] The computed stretching frequency of the O1-O2 bond is found to be *v*945 cm^{-1}, and bond length of the O1-O2 also decreases which shows that O-O bond strength increases with the increase of the oxidation state.[7]

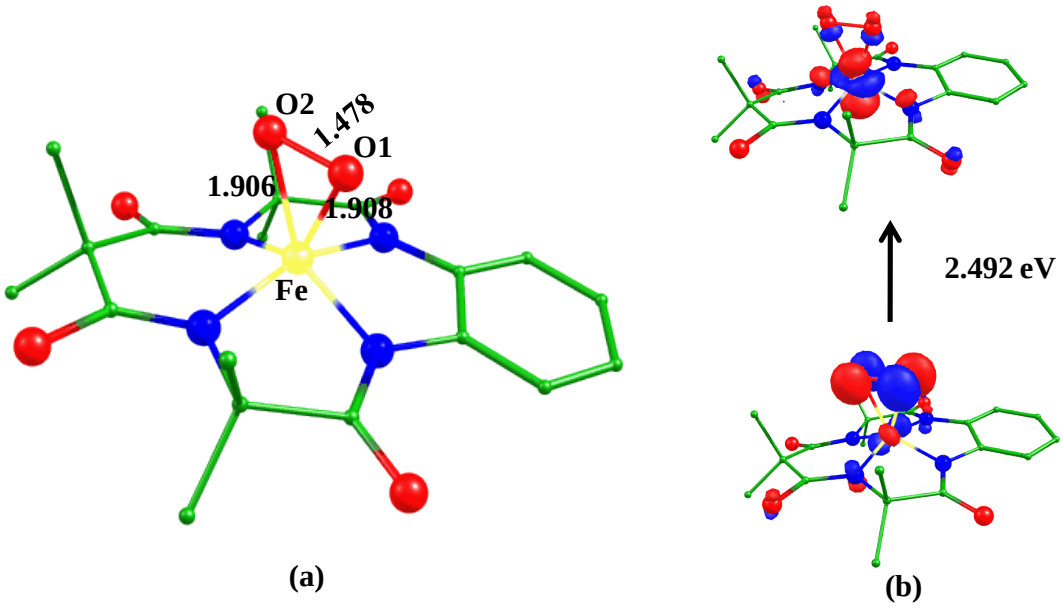

Figure 3.6. B3LYP-D2 (a) optimized structure (bond length in Å) and (b HOMO-LUMO frontier molecular orbitals) of the low spin state of side-on [(TAML)Fe^{IV}-(η ^{2}-O$_2$)]$^{2-}$ (species IIIa)**.**

The HOMO-LUMO gap is found to be 2.492 eV (see Figure 3.6b). The eigenvalue plot is shown in Figure 3.7, and the electronic configuration of the iron is found to be $(d_{xy})^2$, $(d_{yz})^2$, $(d_z^2)^0$, $(d_{xz})^0$, and $(d_{x^2-y^2})^0$. This species can also involve in catalytic reactions. So, here we have also taken side-on species with oxidation state +3 at the iron center and attempted to optimize all three possible spin states (^{6}IIIb$_{hs}$, ^{4}IIIb$_{is}$, and ^{2}IIIb$_{ls}$) for the species IIIb. Our DFT

calculations predicted that the sextet spin state (^{6}IIIb$_{hs}$) is found to be the ground state with ^{4}IIIb$_{is}$ and ^{2}IIIb$_{ls}$ lie at 23.0 and 47.9 kJ/mol, respectively.

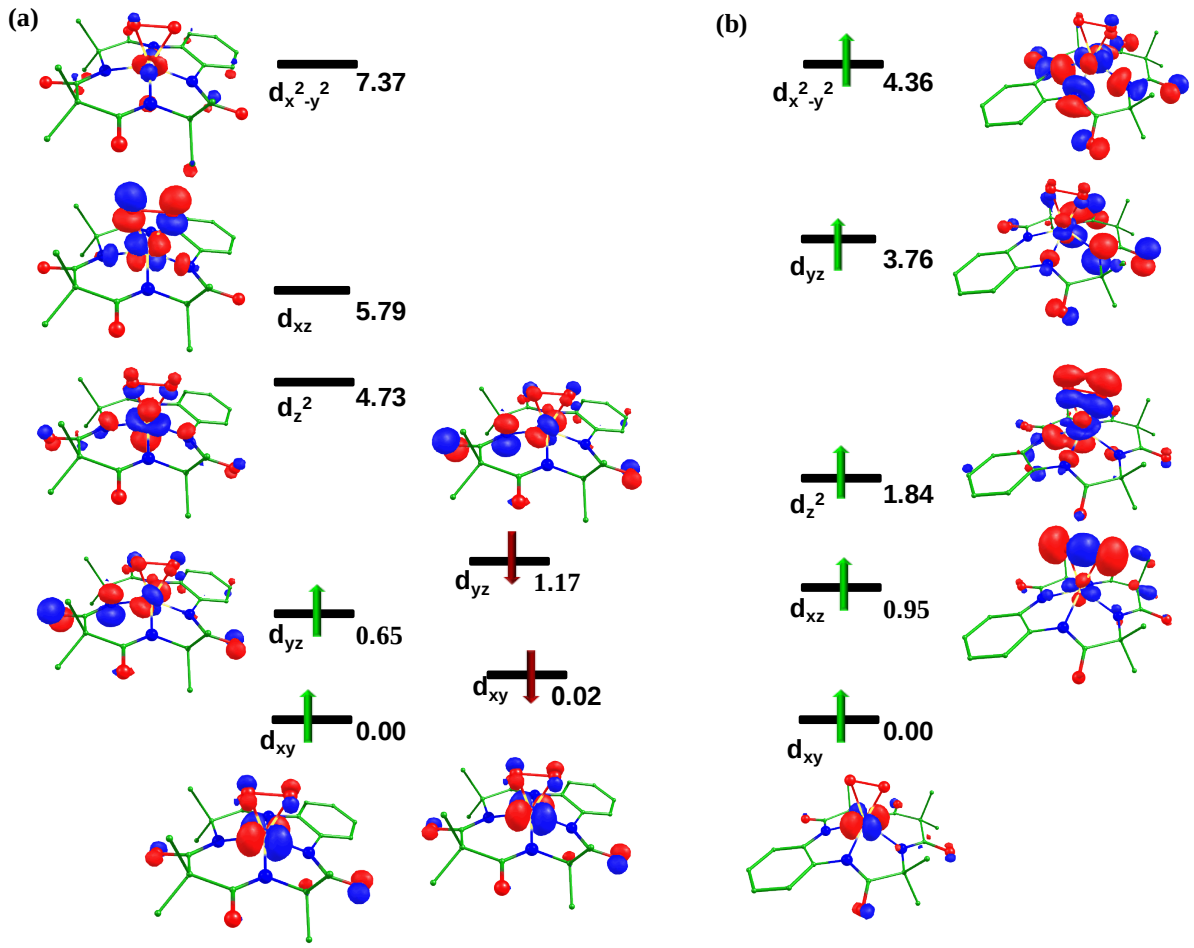

Figure 3.7. Computed Eigenvalue plot incorporating energies computed for *d*-based orbitals for alpha and beta spin corresponding to the a) (^{1}III$_{ls}$a) (energies are given in eV); b) ground state (^{6}IIIb$_{hs}$) (energies are given in eV).

The optimized structure and spin density plot of the ground state is shown in Figure 3.8a,b. The Fe-N$_{avg}$ bond is computed to be 2.093 Å and this is higher than the species II. The computed Fe-O1 and Fe-O2 bond lengths are 2.009 Å and 1.994 Å which are also observed in similar architecture.[98] Computed parameters suggest that the oxygen binds with iron symmetrically. The iron oxygen bond length is found to be smaller while the O1-O2 bond length is slightly higher than the end-on species II and these are also confirmed by the

computed stretching frequency of Fe-O (ν448 cm^{-1}) and O-O (ν821 cm^{-1}) bond.[95] The computed bond angle of O1-Fe-O2 is found to be 45.1º indicates the pseudo square pyramidal geometry of species IIIb. The shift in the position of the iron atom is computed to be 0.72 Å (see Table 3.4).

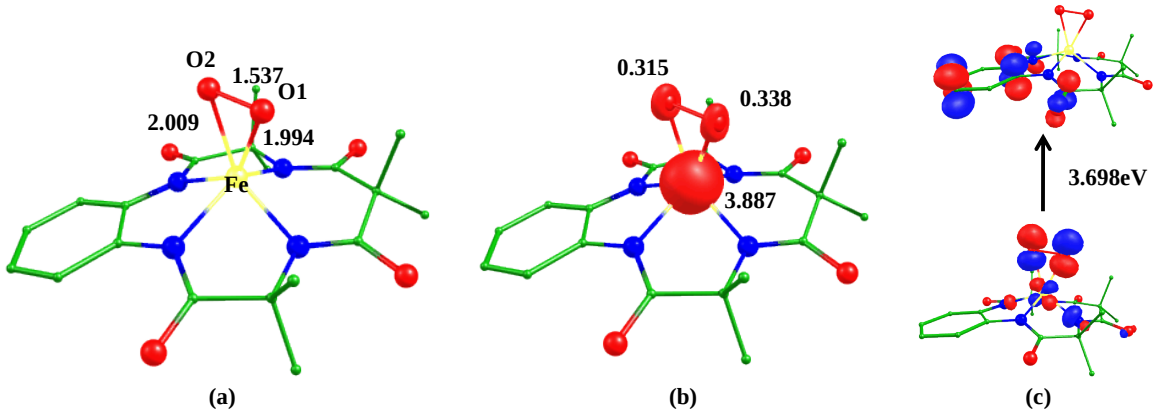

Figure 3.8. B3LYP-D2 a) optimized structure (bond length in Å), b) spin density plot of ^{6}IIIb$_{hs}$ and c) The HOMO-LUMO frontier molecular orbitals of ^{6}IIIb$_{hs}$.

The spin density value of 3.887 is located at the iron center and both the oxygen atoms occupied similar spin density that indicates symmetrical binding mode (see Figure 3.8b). The eigenvalue plot of the ground state is shown in Figure 3.7b. The electronic configuration on Fe metal is found to be $(d_{xy})^1$, $(d_{xz})^1$, $(d_{yz})^1$, $(d_z^2)^1$, and $(d_{x^2-y^2})^1$. The HOMO-LUMO gap of species IIIb is calculated to be 3.698 eV (see Figure 3.8c), and this is greater than species II may indicate the possibility of lesser electron transfer compared to species II. The significant spin densities at both the oxygen atoms indicates that they can participate in catalytic reactions.[61-64] The NBO plots of the ground state show that orbital contributions between both the oxygen atoms and iron center are involved in making σ-bond confirmed the presence of σ-bond between both the oxygen atoms and iron center (see Figure 3.9).

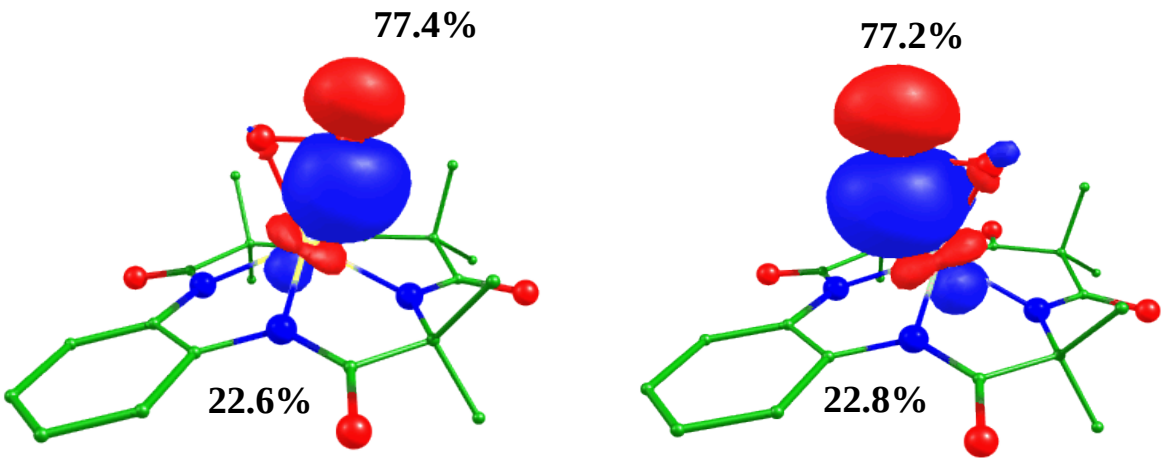

Figure 3.9. Computed NBO plots for species IIIb (^{6}IIIb$_{hs}$).

3.3.4 Electronic structure and energetics of hydroperoxo [(TAML)Fe^{IV}-OOH]$^{\cdot}$ (species IV)

After the abstraction of hydrogen from organic substrates by superoxo/peroxo species can form hydroperoxo species. Similar to the above species, there are three possible spin states of species IV, in which intermediate spin (S=1) is found to be the ground state, and other spin states, S=2 and S=0 lie at 49.1 and 77.9 kJ/mol higher in energy, respectively. The optimized structure and spin density plot of the ground state are shown in Figure 3.10a,b. The Fe-O1 and O1-O2 bond lengths are computed to be 1.889 Å and 1.486 Å. The Fe-O1 bond length decreases while the O1-O2 bond length increases from the superoxo species II. The computed shift in the position of the iron atom is found to be 0.19 Å. The decrease in Fe-O1 bond length is due to the overlapping between *d*-orbital of Fe and *p*-orbital of the oxygen atom. The HOMO-LUMO gap also decreases to 0.059 eV compared to species II and IIIb (see Figure 3.10c). The NBO analysis shows that iron d_z^2 orbital has (20.1%) orbital contribution whereas p_z orbital of oxygen has a 79.9 % orbital contribution (see NBO plot Figure 10d). There is a reduction of spin density at the oxygen atoms also observed. The eigenvalue plot is

shown in Figure 3.5b. The electronic configuration at the metal center is found to be $(d_{xz})^2$, $(d_{yz})^1$, $(d_{xy,})^1$, $(d_z^2)^0$ and $(d_{x^2-y^2})^0$.

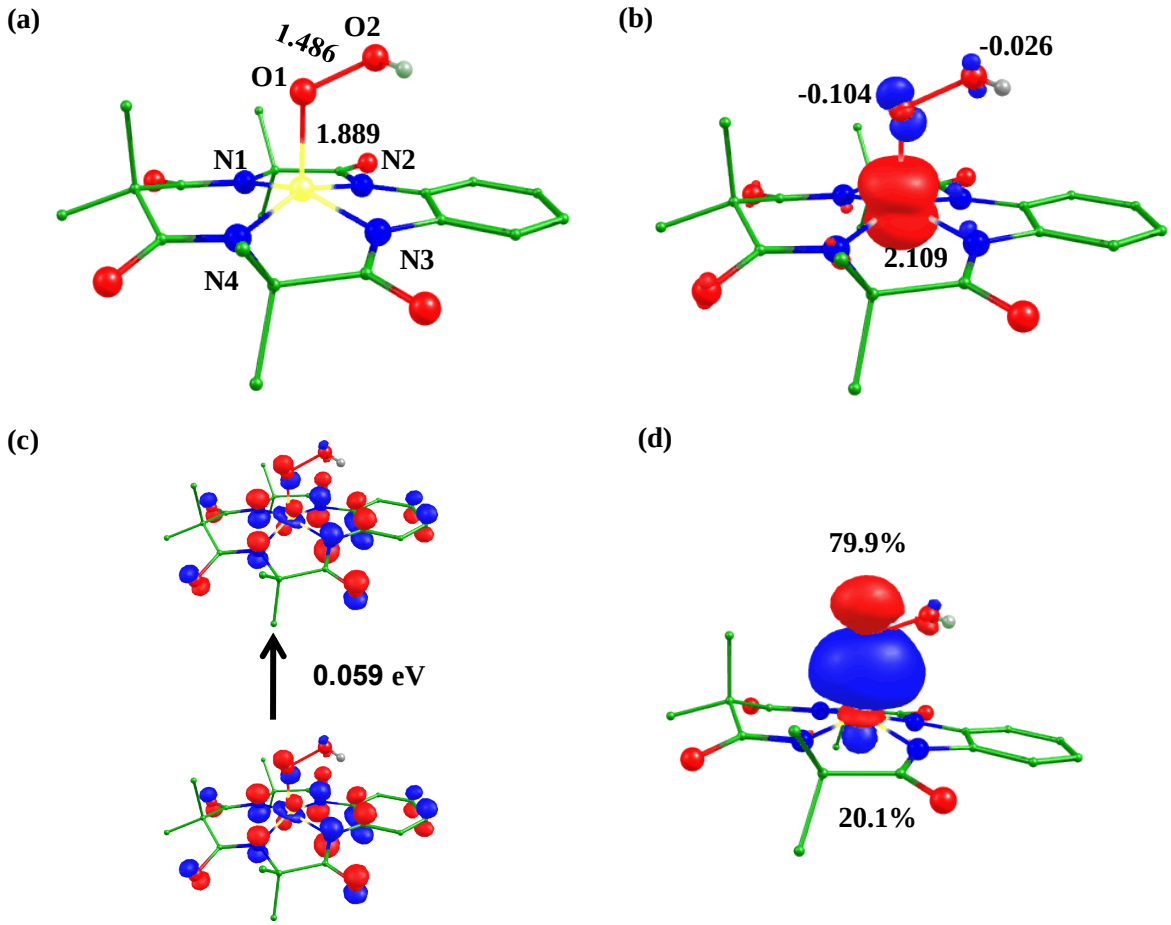

Figure 3.10. B3LYP-D2 a) optimized structure (bond length in Å) and b) its spin density plot of $^3IV_{is}$ d) Computed NBO plot of specie IV ($^3IV_{is}$).

The stretching frequency of the Fe-O and O-O bond is computed to be *v*420cm^{-1} and *v*823cm^{-1}, decrease in O-O stretching frequency by *v*373cm^{-1} compared to end on [(TAML)Fe^{IV}-η ^{1}-O_2]$^{\bullet-}$ species supported an increase in O1-O2 bond length.

3.3.5 Electronic structure and spin energetics of [(TAML)Fe^{IV}-O]$^{2-}$ (species V)

The first direct evidence for the generation of a non-heme Fe^{IV}-O complex was reported by Wieghardt *et al.* at the start of this millennium,[99] and this is well characterized by X-ray and

spectroscopically. Non-heme Fe^{IV}-O species became a popular active oxidant that can show reactivity towards C-H, O-H, N-H, and oxygen atom transfer reactions, etc. in detail.[68-69] Here we have also optimized high (quintet, S=2), intermediate (triplet, S=1) and low spin (singlet, S=1) states of the species, and our DFT calculations reveal that the triplet state is found to be the ground state with the quintet and singlet states lie at 86.4 kJ/mol and 112.6 kJ/mol higher in energy, respectively, (see Figure 3.1) and this ground state is inconsistent with earlier experimental and theoretical reports (see Figure 3.11(a,b)). [54,65-68]

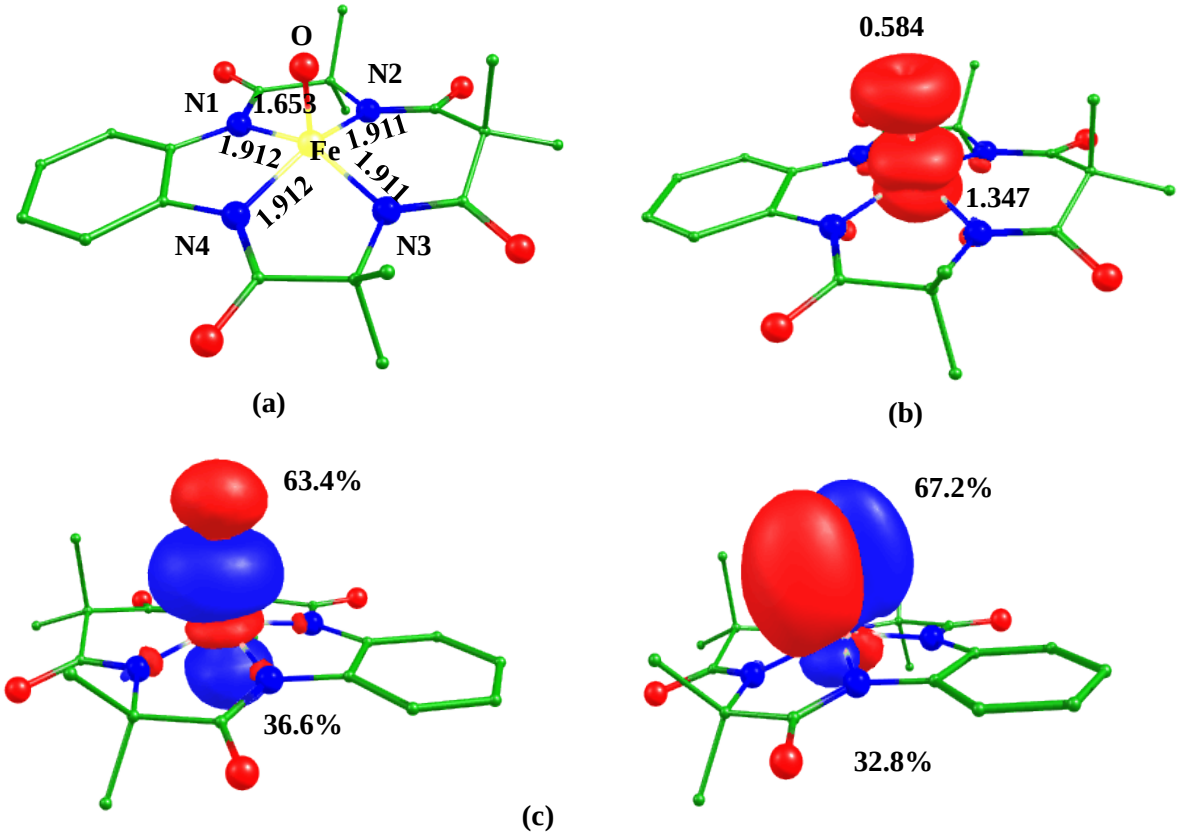

Figure 3.11. B3LYP-D2 a) optimized structure (bond length in Å), b) its spin density plot of $^3V_{is}$, and c) Computed NBO plots of $^3V_{is}$.

The calculated Fe-N_{avg} bond length is 1.929 Å, higher than the species I (see Table 3.1). The Fe-O bond length is found to be 1.653 Å, shorter than the other spin surface quintet and singlet state (see Table 3.1) and this shorter bond length is due to the formation of π bond between iron and oxygen reveals double bond character (see scheme 3.2).

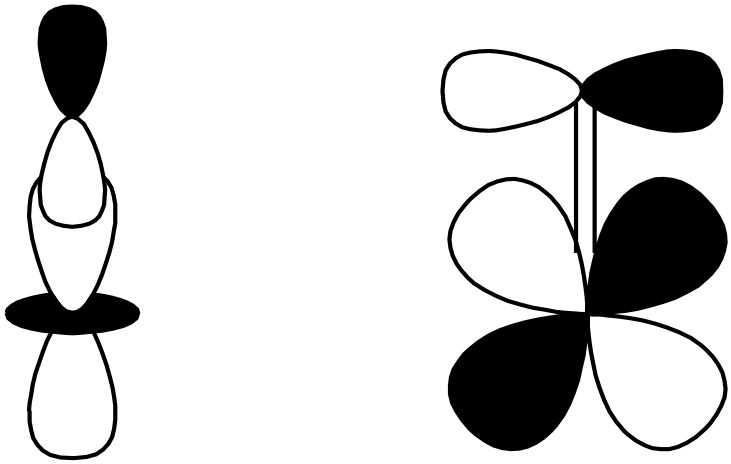

Scheme 3.2. Frontier π-orbitals of Fe^{IV}=O species at S = 3/2 spin surface.

The Fe-O bond length matches with previous experimental and theoretical studies.[53] The orbital contribution of iron d_z^2 (36.6%) and oxygen p_z (63.4%) suggests the formation of σ-bond and also supported the formation of π-bond between $d_{yz,}$ and p-orbital of the oxygen (see Figure 3.11c). However, additional orbital contributions between iron and oxygen atoms show the formation of π-bond and unfold the presence of a double bond character between them.

The electronic configuration of the ground state is computed to be $(d_{xy})^2$, $(d_{yz})^1$, $(d_{xz,})^1$, $(d_z^2)^0$ and $(d_x^2{-}_y^2)^0$ (see Figure 3.12a). A similar electronic configuration is also found with other iron(IV)-oxo species.[53] Here, d_x^2-$_y^2$ orbital has higher energy than the d_z^2 due to the strong equatorial ligand field of the TAML ligand. The stretching frequency of the Fe-O bond is found to be 880 cm^{-1} reveals the strength of the bond. The computed Fe-N_{avg} bond length is found to be 1.971 Å and this is longer than the species I. The iron center of this species is also shifted towards the z-axis by 0.35 Å (see Table 3.4). The computed HOMO-LUMO gap is 3.605 eV (see Figure 3.13a).

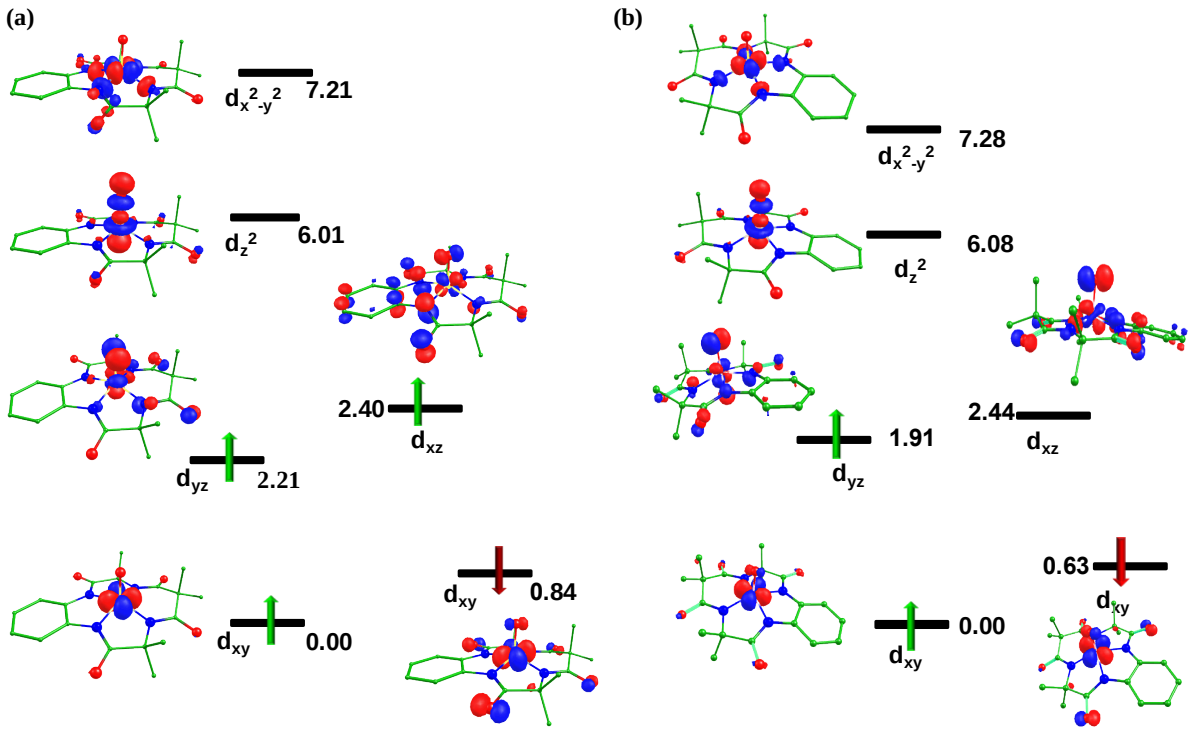

Figure 3.12. Computed eigenvalue plot incorporating energies computed for *d*-based orbitals for alpha and beta spin corresponding to the ground state a) ($^5V_{is}$) b) ^2VI (energies are given in eV).

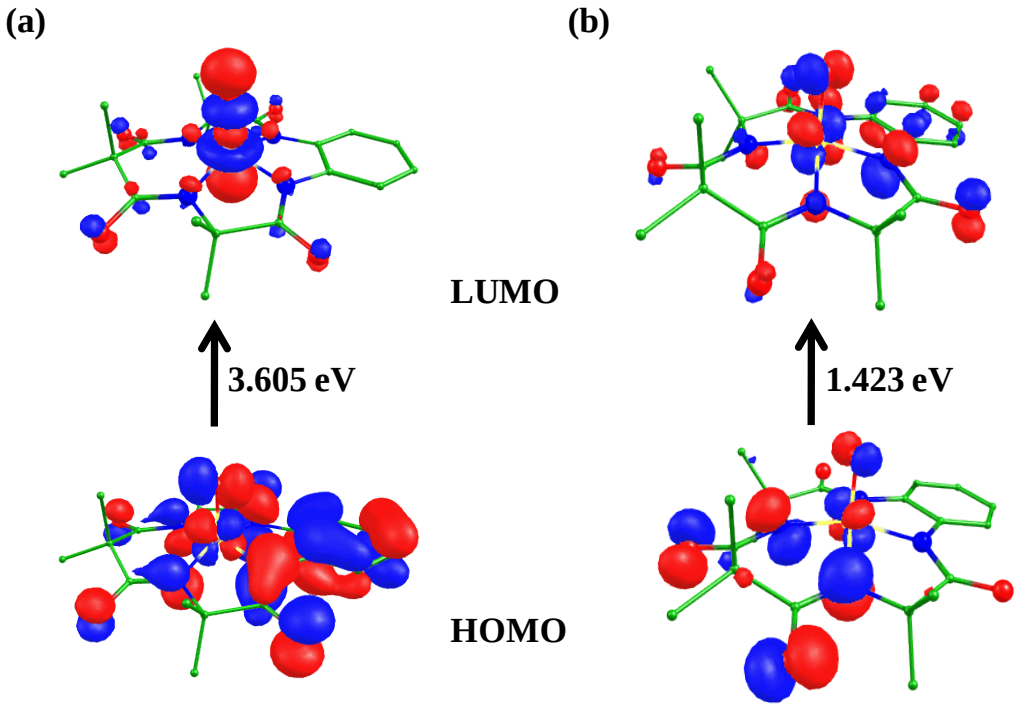

Figure 3.13. The HOMO-LUMO frontier molecular orbitals of (a) species V, and (b) species VI.

The computed spin density value of 1.347 is located at the iron center and the ferryl oxygen is also acquired spin density (ρ = 0.584). The coordinated nitrogen atoms also gained some spin density via electron delocalization. A significant spin density at the oxygen atom can activate the C-H/O-H bond of aliphatic/aromatic hydrocarbons.[71-74]

3.3.6 Electronic structure and spin energetics of [(TAML)Fe^{V}-O]$^{-}$ species (VI)

One electron oxidation of (species V) can produce the [(TAML)Fe^{V}-O]$^{-}$ (species VI) and this species with sufficient thermal stability for extensive spectroscopic characterization was generated by collins's.[50] Our DFT calculations show that the low spin (S=1/2; ^{2}VI) is found to be the ground state with high spin (S=3/2; ^{4}VI) lies at 5.21 kJ/mol higher in energy. The energy gap and the ground state are consistent with previous experimental and theoretical studies on similar architectures.[100]

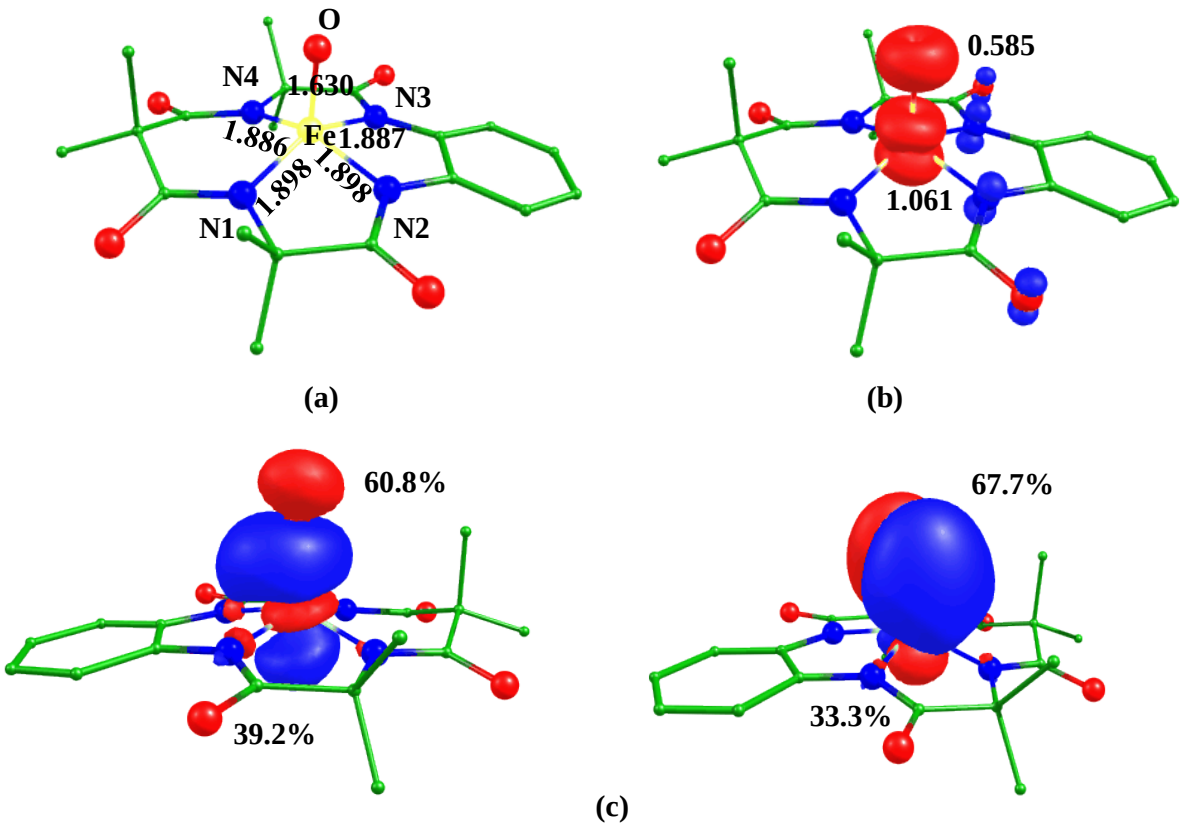

Figure 3.14. B3LYP-D2 a) optimized structure (bond length in Å), b) its spin density plot of $^{3}V_{is}$, and c) computed NBO plot of species VI ($^{2}VI_{ls}$).

Optimized structure and corresponding spin density plot of the ground state (^{2}VI) are shown in Figure 3.14(a,b). The Fe-O bond length of the ground state is calculated to be 1.630 Å which corresponds to a double Fe-O covalent bond character in the ground state and the bond length is slightly elongated to 1.662 Å in the high spin state. The structural parameters are also in agreement with a similar X-ray structure (see Table 3.1).[50] The increment in equatorial Fe-N bond lengths is observed when the spin state changes from low spin to high spin. If Fe^{V}=O species are compared with Fe^{III} species, it is revealed that the bond length of Fe-N bonds gets elongated in the case of Fe^{V}=O species. The eigenvalue plot along with the orbital diagram of the ground state (^{2}I) is shown in Figure 3.12b. For square pyramidal geometry, d_{xz} and d_{yz} are frontier orbitals while d_{xy} is the lowest-lying within the *d*-orbital. The electronic configuration is computed to be $(d_{xy})^2$,$(d_{yz})^1$,$(d_{xz,})^0$,$(d_z^2)^0$ and $(d_x^2{}_{-y}^2)^0$ (see Figure 3.12b). The spin density value of 1.061 has been detected on the Fe center inferring the presence of one unpaired electron. Similarly, all the nitrogen atoms also gain electron density via spin delocalization. Spin densities on the iron and oxygen are of the same signs while nitrogen atoms acquire opposite signs which indicate that the spin of the electrons is the same on iron and oxygen while it is opposite on the nitrogen atoms. The computed Fe-O bond length is found to be smaller than the species V (see Table 3.1) and this is due to the increment in the double bond character between the iron center and oxygen atom. The computed HOMO-LUMO gap is 1.423 eV smaller than species V (see Figure 3.13b). The shift in the position of the iron atom is computed to be 0.40 Å. The redox potential change upon the oxidation at the iron center can also increase the reactivity of species (VI).[71,101] From the NBO calculations, we see that iron d_z^2 (39.2%) which is greater than species VI and oxygen p_z (60.8%) suggests a stronger bond between iron and oxygen than species V (see Figure 3.14c). A spin density at

the oxygen can help in C-H/O-H bond activation as well as in olefin epoxidation/sulfoxidation.[50,102]

3.3.7 Electronic structure and energetics of [(TAML)Fe^{IV}-μO-(TAML)Fe^{IV}]$^{2-}$ (species VII)

The well-characterized [(TAML)Fe^{V}-O]$^{-}$ species can react with [Fe^{III}(TAML)]$^{-}$ species I to generate μ-oxo dinuclear derivative [(TAML)Fe^{IV}-μO-Fe^{IV}(TAML)]$^{2-}$ (species VII).[50,53] This μ-oxo bridged dinuclear species is also well characterized in previous studies.[55] The dimer [(TAML)Fe^{IV}-μO-Fe^{IV}(TAML)]$^{2-}$ (species VII) possesses the same ligand, one can assume that both the iron centers are likely to have an identical spin on both the iron centers. There are five possible spin states such as ^{9}VII$_{hs}$, ^{1}VII$_{hs}$, ^{5}VII$_{is}$, ^{1}VII$_{is,}$ and ^{1}VII$_{ls}$ for species VII, and the schematically electronic interactions for each of the iron centers are shown in Table 3.5.

Table 3.5. Possible spin states of [(TAML)Fe^{IV}-μO-Fe^{IV}(TAML)]$^{2-}$ species.

	Electronic configuration		
Spin state	**Fe(IV)**	**Fe(IV)**	**Relative energy(kJ/mol)**
^{9}VII$_{hs}$	$\pi^{*\uparrow}_{xz}\,\pi^{*\uparrow}_{yz}\,\delta^{\uparrow}_{xy}\,\sigma^{*\uparrow}_{z^2}\,\delta^{\uparrow}_{x^2-y^2}$	$\pi^{*\uparrow}_{xz}\,\pi^{*\uparrow}_{yz}\,\delta^{\uparrow}_{xy}\,\sigma^{*\uparrow}_{z^2}\,\delta^{\uparrow}_{x^2-y^2}$	**68.8**
^{1}VII$_{hs}$	$\pi^{*\uparrow}_{xz}\,\pi^{*\uparrow}_{yz}\,\delta^{\uparrow}_{xy}\,\sigma^{*\uparrow}_{z^2}\,\delta^{\uparrow}_{x^2-y^2}$	$\pi^{*\downarrow}_{xz}\,\pi^{*\downarrow}_{yz}\,\delta^{\downarrow}_{xy}\,\sigma^{*\downarrow}_{z^2}\,\delta^{\downarrow}_{x^2-y^2}$	**82.4**
^{5}VII$_{is}$	$\pi^{*\uparrow\downarrow}_{xz}\,\pi^{*\uparrow}_{yz}\,\delta^{\uparrow}_{xy}\,\sigma^{*\uparrow}_{z^2}\,\delta^{\uparrow}_{x^2-y^2}$	$\pi^{*\uparrow\downarrow}_{xz}\,\pi^{*\uparrow}_{yz}\,\delta^{\uparrow}_{xy}\,\sigma^{*\uparrow}_{z^2}\,\delta^{\uparrow}_{x^2-y^2}$	**3.3**
^{1}VII$_{is}$	$\pi^{*\uparrow\downarrow}_{xz}\,\pi^{*\uparrow}_{yz}\,\delta^{\uparrow}_{xy}\,\sigma^{*\uparrow}_{z^2}\,\delta^{\uparrow}_{x^2-y^2}$	$\pi^{*\uparrow\downarrow}_{xz}\,\pi^{*\downarrow}_{yz}\,\delta^{\downarrow}_{xy}\,\sigma^{*\uparrow}_{z^2}\,\delta^{\uparrow}_{x^2-y^2}$	**0**
^{1}VII$_{ls}$	$\pi^{*\uparrow\downarrow}_{xz}\,\pi^{*\uparrow\downarrow}_{yz}\,\delta^{\uparrow\downarrow}_{xy}\,\sigma^{*\uparrow}_{z^2}\,\delta^{\uparrow}_{x^2-y^2}$	$\pi^{*\uparrow\downarrow}_{xz}\,\pi^{*\uparrow\downarrow}_{yz}\,\delta^{\uparrow\downarrow}_{xy}\,\sigma^{*\uparrow}_{z^2}\,\delta^{\uparrow}_{x^2-y^2}$	**186.1**

We have optimized all five spin surfaces of species VII, and our DFT calculations predicted that the intermediate spin state (^{1}VII$_{is}$) with antiferromagnetic coupling between both the iron centers is found to be the ground state and other spin surfaces such as ^{9}VII$_{hs}$, ^{1}VII$_{hs}$, ^{5}VII$_{is}$,

and $^{1}VII_{ls}$ lie at 68.8, 82.4, 3.3, 186.1 kJ/mol higher in energy, respectively. This ground state is also supported by experimental observation.[55] The optimized structure and spin density plot of the ground state ($^{1}VII_{is}$), and $^{5}VII_{is}$ are shown in Figure 3.15. The Fe1/Fe2-N_{avg} bond lengths are found to be 1.913 Å and 1.895 Å which are greater than species I and these are also in agreement with the experimental data.[55] The bond angle of Fe-O-Fe is found to be 160.5˚ and this bending around bridged oxygen atom is aroused due to the ligated nitrogen atom donates the electron density to the empty d_z^2 which overlap to the *p*-orbital of the oxygen atom, and this also includes the double bond formation between iron and oxygen atoms.

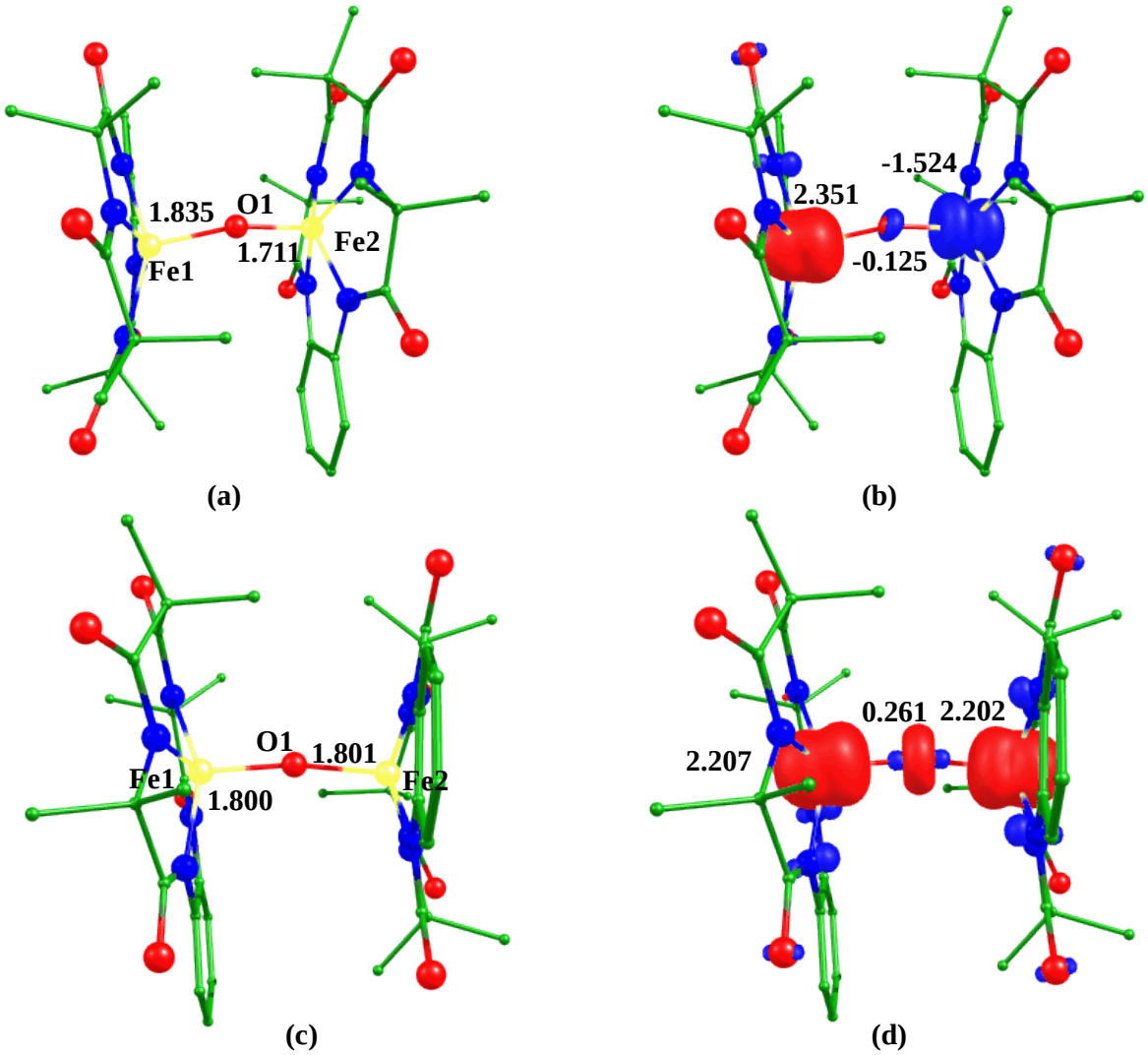

Figure 3.15. B3LYP-D2 a) optimized structure (bond length in Å) of $^{1}VII_{is}$ and its b) spin density plot, c) optimized structure (bond length in Å) and d) its spin density plot of $^{5}VII_{is}$.

Our calculations also reveal that both the iron centers have equivalent formal charges, but there is a significant difference in Fe-O bond lengths. Computed Fe1-μ-oxo and Fe2-μ-oxo bond distances are found to be 1.835 Å and 1.711 Å, respectively, and these are also observed on similar structures in previous reports.[73] Selected bond lengths and spin density values are shown in Table 3.1 and Table 3.2. The iron atom (Fe2) possess beta electron (the negative spin density in Figure 3.15b) has a shorter Fe-O bond length compared to the other Fe atom. Spin density on both the iron centers is found to be 2.351 and -1.524. There is also a significant electron density found at the oxygen atom.

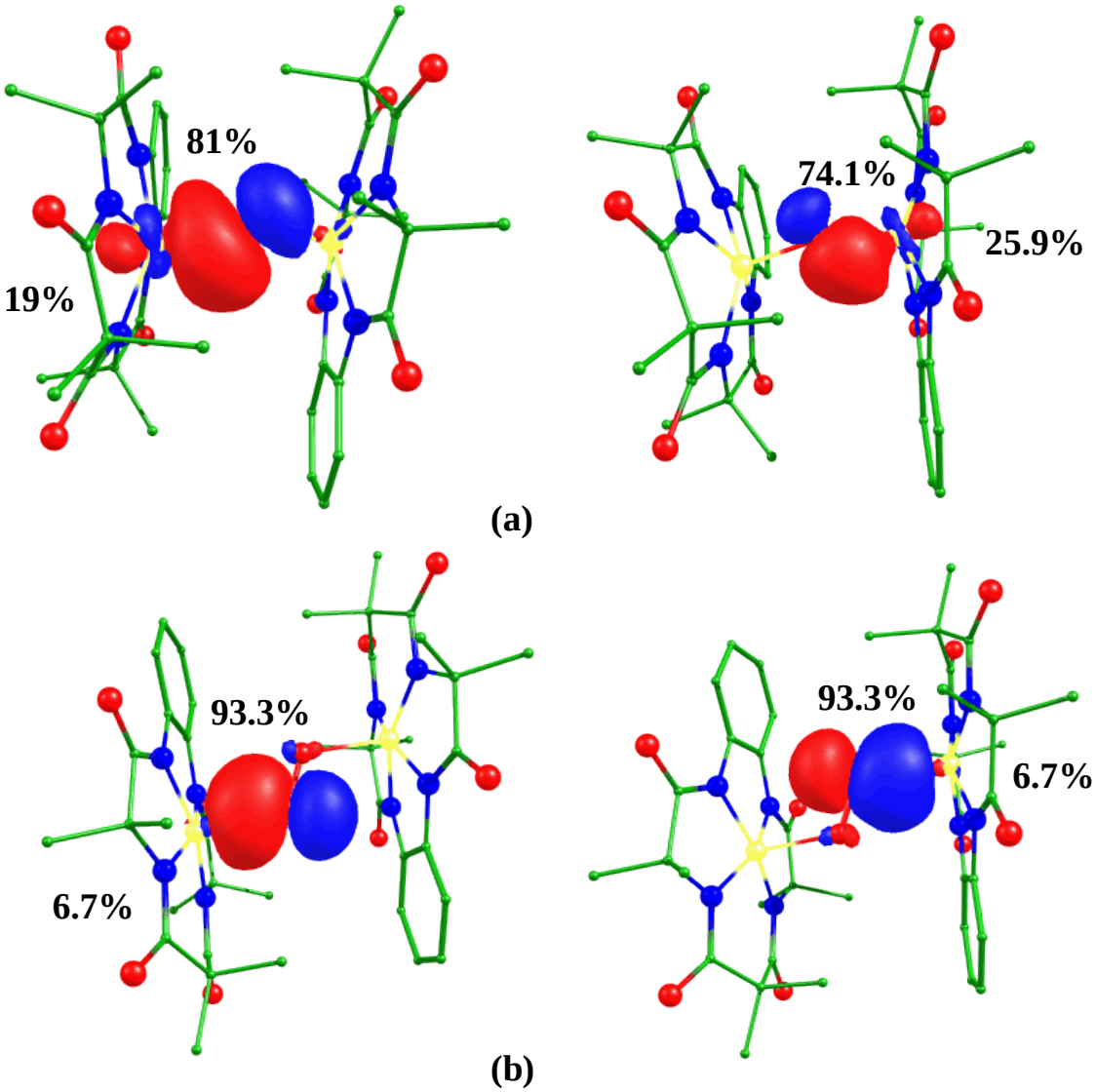

Figure 3.16. Computed NBO plots of the ground state of a) species VII, and b) species VIII.

From the NBO analysis, σ bonding effects also observed between the iron Fe1 (19%) and μ-oxo (81%) whereas the Fe2-μ-oxo possesses the additional π-bond character as the Fe2 (25.9%) and μ-oxo (74.1%) orbital contribution is detected (see Figure 3.16a). From the earlier report, di-μ-oxo-diiron(VII) species, two μ-oxo groups yield a symmetric Fe(IV)-oxo environment.[103] Here, our calculations suggest an asymmetric environment with one shorter and other longer Fe-O bond lengths due to the presence of one μ-oxo group.[73] The Fe-Fe bond distance is 3.495 Å. From Table 3.4, we see that the displacements along z-axis are -0.41 Å and 0.42 Å and these opposite sign indicates that both iron centers are approaching each other.

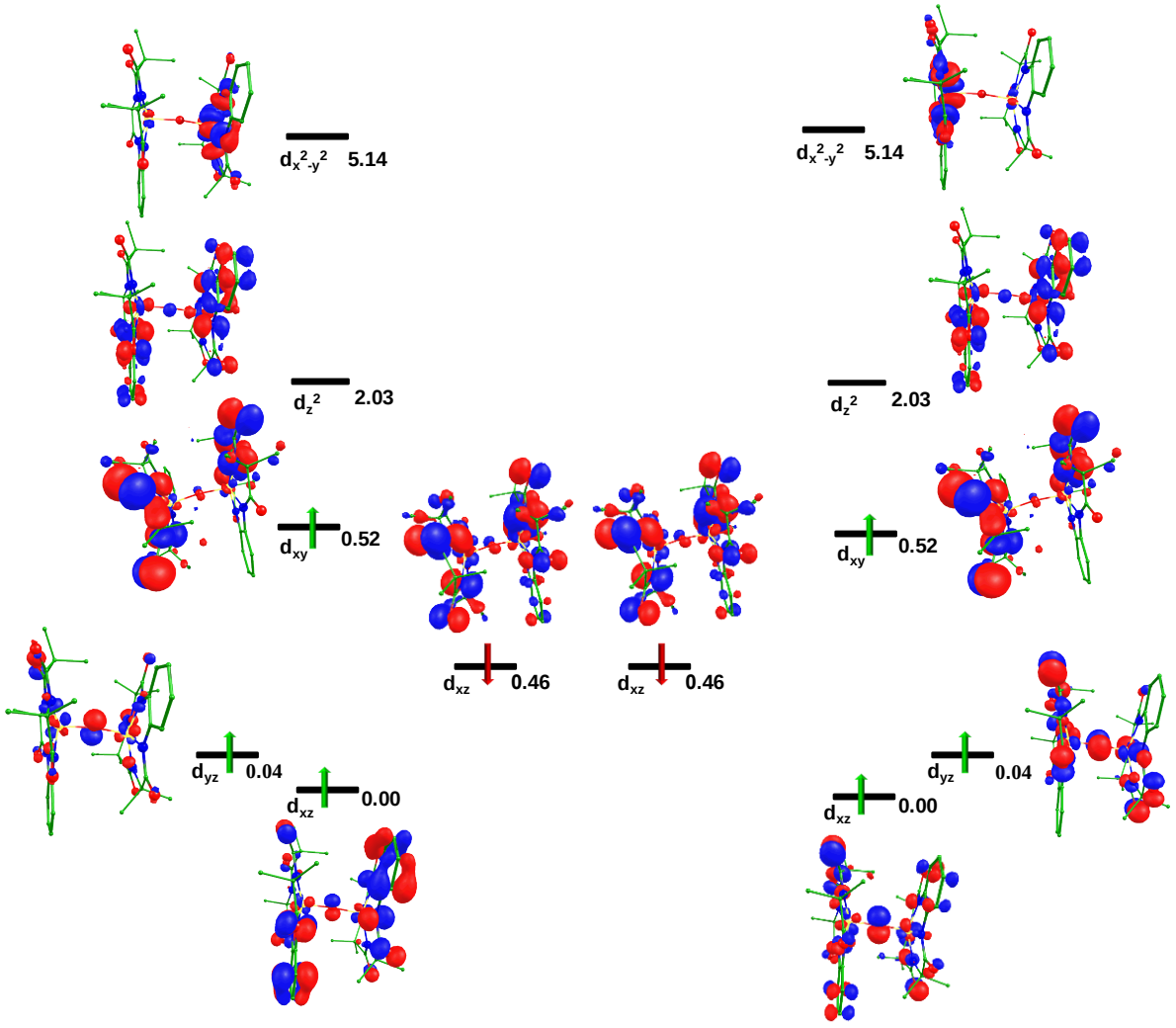

Figure 3.17. Computed Eigen-value plot incorporating energies computed for *d*-based orbitals for alpha and beta spin corresponding to the ground state ($^1VII_{is}$) (energies are given in eV).

Nitrogen atoms coordinated to iron atoms gain significant electron density via the electron delocalization mechanism. The bridged oxygen atom possesses a significant electron density that can help in C-H/O-H bond activation.[72-73] The eigenvalue plot is shown in Figure 3.17, and both the Fe atoms have the similar electronic configuration of $(d_{xy})^2$, $(d_{yz})^1$, $(d_{xz})^1$, $(d_z^2)^0$, and $(d_{x^2-y^2})^0$ with alpha electrons in d_{xz} and d_{yz} at Fe1 center and beta electrons in d_{xz} and d_{yz} at Fe2 center (see Figure 3.17.) The d_z^2 and $d_{x^2-y^2}$ are unoccupied due to much higher in energy. The HOMO-LUMO gap is found to be 0.939 eV (see Figure 3.18a). The computed magnetic exchange coupling constant is found to be J = -88.82 cm^{-1} and this shows that antiferromagnetic coupling occurs between both the iron centers.

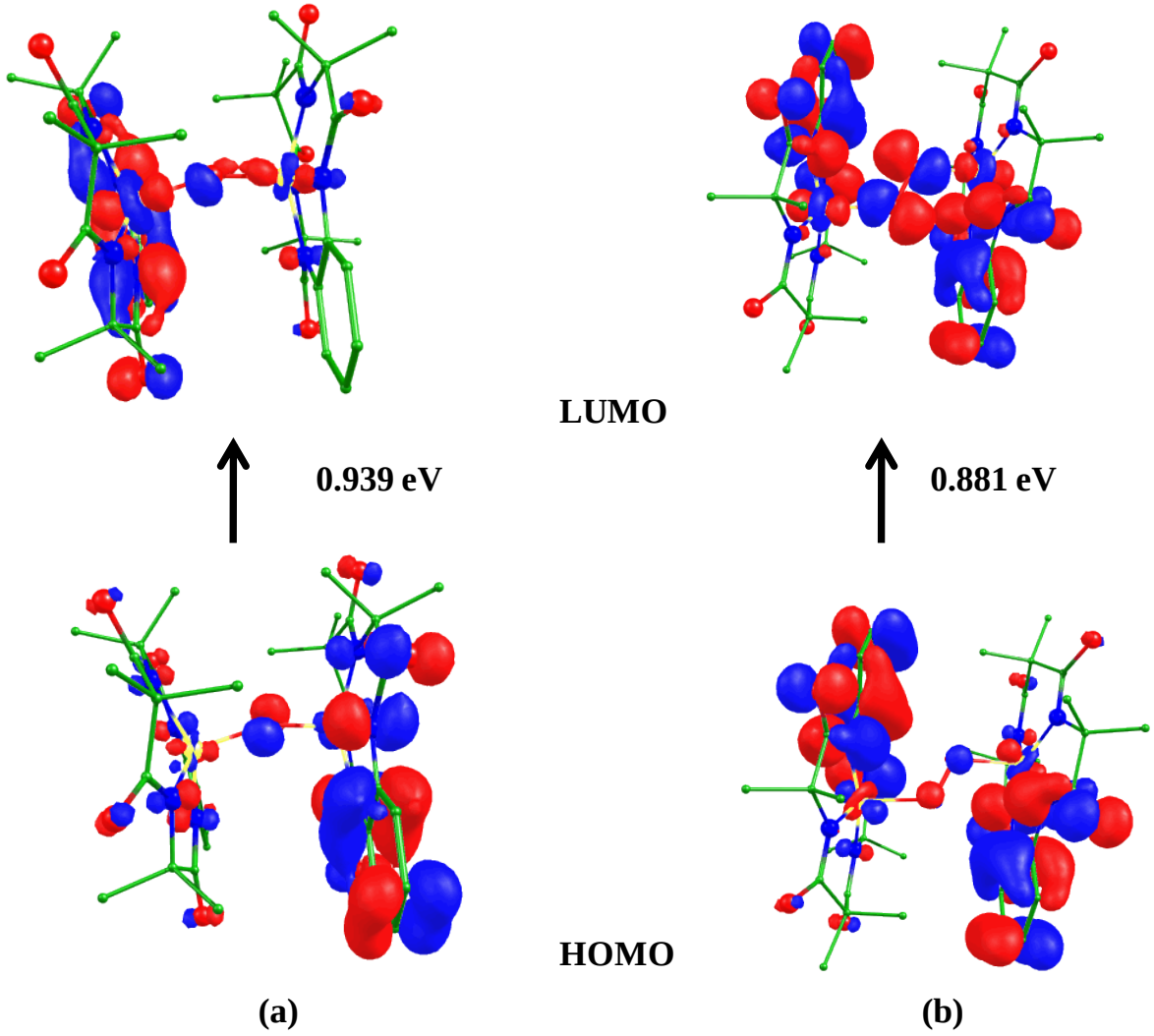

Figure 3.18. The HOMO-LUMO frontier molecular orbitals of species VII ($^1VII_{is}$) and species VIII ($^5VIII_{is}$).

The stretching frequency for Fe1-μO and Fe2-μO are υ 349 cm^{-1} and υ 766 cm^{-1} respectively, these frequencies are supported by the iron-μ-oxo bond distances.

3.3.8. Electronic structure and spin energetics of [(TAML)Fe^{IV}-O-O-Fe^{IV}(TAML)]$^{2-}$ (species VIII)

When they react in 1:2 of species I and dioxygen can generate oxygen bridged dinuclear (μ-1,2-peroxo) species; [(TAML)Fe^{IV}-O-O-Fe^{IV}(TAML)]$^{2-}$ (species VIII).[55] Similar to species VII, we have also optimized five possible spin states of species VIII (see Table 3.6) and our DFT calculations show that the $^{5}VIII_{is}$ spin state is the ground state with $^{9}VIII_{hs}$, $^{1}VIII_{hs,}$ $^{1}VIII_{is}$ and $^{1}VIII_{ls}$ lie at 36.2, 13.0, 12.9, and 356.3 kJ/mol higher in energy, respectively. The optimized structure and spin density plot of the $^{5}VIII_{is}$ (ground state) and the corresponding spin state ($^{1}VIII_{is}$) are shown in Figure 3.19.

Table 3.6 Possible electronic configuration for [(TAML)Fe^{IV}-O-O-Fe^{IV}(TAML)]$^{2-}$ species VIII.

	Electronic configuration		
Spin state	**Fe(IV)**	**Fe(IV)**	**Relative energy(kJ/mol)**
$^{9}VIII_{hs}$	$\pi^{*\uparrow}_{xz}\pi^{*\uparrow}_{yz}\delta^{\uparrow}_{xy}\sigma^{*\uparrow}_{z^2}\delta^{\uparrow}_{x^2-y^2}$	$\pi^{*\uparrow}_{xz}\pi^{*\uparrow}_{yz}\delta^{\uparrow}_{xy}\sigma^{*\uparrow}_{z^2}\delta^{\uparrow}_{x^2-y^2}$	**36.2**
$^{1}VIII_{hs}$	$\pi^{*\uparrow}_{xz}\pi^{*\uparrow}_{yz}\delta^{\uparrow}_{xy}\sigma^{*\uparrow}_{z^2}\delta^{\uparrow}_{x^2-y^2}$	$\pi^{*\downarrow}_{xz}\pi^{*\downarrow}_{yz}\delta^{\downarrow}_{xy}\sigma^{*\downarrow}_{z^2}\delta^{\uparrow}_{x^2-y^2}$	**13.0**
$^{5}VIII_{is}$	$\pi^{*\uparrow\downarrow}_{xz}\pi^{*\uparrow}_{yz}\delta^{\uparrow}_{xy}\sigma^{*}_{z^2}\delta^{\uparrow}_{x^2-y^2}$	$\pi^{*\uparrow\downarrow}_{xz}\pi^{*\uparrow}_{yz}\delta^{\uparrow}_{xy}\sigma^{*}_{z^2}\delta^{\uparrow}_{x^2-y^2}$	**0**
$^{5}VIII_{is}$	$\pi^{*\uparrow\downarrow}_{xz}\pi^{*\uparrow}_{yz}\delta^{\uparrow}_{xy}\sigma^{*}_{z^2}\delta^{\uparrow}_{x^2-y^2}$	$\pi^{*\uparrow\downarrow}_{xz}\pi^{*\downarrow}_{yz}\delta^{\downarrow}_{xy}\sigma^{*}_{z^2}\delta^{\uparrow}_{x^2-y^2}$	**12.9**
$^{1}VIII_{ls}$	$\pi^{*\uparrow\downarrow}_{xz}\pi^{*\uparrow\downarrow}_{yz}\delta_{xy}\sigma^{*}_{z^2}\delta^{\uparrow}_{x^2-y^2}$	$\pi^{*\uparrow\downarrow}_{xz}\pi^{*\uparrow\downarrow}_{yz}\delta_{xy}\sigma^{*}_{z^2}\delta^{\uparrow}_{x^2-y^2}$	**356.3**

The calculated Fe1-μO1 and Fe2-μO2 bond lengths of the $^{5}VIII_{is}$ state are found to be 2.124 Å and 2.127 Å, respectively, and are higher than the corresponding bond lengths of species $^{I}VII_{is}$. The O1-O2 bond length is 1.334 Å, in agreement with the other μ-1,2-peroxo

species,[104] and the computed stretching frequency for the O-O bond is *v*1050 cm^{-1} corresponds to the formation of peroxo linkage.

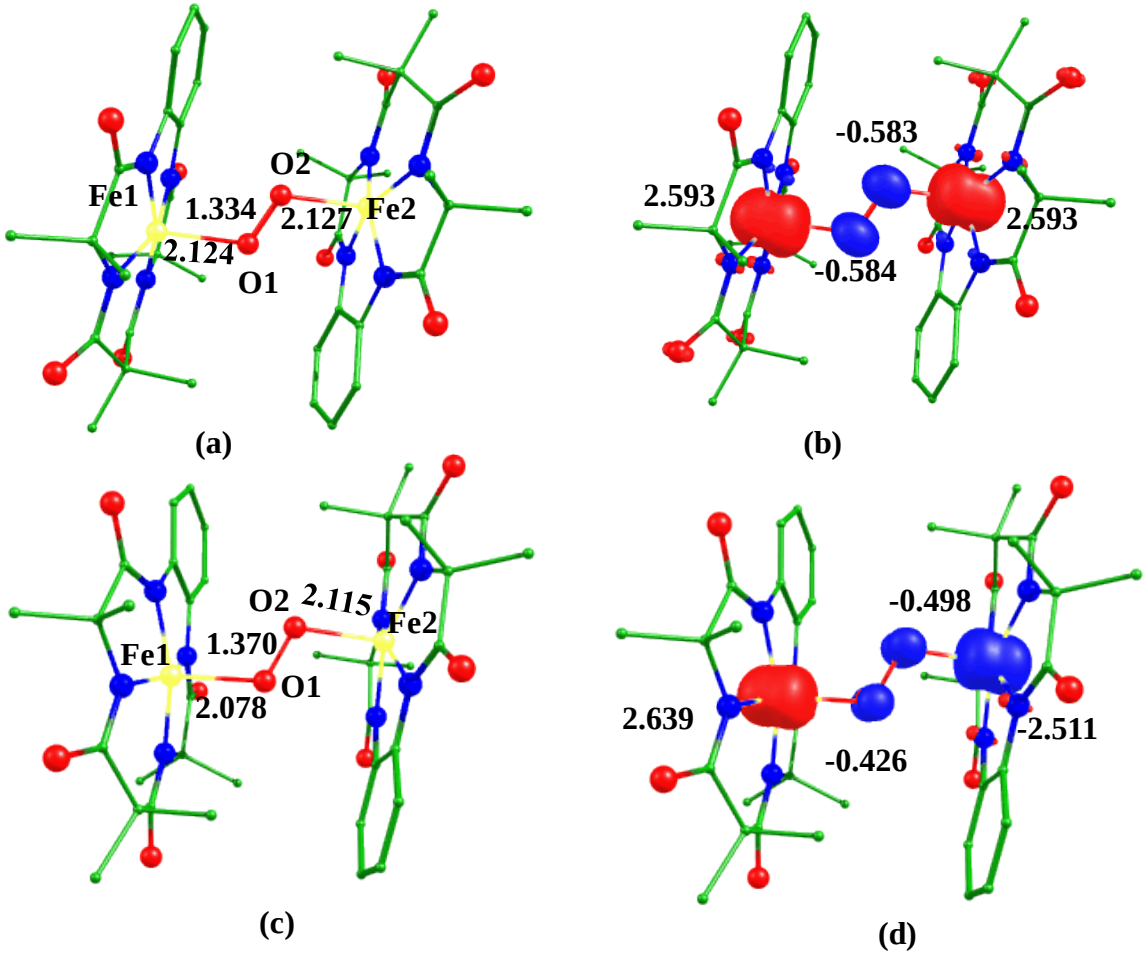

Figure 3.19. B3LYP-D2 a) optimized structure (bond length in Å) and b) its spin density plot of $^{5}VIII_{is,}$ c) optimized structure (bond length in Å) and d) its spin density plot of $^{1}VIII_{is}$.

The same stretching frequencies (*v*258cm^{-1}) are found for both Fe1-O1 and Fe2-O2 bonds, smaller than the μ-oxo bridge species, indicates that Fe-O bond length is longer in (μ-1,2-peroxo) species and suggested the presence of a single bond between both the iron-oxygen bonds (see Table 3.1). The Fe1-N_{avg} and Fe2-N_{avg} bond distances are computed to be 1.882 Å and 1.883 Å, respectively. The spin density plot of the ground state shows that both the iron centers possess the same sign of spin density suggests the presence of ferromagnetic coupling between iron centers and this is also supported by the estimation of the magnetic exchange

with the value of 777.44 cm^{-1}. Although the experimental magnetic exchange value of the species is not observed yet. The coordinated nitrogen atoms to the iron center also acquired electron density due to electron delocalization.

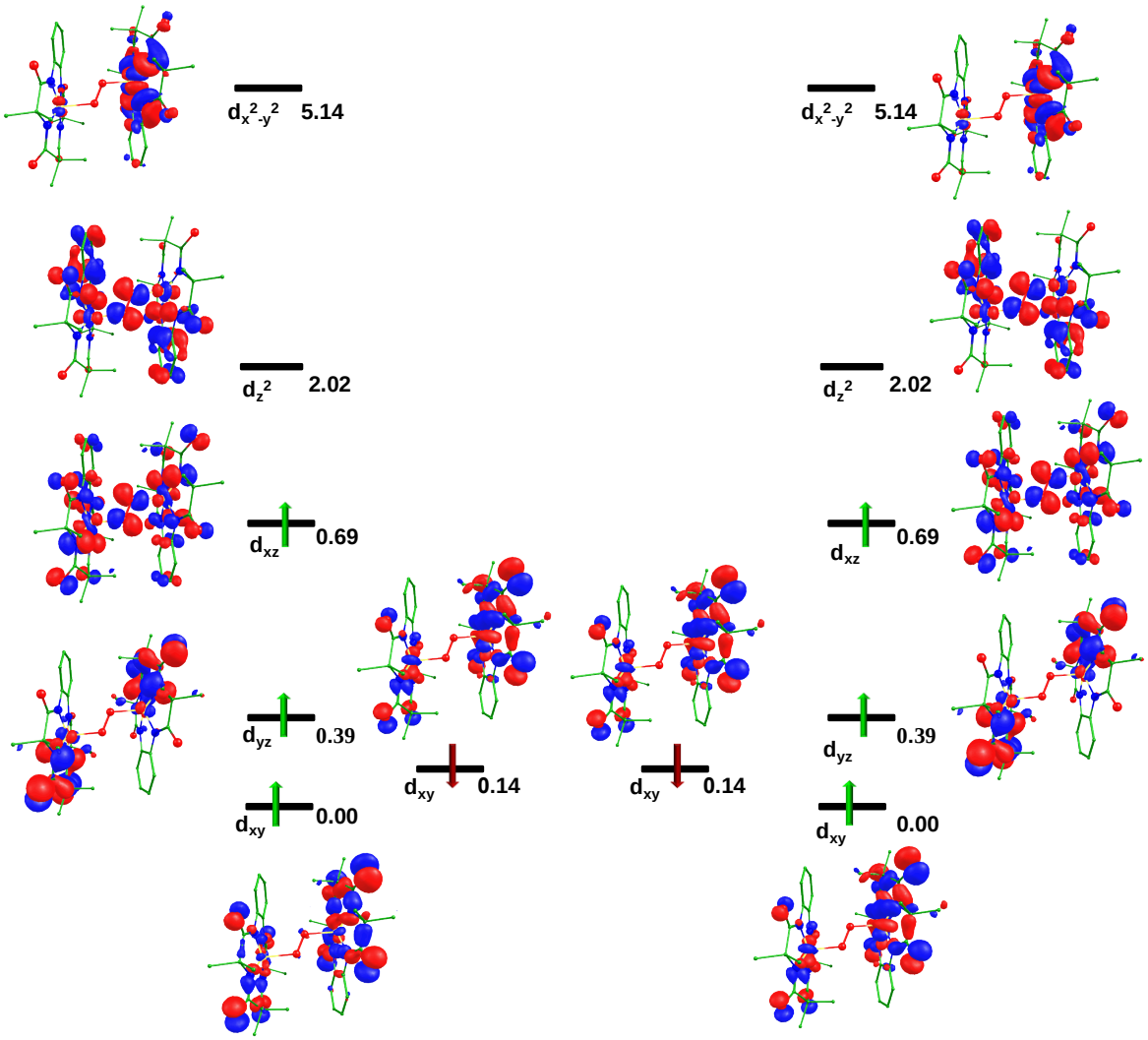

Figure 3.20. Computed Eigen-value plot incorporating energies computed for *d*-based orbitals for alpha and beta spin corresponding to the ground state ($^5VIII_{is}$) (energies are given in eV).

The computed HOMO-LUMO gap is 0.881 eV smaller than species VII (see Figure 3.18b). Similar to species VII, here also, displacements along the z-axis have an opposite sign is 0.04 Å and -0.07 Å, indicating that both iron centers are approaching towards each other, this displacement is smaller as compared to species VII. The eigenvalue plot also describes the

electronic configurations around both the iron centers (see Figure 3.20). It is also found that orbitals of both the Fe atoms are found to be at the same energy levels, and the electronic configuration is found to be $(d_{xy})^2$, $(d_{yz})^1$, $(d_{xz})^1$, $(d_z^2)^0$ and $(d_{x^2-y^2})^0$. The d_z^2 and $d_{x^2-y^2}$ are unoccupied due to much higher energy. The cleavage of the peroxo linkage can generate the $[(TAML)Fe^{IV}\text{-}O]^{2-}$ species V and $[(TAML)Fe^{V}\text{-}O]^{-}$ species VI. Significant electron densities are also located at both the bridged oxygen atoms that can activate the C-H and O-H bond of the $[(TAML)Fe^{IV}\text{-}O]^{2-}$ species V and $[(TAML)Fe^{V}\text{-}O]^{-}$ species VI.

Significant electron densities are also located at both the bridged oxygen atoms can activate the C-H and O-H bond of aliphatic and aromatic compounds.[71,73,99] NBO analysis shows that Fe1-p_y 6.7% and 93.3% of O-p_x and Fe2-p_y 6.7% and 93.3% of O-p_x (see Figure 3.16b). The contribution of the iron orbital is small as compared to μ-oxo bridged complexes iron atom and this may be due to the longer bond length and also the absence of π-bond between Fe1/2-μO1/2 as compared to Fe1-O1 and Fe2-O1 of μ-oxo bridged species.

3.3.9 Comparative study

Species formed after the reactions depend upon the binding modes of dioxygen either η^1 (end-on species) or η^2 (side-on species). Here species I-VI are mononuclear whereas species VII-VIII are bridged dinuclear. Our computed parameters also show that the Fe1-O1 bond distance of species II (2.173 Å) is longer than species III (1.994 Å), whereas the O1-O2 bond length of species II (1.321 Å) is smaller than species III (1.537 Å) due to both the oxygen atoms coordinated to iron center in species III, and these are also supported by computed stretching frequencies. The shifting of the iron center of species II (0.08 Å) out of the plane is found to be smaller than species III (0.72 Å), due to repulsion between charges of both the oxygen atoms coordinated that forces the iron atom out of the plane is comparatively more in species III. The HOMO-LUMO gap of species II (1.524 eV) is computed to be smaller than

species III (3.698 eV). The Fe-O1 bond distance of species IV (1.889 Å) is smaller than species II (2.173 Å) and species III (1.994 Å) may be due to protonation at the distal oxygen atom (-OOH). The HOMO-LUMO gap in species IV (0.059 eV) is smaller than species II and species III. The shift of the iron atom out of the plane in species V (0.19 Å) is larger than species II (0.08 Å) but smaller than species III (0.72 eV). In species V, the Fe-N_{avg} (1.911 Å) and Fe-O (1.653 Å) bond lengths are longer than species VI (1.892 Å and 1.630 Å for Fe-N_{avg} and Fe-O). The shift of the iron atom out of the plane in species VI (0.40Å) is calculated to be larger than the species V (0.35Å) and this may be due to the reflection of a higher charge at the iron center. HOMO-LUMO gap of species V (3.605 eV) is larger than species VI (1.423 eV) indicates higher reactivity of species VI which is also observed in previous reports.[71,53,105-106] From, the NBO analysis of species V and species VI, we have observed that both the species V and species VI have double bond character, In species VI iron atom has 39.2 % contribution which is slightly greater than species V (36.6 %) indicates that the Fe-O bond has more double bond character in species VI than species V.

In dinuclear species, VII and VIII, the Fe1/Fe2-N_{avg} computed bond distances (1.913 Å, 1.895 Å) are longer than the corresponding bond (1.882 Å, 1.883 Å) of species VIII, but iron-μ-oxo bond lengths (1.835 Å and 1.777 Å) of species VII are longer than iron-oxygen bonds (2.124 Å and 2.127 Å) of species VIII, and these are also supported by the computed stretching frequencies. From the NBO analysis of species VII, we have found that the orbital contribution of 19 % at Fe1 and 25.9 % at Fe2 center indicate that Fe2-O1 has a double bond contribution which is also supported by smaller bond Fe2-O1 bond distance.

NBO analysis for species VIII has a small contribution at iron centers (6.7 %) to support the longer Fe1-O1 and Fe2-O2 bond lengths. The shift of the iron atom out of plane along the bridged oxygen (axial ligand) of species VII (-0.41 Å/ 0.42 Å for Fe1/Fe2) are longer than the species VIII (0.04 Å/-0.07) Å for Fe1/Fe2. HOMO-LUMO gap of species VII (0.939 eV) is

larger than species VIII (0.881 eV). Both the Iron center in species VII is antiferromagnetically coupled, while in species VIII both iron centers are ferromagnetically coupled. The HOMO-LUMO gap in binuclear species is relatively smaller than mononuclear species except for species IV.

3.4. Conclusions

Tetraamido macrocyclic ligand coordinated iron species are of great interest because of their wide role in catalytic reactions and they mimic properties of metalloenzymes. Here, we have undertaken the DFT study on mononuclear and dinuclear iron-TAML species for analyzing structures, bonding, energetics, and magnetic interactions. Some salient conclusions derived from this work is highlighted below,

(i) Our computed DFT energies using dispersion corrected hybrid B3LYP-D2 functional predicted that the intermediate spin state for $[Fe^{III}(TAML)]^-$ (species I), $[(TAML)Fe^{IV}\text{-}\eta^1\text{-}O_2]^{\bullet-}$ (species II), $[(TAML)Fe^{IV}\text{-}OOH]^-$ (species IV), $[(TAML)Fe^{IV}\text{-}O]^{2-}$ (species V), $[(TAML)Fe^{V}\text{-}O]^-$ (species VI), $[(TAML)Fe^{IV}\text{-}\mu O\text{-}(TAML)Fe^{IV}]^{2-}$ (species VII) and $[(TAML)Fe^{IV}\text{-}\mu O_2\text{-}Fe^{IV}(TAML)]^{2-}$ (species VIII); high spin state for $[(TAML)Fe^{III}\text{-}\eta^1\text{-}O_2]^{3-}$ (species IIIa); and low spin state for $[(TAML)Fe^{V}\text{-}O]^-$ species (VI) are computed as the ground state. These ground states are in good agreement with the available experimental species.[39,53,55,56]

(ii) Our computed, DFT results also show that antiferromagnetic coupling between both iron centers is found to be in μ-oxo bridge species VII whereas ferromagnetic coupling is in μ-(1,2-peroxo) species VIII.

(iii) Here, we have also observed that the computed Fe-N_{avg} bond length of species I, is smaller than the rest of the studied species II-VIII.

(iv) The increase in the oxidation state increases the bond strength confirmed by decrease in bond length and increase in stretching frequency.

(v) The iron atom gets out of the plane on reaction with dioxygen, the shift in the position of the iron atom along the z-axis of the mononuclear species are computed to be, 0.08 Å (species II), 0.72 Å (species III), 0.19 Å (species IV), 0.35 Å (species V) and 0.40 Å (species VI), and in the dinuclear species, -0.41 Å/ 0.42 Å for Fe1/Fe2 (species VII) and 0.04 Å/-0.07 Å for Fe1/Fe2 (species VIII).

(vi) NBO analysis, orbital contributions of iron and oxygen, and iron atoms explained the ionic and the covalent nature of metal-oxygen bond along with the formation of π-bond.

(vii) The nitrogen atom coordinated to the iron atom gains electrons density via the electron delocalization mechanism. The significant spin density at the oxygen atom can be a witness for C-H/O-H/N-H bond activation.

To this end, these findings have direct relevance to the community working in the area of iron complexes/bioinorganic chemistry and related interface of chemistry.

3.5 References

(1) Nam, W. *Acc. Chem. Res.* **2015**, *8*, 2415-2423.

(2) Barman, P.; Upadhyay, P.; Faponle, A. S.; Kumar, J.; Nag, S. S.; Kumar, D.; Sastri, C. V.; de Visser, S. P. *Angew. Chem., Int. Ed.* **2016**, *55*, 11091-11095.

(3) Jackson, T. A.; Rohde, J.-U.; Seo, M. S.; Sastri, C. V.; DeHont, R.; Stubna, A.; Ohta, T.; Kitagawa, T.; Munck, E.; Nam, W.; Que, L., Jr. *J. Am. Chem. Soc.* **2008**, *130*, 12394-12407.

(4) Dhuri, S. N.; Cho, K.-B.; Lee, Y. M.; Shin, S. Y.; Kim, J. H.; Mandal, D.; Shaik, S.; Nam, W. *J. Am. Chem. Soc.* **2015**, *137*, 8623-8632

(5) Lee, Y.-M.; Dhuri, S. N.; Sawant, S. C.; Cho, J.; Kubo, M.; Ogura, T.; Fukuzumi, S.; Nam, W. *Angew. Chem., Int. Ed.* **2009**, *48*, 1803-1806.

(6) Dhuri, S. N.; Seo, M. S.; Lee, Y.-M.; Hirao, H.; Wang, Y.; Nam, W. Shaik, S. *Angew. Chem., Int. Ed.* **2008**, *47*, 3356-3359.

(7) Dhuri, S. N.; Lee, Y.-M.; Seo, M. S.; Cho, J.; Narulkar, D. D.; Fukuzumi, S.; Nam, W. *Dalton Trans.* **2015**, *44*, 7634-7642.

(8) Punniyamurthy, T.; Velusamy, S.; Iqbal, J. *J. Chem. Rev.* **2005**, *105*, 2329-2364.

(9) Nam, W. *Acc. Chem. Res.* **2007**, *40*, 522-531.

(10) Shaik, S.; Lai, W.; Chen, H.; Wang, Y. *Acc. Chem. Res.* **2010**, *43*, 1154-1165.

(11) de Montellano, P. R. O. *Chem. Rev.* **2010**, *110*, 932-948.

(12) Wackett, L. P. *Enzyme Microb. Technol.* **2002**, *31*, 577-587.

(13) Horn, E. J.; Rosen, B. R.; Chen, Y.; Tang, J.; Chen, K.; Eastgate, M. D.; Baran, P. S. *Nature* **2016**, *533*, 77-81.

(14) Nakamura, A.; Nakada, M. *Synthesis* **2013**, *45*, 1421-1451.

(15) Garcia-Cabeza, A. L.; Moreno-Dorado, F. J.; Ortega, M. J.; Guerra, F. M. *Synthesis* **2016**, *48*, 2323-2342.

(16) White, M. C. *Synlett* **2012**, *23*, 2746-2748.

(17) Jazzar, R.; Hitce, J.; Renaudat, A.; Sofack-reutzer, J.; Baudoin, O. *Chem. -Eur. J.* **2010**, *16*, 2654-2672.

(18) Groves, J. T. *J. Inorg. Biochem.* **2006**, *100*, 434-447.

(19) Groves, J. T.; Haushalter, R. C.; Nakamura, M.; Nemo, T. E.; Evans, B. J. *J. Am. Chem. Soc.* **1981**, *103*, 2884-2886.

(20) Groves, J. T.; Nemo, T. E. *J. Am. Chem. Soc.* **1983**, *105*, 6243-6248.

(21) Meunier, B. *Chem. Rev.* **1992**, *92*, 1411-1456.

(22) Costas, M.; Mehn, M. P.; Jensen, M. P.; Que, L., Jr. *Chem. Rev.* **2004**, *104*, 939-986.

(23) Que, L., Jr. *Acc. Chem. Res.* **2007**, *40*, 493-500

(24) Hitomi, Y.; Arakawa, K.; Funabiki, T.; Kodera, M. *Angew. Chem., Int. Ed.* **2012**, *124*, 3504-3508.

(25) Talsi, E. P.; Bryliakov, K. P. Coord. *Chem. Rev.* **2012**, *256*, 1418-1434.

(26) Zhang, Q.; Gorden, J. D.; Goldsmith, C. R. *Inorg. Chem.* **2013**, *52*, 13546-13556.

(27) Lindhorst, A. C.; Haslinger, S.; Kuhn, F. E. *Chem. Commun.* **2015**, *51*, 17193-17212.

(28) Oloo, W. N.; Que, L., Jr. *Acc. Chem. Res.* **2015**, *48*, 2612-2621.

(29) Sankaralingam, M.; Lee, Y.-M.; Nam, W.; Fukuzumi, S. *Inorg. Chem.* **2017**, *56*, 5096-5104.

(30) Cavani, F.; Teles, J. H. *Chem. Sus. Chem.* **2009**, *2*, 508-534.

(31) Osterberg, P. M.; Niemeier, J. K.; Welch, C. J.; Hawkins, J. M.; Martinelli, J. R.; Johnson, T. E.; Root, T. W.; Stahl, S. S. *Org. Process. Res. Dev.* **2015**, *19*, 1537-1543.

(32) Backvall, J.-E.; Modern Oxidation Methods, Wiley-VCH Verlag GmbH, Weinheim, **2004**.

(33) Solomon, E. I.; Wong, S. D.; Liu, L. V.; Decker, A.; Chow, M. S. *Curr. Opin. Chem. Biol.* **2009**, *13*, 99-113.

(34) Abu-Omar, M. M.; Loaiza, A.; Hontzeas, N. *Chem. Rev.* **2005**, *105*, 2227-2252.

(35) Solomon, E. I.; Neidig, M. L. *Chem. Commun.* **2005**, *105*, 2227-2252.

(36) Chen, M. S.; White, M. C. *Science* **2007**, *318*, 783-787.

(37) Chen, M. S.; White, M. C. *Science* **2010**, *327*, 566-571.

(38) Gormisky, P. E.; White, M. C. *J. Am. Chem. Soc.* **2013**, *135*, 14052-14055.

(39) Chanda, A.; Popescu, D.-L.; de Oliveira, F. T.; Bominaar, E. L.; Ryabov, A. D.; Munck, E.; Collins, T. J. *J. Inorg. Biochem.* **2006**, *100*, 606-619.

(40) Sahu, S.; Goldberg, D. P. *J. Am. Chem. Soc.* **2016**, *138*, 11410-11428.

(41) Kovaleva, E. G.; Lipscomb, J. D. *Nat. Chem.* **2008**, *4*, 186-193.

(42) Pau, M. Y. M.; Lipscomb, J. D.; Solomon, E. I. *Proc. Natl. Acad. Sci. USA* **2007**, *104*, 18355-18362.

(43) Jasniewski, A. J.; Que, L., Jr. *Chem. Rev.* **2018**, *118*, 2554-2592.

(44) Huang, X.; Groves, J. T. *Chem. Rev.* **2018**, *118*, 2491-2553.

(45) Solomon, E. I.; Goudarzi, S.; Sutherlin, K. D. *Biochemistry* **2016**, *55*, 6363-6374.

(46) Wang, J.; Sun, H.; Zhao, X. S. *Catal. Today* **2010**, *158*, 263-268.

(47) Institute for Green Oxidation Chemistry, unpublished results.

(48) Collins, T. J. *Acc. Chem. Res.* **2002**, *35*, 782-790.

(49) Chanda, A.; de Oliveira, F. T.; Collins, T. J.; Munck, E.; Bominaar, E. L. *Inorg. Chem.* **2008**, *47*, 9373-9376.

(50) de Oliveira, F. T.; Chanda, A.; Banerjee, D.; Shan, X.; Mondal, S.; Que, L., Jr.; Bominaar, E. L.; Mu□nck, E.; Collins, T. J. *Science* **2007**, *315*, 835-838.

(51) Collins, T. J.; Walter, C. *Little green molecules Sci. Am.* **2006**, *294*, 82-90.

(52) Collins, T. J.; Gordon-Wylie, S. W.; Bartos, M. J.; Horwitz, C. P.; Woomer, C. G.; Williams, S. A.; Patterson, R. E.; Vuocolo, L. D.; Paterno, S. A.; Strazisar, S. A.; Peraino, D. K.; Dudash, C. A.; In Green chemistry: environmentally benign chemical

syntheses and processes, Anastas, P. T.; Williamson TC, Eds. Oxford University Press: Oxford, **1998** pp 46-71.

(53) Pattanayak, S.; Jasniewski, J. A.; Rana, A.; Draksharapu, A.; Singh, K. K.; Weitz, A.; Hendrich, M.; Que, L., Jr.; Dey, A.; Gupta, S. S. *Inorg. Chem.* **2017**, *56*, 6352-6361.

(54) Nam, W. *Acc. Chem. Res.* **2015**, *48*, 2415-2423.

(55) Ghosh, A.; de Oliveira, F. T.; Yano, T.; Nishioka, T.; Beach, E. S.; Kinoshita, I.; Munck, E.; Ryabov, A. D.; Horwitz, C. P.; Collins, T. J. *J. Am. Chem. Soc.* **2005**, *127*, 2505-2513.

(56) Hong, S.; Sutherlin, K. D.; Park, J.; Kwon, E.; Siegler, M. A.; Solomon, E. I.; Nam, W. *Nat. Commun.* **2014**, *5*, 5440-5447.

(57) Fan, R.; Serrano-Plana, J.; Oloo, W. N.; Draksharapu, A.; Delgado-Pinar, E.; Company, A.; MartinDiaconescu, V.; Borrell, M.; Lloret-Fillol, J.; Garcia-Espana, E.; Guo, Y.; Bominaar, E.; Que L.; Jr.; Costas, M.; Munck, E. *J. Am. Chem. Soc.* **2018**, *140*, 3916-3928.

(58) Ghosh, M.; Pattanayak, S.; Dhar, B. B.; Singh, K. K.; Panda, C.; Gupta, S. S. *Inorg. Chem.* **2017**, *52*, 10852-10856.

(59) Zou, G.; Jing, D.; Zhong, W.; Zhao, F.; Mao, L.; Xu, Q.; Xiao J.; Yin, D. *RSC. Adv.* **2016**, *6*, 3729-3734.

(60) Boudjema, S.; Vispe, E.; Choukchou-Braham, A.; Mayoral, J. A.; Bachir, R.; Fraile, J. M. *RSC. Adv.* **2015**, *5*, 6853-6863.

(61) Ray, K.; Pfaff, F.; Wang, B.; Nam, W. *J. Am. Chem. Soc.* **2014**, *136*, 13942-13958.

(62) Cho, J.; Sarangi, R.; Nam, W. *Acc. Chem. Res.* **2012**, *45*, 1321-1330.

(63) Kang, H.; Cho, J.; Cho, K.-B.; Nomura, T.; Ogura, T.; Nam, W. *Chem. -Eur. J.* **2013**, *19*, 14119-14125.

(64) Cho, J.; Kang, H. Y.; Liu, L. V.; Sarangi, R.; Solomon, E. I.; Nam, W. *Chem. Sci.* **2013**, *4*, 1502-1508.

(65) Rohde, J.-U.; In, J.-H.; Lim, M. H.; Brennessel, W. W.; Bukowski, M. R.; Stubna, A.; Munck, E.; Nam, W.; Que, L., Jr. *Science* **2003**, *299*, 1037-1039.

(66) Seo, M. S.; Kim, N. H.; Cho, K.-B.; So, J. E.; Park, S. K.; Clemancey, M.; Garcia-Serres, R.; Latour, J.-M.; Shaik, S.; Nam, W. *Chem. Sci.* **2011**, *2*, 1039-1045.

(67) Rohde, J.-U.; Stubna, A.; Bominaar, E. L.; Münck, E.; Nam, W.; Que, L., Jr. *Inorg. Chem.* **2006**, *45*, 6435-6445.

(68) Pandey, B.; Jaccob, M.; Rajaraman, G. *Chem. Commun.* **2017**, *53*, 3193-3196.

(69) Bell, S. R.; Groves, J. T. *J. Am. Chem. Soc.* **2009**, *131*, 9640-9641.

(70) Fukuzumi, S.; Morimoto, Y.; Kotani, H.; Naumov, P.; Lee, Y.-M.; Nam, W. *Nat. Chem.* **2010**, *2*, 756-759.

(71) Ansari, A.; Kaushik, A.; Rajaraman, G. *J. Am. Chem. Soc.* **2013**, *135*, 4235-4249.

(72) Ansari, M.; Vyas, N.; Ansari, A.; Rajaraman, G. *Dalton Trans.* **2015**, *44*, 15232-15243.

(73) Ansari, A.; Ansari, M.; Singha, A.; Rajaraman, G. *Chem. -Eur. J.* **2017**, *23*, 10110-10125.

(74) Kumar, R.; Ansari, A.; Rajaraman, G. *Chem. -Eur. J.* **2018**, *24*, 6660-6860.

(75) Horn, E.; Rosen, B.; Chen, Y.; Tang, J.; Chen, K.; Eastgate, M.; Baran, P. *Nature* **2016**, *533*, 77-81.

(76) Yachandra, V.; Sauer, K.; Klein, M. *Chem. Rev.* **1996**, *96*, 2927-2950.

(77) Karlsson, A.; Parales, J.; Parales, R.; Gibson, D.; Eklund, H.; Ramaswamy, S. *Science* **2003**, *299*, 1039-1042.

(78) Frisch, M. J.; Trucks, G. W.; Schlegel, H. B.; Scuseria, G. E.; Robb, M. A.; Cheeseman, J. R.; Scalmani, G.; Barone, V.; ennucci, B.; Petersson, G. A.; Nakatsuji,

H.; Caricato, M.; Li, X.; Hratchian, H. P.; Izmaylov, A. F.; Bloino, J.; Zheng, G.; Sonnenberg, J. L.; Hada, M.; Ehara, M.; Toyota, K.; Fukuda, R.; Hasegawa, J.; Ishida, M.; Nakajima, T.; Honda, Y.; Kitao, O.; Nakai, H.; Vreven, T.; Montgomery, J. A. Jr.; Peralta, J. E.; Ogliaro, F.; Bearpark, M.; Heyd, J. J.; Brothers, E.; Kudin, K. N.; Staroverov, V. N.; Keith, T.; Kobayashi, R.; Normand, J.; Raghavachari, K.; Rendell, A.; Burant, J. C.; Iyengar, S. S.; Tomasi, J.; Cossi, M.; Rega, N.; Millam, J. M.; Klene, M.; Knox, J. E.; Cross, J. B.; Bakken, V.; Adamo, C.; Jaramillo, J.; Gomperts, R.; Startmann, R. E.; Yazyev, O.; Austin, A. J.; Cammi, R.; Pomelli, C.; Ochterski J. W., Martin, R. L.; Morokuma, K.; Zakrzewski, V. G.; Voth, G. A.; Salvador, P.; Dannenbergy, J. J.; Dapprich, S.; Daniels, A. D.; Farkas, O.; Foresman, J. B.; Ortiz, J. V.; Cioslowski, J.; Fox, D. J.; GAUSSIAN 09 Revision(A.01), Gaussian, Inc, Wallingford, CT (2009)

(79) Grimme, S. J. *Comput. Chem.* **2006**, *27*, 1787-1799.

(80) Dunning, T. H. Jr.; Hay, P. J.; In Modern Theoretical Chemistry (Ed: Schaefer, H), Plenum, New York, **1976** Vol. 3.

(81) Hay, P. J.; Wadt, W. R. *J. Chem. Phys.* **1985**, *82*, 270-283.

(82) Hay, P. J.; Wadt, W. R. *J. Chem. Phys.* **1985**, *82*, 299-310.

(83) Wadt, W. R.; Hay, P. J. *J. Chem. Phys.* **1985**, *82*, 284-298.

(84) Schaefer, A.; Horn, H.; Ahlrichs, R. *J. Chem. Phys.* **1992**, *97*, 2571-2577.

(85) Schaefer, C.; Huber, C.; Ahlrichs, R. *Chem. Phys.* **1994**, *100*, 5829-5835.

(86) Jomroz, M. H.; Vibrational Energy Distribution Analysis, VEDA4, Warsaw, **2004**.

(87) James, C.; Raj, A. A.; Reghunathan, R.; Jayakumar, V. S.; Joe, I. H.; *J. Raman Spectrosc.* **2006**, *37*, 1381-1392.

(88) Liu, J.; Chen, Z.; Yuan, S. J *Zhejiang Univ. Sci. B.* **2005**, *6*, 584-589.

(89) Noodleman, L. *J. Chem. Phys.* **1981**, *74*, 5737-5743.

(90) Noodleman, L.; Davidson, E. R. *Chem. Phys.* **1986**, *109*, 131-143.

(91) Vaska, L. *Acc. Chem. Res.* **1976**, *9*, 175-183.

(92) Dickman, M. H.; Pope, M. T. *Chem. Rev.* **1994**, *94*, 569-584.

(93) Shan, X.; Que, L., Jr. *Proc. Natl. Acad. Sci. USA* **2005**, *102*, 5340-5345.

(94) Momenteau, M.; Reed, C. A. *Chem. Rev.* **1994**, *94*, 659-698.

(95) Kundu, S.; Matito, E.; Walleck, S.; Pfaff, F. F.; Heims, F.; Babay, R.; Luis, J. M.; Company, A.; Braun, B.; Glaser, T.; Ray, K. *Chem. -Eur. J.* **2012**, *18*, 2787-2791.

(96) Cramer, C. J.; Tolman, W. B.; Theopold, K. H.; Rheingold, A. L. *Proc. Natl. Acad. Sci. USA*, **2003**, *100*, 3635-3640.

(97) Ansari, A.; Jayapal, P.; Rajaraman, G. *Angew. Chem., Int. Ed.* **2015**, *127*, 564-568.

(98) Seo, M. S.; Kim, J. Y.; Annaraj, J.; Kim, Y.; Lee, Y.-M., Kim, S. J.; Kim, J. Nam, W. *Angew. Chem., Int. Ed.* **2007**, *46*, 377-380.

(99) Grapperhaus, C. A.; Mienert, B.; Bill, E.; Weyhermüller, T.; Wieghardt, K. *Inorg. Chem.* **2000**, *39*, 5306-5317.

(100) Monika, Ansari, A. *New J. Chem.* **2020**, *44*, 7998-8009.

(101) Ansari, A.; Rajaraman, G. *Phys. Chem. Chem. Phys.* **2014**, *16*, 14601-14613.

(102) Kundu, S.; Thompson, J. V. K.; Ryabov, A. D.; Collins, T. J. *J. Am. Chem. Soc.* **2011**, *133*, 18546-18549.

(103) Stoian, S.; Xue, G. Q.; Bominaar, E. L.; Que, L., Jr.; Munck, E. *J. Am. Chem. Soc.* **2014**, *136*, 1545-1558.

(104) Fukuzumi, S.; Mandal, S.; Mase, K.; Ohkubo, K.; Park, H.; Benet-Buchholz, J.; Nam, W.; Llobet, A. *J. Am. Chem. Soc.* **2012**, *134*, 9906-9909

(105) Makhlynets, O. V.; Das, P.; Taktak, P.; Flook, M.; Mas-Ballesté, R.; Rybak-Akimova, E. V.; Que, L., Jr. *Chem. -Eur J.* **2009**, *15*, 13171-13180.

(106) Makhlynets, O. V.; Rybak-Akimova, E. V. *Chem. -Eur J.* **2010**, *16*, 13995-14006.

Chapter 4

Mechanistic Study of Cyclohex-2-enol to Cyclohex-2-enone by High Valent Iron Species: C-H/O-H Bond Activation

4.1 Introduction

The main challenge in synthetic organic chemistry is chemo selective oxidation of C-H bond by natural complexes under mild conditions.[1-5] Heme and non-heme metal complexes with several oxidants such as dioxygen, hydrogen peroxide, m-chloroperbenzoic acid etc. are involved in catalytic oxidation of aliphatic and aromatic C-H bond.[6-8] Ubiquitous dioxygen (O_2) is an ideal oxidant and environmentally benign because water could be obtained as a by-product after reduction, and the redox potential provided by it is more than sufficient to carry out several chemical transformations.[9-14] Normally, the catalytic oxidation of alkenes by dioxygen is not selective, many metal-catalyzed methods have been developed for catalytic oxidation reactions.[15-22] Catalytic properties of iron with dioxygen and its derivatives such as hydrogen peroxide and superoxide are very useful due to the low toxicity of iron in biochemistry.[23] Last several decades, heme and non-heme iron-oxo species have been synthesized and characterized for biomimetic studies.[24-26] High valent Fe^{IV}=O is playing a very important role in the scientific community due to its catalytic properties such as C-H/O-H/N-H activation and oxygen atom transfer reactions of aliphatic and aromatic compounds.[8,27-30] Fe^{IV}=O species have been characterized by X-ray and spectroscopic techniques, and also observed during catalytic reactions with enzymes having iron.[31-43] Role of axial and equatorial ligands can affect the reactivity of iron(IV) during catalytic reactions.[29,38] Most popular example is cytochrome P450, which catalyzes many reactions such as oxidation, reduction, isomerisation and dehydration.[44-45] High valent iron(IV)-oxo containing TMC (1,4,8,11-tetramethyl1,4,8,11-tetraazacyclotetradecane), TPA (tris (2pyridylmethyl)amine), BPMEN (N,N'-dimethyl-N,N'-bis(2-pyridylmethyl)ethane-1,2-diamine) and N_4Py (N,N-bis(2-pyridyl methyl)bis(2-pyridyl)methylamine) are also involved in epoxidation and hydroxylation of aliphatic and aromatic compounds.[6,46]

Apart from Fe^{IV}=O, Fe^{V}=O species is also a very reactive intermediate in many catalytic transformation reactions.[6,46,47] Iron complexes by reacting with oxygen form high valent metal complexes without any electron or proton transfer.[48] But, the reaction of a metal complex with oxygen is rare without any reductant.[49-59] Fe(V) species is reported in several oxidation reactions involving hydrogen and organic peroxide.[60] Fe(V)-oxo species has also been shown as an active intermediate in the Rieske dioxygenase enzyme family.[61-77] The species with TMC, TPA, BPMEN etc. have been reported spectroscopically and their high-resolution crystal is also observed.[31,78-80] Many spectroscopic techniques such as electronic, magnetic circular dichroism, Raman, electron paramagnetic resonance (EPR) and M*ö*ssbauer spectroscopy, are commonly used to characterize the Fe(V)-oxo complexes.[28,30,79-80,81] Synthetic functional models of Fe(V)-oxo complex carry out many C-H and C=C oxidation reactions.[66,82] Fe(V)-oxo with tetra-amido complexes are also reported and well-characterized spectroscopically and shows selective hydroxylation towards aliphatic compounds but has a limited theoretical study on catalytic activity by the complex.[63,83] Allylic oxidation is of great interest because of the easy availability of olefins and the allylic transformation gives either allylic alcohol or α,β-unsaturated carbonyl compounds and these are attractive synthetic targets.[84-90] General methodology creates several issues such as regioselectivity, stereo selectivity, poor compatibility and over oxidation during allylic oxidation.[91-96] The C-H bond activation in preference to the C=C bond is observed by mononuclear non-heme M^{IV}=O (M = Fe and Ru with ligands $RuClCp(PTA)_2$ and $[RuCp(PTA)_2(H_2O\text{-}\kappa O)]OTf$) complexes (where Cp = cyclopentadiene and PTA = 1,3,5-triaza-7-phosphaadamantane).[97-98] Such C-H bond activation depends upon the allylic C-H bond dissociation energies (BDE) of the olefin substrates.[99-103] Iron-oxo complexes are greener, popular and powerful oxidants and these are used for allylic oxidations giving rise to valuable intermediates for the pharmaceutical industry. The cyclohex-2-enone is an important intermediate used in organic synthesis,

medicinal chemistry, pesticide chemistry, materials science, rubber industry etc.[104] Cyclohexene is a good raw material for industry, which can be accessed cheaply by selective hydrogenation of benzene.[105-106] In cyclohexene, two oxidation sites are present, one for hydrogen abstraction of an allylic C-H bond and the other for oxygen-atom transfer to the C=C bond give many products such as *trans/cis*- cyclohexane- 1,2- diol, adipic acid, cyclohex-2-enol or cyclohex-2- enone. Cyclohex-2-enone is useful in organic synthesis, medicinal chemistry, pesticide chemistry, materials science etc.[101-102,107-108] To synthesize cyclohex-2-enone from cyclohex-2-enol is very important and has wide applications in pharmaceutical and synthetic organic industries.[97-98] A very little theoretical study has been done on the O-H bond activation of the cyclohex- 2- enol. A computational investigation of active catalyst species plays an important role in O-H and C-H bond activation to get better insights into electronic structures and mechanistic study of catalytic transformation reactions. Here, we have reported a mechanistic study of selective allylic oxidation of cyclohex-2-enol by Fe(V)-oxo with tetra-amido ligand and electronic structures/energetic of intermediates involves during the catalytic cycle followed by origin of higher reactivity between O-H and C-H activation.

4.2 Computational Details

Gaussian09 suite of programs is used for all calculations.[109] Method assessment on the transition metal complexes had been carried out using several functionals such as B3LYP[110-111], B3LYP-D2[112], wB97XD,[113] B97D,[112] TPSSh,[114] OLYP,[115] MP2,[116] M06,[117] and M06-2X[118-120] in previous studies.[6-8] Among all tested functionals, B3LYP, B3LYP-D2 and wB97XD were predicted correct spin states of the transition metal complexes.[6-8] The functional B3LYP-D2 includes dispersion correction which was found as superior.[6,46,121] So here, we have employed B3LYP-D2 functional for all the calculations. B3LYP-D2 functional

is used for all geometry optimizations and the mechanism of metal-mediated catalytic reactions[7,122-133] is understood by state-of-the-art functional. Although we have also done calculations with other functionals such as B3LYP and wB97XD for further confirming barrier height during the reaction (see Table AX 4.1 - AX 4.6 of appendix). The LACVP basis set comprising the LanL2DZ-Los Alamos effective core potential for the transition metal (Fe)[134-136] and a 6-31G[137] basis set for the other atoms (C, H, N and O) have been employed for geometry optimization, and the optimized geometries are then used to perform single-point energy calculations using a TZVP[29,138-139] basis set on all atoms. PCM solvation model is used for computing the solvation energies using acetonitrile as a solvent. The quoted DFT energies are B3LYP-D2 solvation at TZVP basis set incorporating free-energy corrections at LACVP basis set at a temperature of 298.15 K. The transitions states were characterized by a single imaginary frequency which pertains to the desired motion as visualized in Chemcraft[140] and also by intrinsic reaction coordinate calculations. To confirm the minima on the potential-energy surface (PES) and to obtain zero-point energy corrections frequency calculations are done on the optimized structure at the B3LYP-D2 level. The fragment approach available in Gaussian09 is employed to aid smooth convergence in cases of radical intermediates. Common notation of $^{mult}A_{pathway}$ is used throughout, the mult superscript denotes the total multiplicity of the species, A denotes transition/intermediate/product and the pathway subscript denotes the possible pathways.

4.3 Results and Discussion

Based on experimental studies, electronic structures and bonding aspects of high valent iron species are discussed followed by the mechanism of allylic oxidation along with the oxygen attack of cyclohex-2-enol using tetra-amido iron(V)-oxo species. Two possible mechanistic pathways are proposed based on the O-H (***pathway a***) and C-H (***pathway b***) bond activation

of the cyclohex-2-enol to form cyclohex-2-enone which are discussed separately followed by a comparative study.

4.3.1 Mechanistic study of cyclohex-2-enol to cyclohex-2-enone

After a detailed study on the electronic structure of $[(TAML)Fe^{V}(O)]^{-}$ species in chapter 3, we have a keen interest to do a mechanistic study towards the O-H and C-H bond activation of cyclohex-2-enol using $[(TAML)Fe^{V}(O)]^{-}$ species. A significant spin density on the ferryl oxygen can be witnessed for the O-H/C-H bond activation of the cyclohex-2-enol. Based on previous mechanistic studies,[6-8,27-30] here we have proposed a mechanistic study for the conversion of cyclohex-2-enol to cyclohex-2-enone by the putative Fe^{V}=O species. Here we have proposed two possible pathways (***pathway a:*** O-H and ***pathway b:*** C-H bond activation) by which the reaction can take place for the formation of the final product, cyclohex-2-enone. In ***pathway a***, hydrogen abstraction of the O1-H1 of the cyclohexen-2-enol by ferryl oxygen can proceed via ts_a-1 (see Scheme 4.1) for the generation of radical at the oxygen of cyclohex-2-enol followed by abstraction of the second hydrogen (C1-H2) via ts_a-2 leading to the final product (see Scheme 4.1), while in ***Pathway b***, the abstraction of hydrogen from the carbon atom (C1-H2) can occur via ts_b-1 (see Scheme 4.1) where OH is attached by the ferryl oxygen followed by abstraction of the hydrogen (O2-H1) of the same carbon atom via ts_b-2, leading to the final product (see Scheme 4.1). The mechanism of ***pathway a*** and ***b*** is discussed separately.

4.3.1.1 ***Pathway a*****:** In this pathway, at first, the abstraction of hydrogen of O1-H1 by Fe(V)-oxo takes place via the formation of the transition state ($^{4,2}ts_a$-1; see Scheme 1).[29,141-142] Our DFT calculations show that the barrier height for the abstraction of hydrogen on the low spin surface is computed to be at 64.9 kJ/mol and this is the ground state compared to the high

spin surface ($^{4}ts_{a}$-1) at 71.5 kJ/mol (see Figure 4.1). The low spin as the ground state is also calculated by functionals B3LYP and wB97XD (see Figure AX 4.1 of appendix).

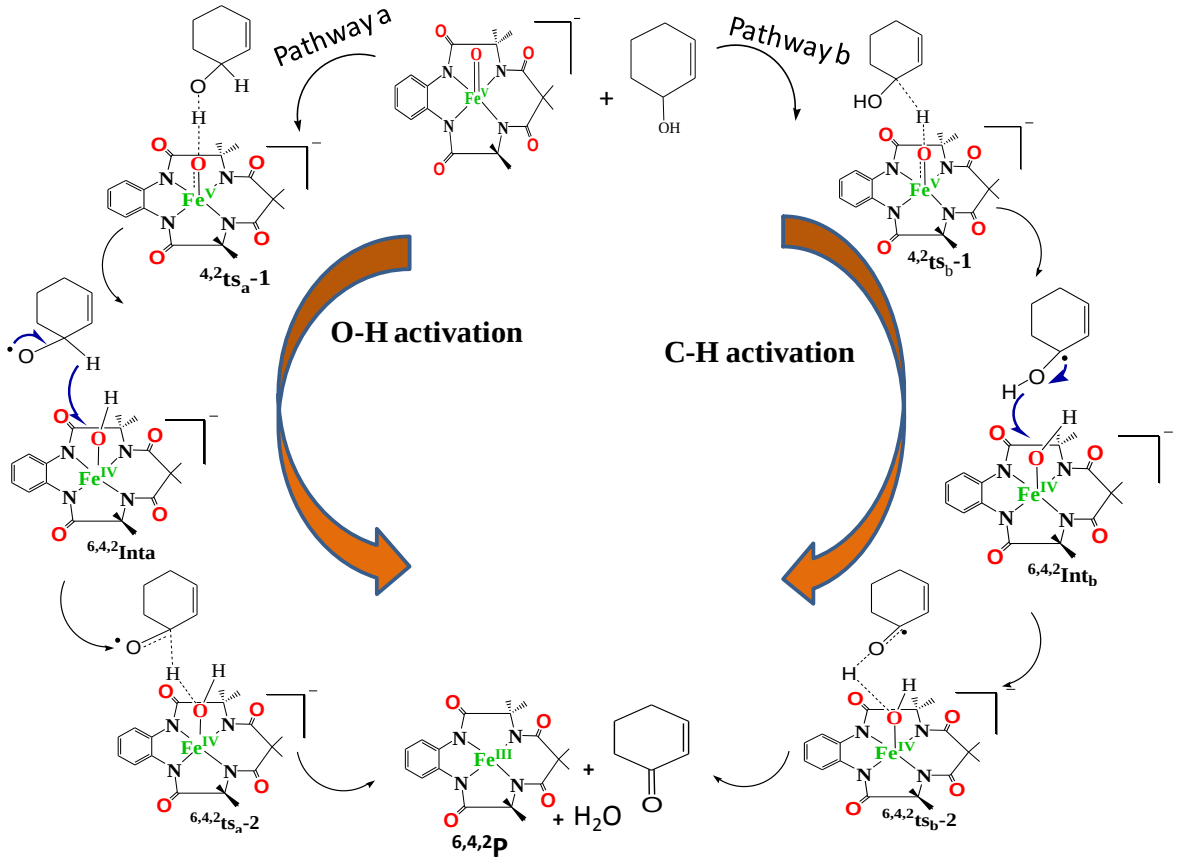

Scheme 4.1. Adapted DFT mechanism for the formation of cyclohex-2-enone from cyclohex-2-enol by Fe^{V}=O species.

The lower computed energy surfaces suggest that the O-H bond activation can show two-state reactivity, and this is also found with the functional B3LYP. The computed energy profile with these functional suggests that the dispersion plays a significant effect on reducing the energy barrier of the transition state which is ca. 20 kJ/mol lower in energy. This shows an interesting impact upon the addition of the dispersion (see Figure AX 4.1 and AX 4.2 of appendix). Imaginary frequency and intrinsic reaction coordinate (IRC) calculations confirm the formation of the transition state.

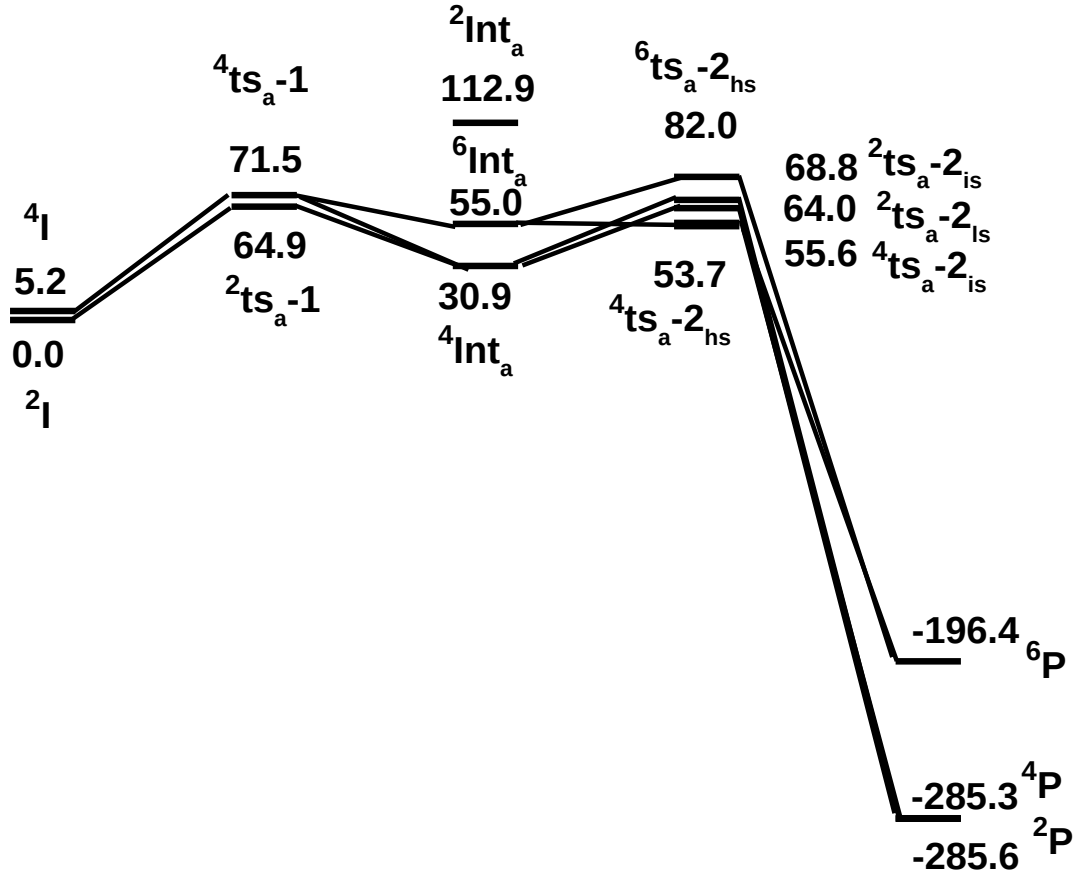

Figure 4.1. B3LYP-D2 computed energy surface for the formation of cyclohex-2-enone from cyclohex-2-enol via O-H bond activation by Fe^{V}=O species (ΔG in kJmol^{-1}).

The computed Fe−O bond in the ^{2}ts$_a$-1 elongates to 1.737 Å compared to its corresponding bond lengths in the Fe(V)=O from 1.630 Å, the O1-H1 bond length comes closer to 1.077 Å, H1-O2 elongates from 0.979 to 1.397 Å and C1-O2 shortens from 1.476 to 1.435 Å (see Table 4.1 and Table 4.2). The DFT optimized structure of the transition state (^{2}ts$_a$-1) and its corresponding spin density plot with B3LYP-D2 functional are shown in Figure 4.2. These computed structural parameters of the ^{2}ts$_a$-1 confirm the formation of the transition state for the abstraction of hydrogen from the cyclohex-2-enol by the ferryl oxo oxidant as shown in Figure 4.2. These parameters of the transition states show that the ^{2}ts$_a$-1 looks more towards the next step (Int$_a$) compared to the ^{2}ts$_a$-1 and this unfolds the reason for the lowest barrier at the low spin surface (see Table 4.1).

Table 4.1. B3LYP-D2 computed structural parameters of the $[Fe^{V}(TAML)O]^{-}$ species, intermediates transition states and product of *Pathway a*.

	Bond lengths (Å)										Bond angle (°)					
	Fe-N1	Fe-N2	Fe-N3	Fe-N4	Fe-O1	O1-H1	O1-H2	H1-O2	H2-C1	C1-O2	Fe-O1-H1	Fe-O1-H2	O1-H1-O2	O1-H2-C1	N1-Fe-N3	N2-Fe-N4
^{4}I	1.914	1.914	1.878	1.878	1.664	-	-	-	-	-	-	-	-	-	155.7	155.8
^{2}I	1.898	1.898	1.887	1.886 1.87[1]	1.630 1.58[1]	-	-	-	-	-	-	-	-	-	152.2	152.1
$^{4}ts_{a}$-1	1.892	1.882	1.871	1.875	1.752	1.067	-	1.387		1.423	119.0		169.6		153.8	156.9
$^{2}ts_{a}$-1	1.894	1.897	1.874	1.872	1.737	1.077	-	1.397		1.435	109.0		169.7		156.9	152.0
^{6}Int	1.911	1.919	1.889	1.905	1.906	154.7	-	-	-	-	-	-	-	-	154.7	150.3
^{4}Int	1.877	1.877	1.879	1.879	1.803	0.982	-	-	-	-	-	-	-	-	155.0	155.0
^{2} Int	1.932	1.834	1.910	1.830	1.760	161.5	-	-	-	-	-	-	-	-	161.5	143.6
$^{6}ts_{a\text{-}hs}$	1.884	1.912	1.875	1.877	2.010	-	1.297		1.327	-	-	115.9	-	173.8	160.4	153.1
$^{4}ts_{a\text{-}hs}$	1.901	1.904	1.887	1.881	1.974	-	1.470		1.226	-	-	129.7	-	170.7	155.6	155.9
$^{4}ts_{a}$-2_{is}	1.887	1.898	1.883	1.890	1.886	-	1.598		1.174	-	-	130.5	-	166.7	156.2	153.9
$^{2}ts_{a}$-2_{is}	1.903	1.911	1.883	1.889	1.956	-	1.276		1.335	-	-	132.8	-	174.9	156.9	155.1
$^{2}ts_{a}$-2_{ls}	1.877	1.878	1.880	1.870	1.848	-	1.457		1.224	-	-	131.8	-	173.3	160.2	155.7
^{6}P	1.984	1.984	1.924	1.924	-	-	-	-	-	-	-	-	-	-	159.7	159.7
^{4}P	1.864	1.867	1.868	1.864	-	-	-	-	-	-	-	-	-	-	171.9	171.9
^{2}P	1.851	1.872	1.853	1.865	-	-	-	-	-	-	-	-	-	-	170.9	171.2

Table 4.2. B3LYP-D2 computed spin density values of the $[Fe^{V}(TAML)O]^{-}$ species, intermediates, transition states and product of *Pathway a*.

	Fe1	O1	H1	H2	O2	C1
^{4}I	1.279	0.757	-	-	-	-
^{2}I	1.061	0.585	-	-	-	-
$^{4}ts_{a}$-1	1.607	0.290	-0.017	-	0.519	-
$^{2}ts_{a}$-1	1.690	0.139	0.012	-	-0.447	-
^{6}Int	3.202	0.381	0.005	-	-	-
^{4}Int	1.788	0.036	0.010	-	-	-
^{2}Int	0	0	0	-	-	-
$^{6}ts_{a}$-2_{hs}	3.173	0.216	-	0.109	0.557	0.141
$^{4}ts_{a}$-2_{hs}	3.143	0.201	-	-0.119	-0.698	0.010
$^{4}ts_{a}$-2_{is}	2.319	0.038	-	0.110	0.795	-0.031
$^{2}ts_{a}$-2_{is}	2.468	0.051	-	-0.108	-0.625	-0.095
$^{2}ts_{a}$-2_{ls}	0.513	0.026	-	0.120	0.717	-0.016
^{6}P	3.914	-	-	-	-	-
^{4}P	2.663	-	-	-	-	-
^{2}P	1.187	-	-	-	-	-

Although all the three functionals show similar architecture the plot of the transition state ($^{4}ts_{a}$-2) (see Figure AX 4.1 of appendix) but the computed structural parameters are in the good agreement with B3LYP-D2 compared to B3LYP and wB97XD suggesting that dispersion drives transition state much nearer to the next step. The bond angle of Fe-O1-H1 is 109.0˚ suggests that electron transfer can take place by π-pathway (see Scheme 4.2) and this is also confirmed by the eigenvalue plot (see Figure 4.3 and Figure 4.4).[6,27] In the transition state $^{2}ts_{a}$-1, one of the C-H bond electrons is found to be transferred to $(d_{xz,})^{1}$ orbital (vide infra) and here we have also observed that the energy gap between the (d_{yz}) and (d_{xz}) orbitals increase slightly. Spin density plots (see Figure 4.2a') show that there is a significant increment of electron density at the iron center of the transition state which means an extra electron is coming to the metal center (see Figure 4.3) by π-mechanism (see Scheme 4.2).

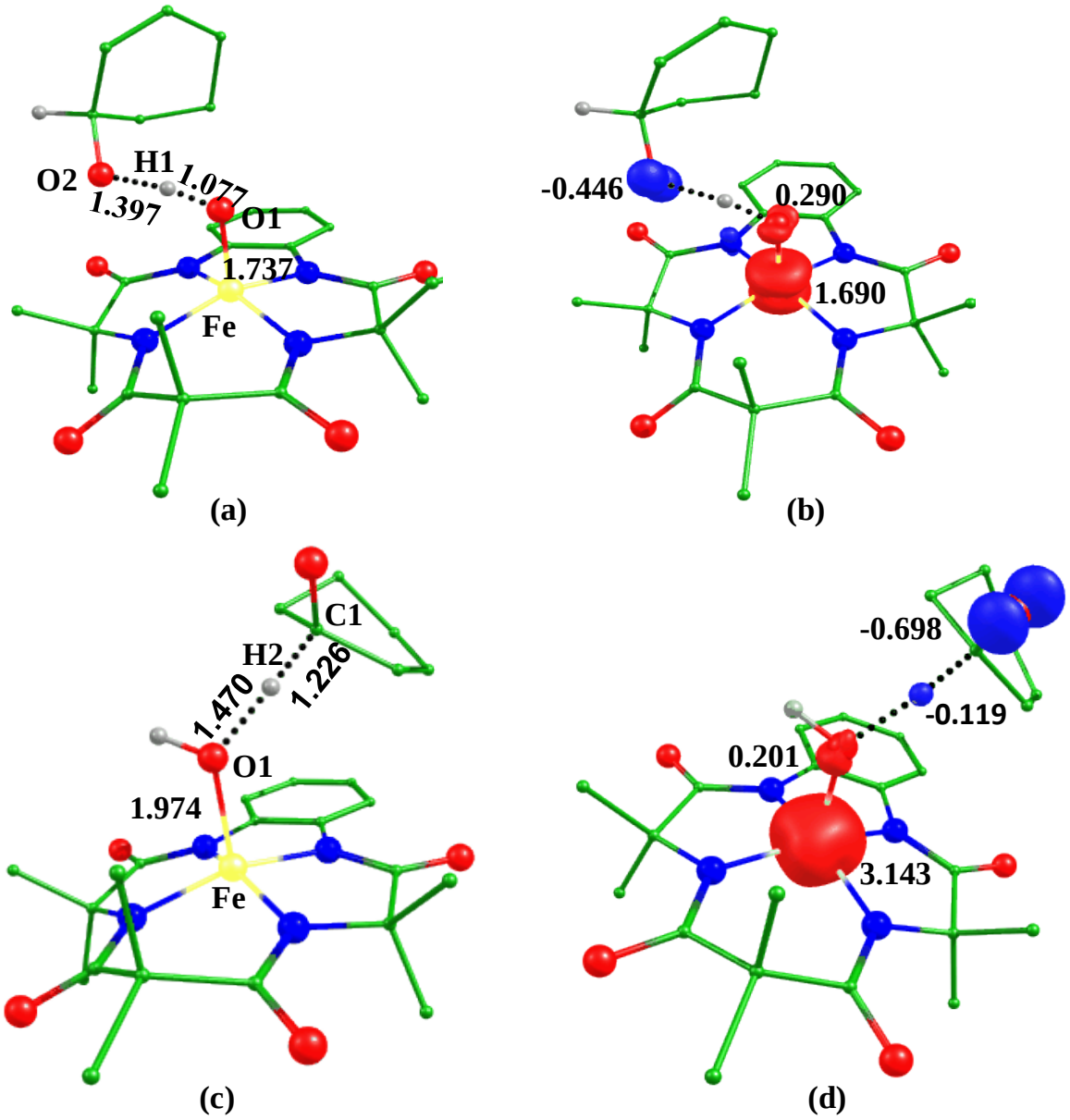

Figure 4.2. B3LYP-D2 a) optimized structure (bond length in Å) and b) its spin density plot of the transition state, $^{2}ts_{a}$-1 c) optimized structure (bond length in Å) and d) its spin density.

This suggests that hydrogen abstraction proceeds by the proton-coupled electron transfer mechanism.[8,28,144] The spin density plot and optimized structure of the ground state are shown in Figure 4.2a,b. The transition state shows that a significant spin density also found on the oxygen of the cyclohex-2-enol indicates radical character generation on it along with carbon center.

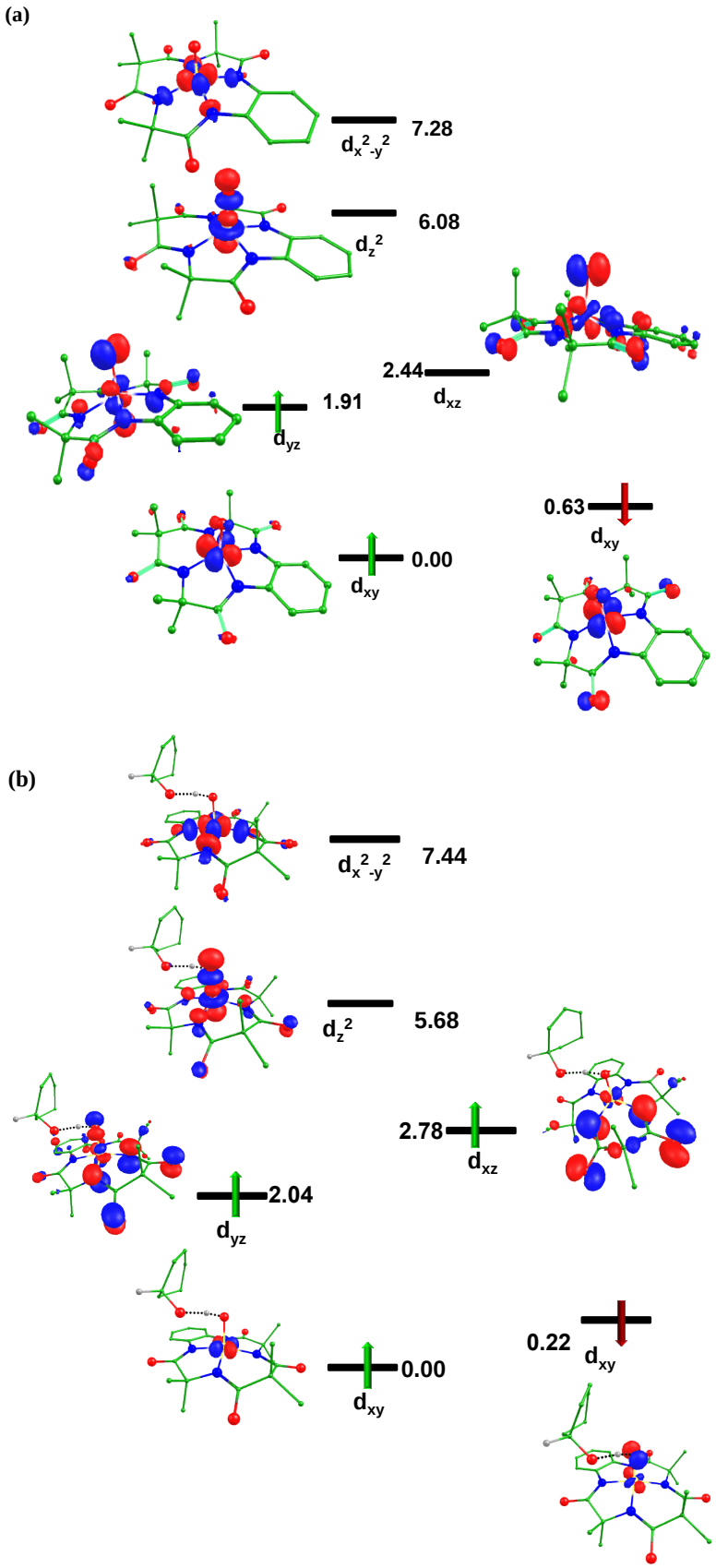

Figure 4.3. Computed Eigen-value plot incorporating energies computed for *d*-based orbitals for alpha and beta spin corresponding to the ground state (^2ts_a-1) (energies are given in eV).

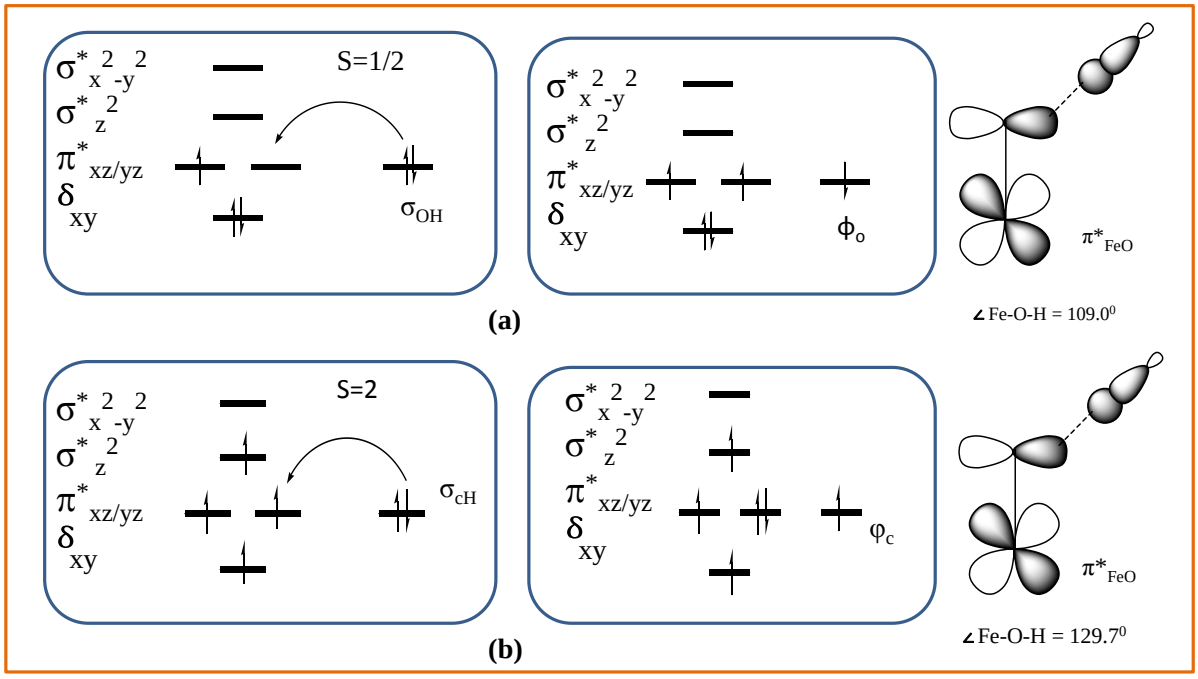

Scheme 4.2. Orbital occupancy diagrams for the H-abstraction of (a) $^{2}ts_{a}$-1 and (b) $^{4}ts_{a}$-2_{hs}.

The absolute variation in the magnitude of spin densities are found to be larger in the B3LYP-D2 compared to B3LYP (see Table 4.3 and Table AX 4.4 of appendix) revealing that dispersion drives the transition state much closer to the next step. After the first hydrogen abstraction, the intermediate Int_a is formed which has three possible spin states ($^{6,4,2}Int_a$). Our results show that the $^{4}Int_a$ is found to be the ground state with 24.1 and 82.0 kJ/mol, respectively, for $^{6}Int_a$ and $^{2}Int_a$ states are higher in energy (see Figure 4.1). The results are also almost inconsistent with functional B3LYP and wB97XD (see Table AX 4.1 and AX 4.2) and the ground state is also observed in previous studies with other architectures.[6,144] In the next step, the abstraction of the second hydrogen which is directly attached to carbon (C1) of cyclohex-2-enoxide radical (see Scheme 4.1) to form transition state ts_a-2. The barrier height for the hydrogen abstraction is found to be 53.6 kJ/mol on the $^{4}ts_{a}$-2 transition state with other spin surfaces that are higher in energy (see Figure 4.1 and 4.2c,d). The Fe-O1, O1-H2 and H2-C1 bond lengths are computed to be 1.974 Å, 0.980 Å and 1.226 Å. Computed

structural parameters with the other two functionals are also shown in Table AX 4.1 and Table AX 4.2 of appendix. After this, leads to the formation of final product cyclohexen-2-one. The energetic reveals the doublet spin state is the most stable for product and the overall thermodynamic stabilization of -285.6 kJ/mol (see Figure 4.1). A significantly large thermodynamic stability of the final product can be abled for C-H/O-H bond activation for forthcoming catalytic cycles.

4.3.2.2 ***Pathway b:*** Similar to ***Pathway a***, Fe(V)-oxo abstracts hydrogen (H2) which is directly attached to the carbon from cyclohex-2-enol to form a transition state ($^{4,2}ts_b$-1).[6-8,27-30,83,103,145,146] The barrier height for the hydrogen abstraction for high and low spin surfaces is found to be 84.5 and 60.7 kJ/mol, respectively (see Figure 4.4).

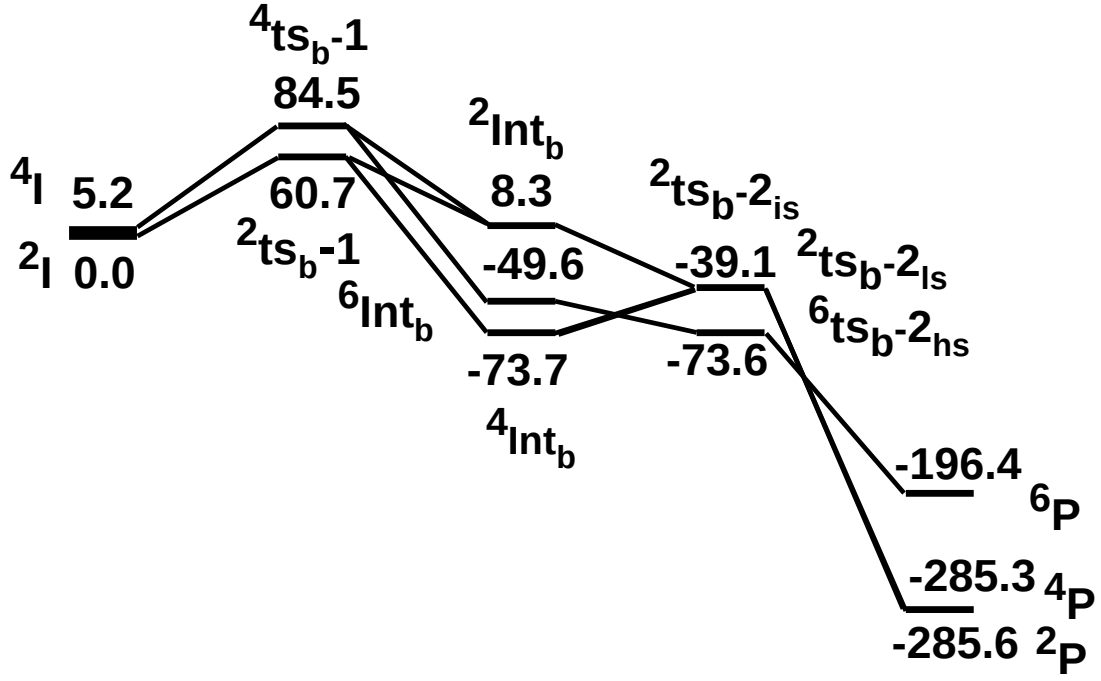

Figure 4.4. B3LYP-D2 computed energy surface for the formation of cyclohex-2-enone from cyclohex-2-enol via C-H bond activation by Fe^{V}=O species (ΔG in $kJmol^{-1}$).

The low spin state ($^{2}ts_b$-1) is found to be the ground state and this barrier is comparatively lower than the C-H bond activation of cyclic aliphatic compounds by other iron(IV)-oxo

species.[8,26] The optimized structure and spin density plot of the ground state is shown in Figure 4.5a,b. Our computed structural parameters show that the Fe-O bond in $^{2}ts_{a}$-1 elongates to 1.740 Å from 1.630 Å, and the O1-H2 bond length is 1.470 Å and the H2-C1 is 1.178 Å in the $^{2}ts_{b}$-1.

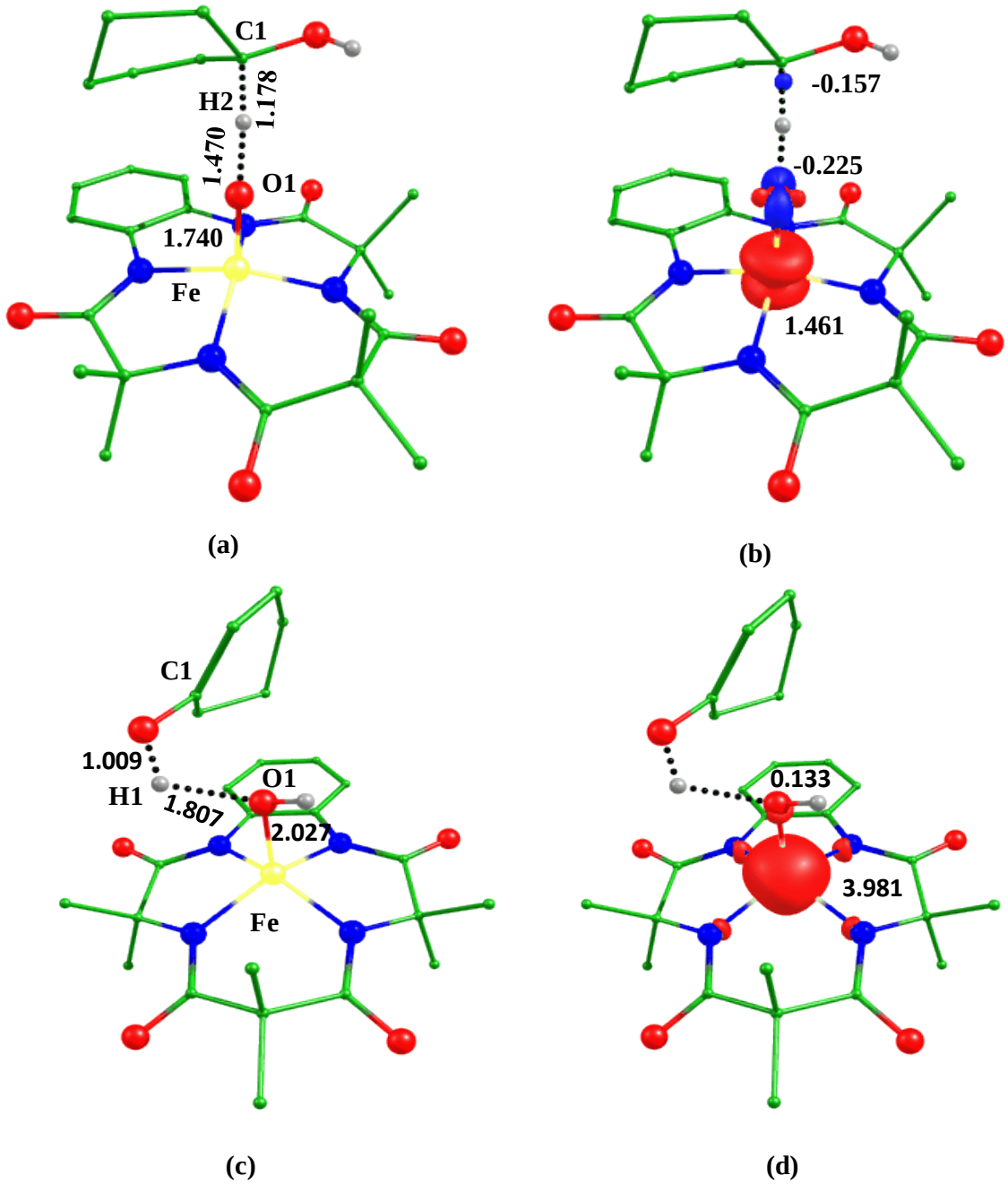

Figure 4.5. B3LYP-D2 a) optimized structure (bond length in Å), b) its spin density plot of the transition state $^{6}ts_{b}$-2_{hs}, c) optimized structure (bond length in Å) and d) its spin density plot of the transition state $^{6}ts_{b}$-2_{hs}.

These parameters confirm the formation of the transition state. The formation of the transition state is also confirmed by the IRC calculation. The bond angle between Fe-O1-H2 is 116.0˚. This shows that the hydrogen abstraction takes place by π-pathway (see Table AX 4.5 of appendix). There is a significant increment in spin density ($\Delta\rho$ = 0.460; see Table AX 4.6 of appendix) indicates that an extra electron is coming to d_{xz} orbital which is also be seen in the eigenvalue plot (see Figure 4.3(a) and 4.6). From all these observations, we can see that the hydrogen abstraction takes place along with electron transfer and this is known as proton-coupled electron transfer which is similar to the $^{2}ts_{a}$-1.[8,28,143] After the hydrogen abstraction, an intermediate is formed ($^{6,4,2}Int_{b}$). The $^{4}Int_{b}$ is computed to be the ground state and the other surfaces $^{6}Int_{b}$ and $^{2}Int_{b}$ are found at 24.0 kJ/mol and 65.3 kJ/mol higher in energy. In the next step, ferryl hydroxide abstracts the hydrogen from the hydroxyl group of cyclohexenolyl radical to form transition states (ts_{b}-2) with five possible spin states due to the interaction of metal electrons with an unpaired electron on the allyl carbon atom, but unfortunately, we are not able to get three transitions due to convergence issues.

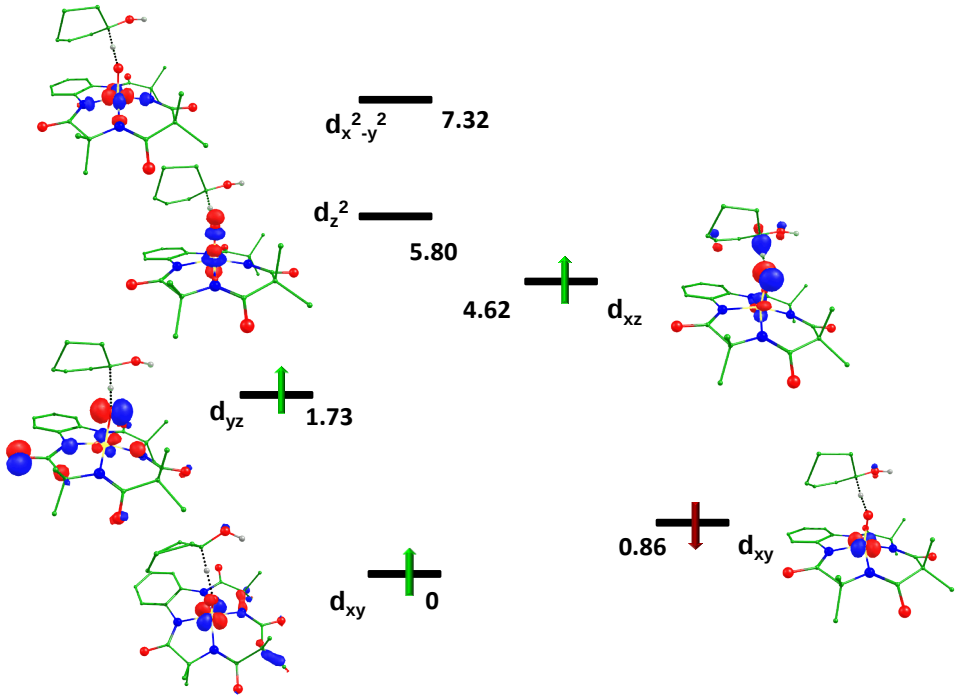

Figure 4.6. Computed Eigen-value plot incorporating energies computed for d-based orbitals for alpha and beta spin corresponding to the ground state ($^{2}ts_{b}$-1) (energies are given in eV).

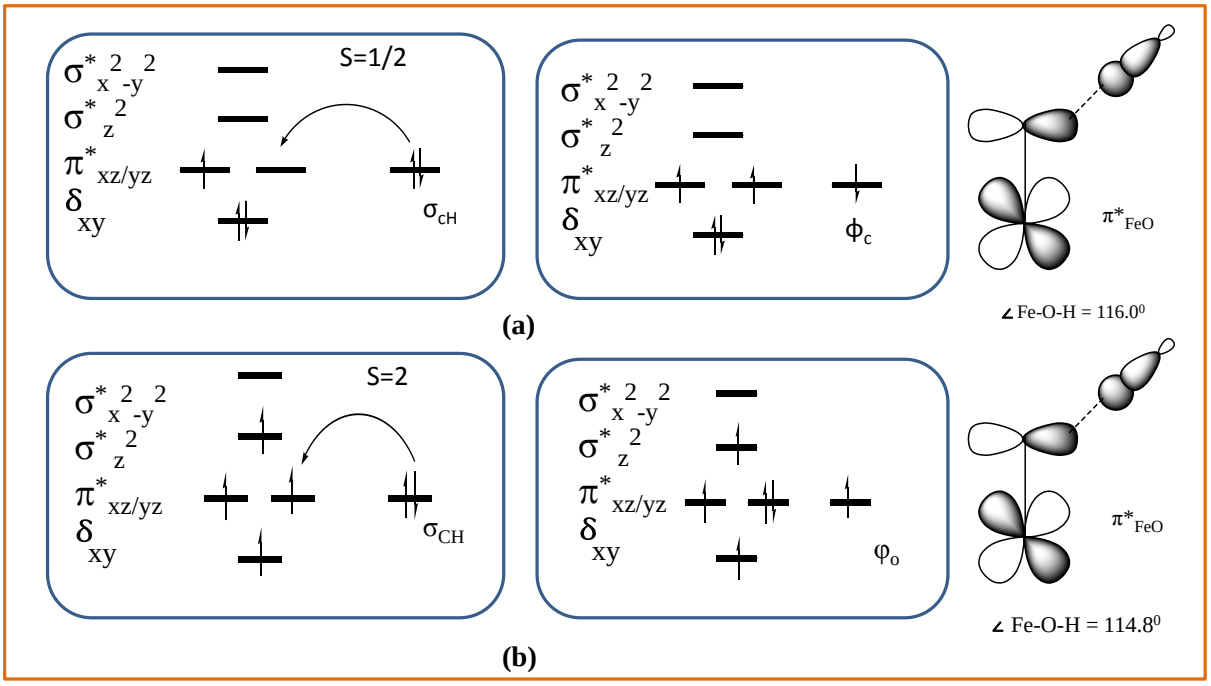

Scheme 4.3. Orbital occupancy diagrams for the H-abstraction of (a) $^{2}ts_{b}$-1, and (b) $^{6}ts_{b}$-2_{hs}.

Although this is a barrier-less transition state (see Figure 4.4). However, we are able to get transition state on four possible spin surfaces of the ts_{b}-2 with the functional B3LYP (see Table AX 4.5 and 4.6 of appendix) and these computed results also support the barrier-less transition (also see Figure 4.4). The spin density plot and optimized structure of the ground state of the transition ts_{b}-2 are shown in Figure 4.5c,d. After this, it is converted into the product which is stabilized by -285.6 kJ/mol on the doublet surface and the overall thermodynamic stabilization is already discussed in ***pathway a***.

4.3.2 Epoxidation of cyclohex-2-enol

Apart from the C-H/O-H bond activation, we have further elucidated the epoxidation on the C=C bond of cyclohex-2-enol by the Fe^{V}=O oxidant. For this, we have also optimized the transition state of oxygen attack on cyclohex-2-enol and our DFT calculations show that the barrier height of this transition is computed to be 78.3 kJ/mol on the low spin surface (^{2}ts)

with a high spin surface lies at (^{4}ts) at 88.4 kJ/mol (see Figure 4.7). The optimized structure and spin density plot of the ground state (^{2}ts) are shown in Figure 4.8a,b. The Fe-O1 bond length elongates to 1.683 Å from 1.630 Å and the C1-O1 bond length is 1.940 Å confirm the formation of the transition state of oxygen attack. A significant spin density (ρ = 0.483) on C2 shows the formation of radical at the carbon atom. This leads to the formation of intermediate (Int) lie at 45.8 kJ/mol (^{6}Int), 19.9 kJ/mol (^{4}Int), and 53.9 kJ/mol (^{2}Int). Second transition state lie at 16.4 kJ/mol (^{4}ts-2$_{hs}$), 43.2 kJ/mol (^{2}ts-2$_{hs}$) and 59.1 kJ/mol (^{6}ts-2$_{hs}$) (see Figure 4.7).

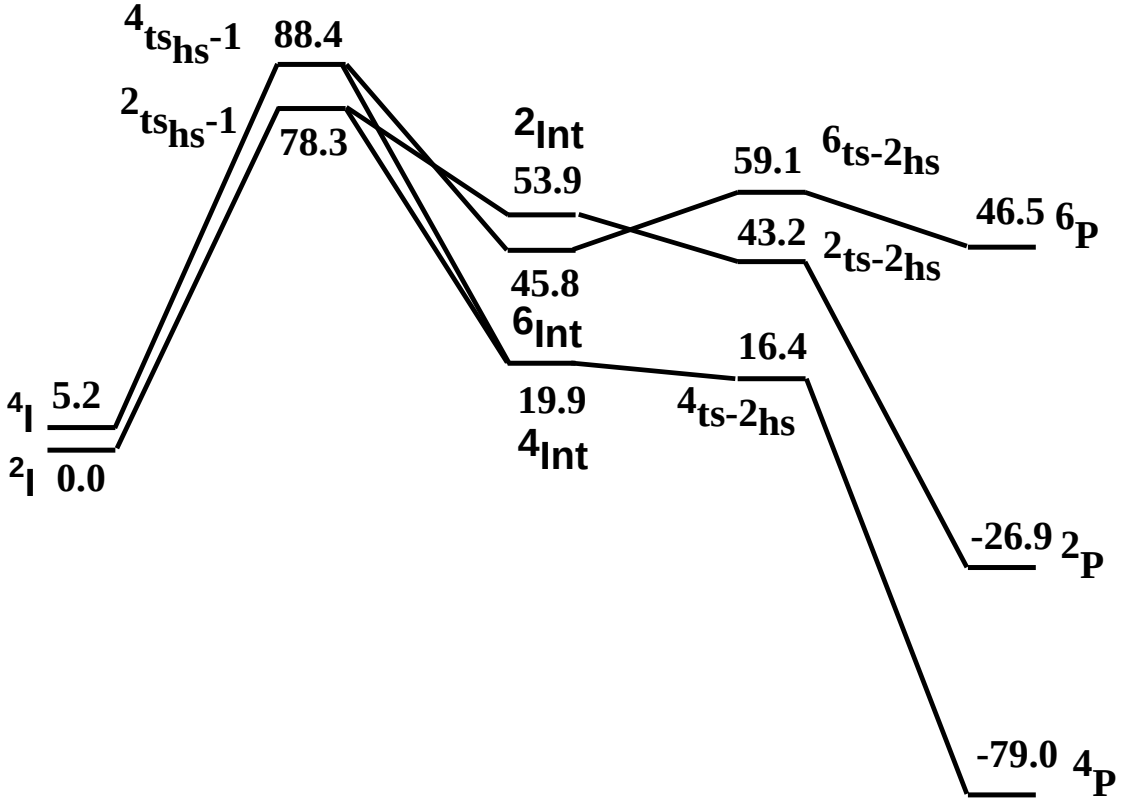

Figure 4.7. B3LYP-D2 computed energy surface for the formation of cyclohexane epoxide from cyclohex-2-enol via O atom transfer by Fe^{V}=O species (ΔG in $kJmol^{-1}$).

This barrier shows that the first step is the rate-determining step. During the second transition state, the C2-O1 bond distance is 2.204 Å. The optimized structure and spin density plot of ^{4}ts-2$_{hs}$ is shown in Figure 4.8c,d. The second transition state leads to the formation of the

epoxide. The barrier height of the oxygen attack is significantly larger as compared to C-H and O-H bond activation of cyclohex-2-enol, so we can safely ignore the epoxidation pathway here.

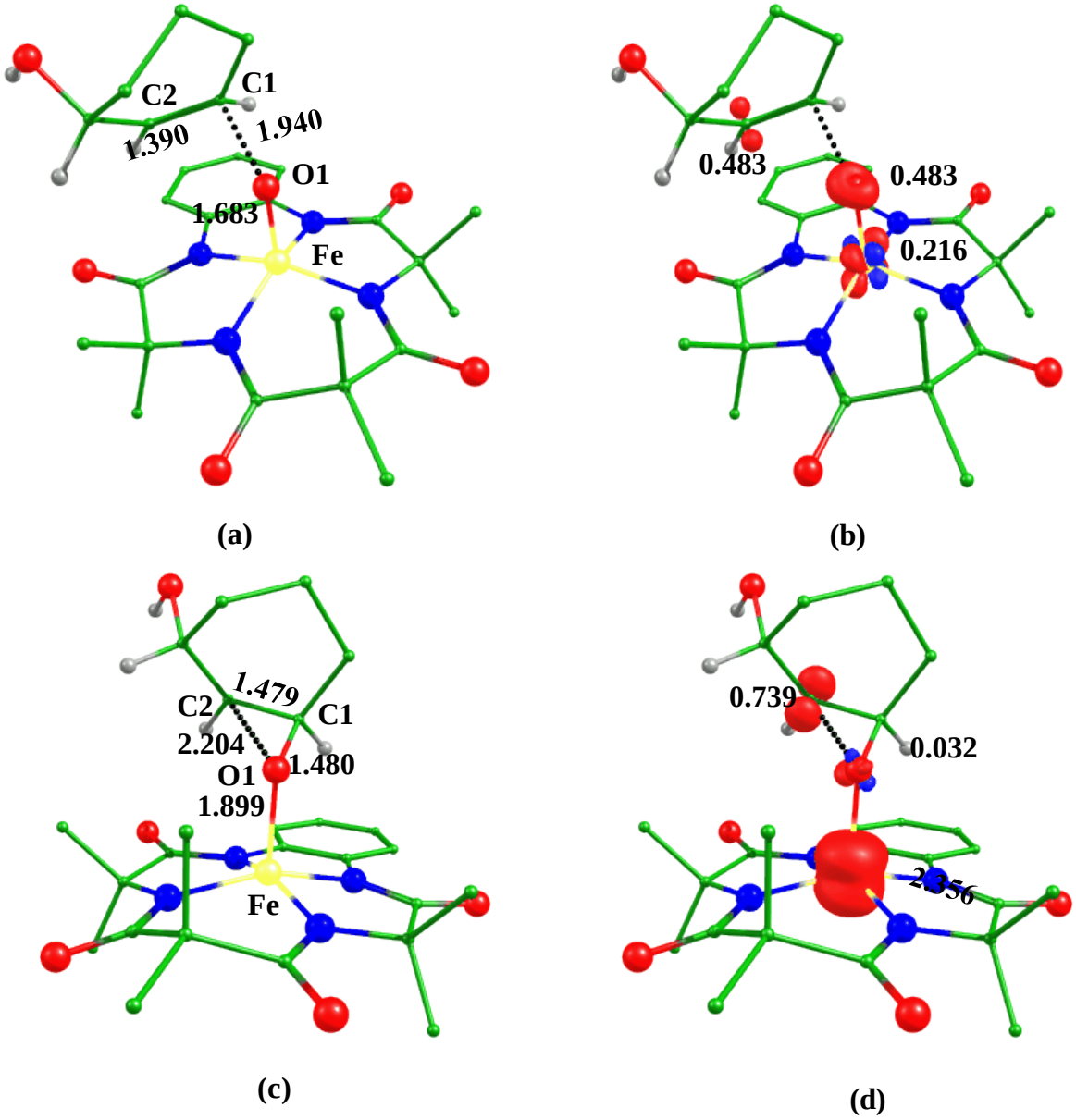

Figure 4.8. B3LYP-D2 a) optimized structure (bond length in Å) of low spin surface (^{2}ts) and b) its spin density plot.

4.3.3 Comparative study of O-H *vs.* C-H bond activation

Dual catalytic abilities are observed for the TAML iron-oxo complex, where it is found to activate inert O-H/C-H bonds of cyclohex-2-enol.[83,103] The O-H/C-H bond activation

proceeds via doublet spin surface of the Fe(V)=O center. The computed barrier height for the O-H bond activation is relatively larger than that of the C-H bond activation (64.7 *vs.* 60.9 kJ/mol; see Figure 4.9) and this step is the rate-determining step. The Fe-O1 bond length is found in the $^{2}ts_{a}$-1 is 1.737 Å whereas 1.684 Å in the $^{2}ts_{b}$-1 suggested that the Fe-O bond is more shortened in the $^{2}ts_{b}$-1 i.e. transition state looks like more towards the further step (Int_{b}). This unfolds the relatively lower barrier height of the Fe^{V}=O oxidant towards the C-H bond activation rather than the O-H activation. We have also observed that if the bond angle of the ground state of the transition states is nearer to 120° suggests smoothly entering an extra electron into metal *d*-orbital and this can control energy barrier height (see Scheme 4.2 and Scheme 4.3). Both the HOMO of the transition states $^{2}ts_{a}$-1 and $^{2}ts_{b}$-1 clearly show involvement of the π_{OH} and π_{CH} bond activation but larger orbital contribution in C-H bond can reduce barrier height (see Figure 4.10). A significant electron density acquired at the oxygen ($^{2}ts_{a}$-1) and carbon ($^{2}ts_{b}$-1) centers show that the reaction takes place via radical mechanism rather than cationic or anionic. The iron center of the transition $^{2}ts_{a}$-1 gains more electrons compared to the $^{2}ts_{b}$-1 ($\Delta\rho$ = 0.229) indicates proton-coupled electron transfer can take place relatively faster in the O-H bond activation. The energy required for the abstraction of the second hydrogen in the $^{4}ts_{a}$-2 is 53.7 kJ/mol and in the $^{6}ts_{b}$-2 is -73.6 kJ/mol. The activation energy for the second hydrogen abstraction in the ***pathway a*** required 22.8 kJ/mol and it is computed barrier less transition in the ***pathway b*** although the first step in both the pathways is the rate-determining step. Computed structural parameters show that the Fe-O bond elongation during the ts-2 is more in ***pathway b*** than the ***pathway a*** suggested that the $^{4}ts_{b}$-2 is more likely towards the product. The spin density at the iron center in the $^{4}ts_{a}$-2_{hs} is 3.143 and in the $^{6}ts_{b}$-2_{hs} is 3.981. We have observed that the spin density on the iron center has decreased by 0.032 in the case of O-H whereas it has increased by 0.779 in C-H activation during the second transition. The increased spin density at the metal center

indicates that the reaction can take place via the electron transfer which is also confirmed by the eigenvalue plot. Electron and proton transfer takes place simultaneously in both the pathways O-H and C-H bond activation and this indicates the process of formation of cyclohex-2-enone from cyclohex-2-enol proceeds via proton-coupled electron transfer (PCET) mechanism.[28,143] From our DFT calculations, the second transition state in the C-H bond activation is found as the barrier-less step.[6,27,46,147-148]

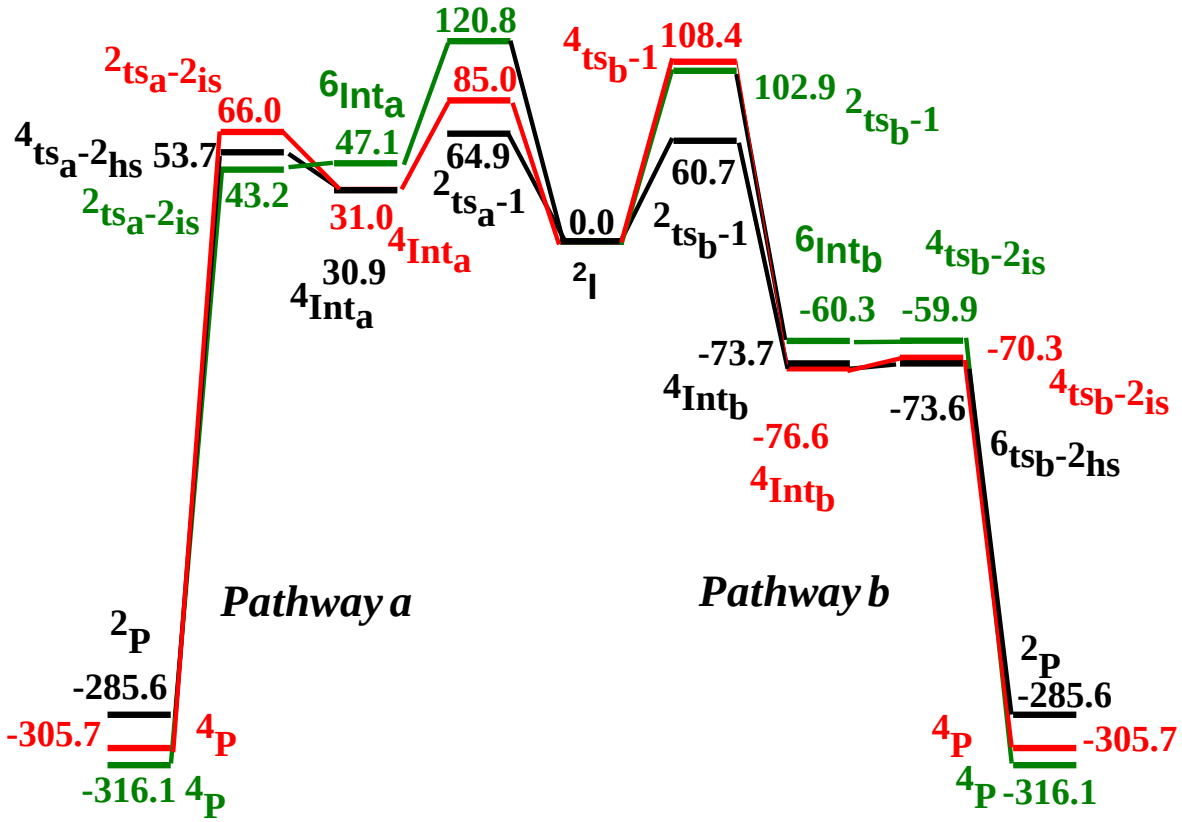

Figure 4.9. B3LYP-D2 (black), B3LYP (red) and wB97XD (olive) computed energy surface for the ground state of the ***pathway a*** and ***b*** (ΔG in $kJmol^{-1}$).

4.4. Conclusions

DFT calculations have been performed to explore the electronic structures and mechanism of formation of cyclohex-2-enone with the Fe(V)=O species. The dispersion corrected B3LYP-

D2 functional is found to perform better in predicting the correct spin states for these high valent iron-oxo species compared to B3LYP and wB97XD.[6,46]

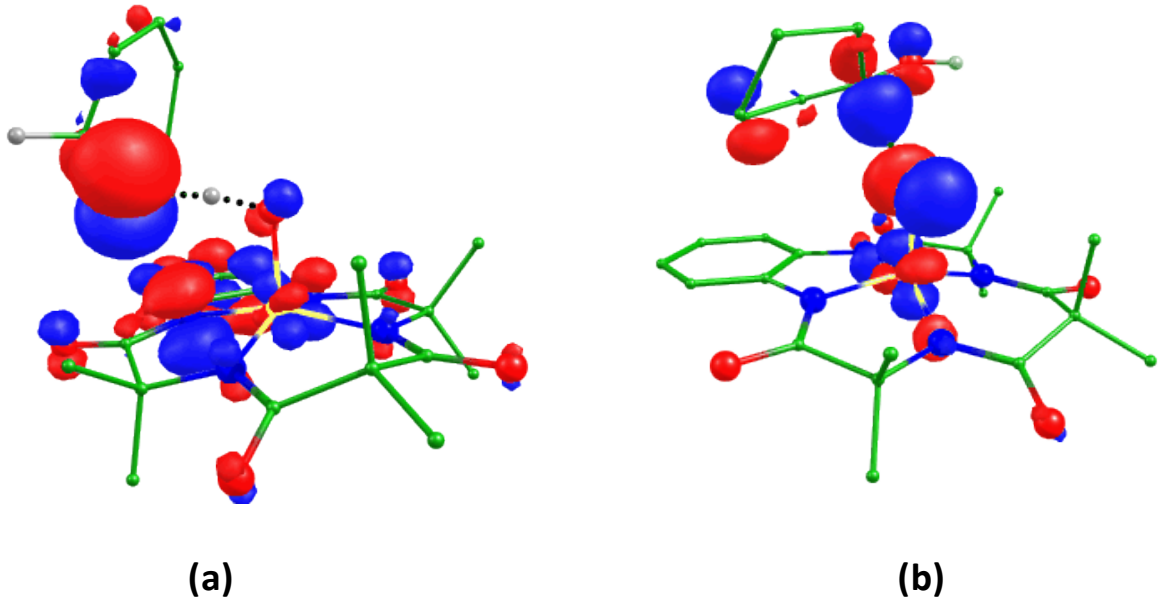

Figure 4.10. B3LYP-D2 computed HOMO of (a) $^{2}ts_{a}$-1 and (b) $^{2}ts_{b}$-1.

B3LYP-D2 also yields a lower energy barrier for the transition states compared to B3LYP and this implies that accurate estimation of the kinetics requires the incorporation of dispersion effects using density functional methods. We have explored the electronic structures and possible reaction pathways (***pathway a*** and ***pathway b***) in the course of the formation of cyclohex-2-enone from cyclohex-2-enol. We have also computed oxygen attacks on cyclohex-2-enol. DFT calculations have been used to investigate the kinetic aspects of the C-H bond activation reactions of monomeric Fe(V)-oxo unit with the tetradentate ligand. The initial H-abstraction on the low spin surface is found to be the rate-determining step for both ***pathway a*** and ***pathway b***. The computed energetic suggests that the O-H bond activation show two-state reactivity but this may not be possible in the C-H bond activation. Our calculations also predicted that the O-H/C-H bond undergoes homolytic cleavage, and it is confirmed by the significant spin density on the carbon and oxygen atoms. From the computed PES of O-H and C-H bond activation, it is apparent that the C-H bond

activation is relatively favored over the O-H bond activation which is also well supported by our computed structural parameters. Our DFT study also shows that the bond angle of the ground state of the transition state may control the reactivity. In ***pathway a***, after the O-H activation and intermediate formation, the activation of the C-H bond (second transition step) takes place which needs the barrier height of 22.8 kJ/mol, while in the ***pathway b***, after the C-H activation and formation of intermediate, there should be the O-H activation (second transition step) but it is barrier less step, and it is directly converted into the product, and formation of the product is thermodynamically favorable.

To this end, our DFT study has been employed to discuss electronic structures of a potential iron(V) oxidant and probe the mechanistic study towards allylic oxidation via C-H *vs*. O-H bond activation. This is the first computational study to discuss a comparative study on C-H *vs*. O-H bond activation along with oxygen attack towards cyclohex-2-enol by Fe(V)-oxo species. A significant exchange of metal electrons and change in structural parameters during transition states can influence reactivity and help to design a potential oxidant for catalytic transformation reactions.

4.5. References

(1) Horn, E. J.; Rosen, B. R.; Chen, Y.; Tang, J.; Chen, K.; Eastgate M. D.; Baran, P. S. *Nature* **2016**, *533*, 77-81.

(2) Nakamura, A.; Nakada, M. *Synthesis* **2013**, *45*, 1421-1451.

(3) Garcia-Cabeza, A. L.; Moreno-Dorado, F. J.; Ortega, M. J.; Guerra, F. M. *Synthesis* **2016**, *48*, 2323-2342.

(4) White, M. C. *Synlett* **2012**, *23*, 2746-2748.

(5) Groves, J. T. J. *Inorg. Biochem.* **2006**, *100*, 434-447.

(6) Ansari, A.; Kaushik, A.; Rajaraman, G. *J. Am. Chem. Soc.* **2013**, *135*, 4235-4249.

(7) Ansari, A.; Jayapal, P.; Rajaraman, G. *Angew. Chem., Int. Ed.* **2015**, *127*, 564-568.

(8) Ansari, A.; Ansari, M.; Singha, A.; Rajaraman, G. *Chem. -Eur. J.* **2017**, *23*, 10110-10125.

(9) Cavani, F.; Teles, J. H. *Chem. Sus. Chem.* **2009**, *2*, 508-534.

(10) Osterberg, P. M.; Niemeier, J. K.; Welch, C. J. ;Hawkins, J. M.; Martinelli, J. R.; Johnson, T. E.; Root, T. W.; Stahl, S. S. *Org. Process Res. Dev.* **2015**, *19*, 1537-1543.

(11) Backvall, J.-E.; Modern Oxidation Methods, Wiley-VCH Verlag GmbH, Weinheim, **2004**.

(12) Solomon, E. I.; Wong, S. D.; Liu, L. V.; Decker A.; Chow, M. S. *Curr. Opin. Chem. Biol.* **2009**, *13*, 99-113.

(13) Abu-Omar, M. M.; Loaiza, A.; Hontzeas, N. *Chem. Rev.* **2005**, *105*, 2227-2252.

(14) Solomon, E. I.; Neidig, M. L. *Chem. Commun.* **2005**, *47*, 5843-5863.

(15) Cao, Y.; Yu, H.; Peng, F.; Wang, H. *ACS Catal*. **2014**, *4*, 1617-1625.

(16) Kojima, T.; Nakayama, K.; Sakaguchi, M.; Ogura, T.; Ohkubo, K.; Fukuzumi, S. *J. Am. Chem. Soc.* **2011**, *133*, 17901-17911.

(17) Hirai, Y.; Kojima, T.; Mizutani, Y.; Shiota, Y.; Yoshizawa, K.; Fukuzumi, S. *Angew. Chem., Int. Ed.* **2008**, *47*, 5772-5776.

(18) Kojima, T.; Matsuda, Y. *Chem. Lett.* **1999**, *28*, 81-82.

(19) Que, L., Jr.; Ho Raymond, Y. N. *Chem. Rev.* **1996**, *96*, 2607-2624.

(20) Ohzu, S.; Ishizuka, T.; Hirai, Y.; Jiang, H.; Sakaguchi, M.; Ogura, T.; Fukuzumi, S.; Kojima, T. *Chem. Sci.* **2012**, *3*, 3421-3431.

(21) Qi, Y.; Luan, Y.; Yu, J.; Peng, X.; Wang, G. *Chem. -Eur. J.* **2015**, *21*, 1589-1597.

(22) Wang, J.; Yang, M.; Dong, W.; Jin, Z.; Tang, J.; Fan, S.; Lu, Y.; Wang, G. *Catal. Sci. Technol.* **2016**, *6*, 161-168.

(23) Mitra, M.; Nimir, H.; Demeshko, S.; Bhat, S. S.; Malinkin, S. O.; Haukka, M.; Lloret-Fillol, J.; Lisensky, G. C.; Meyer, F.; Shteinman, A. A. *Inorg. Chem.* **2015**, *54*, 7152-7164.

(24) Chanda, A.; Popescu, D.-L.; de Oliveira, F. T.; Bominaar, E. L.; Ryabov, A. D.; Munck, E.; Collins, T. J. *J. Inorg. Biochem*. **2006**, *100*, 606-619.

(25) Meyer, S.; Klawitter, I.; Demeshko, S.; Bill, E.; Meyer, F. *Angew. Chem., Int. Ed.* **2013**, *52*, 901-905.

(26) Rana, S.; Biswas, J. P.; Sen, A.; Clémancey, M.; Blondin, G.; Latour, J.-M.; Rajaraman, G.; Maiti, D. *Chem. Sci*. **2018**, *9*, 7843-7858.

(27) Ansari, M.; Vyas, N.; Ansari, A.; Rajaraman, G. *Dalton Trans.* **2015**, *44*, 15232-15243.

(28) Jaccob, M.; Ansari, A.; Pandey, B.; Rajaraman, G. *Dalton Trans.* **2013**, *42*, 16518-16526.

(29) Kumar, R.; Ansari, A.; Rajaraman, G. *Chem. -Eur. J.* **2018**, *24*, 6660-6860.

(30) Pandey, B.; Jaccob, M.; Rajaraman, G. *Chem. Commun*. **2017**, *53*, 3193-3196.

(31) Rohde, J.-U.; In, J.-H.; Lim, M. H.; Brennessel, W. W.; Bukowski, M. R.; Stubna, A.; Munck, E.; Nam, W.; Que, L., Jr. *Science* **2003**, *299*, 1037-1039.

(32) Nam, W. *Acc. Chem. Res*. **2007**, *40*, 522-531.

(33) Comba, P.; Rajaraman, G. *Inorg. Chem*. **2007**, *47*, 78-93.

(34) Solomon, E. I.; Brunold, T. C.; Davis, M. I.; Kemsley, J. N.; Lee, S. K.; Lehnert, N.; Neese, F.; Skulan, A. J.; Yang, Y. S.; Zhou, J. *Chem. Rev*. **2000**, *100*, 235-349.

(35) Decker, A.; Solomon, E. I. *Angew. Chem., Int. Ed.* **2005**, *44*, 2252-2255.

(36) Neese, F. *J. Inorg. Biochem*. **2006**, *100*, 716-726.

(37) Ghosh, A.; Tangen, E.; Ryeng, H.; Taylor, P. R. *Inorg. Chem*. **2004**, *2004*, 4555-4560.

(38) Kumar, D.; Hirao, H.; Que, L., Jr.; Shaik, S. *J. Am. Chem. Soc.* **2005**, *127*, 8026-8027.

(39) Kamachi, T.; Kouno, T.; Nam, W.; Yoshizawa, K. *J. Inorg. Biochem.* **2006**, *100*, 751-754.

(40) de Visser, S. P. *Angew. Chem., Int. Ed*. **2006**, *45*, 1790-1793.

(41) Pestovsky, O.; Stoian, S.; Bominaar, E. L.; Shan, X.; Münck, E.; Que, L., Jr.; Bakac, A. *Angew. Chem., Int. Ed*. **2005**, *117*, 6871-6874.

(42) Anastasi, A. E.; Comba, P.; McGrady, J.; Lienke, A.; Rohwer, H. *Inorg. Chem*. **2007**, *46*, 6420-6426.

(43) Dey, A.; Ghosh, A. *J. Am. Chem. Soc*. **2002**, *124*, 3206-3207.

(44) Filatov, M.; Harris, N.; Shaik, S. *Angew. Chem., Int. Ed.* **1999**, *38*, 3510-3512.

(45) Siegbahn, P. E. M. *Inorg. Chem.* **1999**, *38*, 2880-2889.

(46) Ansari, A.; Rajaraman, G. *Phys. Chem. Chem. Phys.* **2014**, *16*, 14601-14613.

(47) Pattanayak, S.; Jasniewski, J. A.; Rana, A.; Draksharapu, A.; Singh, K. K.; Weitz, A.; Hendrich, M.; Que, L., Jr.; Dey, A.; Gupta, S. S. *Inorg. Chem.* **2017**, *56*, 6352-6361.

(48) Sankaralingam, M.; Lee, Y.-M.; Lu, X.; Vardhaman, A. K.; Nam, W.; Fukuzumi, S. *Chem. Commun.* **2017**, *53*, 8348-8351.

(49) Kim, S. O.; Sastri, C. V.; Seo, M. S.; Kim, J.; Nam, W. *J. Am. Chem. Soc.* **2005**, *127*, 4178-4179.

(50) Groves, J. T.; Quinn, R. *J. Am. Chem. Soc.* **1985**, *107*, 5790-5792.

(51) Hong, S.; Lee, Y.-M.; Shin, W.; Fukuzumi, S.; Nam, W. *J. Am. Chem. Soc.* **2009**, *131*, 13910-13911.

(52) Lee, Y.-M.; Hong, S.; Morimoto, Y.; Shin, W.; Fukuzumi, S.; Nam, W. *J. Am. Chem. Soc.* **2010**, *132*, 10668-10670.

(53) Thibon, A. J.; Martinho, M.; Young, V. G.; Frisch, J. R., Jr.; Guillot, R. J.; Girerd, J.-J.; Munck, E.; Que, L., Jr.; Banse, F. *Angew. Chem., Int. Ed*. **2008**, *47*, 7064-7067.

(54) Hong, S.; Lee, Y.-M.; Sankaralingam, M.; Vardhaman, A. K.; Park, Y. J.; Cho, K.-B.; Ogura, T.; Sarangi, R.; Fukuzumi, S.; Nam, W. *J. Am. Chem. Soc.* **2016**, *138*, 8523-8532.

(55) Nishida, Y.; Lee, Y.-M.; Nam, W.; Fukuzumi, S. *J. Am. Chem. Soc.* **2014**, *136*, 8042-8049.

(56) Li, F.; Van Heuvelen, K. M.; Meier, K. K.; Munck, E.; Que, L., Jr. *J. Am. Chem. Soc.* **2013**, *135*, 10198-10201.

(57) Comba, P.; Lee, Y.-M.; Nam, W.; Waleska, A. *Chem. Commun.* **2014**, *50*, 412-414.

(58) Mahammed, A.; Gray, H. B.; Meier-Callahan, A. E.; Gross, Z. *J. Am. Chem. Soc.* **2003**, *125*, 1162-1163.

(59) Liu, S.; Mase, K.; Bougher, C.; Hicks, S. D.; Abu-Omar, M. M.; Fukuzumi, S. *Inorg. Chem.* **2014**, *53*, 7780-7788.

(60) Mills, M. R.; Burton, A. E.; Mori, D. I.; Ryabov, A. D.; Collins, T. J. *J. Coord. Chem.* **2015**, *68*, 3046-3057.

(61) Price, J. C.; Barr, E. W.; Glass, T. E.; Krebs, C.; Bollinger, J. M. *J. Am. Chem. Soc.* **2003**, *125*, 13008-13009.

(62) Price, J. C.; Barr, E. W.; Tirupati, B.; Bollinger, J. M.; Krebs, C. *Biochemistry* **2003**, *42*, 7497-7508.

(63) de Oliveira, F. T.; Chanda, A.; Banerjee, D.; Shan, X.; Mondal, S.; Que, L., Jr.; Bominaar, E. L.; Munck, E.; Collins, T. J. *Science* **2007**, *315*, 835-838.

(64) Lyakin, O. Y.; Bryliakov, K. P.; Britovsek, G. J. P.; Talsi, E. P. *J. Am. Chem. Soc.* **2009**, *131*, 10798-10799.

(65) Prat, I.; Mathieson, J. S.; Guell, M.; Ribas, X.; Luis, J. M.; Cronin, L.; Costas, M. *Nat. Chem.* **2011**, *3*, 788-793.

(66) McDonald, A. R.; Que, L., Jr. *Nat. Chem.* **2011**, *3*, 761-762.

(67) Van Heuvelen, K. M.; Fiedler,A. T.; Shana, X.; De Hont, R. F.; Meier, K. K.; Bominaar, E. L.; Munck, E.; Que, L., Jr. *Proc. Natl. Acad. Sci. U.S.A.*, **2012**, *109*, 11933-11938.

(68) Makhlynets, O. V.; Rybak-Akimova, E. V. *Chem. -Eur. J.* **2010**, *16*, 13995-14006.

(69) Que, L., Jr.; Tolman, W. B. *Nature* **2008**, *455*, 333-340.

(70) Ho, R. Y. N.; Roelfes, G.; Feringa, B. L.; Que, L., Jr. *J. Am. Chem. Soc.* **1999**, *121*, 264-265.

(71) Weiss, R.; Bulach, V.; Gold, A.; Terner, J.; Trautwein, A. X. *J. Biol. Inorg. Chem.* **2001**, *6*, 831-845.

(72) Comba, P.; Maurer, M.; Vadivelu, P. *J. Phys. Chem. A* **2008**, *112*, 13028-13036.

(73) Quinonero, D.; Morokuma, K.; Musaev, D. G. *J. Am. Chem. Soc.* **2005**, 127, 6548-6549.

(74) Chakrabarty, S.; Austin, R. N.; Deng, D.; Groves, J. T.; Lipscomb, J. D. *J. Am. Chem. Soc.* **2007**, *129*, 3514-3515.

(75) Bassan, A.; Blomberg, M. R.; Siegbahn, A. P. E. M.; Que, L., Jr. *Chem. -Eur. J.* **2005**, *11*, 692-705.

(76) Comba, P.; Maurer, M.; Vadivelu, P. *J. Phys. Chem.* A **2008**, *112*, 13028-13036.

(77) Costas, M.; Mehn, M. P.; Jensen, M. P.; Que, L., Jr. *Chem. Rev*. **2004**, *104,* 939-986.

(78) Klinker, E. J.; Kaizer, J.; Brennessel, W. W.; Woodrum, N. L.; Cramer, C. J.; Que, L., Jr. *Angew. Chem., Int. Ed.* **2005**, *44*, 3690-3694.

(79) Decker, A.; Rohde, J.-U.; Que, L., Jr.; Solomon, E. I. *J. Am. Chem. Soc.* **2004**, *126*, 5378-5379.

(80) Jensen, M. P.; Lange, S. J.; Mehn, M. P.; Que, E. L.; Que, L., Jr. *J. Am. Chem. Soc.* **2003**, *125*, 2113-2128.

(81) Aquino, F.; Rodriguez, J. H. *J. Chem. Phys.* **2005**, *123*, 204902-204906.

(82) Chow, T. W.-S.; Wong, E. L.-M.; Guo, Z.; Liu, Y.; Huang, J.-S.; Che, C.-M. *J. Am. Chem. Soc.* **2010**, *132*, 13229-13239.

(83) Sankaralingam, M.; Lee, Y.-M.; Nam, W.; Fukuzumi, S. *Inorg. Chem.* **2017**, *56*, 5096-5104.

(84) Punniyamurthy, T.; Rout, L. *Coord. Chem. Rev*. **2008**, *252*, 134-154.

(85) Dapurkar, S. E.; Kawanami, H.; Komura, K.; Yokoyama, T.; Ikushima, Y. *Appl. Catal.* **2008**, *346*, 112-116.

(86) Salavati-Niasari, M. M.; Elzami, R.; Mansournia, M. R.; Hydarzadeh, S. *J. Mol. Catal. A: Chem.* **2004**, *221*, 169-175.

(87) Mukherjee, S.; Samanta, S.; Roy, B. C.; Bhaumik, A. *Appl. Catal. A* **2006**, *301*, 79-88.

(88) Jiang, D.; Mallat, T.; Meier, D. M.; Urakawa, A.; Baiker, A. *J. Catal.* **2010**, *270*, 26-33.

(89) Wang, R. M.; Duan, Z. F.; He, Y. F.; Lei, Z. Q. *J. Mol. Catal. A: Chem*. **2006**, *260*, 280-287.

(90) Newhouse, T.; Baran, P. S. *Angew. Chem., Int. Ed.* **2011**, *50*, 3362-3374.

(91) Fraunhoffer, K. J.; Prabagaran, N.; SiroisL, E.; White, M. C. *J. Am. Chem. Soc*. **2006**, *128,* 9032-9033.

(92) Covell, D. J.; Vermeulen, N. A.; Labenz, N. A.; White, M. C. *Angew. Chem., Int. Ed.* **2006**, *118,* 8397-8400.

(93) Ginotra S. K.; Singh, V. K. *Org. Biomol. Chem*. **2006**, *4*, 4370-4374.

(94) Fraunhoffer, K. J.; Bachovchin, D. A.; White, M. C. *Org. Lett*. **2005**, *7,* 223-226.

(95) Zhou, J.; Tang, Y. *Chem. Soc. Rev.* **2005**, *34*, 664-676.

(96) Andrus, M. B.; Asgari, D. *Tetrahedron* **2000**, *56*, 5775-5780.

(97) Kwon, Y. H.; Mai, B. K.; Lee, Y.-M.; Dhuri, S. N.; Mandal, D.; Cho, K.-B.; Kim, Y.; Shaik, S.; Nam, W. *J. Phys. Chem. Lett.* **2015**, *6*, 1472-1476.

(98) Dhuri, S. N.; Cho, K.-B.; Lee, Y.-M.; Shin, S. Y.; Kim, J. H.; Mandal, D.; Shaik, S.; Nam, W. *J. Am. Chem. Soc.* **2015**, *137*, 8623-8632.

(99) Mandal, D.; Ramanan, R.; Usharani, D.; Janardanan, D.; Wang, B.; Shaik, S. *J. Am. Chem. Soc.* **2015**, *137*, 722-733.

(100) Dakdouki, S. C.; Villemin, D.; Bar, N. *Eur. J. Org. Chem.* **2011**, *2011*, 4448-4454.

(101) Cusso, O.; Cianfanelli, M.; Ribas, X.; Gebbink, R. J. M. K.; Costas, M. *J. Am. Chem. Soc.* **2016**, *138*, 2732-2738.

(102) Li, J. S.; Qiu, Z.; Li, C. J. *Adv. Synth. Catal.* **2017**, *359*, 3648-3653.

(103) Ghosh, M.; Nikhil, Y. L. K.; Dhar, B. B.; Sen Gupta, S. *Inorg. chem.* **2015**, *54*, 11792-11798.

(104) Wang, Z. B.; Zhang, Q.; Lu, X. F.; Chen S. J.; Liu, C. J. *Chin. J. Catal.* **2015**, *36*, 400-407.

(105) Zhou, G. B.; Dou, R. F.; Bi, H. Z.; Xie, S. H.; Pei, Y.; Fan, K. N. M.; Qiao, H.; Sun, B.; Zong, B. N. *J. Catal.* **2015**, *332*, 119-126.

(106) Sun, H. J.; Pan, Y. J.; Li, S. H.; Zhang, Y. X.; Dong, Y. Y.; Liu, S. C.; Liu, Z. Y. *J. Energy. Chem.* **2013**, *22*, 710-716.

(107) Li, Z. L.; Lv, A.; Li, L.; Deng, X. X.; Zhang, L. J.; Du, F. S.; Li, Z. C. *Polymer* **2013**, *54*, 3841-3849

(108) Dakdouki, S. C.; Villemin, D.; Bar, N. *Eur. J. Org. Chem.* **2011**, *23*, 4448-4454.

(109) Frisch, M. J.; Trucks, G. W.; Schlegel, H. B.; Scuseria, G. E.; Robb, M. A.; Cheeseman, J. R.; Scalmani, G.; Barone, V.; Petersson, G. A.; Nakatsuji, H.; Li, X.; Caricato, M.; Marenich, A. V.; Bloino, J.; Janesko, B. G.; Gomperts, R.; Mennucci, B.; Hratchian, H. P.; Ortiz, J. V.; Izmaylov, A. F.; Sonnenberg, J. L.; Williams-Young, D.; Ding, F.; Lipparini, F.; Egidi, F.; Goings, J.; Peng, B.; Petrone, A.; Henderson, T.; Ranasinghe, D.; Zakrzewski, V. G.; Gao, J.; Rega, N.; Zheng, G.; Liang, W.; Hada, M.; Ehara, M.; Toyota, K.; Fukuda, R.; Hasegawa, J.; Ishida, M.; Nakajima, T.; Honda, Y.; Kitao, O.; Nakai, H.; Vreven, T.; Throssell, K.; Montgomery, J. A., Jr.; Peralta, J. E.; Ogliaro, F.; Bearpark, M. J.; Heyd, J. J.; Brothers, E. N.; Kudin, K. N.; Staroverov, V. N.; Keith, T. A.; Kobayashi, R.; Normand, J.; Raghavachari, K. A.; Rendell, P.; Burant, J. C.; Iyengar, S. S.; Tomasi, J.; Martin, C. M.; Millam, J. M.; Klene, M.; Adamo, C.; Cammi, R.; Ochterski, J. W.; Morokuma, R. L. K. O.; Farkas, F. J. B.; Fox, D. J. Gaussian, Inc., Wallingford CT, 2016.

(110) Becke, A. D. *J. Chem. Phys*. **1993**, *98*, 5648-5652.

(111) Lee, C.; Yang, W.; Parr, R. G. *Phys. Rev. B: Condens. Matter Mater. Phys*. **1988**, *37*, 785-789.

(112) Grimme, S. *J. Comput. Chem.* **2006**, *27*, 1787-1799.

(113) Chai, J. D.; Head-Gordon, M. *Phys. Chem. Chem. Phys.* **2008**, *10*, 6615-6620.

(114) Tao, J. M.; Perdew, J. P.; Staroverov, V. N.; Scuseria, G. E. *Phys. Rev. Lett.* **2003**, *91*, 146401-146404.

(115) Handy, N. C.; Cohen, A. *J. Mol. Phys.* **2001**, *99*, 401-413.

(116) Møller, C.; Plesset, M. S. *Phys. Rev.* **1934**, *46*, 618-622.

(117) Zhao, Y.; Truhlar, D. G. *Theor. Chem. Acc.* **2008**, *120*, 215-241.

(118) Grimme, S. *J. Comput. Chem.* **2006**, *27*, 1787-1799.

(119) Becke, A. D. *J. Chem. Phys*. **1993**, *98*, 5648-5652.

(120) Lee, C.; Yang, W.; Parr, R. G. *Phys. Rev. B: Condens. Matter Mater. Phys*. **1988**, *37*, 785-789.

(121) Kepp, K. P. *J. Inorg. Biochem*. ***2011***, *105*, 1286-1292.

(122) Hirao, H.; Kumar, D.; Que, L., Jr.; Shaik, S. *J. Am. Chem. Soc.* **2006**, *128*, 8590-8606.

(123) Hiro, H.; Kumar, D.; Thiel, W.; Shaik, S. *J. Am. Chem. Soc.* **2005**, *127*, 13007-13018.

(124) Bathelt, C. M.; Zurek, J.; Mulholland, A. J.; Harvey, J. N. *J. Am. Chem. Soc.* **2005**, *127*, 12900-12908.

(125) Bassan, A.; Blomberg, M. R. A.; Siegbahn, P. E. M.; Que, L., Jr. *Angew. Chem., Int. Ed.* **2005**, *44*, 2939-2941.

(126) Siegbahn, P. E. M. *J. Biol. Inorg. Chem*. **2006**, *11*, 695-701.

(127) Siegbahn, P. E. M.; Borowski, T. *Acc. Chem. Res*. **2006**, *39*, 729-738.

(128) Ghosh, A. *J. Biol. Inorg. Chem*. **2006**, *11*, 671-673.

(129) Ghosh, A. *J. Biol. Inorg. Chem*. **2006**, *11*, 712-724.

(130) Neese, F. *J. Biol. Inorg. Chem.* **2006**, *11*, 702-711.

(131) Noodleman, L. W.; Han, G. *J. Biol. Inorg. Chem*. **2006**, *11*, 674-694.

(132) Olsson, E.; Martinez, A.; Teigen, K.; Jensen, V. R. *Chem. -Eur. J.* **2011**, *17*, 3746-3758.

(133) Olsson, E.; Mertinez, A.; Teigen, K.; Jensen, V. R. *Inorg. Chem.* **2011**, *17*, 2720-2732.

(134) Dunning, T. H., Jr.; Hay, P. J. *In Modern Theoretical Chemistry* (Ed: Schaefer, H. F.), Plenum, New York, **1976**; Vol. 3.

(135) Hay, P. J.; Wadt, W. R. *J. Chem. Phys.* **1985**, 82, 270-283.

(136) Hay, P. J.; Wadt, W. R. *J. Chem. Phys.* **1985**, *82,* 299-310.

(137) Wadt, W. R.; Hay, P. J. *J. Chem. Phys.* **1985**, *82,* 284-298.

(138) Schaefer, A.; Horn, H.; Ahlrichs, R. *J. Chem. Phys.* **1992**, *97*, 2571-2577.

(139) Schaefer, C.; Huber, C. ;Ahlrichs, R. *Chem. Phys.* **1994**, *100*, 5829-5835.

(140) Zhurko, G. A. *Chemcraft software, version 1.6*, **2014**.

(141) Dunn, P. J.; Hii, K. K.; Krische, M. J.; Williams, M. T. Sustainable Catalysis: Challenges and Practices for the Pharmaceutical and Fine Chemical Industries, John Wiley & Sons, Inc, 1st Ed., Weinheim, **2013**, pp. 121-137

(142) Kaloglu, M.; Gürbüz, N.; Semeril, D.; Ozdemir, I. *Inorg. Chem.* **2018**, *10*, 1236-1243.

(143) Warren, J. J.; Tronic, T. A.; Mayer, J. M. *Chem. Rev.* **2010**, *110*, 6961-7001.

(144) Fiedler, T.; Que, L., Jr. *Inorg. Chem.* **2009**, *48,* 11038-11047.

(145) Cho, K.-B.; Wu, X.; Lee, Y.-M.; Kwon, Y. H.; Shaik, S.; Nam, W. *J. Am. Chem. Soc.* **2012**, *134*, 20222-20225**.**

(146) Gaggioli, C. A.; Sauer, J.; Gagliardi, L. *J. Am. Chem. Soc.* **2019**, *141*, 14603-14611.

(147) Mondal, B.; Neese, F.; Bill, E.; Ye, S. *J. Am. Chem. Soc.* **2018**, *140*, 9531-9544.

(148) Mukherjee, G.; Lee, C. W. Z.; Nag, S. S.; Alili, A.; Reinhard, F. G. C.; Kumar, D.; Sastri, C. V.; de Visser, S. P. *Dalton Trans.* **2018**, *47*, 14945-14957.

Chapter 5

Effect of TMC Ring Size in Mononuclear Metal Complexes: A DFT Exploration

5.1 Introduction

Dioxygen activation in metalloenzyme results in the formation of metal-dioxygen ($M-O_2$) as the reactive intermediate.[1-3] In $M-O_2$ species, the binding nature of dioxygen with metal defines the formation of metal-superoxo (η^1) and metal-peroxo (η^2). Metal-peroxo species are involved in catalase, superoxide dismutase, and the oxygen-evolving complex in photosystem-II are the enzymes that have manganese as a central metal.[4-7] In cytochrome P450 and Riseke-dioxygenase, iron-peroxo species are involved.[8-14] Several metal-peroxo/superoxo complexes have been synthesized and characterized spectroscopically.[15-19] Metal-superoxo species are reported as the reactive intermediate in many catalytic transformation reactions such as hydroxylation, aminationtion, dehydrogenation, and epoxidation which involves C-H bond activation and oxygen atom transfer reactions.[20-29] The powerful oxidative properties of high valent superoxo species mimic their catalytic activity and are inspired to prepare complexes having such units. Considerable efforts have been devoted to synthesize and characterize models of these transient species with various spectroscopic techniques and X-ray crystallography.[30-44] Structure and chemical reactivity of short-lived metal-superoxo intermediate are found in biomimetic studies.[45-51] The binding modes of the oxygen unit and metal were elucidated by the X-ray crystallographic analysis and the resonance measurements.[52] From last few decades, several high valent vanadium, chromium, manganese, iron, and cobalt, -oxo, peroxo, superoxo and hydroperoxo species are reported in the literature.[31-35,53-58] Recently, metal-superoxo species have attracted much more attention because of their wide application in C-H bond activation and oxygen atom transfer reaction by non-heme iron, manganese, and chromium species.[59-77] The biomimetic approach is interned because cheap and non-toxic reactants, O_2 and H_2O_2 as oxidants are used in such reactions and also provide the capability of C-H bond activation of organic substrates. By bioinorganic chemistry studies, we can understand the structure of active sites of reactive

intermediates and the mechanism of reaction occurring at the active sites, and the factors which determine the ability of catalytic transformation reactions. Electronic structures and geometries of molecules are determined by several factors as the nature of metal ion and ring size of ligand.[15,17,78-79] Single crystal of Cr(III)-superoxo bearing the chloride ion *trans* to the superoxo species has been reported in which orientation of methyl groups of TMC ligand is *trans* to the superoxo unit.[22] Reactivity of the metal-superoxo complexes explained experimentally by Wonwoo Nam group.[22,58,80] Interaction of organic substrates with the superoxo species is easier than the oxo group and bond strength between chromium and oxygen in the case of superoxo is relatively weaker than the corresponding oxo species. A few theoretical studies have been accounted on the chromium-superoxo towards reactivity.[22,58] Peroxo-complexes with Mn(III), Fe(III), Co(III), and Ni(III) have been reported in which methyl groups of TMC-ring lies syn to peroxo unit. It is also found that in a higher oxidation state it forms the peroxo species due to greater electron-donating power of peroxo unit than superoxo unit as Cr(III)-superoxo is formed with 14-TMC(1,4,8,11-tetramethyl-1,4,8,11-tetraazacyclotetradecane) and the Cr(IV)-peroxo with the 12-TMC (1,4,7,10-tetramethyl-1,4,7,10-tetraazacyclododecane) ligand[19,21,80] Mn(III)/Fe(III)/Co(III) metal forms peroxo complex while Ni(II) forms superoxo complex, ring size also affects the geometry of complex.

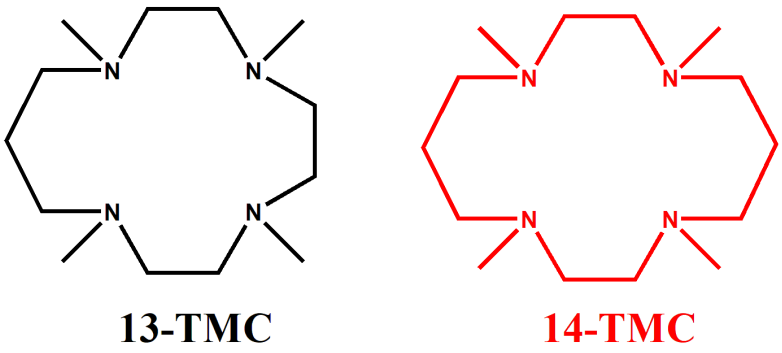

Scheme 5.1. TMC Ligands Used in the Synthesis of M-$O2^{\bullet-}$ Complexes.

Several TMC ligated metal oxo/peroxo/superoxo have been found in earlier studies.[16] Ring size of TMC ligands can affect the electronic structure of metal-superoxo species and also control the reactivity. To clarify the origin of the difference in reactivity due to different ring sizes of ligands and explore the ring size effect of TMC ligand on the stability and C-H activation by the superoxo species. Here, we have undertaken the theoretical studies on the first transition series focused mainly on V, Cr, Mn, Fe, and Co to answer the following questions; (i) to study the structure of metal-superoxo species of the metals with 13/14-TMC ligand followed by (ii) Effect of ring size on C-H activation and (iii) comparative study among them**.**

5.2 Computational Details

All calculations are performed by using the Gaussian16 program.[81] There is a fragment approach available in Gaussian16, which is used for all calculations. In previous studies, method assessment has been done by using the functionals such as B3LYP,[82-83] B3LYPD-2,[84] wB97XD,[85] B97D,[84] M06-2X,[86] TPPSh,[87] and MP2[88] and it was found that B3LYP, B3LYP-D2, and wB97XD functional predicts the correct spin state of transition metal complexes.[71,89-91] Among these three functionals, B3LYP-D2 was also found as the superior. So, we have restricted our calculations to B3LYP-D2 functional. LanL2DZ basis set compromising the double-ζ with Los Alamos effective core potential used for transition metals (V, Cr, Mn, Fe, and Co),[92-94] and 6-31G[95] basis set for other atoms such as H, C, N, O, and Cl are used for geometry optimization. The frequency calculations are performed on the optimized structures to verify the minima on the potential energy surface (PES) and also to calculate free energy corrections. Transition states are confirmed by a single imaginary frequency and are verified by animating the imaginary frequency using visualization software such as GaussView6. The optimized geometries are used for the single point energy calculations using TZVP[96-98] basis

set for all the atoms. Acetonitrile is employed as a solvent for computing solvation energies using the polarizable continuum solvent (PCM) model. The quoted DFT energies are B3LYP-D2 solvation energies incorporating the free energies computed at 298.15 K. Intrinsic reaction coordinates (IRC) calculations are performed on the selected transition states to verify that the minimum stationary point that is associated with the reactant and product are connected by the transition state. In metal-superoxo species, the magnetic exchange between the metal center and the distal oxygen is computed by using a spin Hamiltonian.

$$\hat{H} = -JS_1.S_2$$

Where, *J* denotes the magnetic exchange coupling constant. Noodleman's broken symmetry is used to calculate the magnetic exchange coupling constant. Positive *J* values indicate the ferromagnetic coupling whereas negative *J* values indicate antiferromagnetic coupling.[99-100] Here, $^{X}M_{a/b\text{-}y}$ notation (where x is overall multiplicity, M is the transition metal (I=V, II=Cr, III=Mn, IV= Fe, V=Co), subscripts a, and b are corresponding for 13-TMC and 14-TMC, respectively, and y is spin-state of metal.

5.3 Results and Discussion

Here, we have modeled vanadium, chromium, manganese, iron, and cobalt-superoxo species with 13/14-TMC started with the available X-ray structure of chromium(III)-superoxo.[22]

(a)

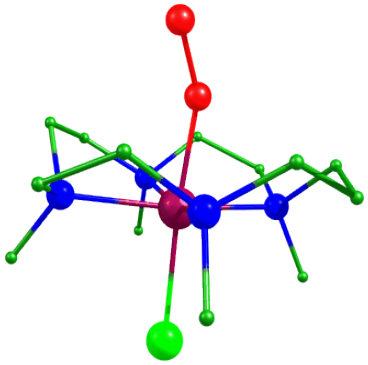

Isomer A

(b)

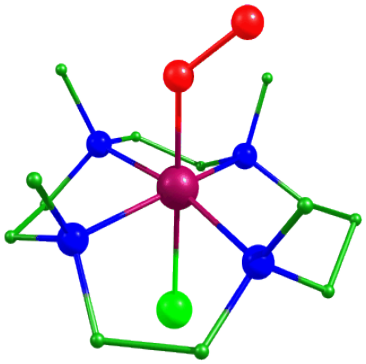

Isomer B

Figure 5.1. B3LYP-D2 optimized structures a) Isomer A and b) Isomer B.

Table 5.1. B3LYP-D2 computed relative energy (ΔG in kJ mol^{-1}) for species I to IV with both the isomer A and B.

Spin state	13-TMC	14-TMC	
([V(13/14-TMC)O$_2$Cl]$^+$, I)			
^{4}IA$_{a\text{-}hs}$	43.6	^{4}IA$_{b\text{-}hs}$	51.5
^{2}IA$_{a\text{-}hs}$	0	^{2}IA$_{b\text{-}hs}$	0
^{4}IB$_{a\text{-}hs}$	62.1	^{4}IB$_{b\text{-}hs}$	67.1
^{2}IB$_{a\text{-}hs}$	10.6	^{2}IB$_{b\text{-}hs}$	14.7
([Cr(13/14-TMC)O$_2$Cl]$^+$, II)			
^{5}IIA$_{a\text{-}hs}$	13.1	^{5}IIA$_{b\text{-}hs}$	16.5
^{3}IIA$_{a\text{-}hs}$	0	^{3}IIA$_{b\text{-}hs}$	0
^{3}IIA$_{a\text{-}ls}$	3.9	^{3}IIA$_{b\text{-}ls}$	4.1
^{1}IIA$_{a\text{-}ls}$	274.1	^{1}IIA$_{b\text{-}ls}$	264.4
^{5}IIB$_{a\text{-}hs}$	28.9	^{5}IIB$_{b\text{-}hs}$	24.9
^{3}IIB$_{a\text{-}hs}$	6.6	^{3}IIB$_{b\text{-}hs}$	5.5
^{3}IIB$_{a\text{-}ls}$	13.7	^{3}IIB$_{b\text{-}ls}$	7.8
^{1}IIB$_{a\text{-}ls}$	273.4	^{1}IIB$_{b\text{-}ls}$	265.5
([Mn(13/14-TMC)O$_2$Cl]$^+$, III)			
^{6}IIIA$_{a\text{-}hs}$	0	^{6}IIIA$_{b\text{-}hs}$	26.4
^{4}IIIA$_{a\text{-}hs}$	17.2	^{4}IIIA$_{b\text{-}hs}$	0
^{4}IIIA$_{a\text{-}is}$	26.5	^{4}IIIA$_{b\text{-}is}$	86.0
^{2}IIIA$_{a\text{-}is}$	35.3	^{2}IIIA$_{b\text{-}is}$	60.9
^{2}IIIA$_{a\text{-}ls}$	35.2	^{2}IIIA$_{b\text{-}ls}$	63.1
^{6}IIIB$_{a\text{-}hs}$	15.6	^{6}IIIB$_{b\text{-}hs}$	28.6
^{4}IIIB$_{a\text{-}hs}$	30.9	^{4}IIIB$_{b\text{-}hs}$	3.5
^{4}IIIB$_{a\text{-}is}$	61.8	^{4}IIIB$_{b\text{-}is}$	93.9
^{2}IIIB$_{a\text{-}is}$	40.4	^{2}IIIB$_{b\text{-}is}$	65.1
^{2}IIIB$_{a\text{-}ls}$	142.5	^{2}IIIB$_{b\text{-}ls}$	65.0
([Fe(13/14-TMC)O$_2$Cl]$^+$, IV)			
^{7}IVA$_{a\text{-}hs}$	0	^{7}IVA$_{b\text{-}hs}$	0
^{5}IVA$_{a\text{-}hs}$	20.2	^{5}IVA$_{b\text{-}hs}$	6.8
^{5}IVA$_{a\text{-}is}$	37.5	^{5}IVA$_{b\text{-}is}$	38.8
^{3}IVA$_{a\text{-}is}$	96.4	^{3}IVA$_{b\text{-}is}$	71.7
^{3}IVA$_{a\text{-}ls}$	54.4	^{3}IVA$_{b\text{-}ls}$	43.9
^{1}IVA$_{a\text{-}ls}$	145.6	^{1}IVA$_{b\text{-}ls}$	135.1
^{7}IVB$_{a\text{-}hs}$	27.6	^{7}IVB$_{b\text{-}hs}$	8.2
^{5}IVB$_{a\text{-}hs}$	27.6	^{5}IVB$_{b\text{-}hs}$	18.8
^{5}IVB$_{a\text{-}is}$	40.7	^{5}IVB$_{b\text{-}is}$	75.4
^{3}IVB$_{a\text{-}is}$	62.7	^{3}IVB$_{b\text{-}is}$	56.7
^{3}IVB$_{a\text{-}ls}$	48.9	^{3}IVB$_{b\text{-}ls}$	131.9
^{1}IVB$_{a\text{-}ls}$	136.2	^{1}IVB$_{b\text{-}ls}$	132.0

There are two possible isomers (A and B) based on methyl groups of TMC ring lie anti (A) or syn (B) to the superoxo unit (see Figure 5.1). From our calculations, it was found that the methyl group lies syn to superoxo species (B) has higher energy by 10.6/14.7 kJ/mol of $[V(13/14\text{-TMC})O_2Cl]^+$, 6.5/5.5 kJ/mol with $[Cr(13/14\text{-TMC})O_2Cl]^+$, 15.6/3.6 kJ/mol with $[Mn(13/14\text{-TMC})O_2Cl]^+$ and 27.1/1.6 kJ/mol with $[Fe(13/14\text{-TMC})O_2Cl]^+$ than the corresponding anti isomer (A) respectively, (see Table 5.1) and are in agreement with the available experimental studies.[15] These energy differences may be due to steric repulsion between methyl groups and superoxo units. The space-filling model of optimized geometry of the isomer B is more sterically hindered than the corresponding isomer A (see Figure 5.2). Therefore, we have restricted our calculations to the anti-isomer (A) species. We have also computed the formation energy for superoxo species with metals (V, Cr, Mn, Fe, and Co) along with 13/14-TMC rings and our results show that all these energies are exothermic (see Table 5.2) which indicates a favorable formation of these species.

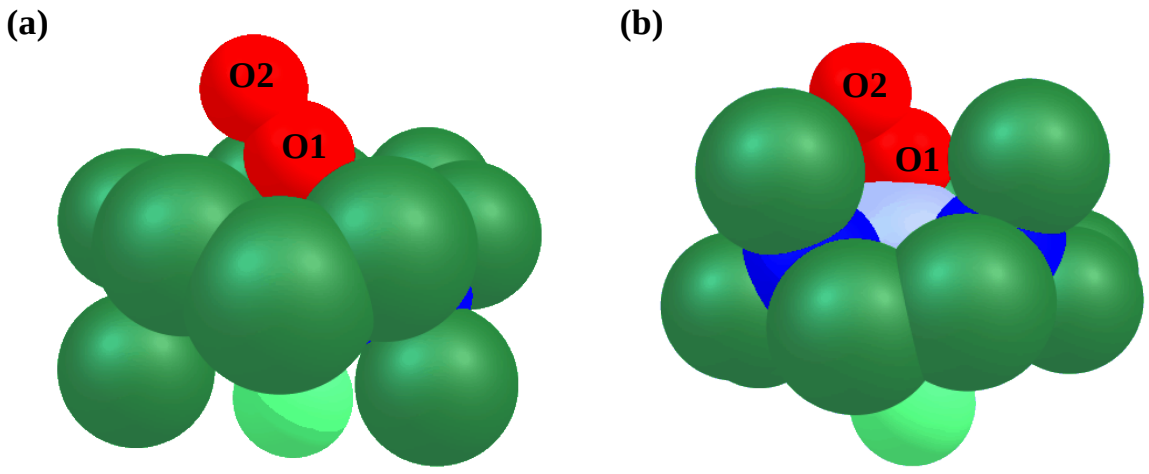

Figure 5.2. Space-filling model of vanadium -superoxo species with a) 13-TMC syn; b) 13-TMC anti, metal silver, C (olive), N (blue), O (red).

Here, we have started our DFT calculations on the vanadium-superoxo species (I) along with a detailed mechanistic study of C-H bond activation of cyclohexa-1,4-diene and then followed with the other metal-superoxo species.

Table 5.2. B3LYP-D2 computed formation energies of I to V species with the ground state.

Formation energy(kJ/mol)		
Spin State	**13-TMC**	**14-TMC**
$^{2}I_{hs}$	-727.4	-725.5
$^{3}II_{hs}$	-688.2	-670.7
$^{6/4}III_{hs}$	-586.9	-646.0
$^{7}IV_{hs}$	-652.9	-642.7
$^{2}V_{ls}$	-686.1	-1515.1

5.3.1 Vanadium-superoxo species ($[V(13/14\text{-}TMC)O_2Cl]^+$, $I_{a/b}$)

There are two possible spin interactions between vanadium center and superoxo unit (such as $^{4}I_{a/b\text{-}hs,}$ and $^{2}I_{a/b\text{-}hs}$) are shown in Scheme 5.1 of ESI and our DFT calculations predicted that $^{2}I_{a\text{-}hs}$ and $^{2}I_{b\text{-}hs}$ are found to be the ground state with $^{4}I_{a\text{-}hs,}$ and $^{4}I_{b\text{-}hs}$ lie at 43.6, and 51.5 kJ/mol higher in energy, respectively (see Figure 5.3). The optimized structure and spin density plot of the ground state of both the vanadium species ($^{2}I_{a/\mathbf{b}\text{-}hs}$) are shown in Figure 5.4. The computed angle ∠V-O1-O2 of the ground state ($^{2}I_{a/b\text{-}hs}$) are 176.4˚, and 173.7˚, respectively, and these show that the angle decreases upon the ring size increases, and also indicates towards linearity of V-O-O$^{\bullet}$ (see Table AX 5.1 and Table AX 5.2 of appendix). The $d_{yz/xz}$ orbital of vanadium and *p*-orbital of oxygen unit are orthogonal to each other. The computed V-O1 bond length of $^{2}I_{a\text{-}hs}$ and $^{2}I_{b\text{-}hs}$ is 1.740 Å, and 1.741 Å and it is found that, as the ring size increases, V-N_{avg}/V-Cl bond lengths also increase 2.159/2.369 Å ($^{2}I_{a\text{-}hs}$), and 2.203/2.371 Å ($^{2}I_{b\text{-}hs}$), whereas the O1-O2 bond lengths decrease as 1.347 Å ($^{2}I_{a\text{-}hs}$) and 1.343 Å ($^{2}I_{b\text{-}hs}$). The computed spin density at the vanadium center and the distal oxygen of $^{2}I_{a/b\text{-}hs}$ is found as 1.960/2.014, and -0.451/-0.478 (see Table AX 5.3. and Table AX 5.4. of appendix).

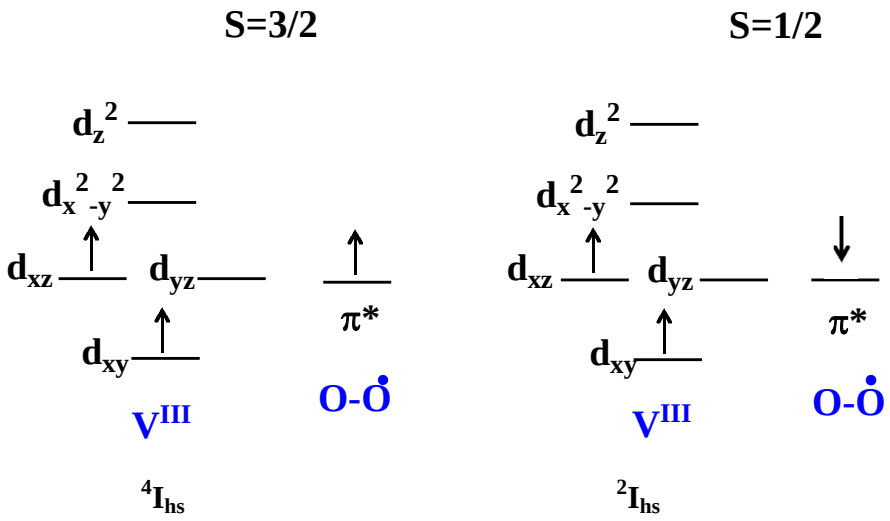

Scheme 5.1. A model structure of vanadium-superoxo species with the existence of quartet, and doublet spin states.

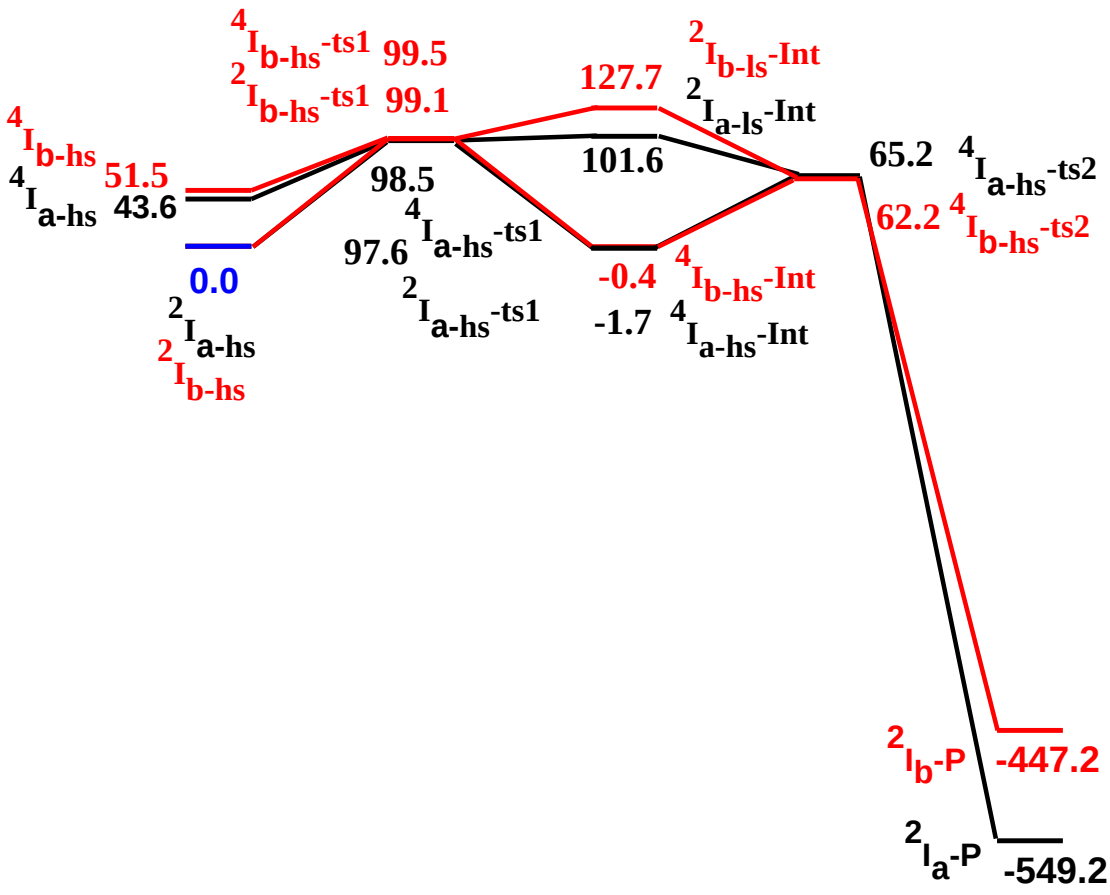

Figure 5.3. B3LYP-D2-computed potential energy surface (ΔG in kJmol^{-1}) for C-H activation by vanadium-superoxo species $^2I_{a\text{-}hs}$ and $^2I_{b\text{-}hs}$(13-TMC (black), 14-TMC (red).

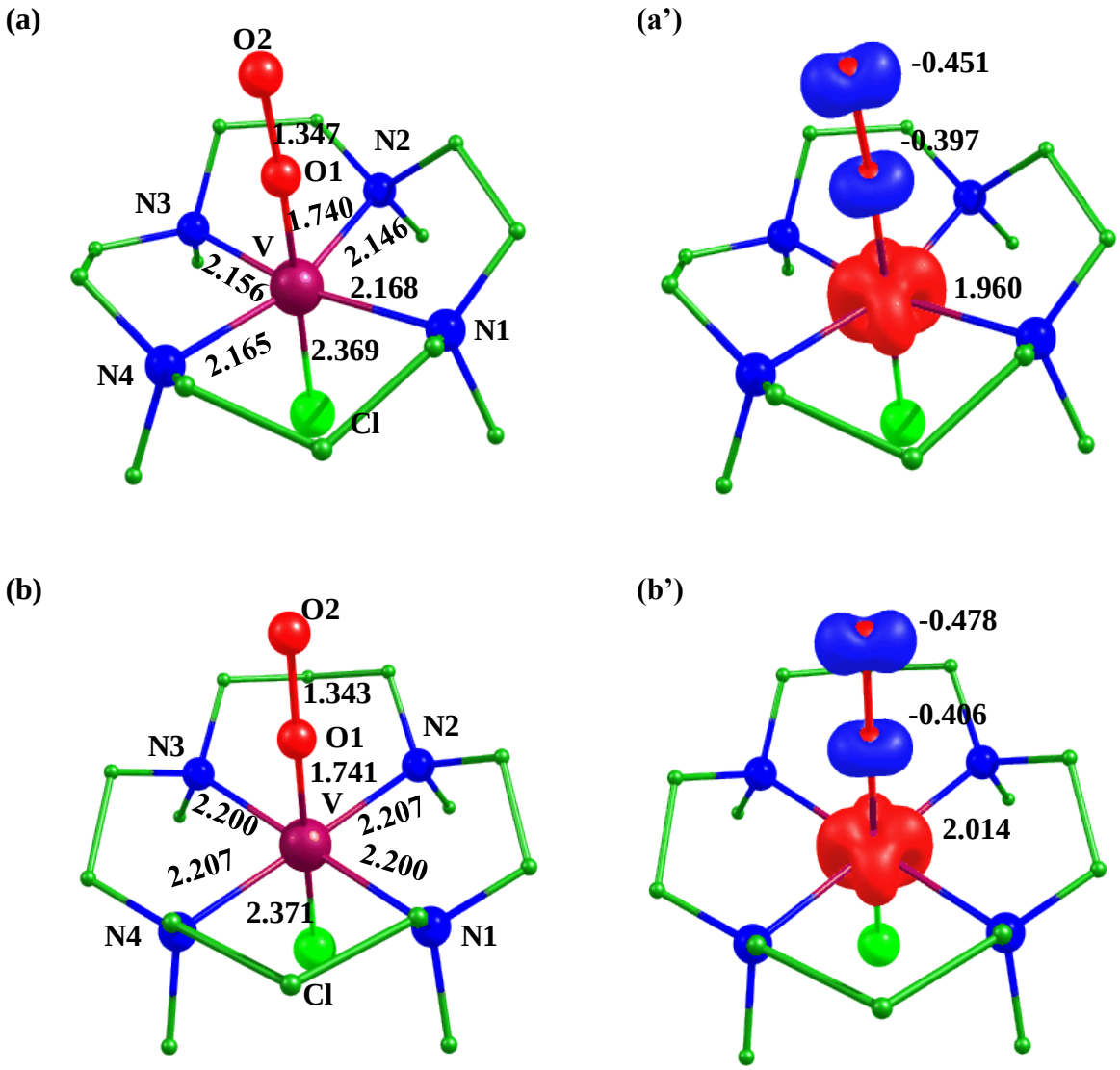

Figure 5.4. B3LYP-D2 a) Optimized structure (bond lengths in Å), a') corresponding spin density plot of $^{2}I_{a\text{-}hs}$, b) optimized structure (bond lengths in Å), and b') corresponding spin density plot of $^{2}I_{b\text{-}hs}$.

The electronic configuration at the vanadium center of the $^{2}I_{a\text{-}hs}$ and $^{2}I_{b\text{-}hs}$ is found the same as $(d_{xy})^1$, $(d_{xz})^1$, $(d_{yz})^0$, $(d_{x^2\text{-}y^2})^0$, $(d_{z^2})^0$ (see Figure 5.5). The magnetic exchange coupling constant (J) of the species I_a and I_b have computed to -1945.1 cm^{-1} and -1965.7 cm^{-1} show the strong antiferromagnetic interaction between metal and superoxo unit. A significant electron density at distal oxygen indicates the reactive nature of superoxo species and may be responsible for C-H activation.

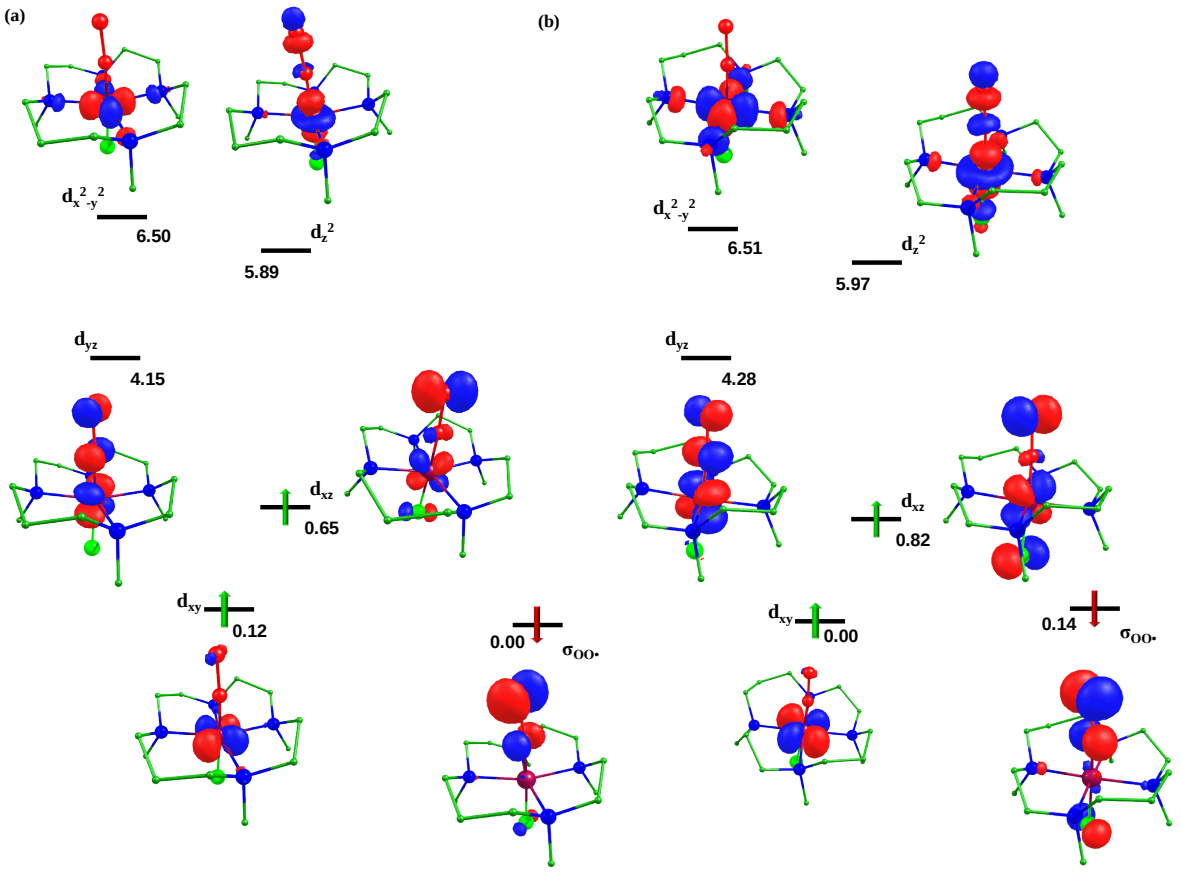

Figure 5.5. Computed eigenvalue plot incorporating energies computed for *d* based orbitals for alpha and beta spin corresponding to the ground state a) ($^2I_{a\text{-}hs}$) of vanadium-superoxo species (energies are given in eV), and b) ($^2I_{b\text{-}hs}$).

Here, we have also tested the reactivity of vanadium-superoxo species towards C-H bond activation with cyclohexa-1,4-diene. There are two possible pathways for C-H bond activation, either attacking by proximal oxygen or distal oxygen. In our previous report, it is found that C-H bond activation by the distal oxygen is more favorable.[56] It can also be seen from space-filling model where the proximal oxygen is showing more sterically hindered than the distal oxygen due to which substrate can easily access by the distal oxygen (see Figure 5.2). So, here we have opted for the distal oxygen for our further calculations. The proposed mechanism of C-H bond activation by superoxo species is shown in Scheme 5.2. From our calculations, it is found that the barrier heights for the C-H bond activation are found as 97.6 and 99.1 kJ/mol at the spin surfaces $^2I_{a\text{-}hs}$-ts1, and $^2I_{b\text{-}hs}$-ts1, respectively.

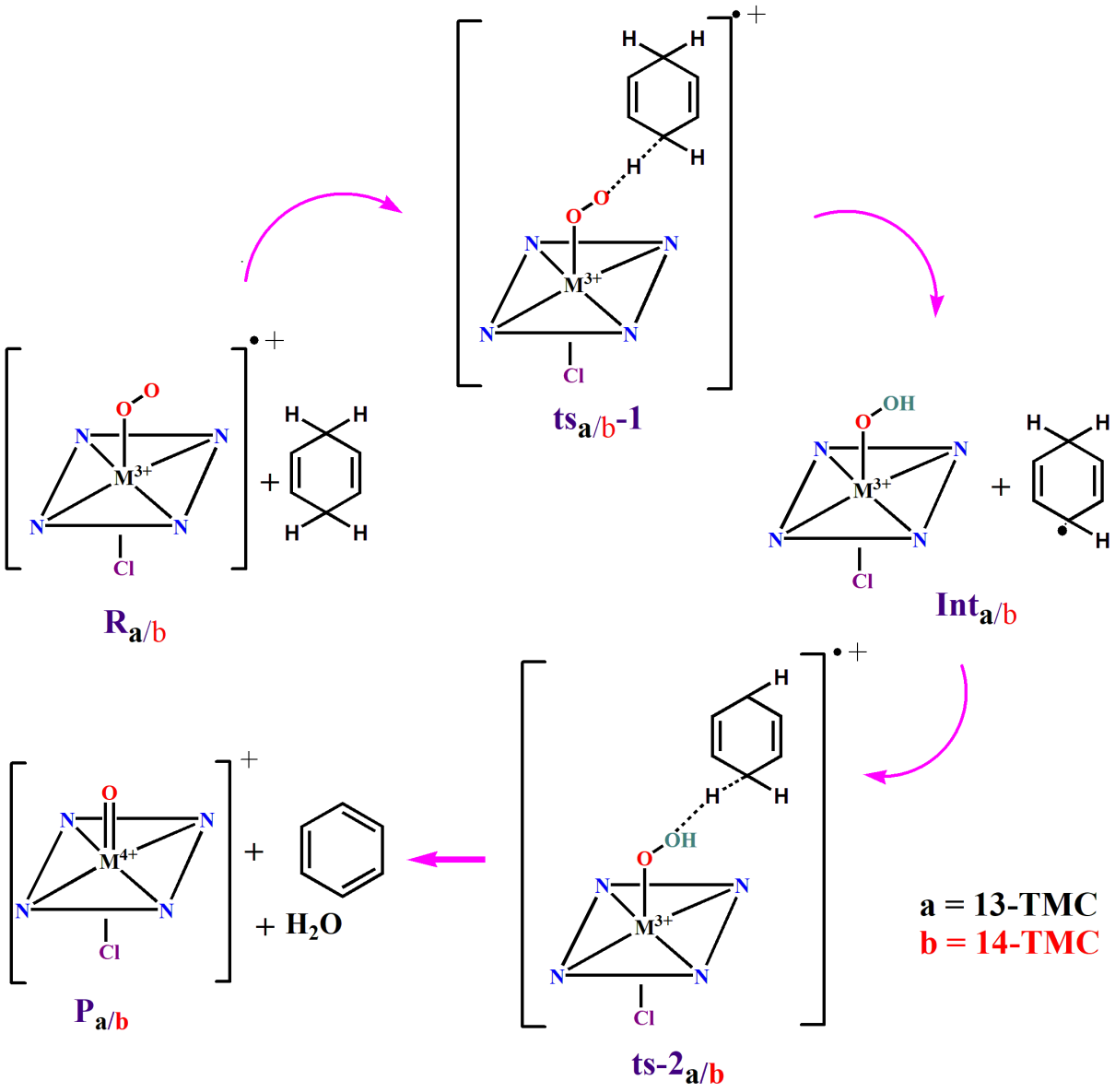

Scheme 5.2. Mechanism of C-H bond activation of cyclohexa-1,4-diene by superoxo species.

The optimized structures along with spin density plots of the transition state ($^2I_{a\text{-}hs}$-ts1 and $^2I_{b\text{-}hs}$-ts1) are shown in Figure 5.6(a/a'b/b'). Spin density on vanadium centers during transition states ($^2I_{a/b\text{-}hs}$-ts1) increases by ($\Delta\rho$=0.202/0.167), indicates that extra electron is coming to the metal center. A significant spin density is also located at the C1 center -0.283 ($^2I_{a\text{-}hs}$-ts1), -0.272 ($^2I_{b\text{-}hs}$-ts1) indicates the formation of radical character rather than cation or anion. The computed spin densities show that C-H bond activation occurs via proton-coupled electron transfer (PCET) mechanism,

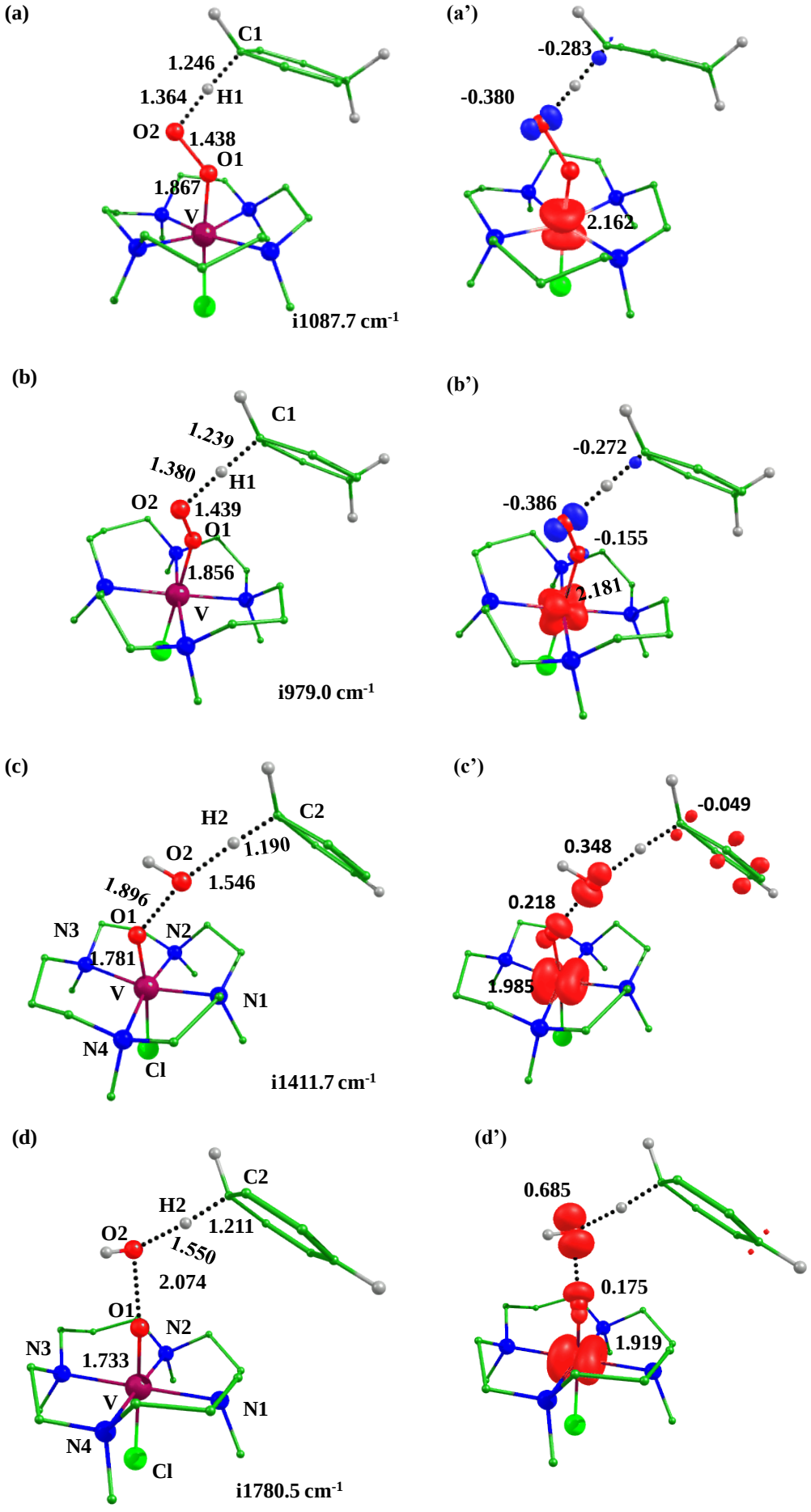
(a)
C1
1.246
1.364
H1
O2
1.438
O1
1.867
V
i1087.7 cm-1
(a')
-0.283
-0.380
2.162
(b)
C1
1.239
1.380
H1
O2
1.439
O1
1.856
V
i979.0 cm-1
(b')
-0.272
-0.386
-0.155
2.181
(c)
H2
C2
O2
1.190
1.546
1.896
O1
N3
N2
1.781
V
N1
N4
Cl
i1411.7 cm-1
(c')
-0.049
0.348
0.218
1.985
(d)
C2
H2
1.211
O2
1.550
2.074
O1
N2
N3
1.733
V
N1
N4
Cl
i1780.5 cm-1
(d')
0.685
0.175
1.919

Figure 5.6. B3LYP-D2 a) optimized structures and a‘) spin density plots of $^{2}I_{a\text{-}hs}$-ts1, b) optimized structures and b‘) spin density plots of $^{2}I_{b\text{-}hs}$-ts1, c) optimized structures and d‘) spin density plots of $^{2}I_{a\text{-}hs}$-ts2, d) optimized structures and d‘) spin density plots of $^{2}I_{b\text{-}hs}$-ts2.

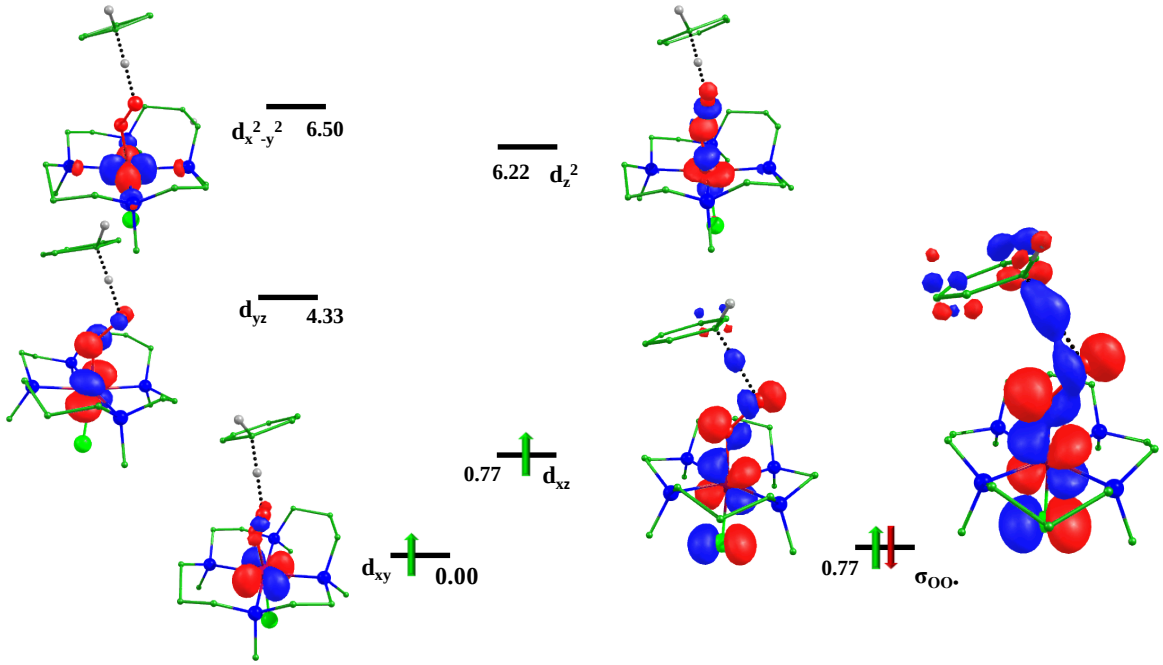

Figure 5.7. Computed eigenvalue plot incorporating energies computed for *d* based orbitals for alpha and beta spin corresponding to the ground state ($^{2}I_{a\text{-}hs}$-ts1) of vanadium-superoxo species (energies are given in eV).

which is confirmed by the eigenvalue plot (see Figure 5.5a and Figure 5.7). The ∠O2-H1-C1 during the C-H bond activation with 13/14-TMC are found to be 17 7.2˚/178.1˚ (see Table AX 5.1 and Table AX 5.2 of appendix), respectively, reveals that C-H activation occurs via the σ pathway (see Scheme 5.3). The V-O1 bond increases by 0.127 Å ($^{2}I_{a\text{-}hs}$-ts1), and 0.115 Å ($^{2}I_{b\text{-}hs}$-ts1) whereas the O1-O2 bond increases by 0.091 Å, and 0.096 Å during the transition state. After abstraction of hydrogen vanadium- superoxo species form hydroperoxo ($^{4}Int_{a/b\text{-}hs}$) and ($^{2}Int_{a/b\text{-}ls}$) and cyclohexa-1,4-dienyl radical, and $^{4}Int_{a\text{-}hs}$ and $^{4}Int_{b\text{-}hs}$ lie at -1.7 and -0.4 kJ/mol (see Scheme 5.2 and Figure 5.3). After the formation of the vanadium hydrogen peroxide intermediate the reaction may proceed in two possible pathways;

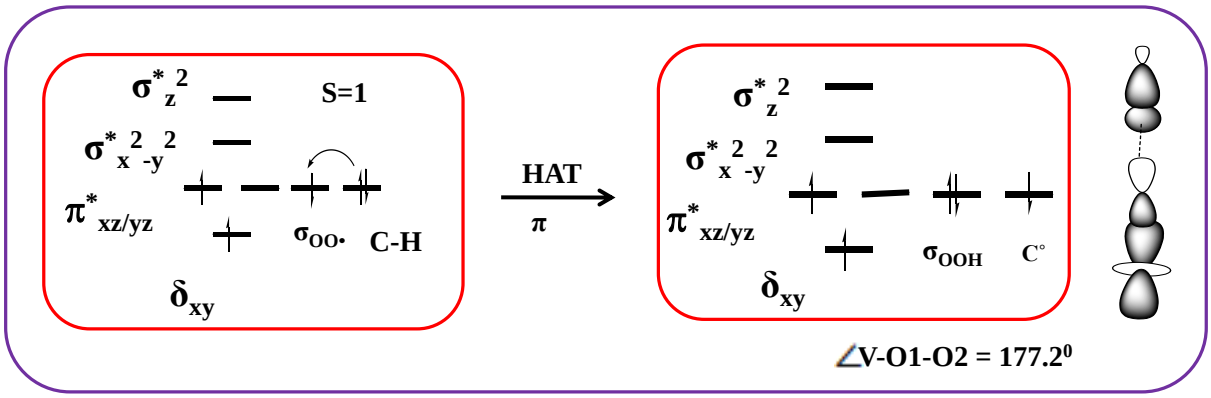

Scheme 5.3. Orbital diagram for sigma (σ) pathway.

(i) the hydrogen peroxide vanadium species obtained from the earlier reaction can attack the cyclohexa-1,4-dienyl radical (pathway 1) and (ii) generation of homolytic/heterolytic cleavage of the O---O bond of the V^{III}O-OH to generate V^{IV}=O/V^{V}=O oxidants which could abstract the second hydrogen atom from cyclohexa-1,4-dienyl radical to form the final product (pathway 2). But it was found that pathway 1 is more favorable over the pathway 2 in the previous report.[71] In the next step, vanadium hydroperoxo further abstracts the hydrogen of cyclohexa-1,4-dienyl radical leads to the formation of vanadium(IV)-oxo species, water, and benzene (see Scheme 5.2) via homolytic O---O bond cleavage. The barrier for the second hydrogen atom abstraction is found to be 65.2 kJ/mol ($^{4}I_{a\text{-}hs}$-ts2) and 62.2 kJ/mol ($^{4}I_{b\text{-}hs}$-ts2). The optimized structures and spin density plots of $^{4}I_{a\text{-}hs}$-ts2 and $^{4}I_{b\text{-}hs}$-ts2 are shown in Figure 5.7c,d. The formation of vanadium-oxo species is found to be exothermic by a large margin (see Figure 5.3). As doublet spin state is predicted as the ground state of the vanadium(IV) species which is in agreement with earlier reports.[101-109] A significant spin density is also observed at the oxygen of vanadium-oxo may further involve in C-H bond activation of organic compounds (Table AX 5.3, Table AX 5.4 and see Figure 5.4 of appendix). Our computed barrier heights show that 13-TMC ligated vanadium species are more reactive than the corresponding 14-TMC species (see Figure 5.3).

5.3.2 Chromium-superoxo species ([Cr(13/14-TMC)O_2Cl]$^+$, $II_{a/b}$)

As we go from vanadium to chromium, one extra electron is added to the *d*-orbital. Crystal structure of $[Cr^{III}(O_2)(TMC)(Cl)]^+$ along with spectroscopic, structural characterization, and reactivity studies are reported.[22] We have also computed all possible spin states ($^5II_{a/b\text{-}hs}$, $^3II_{a/b\text{-}hs}$, $^3II_{a/b\text{-}ls}$, and $^1II_{a/b\text{-}ls}$) of chromium-superoxo species (see Figure 5.8). From the calculations, it is found that $^3II_{a\text{-}hs}$ and $^3II_{b\text{-}hs}$ are the ground state of the species II_a and II_b. The optimized structure and spin density plot of $^3II_{a\text{-}hs}$ and $^3II_{b\text{-}hs}$ are shown in Figure 5.9.

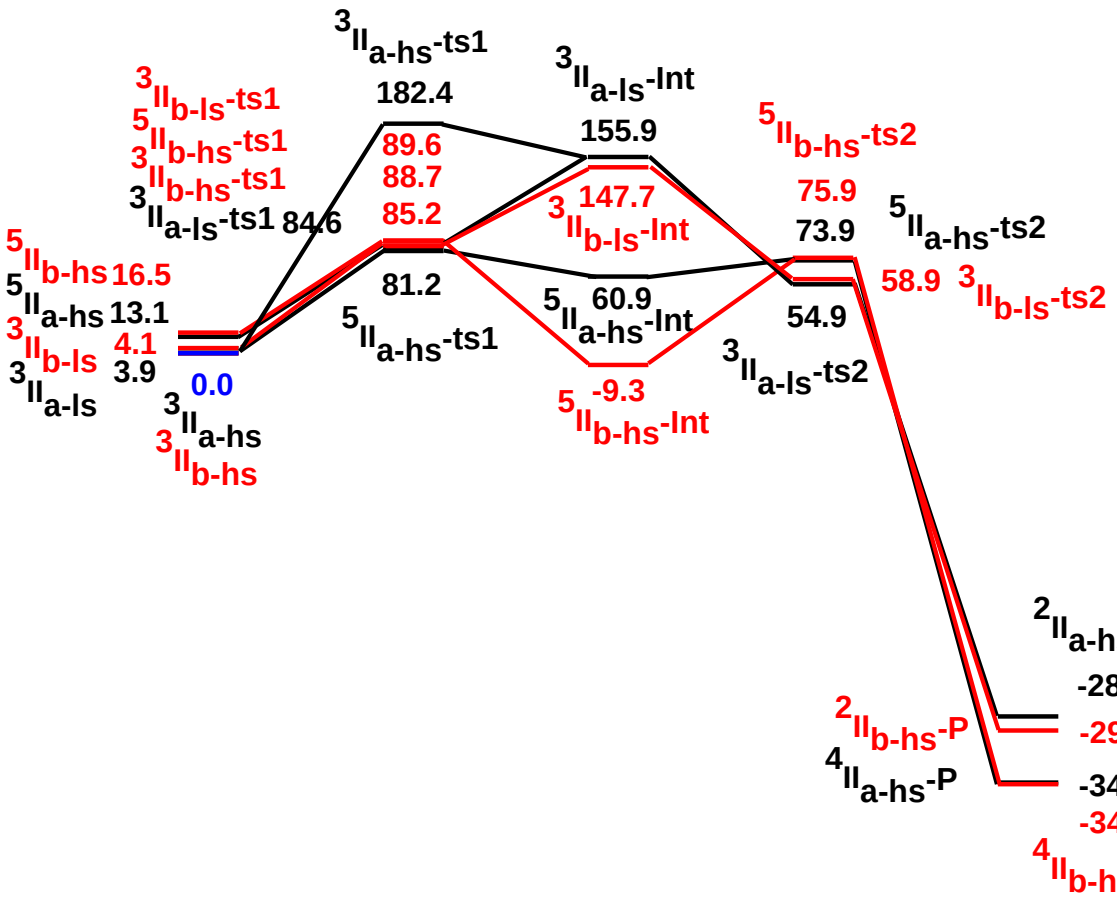

Figure 5.8. B3LYP-D2-computed potential energy surface (ΔG in kJmol^{-1}) for C-H activation by chromium-superoxo species $^2I_{a\text{-}hs}$ and $^2I_{b\text{-}hs}$(13-TMC (black), 14-TMC (red).

Computed structural parameters are good in agreement with the experimental observation (see Table AX 5.1 of appendix).[22] Computed Cr-O1, O1-O2, Cr-Cl, Cr-N_{avg} bond lengths

decrease as ring size increase (see Figure 5.9). Computed ∠Cr-O1-O2 of $^{3}II_{a\text{-}hs}$ and $^{3}II_{b\text{-}hs}$ are 135.6˚ and 134.7˚ respectively, show that O2 is not orthogonal to Cr and O1. Unpaired electron at distal oxygen may couple with the unpaired electron at chromium center. Computed magnetic exchange coupling constant of the species II_a is found to -546.3 cm^{-1} suggests strong antiferromagnetic coupling occurs in between the metal center and the distal oxygen and such interaction is also found for the species II_b in previous reports.[22,56,71]

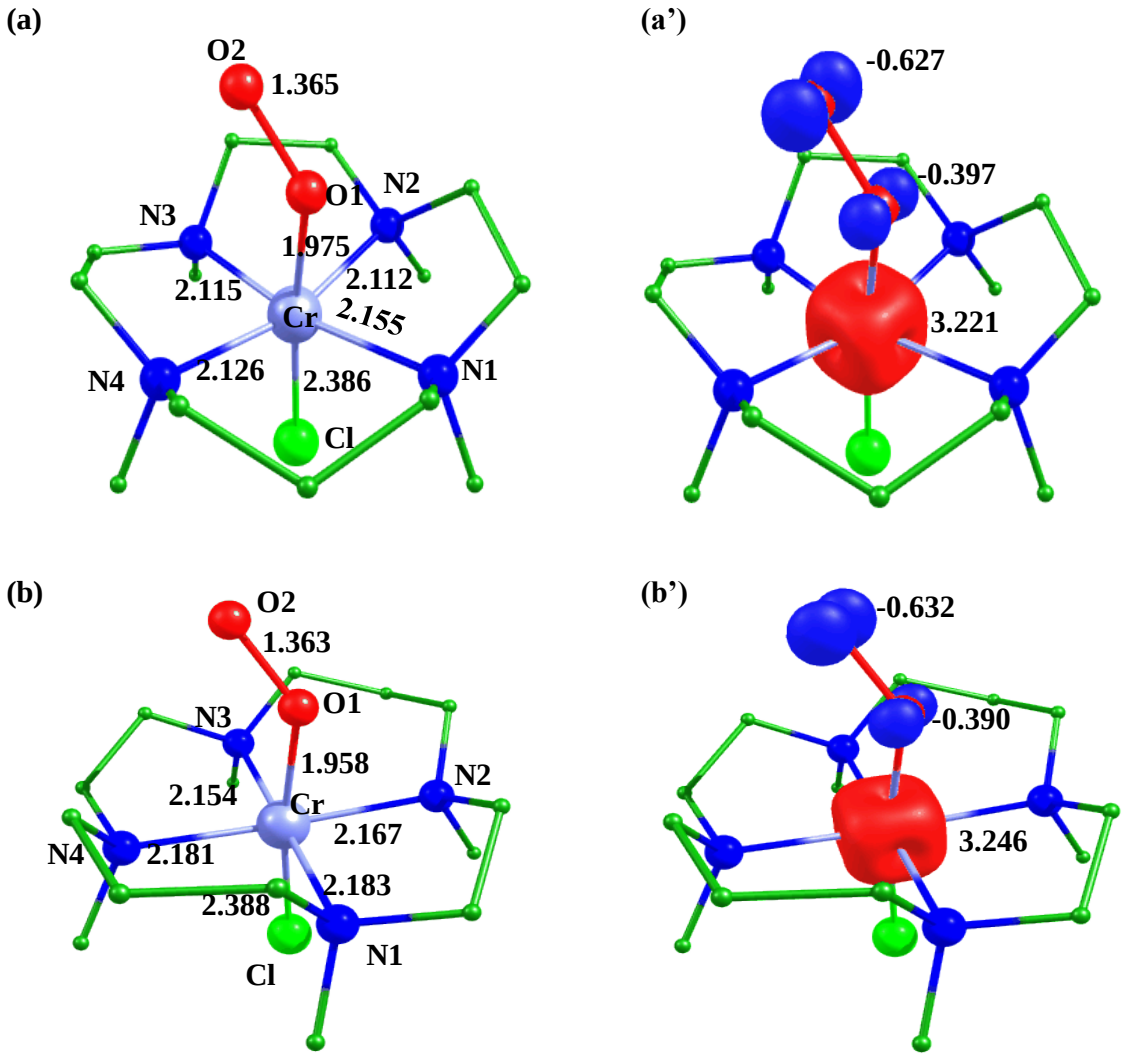

Figure 5.9. B3LYP-D2 a) optimized structures (bond lengths in Å), a') corresponding spin density plots of the ground state $^{2}II_{a\text{-}hs}$, b) optimized structures (bond lengths in Å) and b') corresponding spin density plots of the ground state $^{2}II_{b\text{-}hs}$.

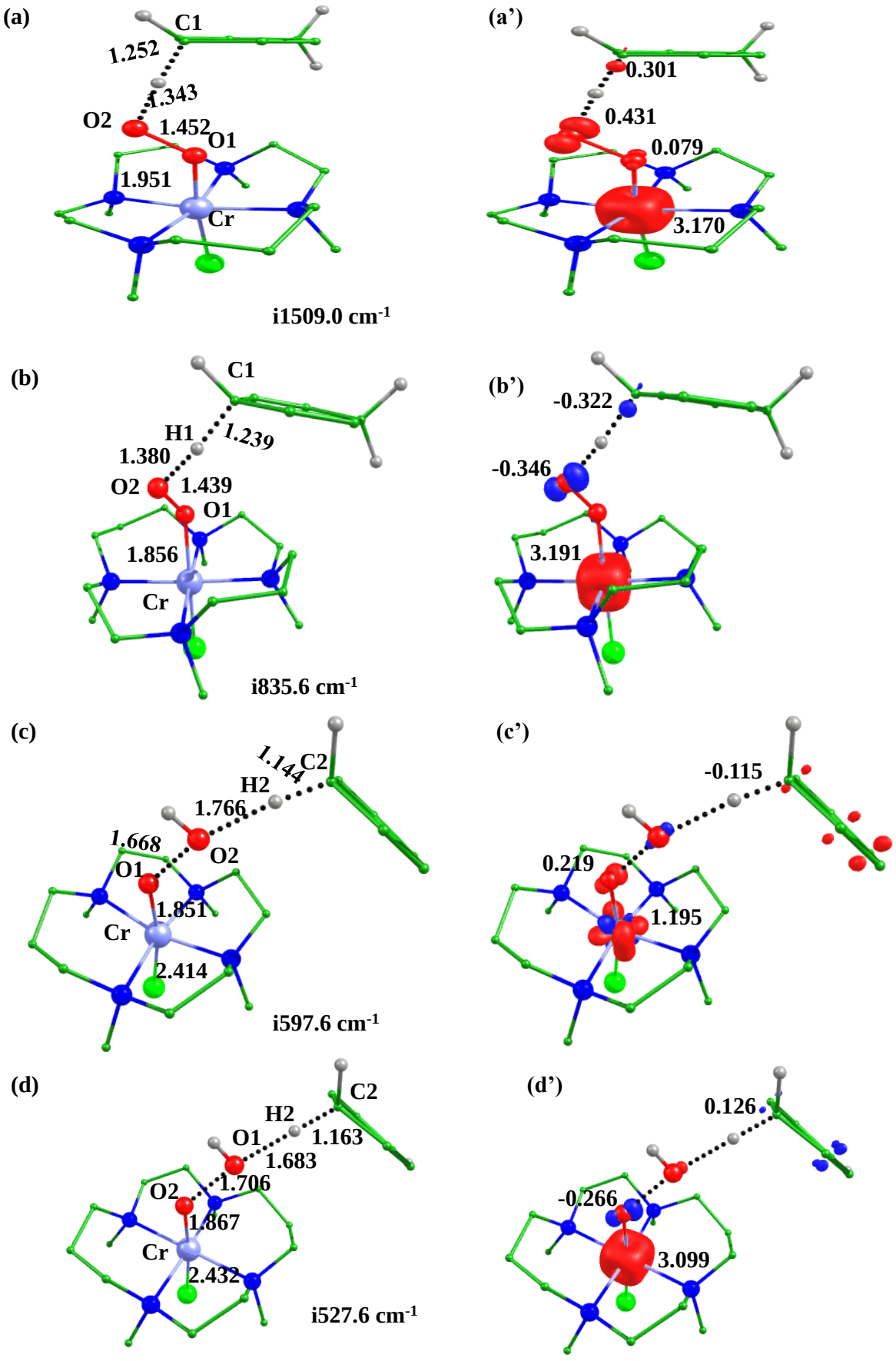
(a)
C1
1.252
1.343
O2
1.452
O1
1.951
Cr
i1509.0 cm-1
(a')
0.301
0.431
0.079
3.170
(b)
C1
H1
1.239
1.380
O2
1.439
O1
1.856
Cr
i835.6 cm-1
(b')
-0.322
-0.346
3.191
(c)
1.144
C2
H2
1.766
1.668
O2
O1
1.851
Cr
2.414
i597.6 cm-1
(c')
-0.115
0.219
1.195
(d)
C2
H2
O1
1.163
1.683
1.706
O2
1.867
Cr
2.432
i527.6 cm-1
(d')
0.126
-0.266
3.099

Figure 5.10. B3LYP-D2 a) optimized structures and a‘) spin density plots of $^{3}II_{a\text{-}hs}$-ts1, b) optimized structures and b‘) spin density plots of $^{3}II_{b\text{-}hs}$-ts1 and c) optimized structures and c‘) spin density plots of $^{2}II_{a\text{-}hs}$-ts2, d) optimized structures and d‘) spin density plots of $^{2}II_{b\text{-}hs}$-ts2.

Its reactivity is also tested with a cyclohexa-1,4-diene[22-23] and computed barrier height of C-H bond activation of the first hydrogen abstraction is found to be 81.2 kJ/mol ($^{5}II_{a\text{-}hs}$-ts1) and 85.2 kJ/mol ($^{3}II_{b\text{-}hs}$-ts1) (see Figure 5.8). The optimized structure and spin density plots of $^{5}II_{a\text{-}hs}$-ts1 and $^{3}II_{b\text{-}hs}$-ts1 are shown in Figure 5.10. It is found that the Cr-O bond length decreases by 0.056 Å ($^{5}II_{a\text{-}hs}$-ts1) and 0.028 Å ($^{3}II_{a\text{-}hs}$-ts1) and the Cr-Cl bond length increases by 0.011 Å ($^{5}II_{a\text{-}hs}$-ts1) and 0.041Å ($^{3}II_{b\text{-}hs}$-ts1). This abstraction leads to the formation of chromium hydroperoxo species and cyclohexa-1,4-dienyl radical which lie at 60.9 ($^{4}II_{a\text{-}hs}$-Int) and -9.3 kJ/mol ($^{4}II_{b\text{-}hs}$- Int). The ground state is also inconsistent with the earlier report.[71] The second hydrogen abstraction requires 54.9 ($^{3}II_{a\text{-}hs}$-ts2) and 58.9 kJ/mol ($^{3}II_{b\text{-}hs}$-ts2) (see Figure 5.8 and 5.10) leads to the formation of the Cr(IV)=O species. The triplet state is also found as the ground state of the Cr(IV)=O. A significant spin density observed at oxygen can also further activate the C-H bond of organic substrates. The computed energy of the transition states suggests that the first step is the rate-determining step (see Figure 5.8). Formed Cr(IV)=O is highly exothermic with both the ligands (see Figure 5.8) and agrees with the available experimental report.[23] Similar, to vanadium-superoxo species, our computed energy barriers show that the chromium-superoxo ligated with 13-TMC is more reactive than with 14-TMC.

5.3.3 Manganese-superoxo species ($[Mn(13/14\text{-}TMC)O_2Cl]^{+}$, $III_{a/b}$)

As we move to manganese, one more extra electron is added to the *d*-orbital. Here, we have also optimized all the possible electronic configurations i.e. $^{6}III_{a/b\text{-}hs}$, $^{4}III_{a/b\text{-}hs}$, $^{4}III_{a/b\text{-}is}$, $^{2}III_{a/b\text{-}is,}$ and $^{2}III_{a/b\text{-}ls}$. From the calculations, it is found that $^{6}III_{a\text{-}hs}$ and $^{4}III_{b\text{-}hs}$ spin states are the ground

state of the respective species (see Figure 5.11). The optimized structure and spin density plot of the ground states ($^{6}III_{a\text{-}hs}$ and $^{4}III_{b\text{-}hs}$) are shown in Figure 5.12.

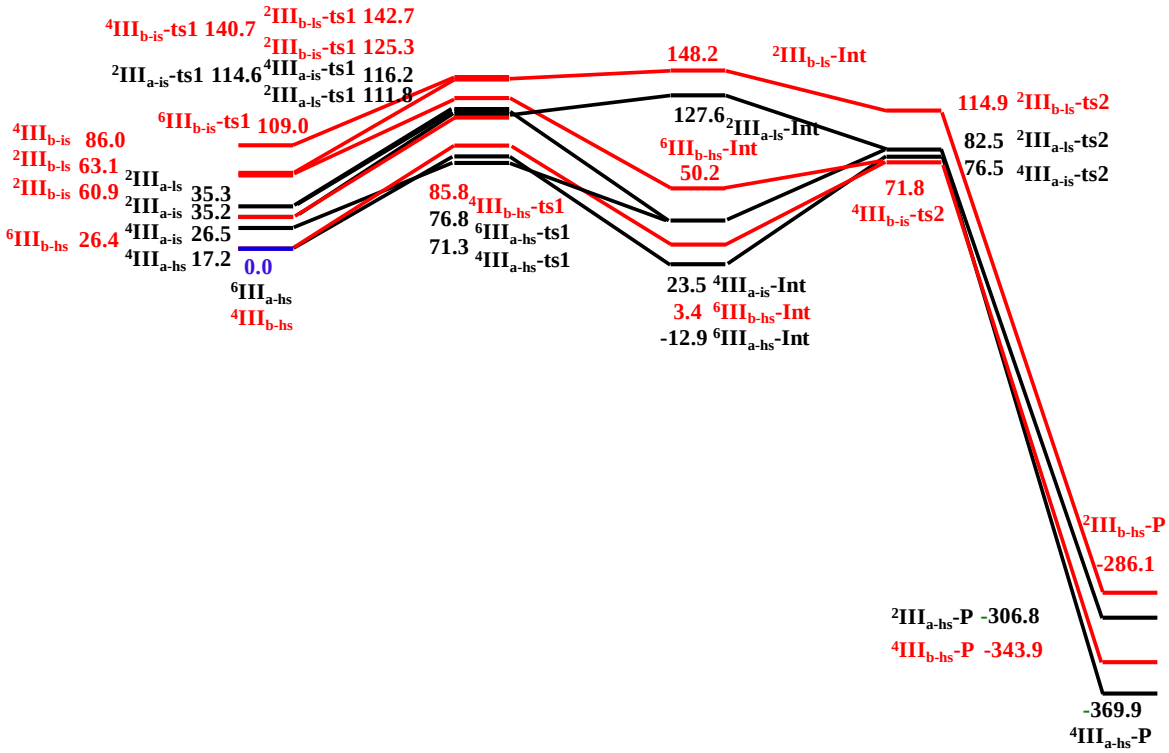

Figure 5.11. B3LYP-D2 computed potential energy surface (ΔG in kJmol^{-1}) for C-H activation by manganese-superoxo species (13-TMC (black), 14-TMC (red).

Computed Mn-O1, O1-O2, Mn-Cl bond lengths decrease while Mn-N_{avg} bond length increases upon an increment of the ring size. The computed magnetic exchange coupling constant of the species III_a and III_b are -523.7 cm^{-1} ($^{6}III_{a\text{-}hs}$) and -735.0 cm^{-1} ($^{4}III_{b\text{-}hs}$) suggests antiferromagnetic coupling.[71] Here, we have also computed transition state of the C-H bond activation of cyclohexa-1,4-diene and barrier height is found to be 71.3 kJ/mol ($^{4}III_{a\text{-}hs}$-ts1), 85.8 kJ/mol ($^{4}III_{b\text{-}hs}$-ts1) (see Figure 5.11 and 5.13). During the transition state, Mn-O and Mn-Cl bond lengths decreased by 0.346 Å/0.115 Å and 0.138 Å/0.001 Å ($^{4}III_{a\text{-}hs}$-ts1/$^{4}III_{b\text{-}hs}$-ts1) shown in Figure 5.13. After this, the manganese hydroperoxo and cyclohexa-1,4-dienyl radical are formed which lie at -12.9 kJ/mol ($^{5}III_{a\text{-}hs}$Int) and 3.4 kJ/mol ($^{5}III_{b\text{-}hs}$-Int). The barrier height for the abstraction of the second hydrogen is found to be at 76.5 kJ/mol ($^{4}III_{a\text{-}hs}$-

ts2) and 71.8 kJ/mol (^{4}III$_{b\text{-}hs}$-ts2) (see Figure 5.11 and 5.13). After the second hydrogen abstraction leads to the formation of manganese-oxo species and this is also exothermic. Here also, our computed energy barriers show that the manganese superoxo ligated with 13-TMC is more reactive than with 14-TMC.

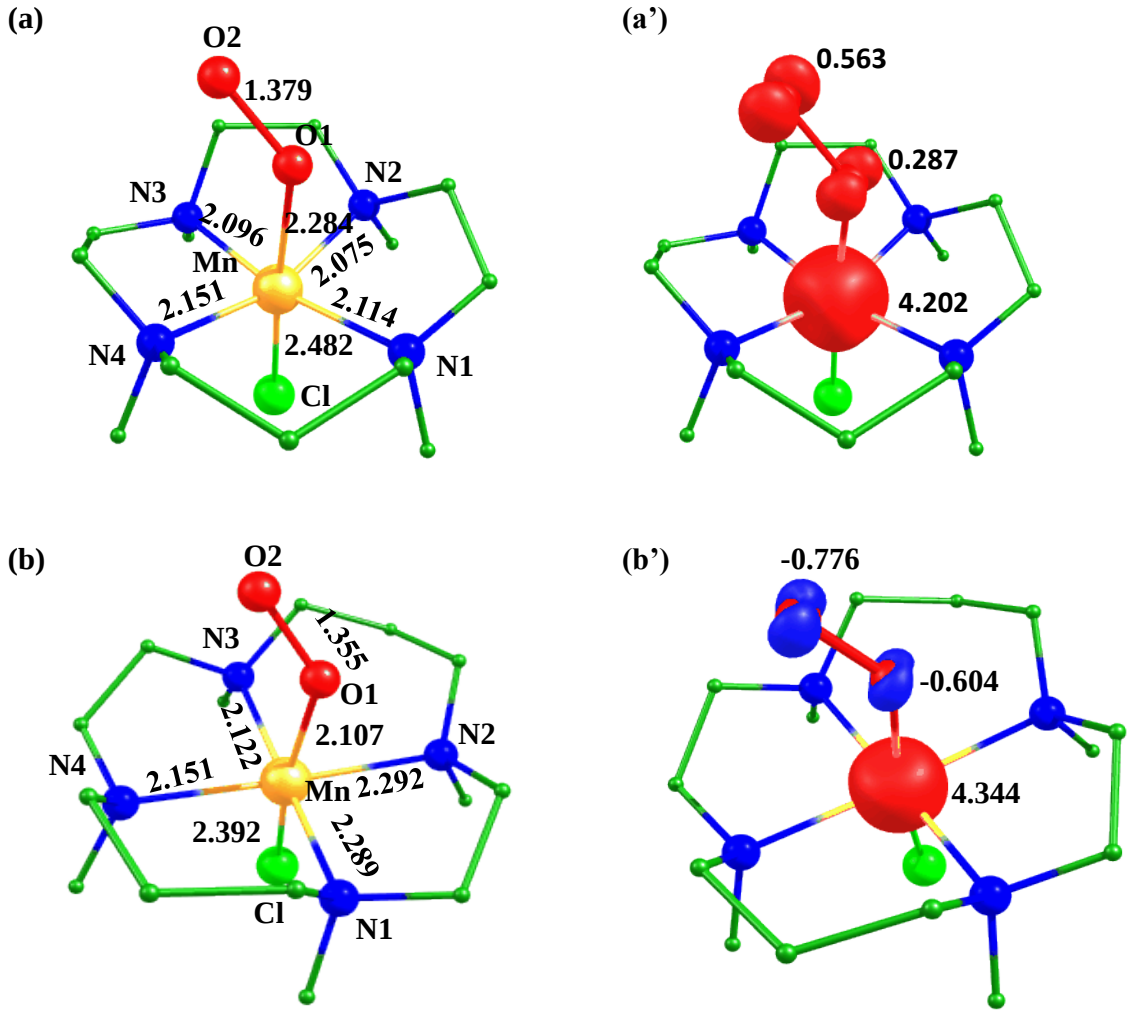

Figure 5.12. B3LYP-D2 a) optimized structures (bond lengths in Å), a') corresponding spin density plots of ^{6}III$_{a\text{-}hs}$, b) optimized structures (bond lengths in Å), and b') corresponding spin density plots of ^{4}III$_{b\text{-}hs}$.

5.3.4 Iron-superoxo species ([Fe(13/14-TMC)O$_2$Cl]$^+$, IV$_{a/b}$)

Similar to V, Cr, and Mn, we have also computed DFT calculations on possible electronic configurations (^{7}IV$_{a/b\text{-}hs}$, ^{5}IV$_{a/b\text{-}hs}$, ^{5}IV$_{a/b\text{-}is}$, ^{3}IV$_{a/b\text{-}is}$, ^{3}IV$_{a/b\text{-}ls}$, and ^{1}IV$_{a/b\text{-}ls}$) of the iron-superoxo species and spin states ^{7}IV$_{a\text{-}hs}$, and ^{7}IV$_{b\text{-}hs}$ are found to be the ground state (see Figure 5.14).

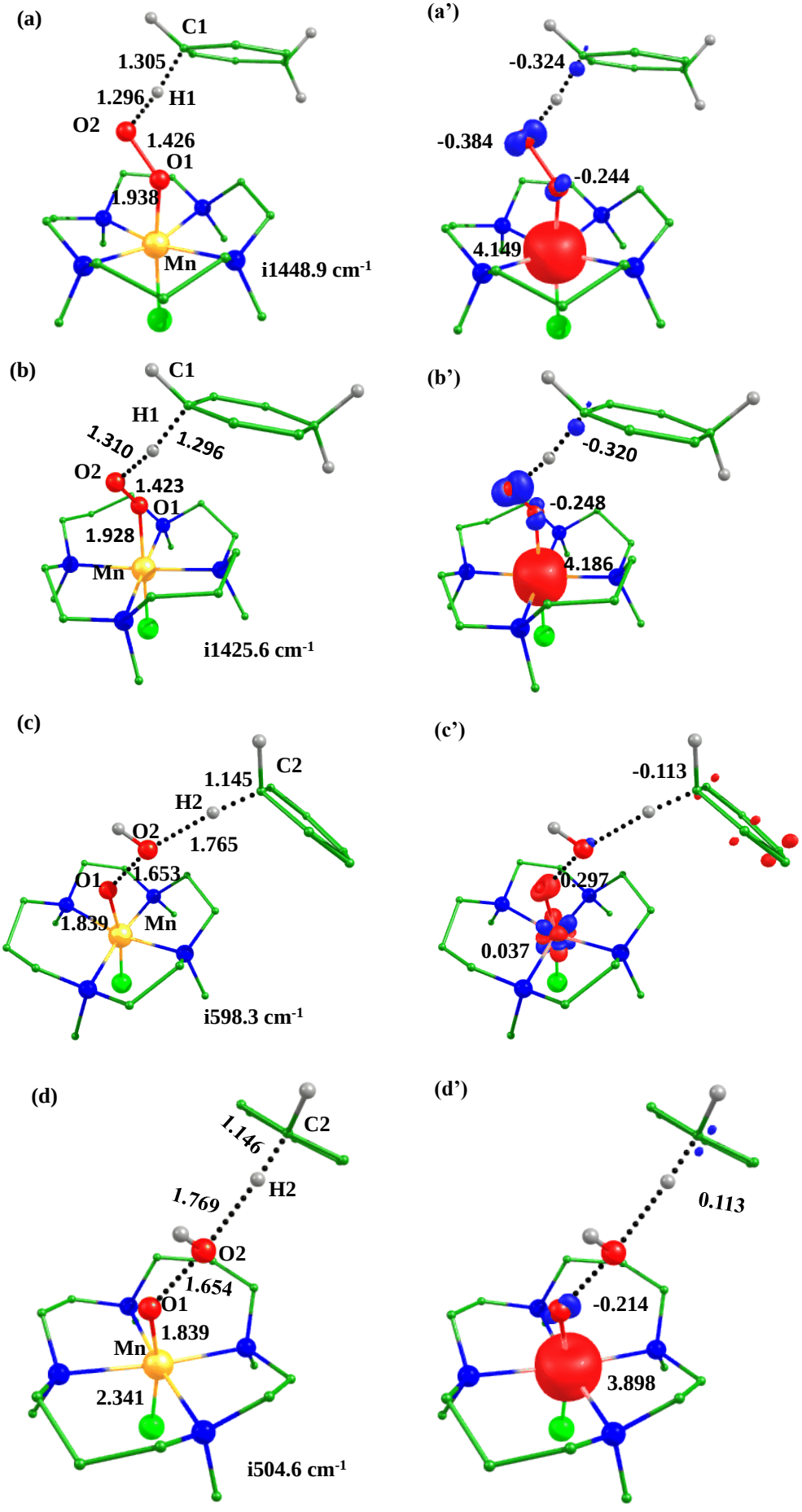
(a)
C1
1.305
1.296
H1
O2
1.426
O1
1.938
Mn
i1448.9 cm-1
(a')
-0.324
-0.384
-0.244
4.149
(b)
C1
H1
1.310
1.296
O2
1.423
O1
1.928
Mn
i1425.6 cm-1
(b')
-0.320
-0.248
4.186
(c)
1.145
C2
H2
O2
1.765
1.653
O1
1.839
Mn
i598.3 cm-1
(c')
-0.113
0.297
0.037
(d)
1.146
C2
1.769
H2
O2
1.654
O1
1.839
Mn
2.341
i504.6 cm-1
(d')
0.113
-0.214
3.898

Figure 5.13. B3LYP-D2 a) optimized structures and a‘) spin density plots of $^{4}III_{a\text{-}hs}$-ts1, b) optimized structures and b‘) spin density plots of $^{4}III_{b\text{-}hs}$-ts1 c) optimized structures (bond lengths in Å), c’) corresponding spin density plots of $^{4}III_{a\text{-}hs}$-ts2, d) optimized structures and d’) corresponding spin density plots of $^{4}III_{b\text{-}hs}$-ts2.

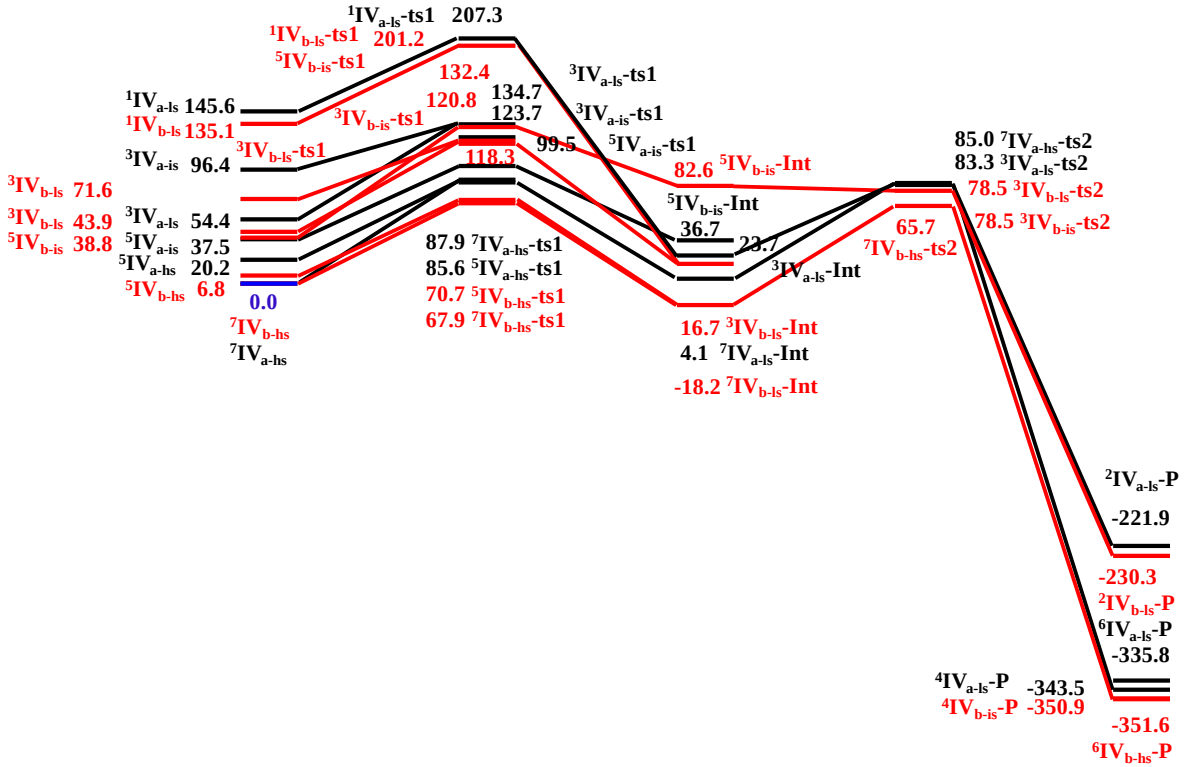

Figure 5.14. B3LYP-D2-computed potential energy surface (ΔG in kJmol^{-1}) for C-H activation by iron-superoxo species (13-TMC (black), 14-TMC (red).

Here, Fe-O1, O1-O2, Fe-Cl, Fe-N_{avg} bond lengths increase as the ring size increase. The computed magnetic exchange coupling constant of the species IV_a and IV_b are 563.2 cm^{-1} ($^{7}IV_{a\text{-}hs}$) and 188.6 cm^{-1} ($^{7}IV_{b\text{-}hs}$), showing ferromagnetic coupling in between the iron center and the distal oxygen.[56,71] It is also an active oxidant and involved in the H-abstraction atom of organic substrates. Reactivity towards the C-H bond activation by the iron-superoxo species is also tested and found that the $^{5}IV_{a\text{-}hs}$-ts1 and $^{5}IV_{b\text{-}hs}$-ts1 have 85.6 and 67.9 kJ/mol (see Figure 5.14). The optimized structure and spin density plot of the ground state of transition state are shown in Figure 5.15.

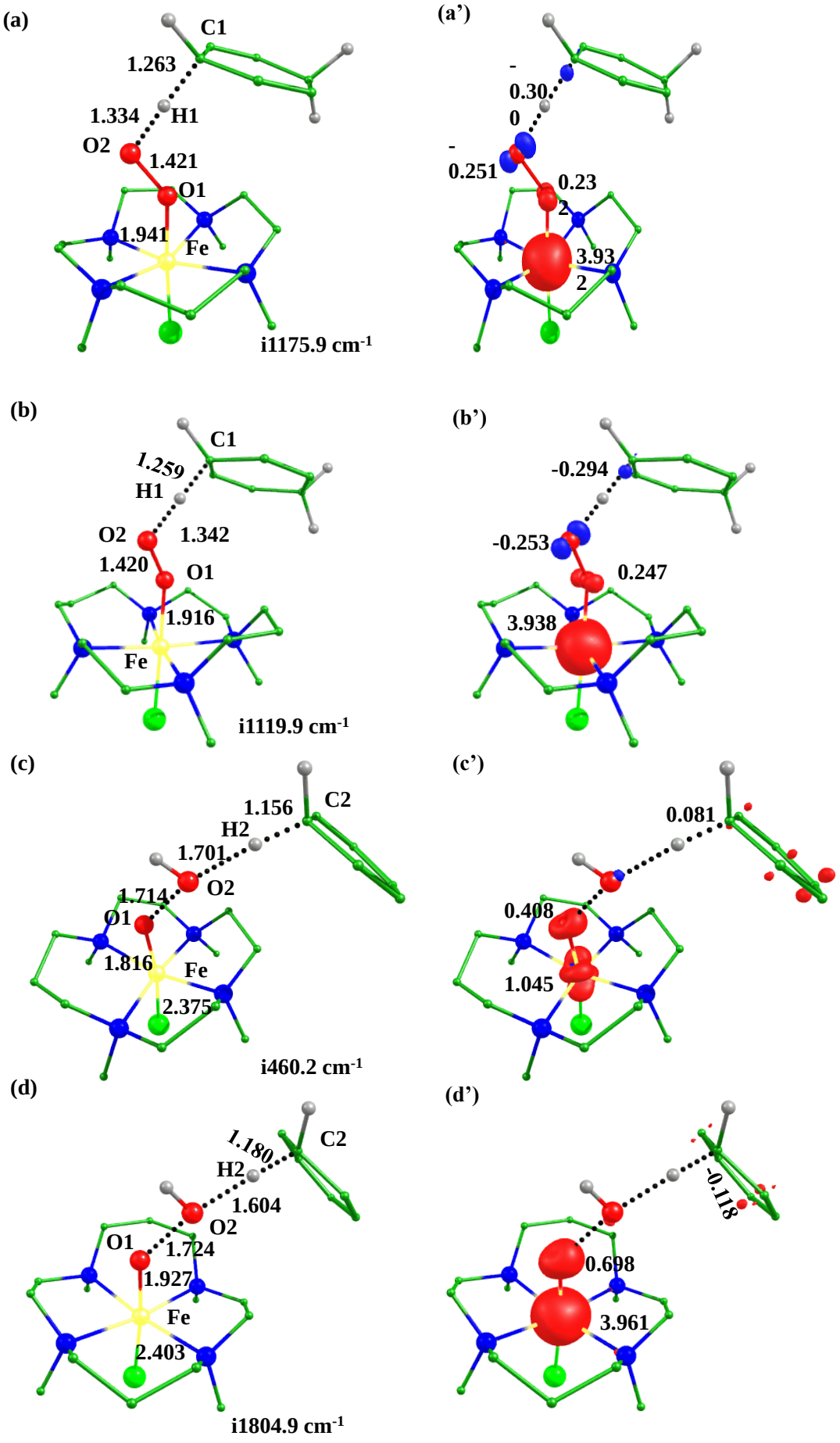
(a)
C1
1.263
1.334
H1
O2
1.421
O1
1.941
Fe
i1175.9 cm-1
(a')
-
0.30
0
-
0.251
0.23
2
3.93
2
(b)
C1
1.259
H1
O2
1.342
1.420
O1
1.916
Fe
i1119.9 cm-1
(b')
-0.294
-0.253
0.247
3.938
(c)
1.156
C2
H2
1.701
O2
1.714
O1
1.816
Fe
2.375
i460.2 cm-1
(c')
0.081
0.408
1.045
(d)
1.180
C2
H2
1.604
O2
O1
1.724
1.927
Fe
2.403
i1804.9 cm-1
(d')
-0.118
0.698
3.961

Figure 5.15. B3LYP-D2 a) optimized structures and a‘) spin density plots of $^{5}IV_{a\text{-}hs}$-ts1 and b) optimized structures and b‘) spin density plots of $^{5}IV_{b\text{-}hs}$-ts1 c) optimized structures (bond lengths in Å), c’) corresponding spin density plots of $^{3}IV_{a\text{-}hs}$-ts2, d) optimized structures (bond lengths in Å) and d’) corresponding spin density plots of $^{7}IV_{b\text{-}hs}$-ts2.

Structural parameters also show that the Fe-O1 bond length decreases while O1-O2, Fe-Cl, and Fe-N_{avg} bond distances increase on the increment of the ring size. The Fe-O1 bond distance also decreases from the reactant to the corresponding transition state by 1.263 Å ($^{5}IV_{a\text{-}hs}$-ts1) and 1.259 Å ($^{5}IV_{b\text{-}hs}$-ts1) while the Fe-Cl bond length increase by 0.021 Å ($^{5}IV_{a\text{-}hs}$-ts1) and 0.024 Å ($^{5}IV_{b\text{-}hs}$-ts1). Iron-hydroperoxo species lie at 23.7 ($^{2}IV_{a\text{-}ls}$-Int) and -18.2 kJ ($^{2}IV_{b\text{-}ls}$-Int). The transition states for the second hydrogen abstraction of species IV_a and IV_b lie at 83.3 kJ/mol ($^{2}IV_{a\text{-}hs}$-ts2), and 65.7 kJ/mol ($^{7}IV_{b\text{-}hs}$-ts2), respectively (see Figure 5.14 and 5.15). This transition state leads to the formation of iron(IV)-oxo species which is also found exothermic (see Figure 5.14). Computed structural parameters of iron(IV)=O species are in good agreement with the experimental.[66] In this case, 14-TMC species is more reactive than the corresponding 13-TMC.

5.3.5 Cobalt-superoxo species ($[Co(13/14\text{-}TMC)O_2Cl]^{+}$,$V_{a/b}$)

Similar to the earlier species, we have also performed calculations on the corresponding cobalt species and $^{2}V_{a\text{-}ls}$ and $^{2}V_{b\text{-}ls}$ are found to be the ground state (see Figure 5.16). These are also in good agreement with the experimental reports.[101] The energy barrier towards the C-H bond activation by species V is found to be 90.4 kJ/mol and 93.5 kJ/mol at spin surfaces $^{2}V_{a\text{-}ls}$-ts1 and $^{2}V_{b\text{-}ls}$-ts1, respectively (see Figure 5.16). Computed Co-O1 and O1-O2 bond distances decrease on an increment of the ring size while Co-N_{avg} bond length increases in same. It is found that the Co-O bond length decreases from the reactant to the corresponding transition state by 0.041 Å ($^{2}V_{a\text{-}ls}$-ts1) and 0.020 Å ($^{2}V_{b\text{-}ls}$-ts1) and the Co-Cl bond length increases by 0.016 Å ($^{2}V_{a\text{-}ls}$-ts1) and 0.011 Å ($^{2}V_{b\text{-}ls}$-ts1).

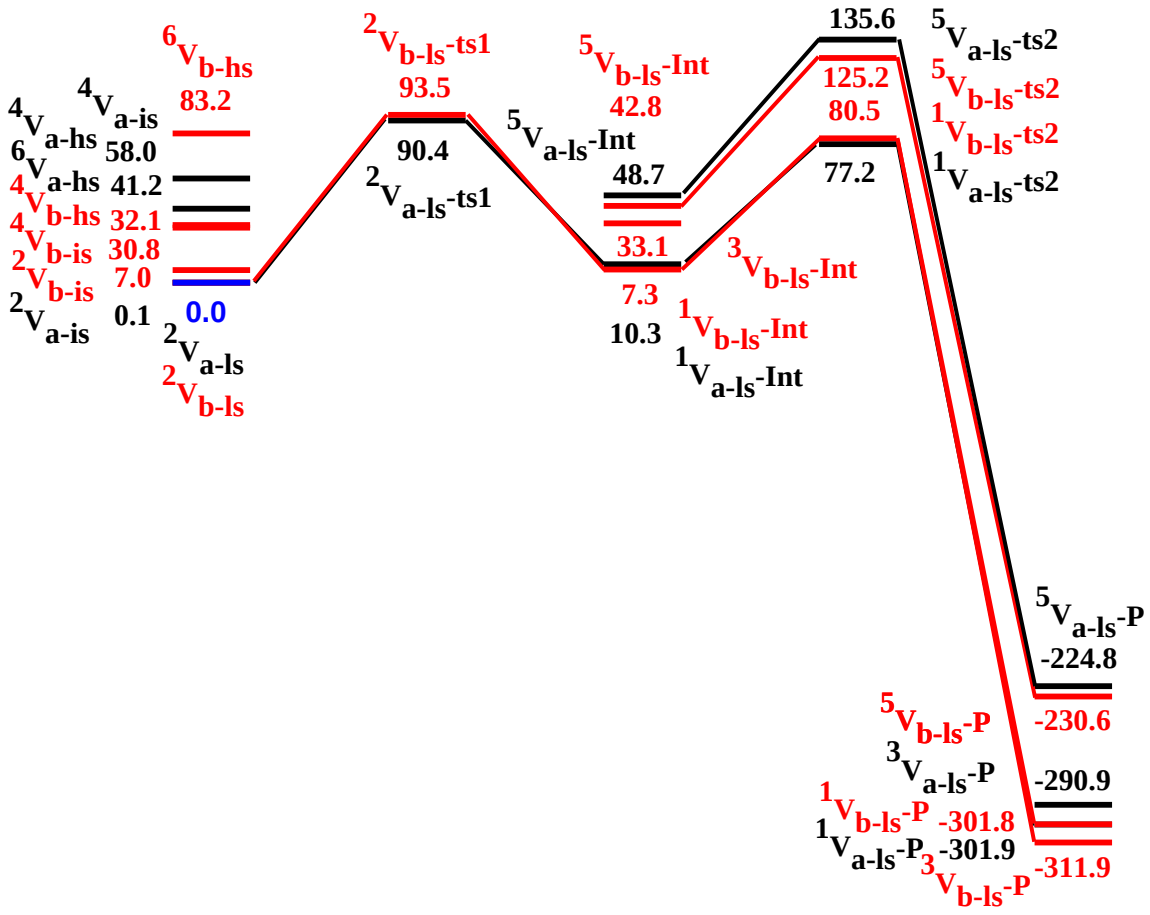

Figure 5.16. B3LYP-D2-computed potential energy surface (ΔG in kJmol^{-1}) for C-H activation by cobalt-superoxo species (13-TMC (black), 14-TMC (red).

After the hydrogen abstraction, cobalt hydroperoxo species are formed which lie at 10.3 and 7.3 kJ/mol with $^{2}V_{a\text{-}ls}$-Int and $^{2}V_{b\text{-}ls}$-Int, respectively. Second transition state by species V_a and V_b lie at 77.2 kJ/mol ($^{2}V_{a\text{-}ls}$-ts2) and 80.5 kJ/mol ($^{2}V_{b\text{-}ls}$-ts2), respectively, (see Figure 5.16 and 5.17e,f). Here, also first transition state is the rate determing step. It also supports that smaller ring TMC metal-superoxo species are more reactive. The second transition state leads to the formation of cobalt(IV)-oxo species. Formed cobalt(IV)-oxo species is exothermic and its structural parameters are in agreement with the earlier cobalt(IV)=oxo species reported.

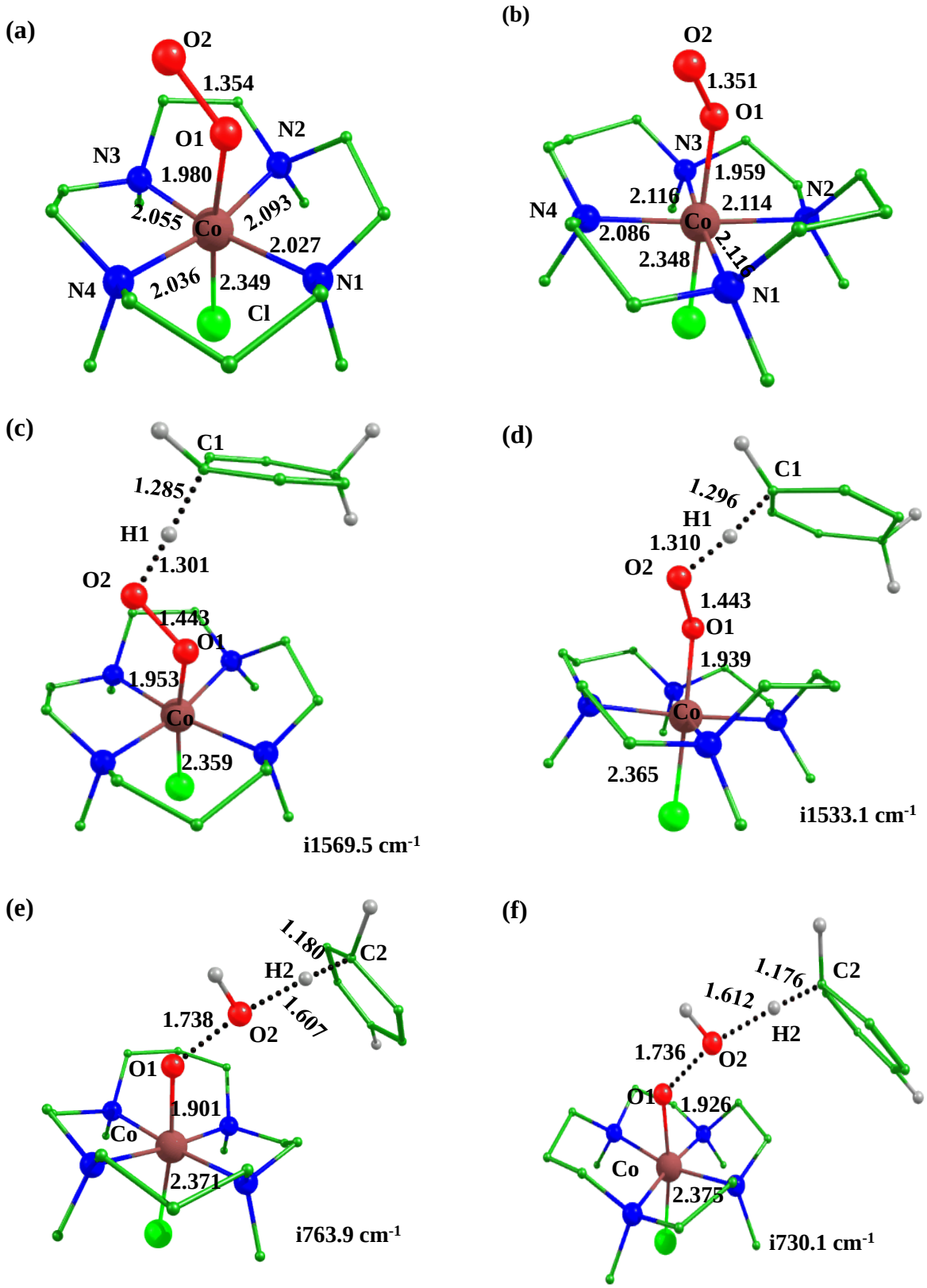

Figure 5.17. B3LYP-D2 a) optimized structure (bond lengths in Å) of $^{2}V_{a\text{-}ls}$, b) optimized structure (bond lengths in Å) of $^{2}V_{b\text{-}ls}$, c) optimized structures and $^{2}V_{a\text{-}hs}$-ts1, d) optimized

structures of $^{2}V_{b\text{-}hs}$-ts1, e) optimized structure (bond lengths in Å) of $^{2}V_{a\text{-}ls}$-ts2, f) optimized structure (bond lengths in Å) of $^{2}V_{b\text{-}ls}$-ts2.

5.3.6 Origin of difference in reactivity during C-H activation

Metal complexes show the difference in reactivity towards catalytic transformation reactions due to several factors such as different architectures of ligands, the effect of axial/equatorial ligands, and the size of ligands. The ring size of ligands is also one of the important factors that regulate reactivity. Here, we have focused on two different ring sizes of TMC ligands such as 13-TMC (smaller ring) and 14-TMC (larger ring) in our studies. We have carried out thorough DFT calculations on both the ring size species.

We have computed the formation energies from the $[M(13/14\text{-}TMC)(Cl)]^{n+}$ complex and the computed energies are exothermic and this suggests a favorable formation energy for superoxo species. Our calculated results show antiferromagnetic coupling in the V(III)-$O_2^{\bullet-}$, Cr(III)-$O_2^{\bullet-}$ and Mn(III)-$O_2^{\bullet-}$ and ferromagnetic coupling in Fe(III)-$O_2^{\bullet-}$ and Co(III)-$O_2^{\bullet-}$ species with both the rings. Our computed electron density at the distal oxygen of the metal-superoxo species are found to be -0.451/-0.478 ($^{2}I_{a\text{-}hs}/^{2}I_{b\text{-}hs}$), -0.627/-0.632 ($^{3}II_{a\text{-}hs}/^{3}II_{b\text{-}hs}$), -0.765/-0.776 ($^{6}III_{a\text{-}hs}/^{4}III_{b\text{-}hs}$), 0.810/0.799 ($^{7}IV_{a\text{-}hs}/^{7}IV_{b\text{-}hs}$) and 0.638/0.642 ($^{2}V_{a\text{-}ls}/^{2}V_{b\text{-}ls}$) these different electron densities can play an important role towards C-H activation barrier. So we have also tested reactivity with the distal oxygen of the superoxo group towards C-H activation of 1,4-cyclohexadiene. Our DFT calculations show that first hydrogen abstraction is the rate-determining step in all the studied species and the C-H activation barrier by species I_a/I_b, II_a/II_b, III_a/III_b, IV_a/IV_b, and V_a/V_b are found to be 97.6/99.1, 81.2/85.2, 71.3/85.8, 85.6/67.9, 90.4/93.5 kJ/mol, respectively.

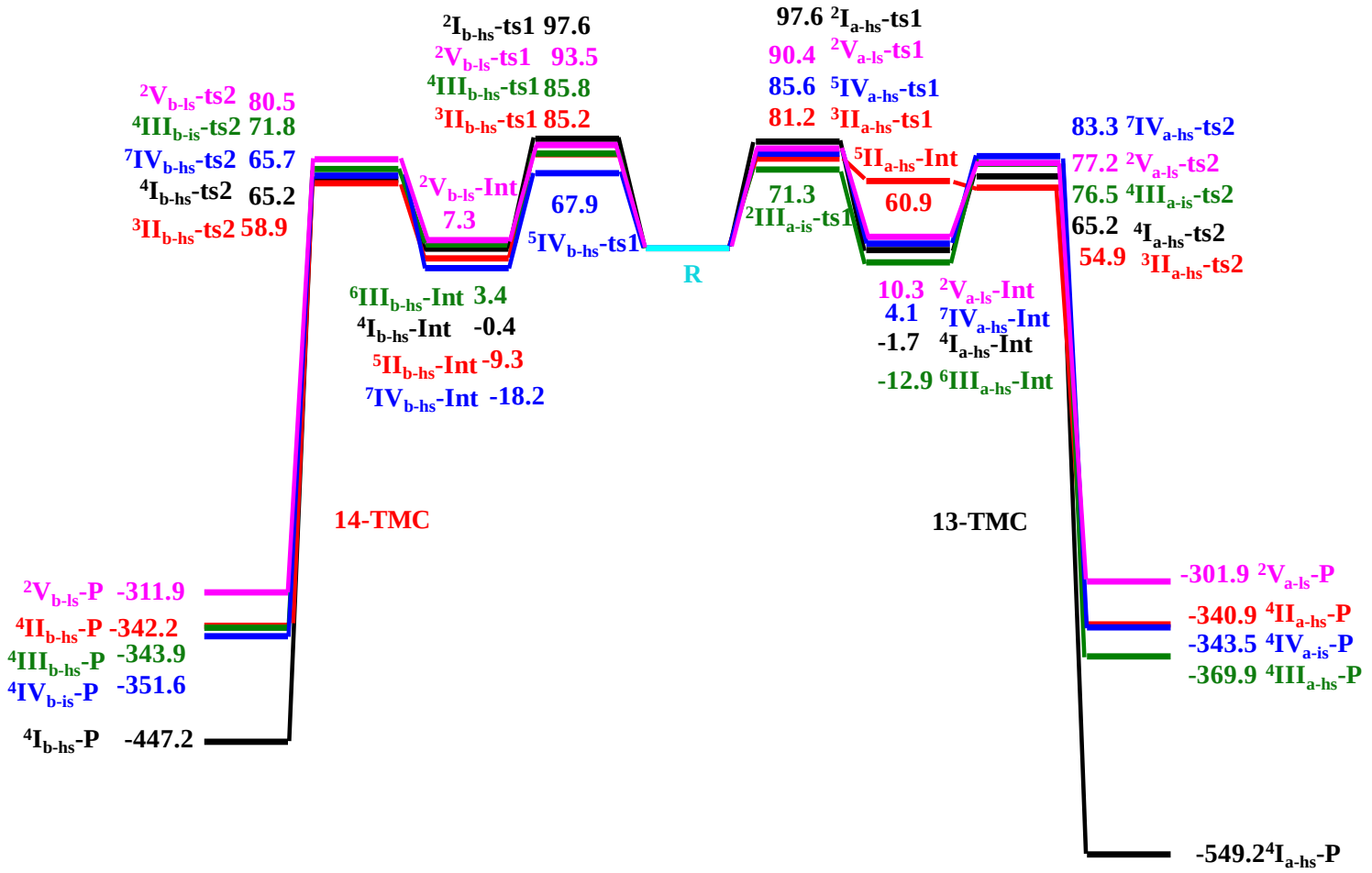

Figure 5.18. B3LYP-D2-computed potential energy surface (ΔG in kJmol^{-1}) for C-H activation by species I (black), II(red), III(olive), IV(blue), V(magenta) species with13-TMC and 14-TMC.

Our computed data unequivocally reveal that M-$O_2^{\bullet-}$ are extremely reactive and activate the C-H bond in 1,4-cyclohexadiene with lower kinetic barrier heights. The energy barrier trend reflected that 13-TMC ligated metal-superoxo species are more reactive towards C-H activation than the corresponding 14-TMC except by iron-superoxo species (see Figure 5.18). Computed spin density at C1 of the transition state of I_a/I_b, II_a/II_b, III_a/III_b, IV_a/IV_b, and V_a/V_b species is -0.283/-0.272, -0.301/-0.322, -0.324/-0.320, -0.300/-0.294/, 0.322/0.323 indicate that the C-H activation occurs via proton-coupled electron transfer mechanism which is also shown in earlier reports.[56,91] The computed bond angles ∠N1-M-N3 and ∠N2-M-N4 of I_a/I_b, II_a/II_b, III_a/III_b, IV_a/IV_b, and V_a/V_b species also show more contraction with 13-TMC species than the 14-TMC (see Table AX 5.1 and 5.2 of appendix) which in turn push the metal out of the plane (see Figure 5.19) and hence increase the reactivity of electrophilic reaction. The computed parameters of O---O bond during the transition state are observed 1.438/1.439, 1.447/1.451, 1.426/1.423, 1.420/1.420, 1.443/1.443 Å, and these parameters lead towards the further step indicates the higher reactivity with species 13-TMC. Space-filling of metal-superoxo also clearly shows slightly more steric hindrance at distal oxygen towards hydrogen atom retard the reactivity (see Figure 5.2). Our computed imaginary frequency of the first transition state of species a/b is found to be 1087.7/979.0, 1509.0/835.6, 1448.9/1425.6, 1175.9/1119.9, and 1569.5/1533.1 cm^{-1}, respectively, also indicate that the higher imaginary frequency can show a large tunneling contribution and hence suggest the higher C-H bond reactivity. Our energy barriers and structural correlations suggest the higher reactivity with 13-TMC ligated complexes towards C-H bond activation than the 14-TMC except for iron species.

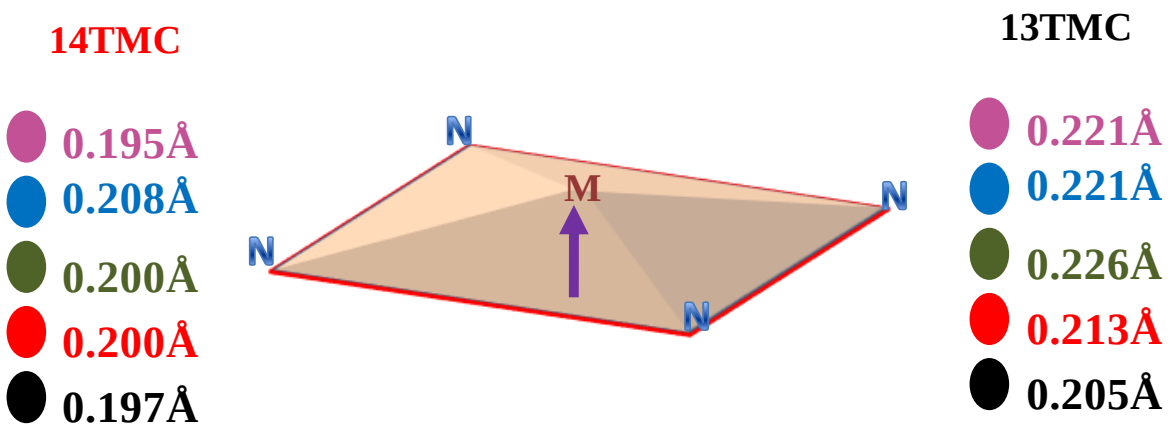

Figure 5.19. Computed displacement in the position of metal along the Z-axis.

5.4 Conclusions

Here, we have studied the electronic structures of metal-superoxo species (vanadium, chromium, manganese, iron, and cobalt) with two different 13/14-TMC ligands in detail. There are two possible isomers (A and B), by our calculations, it is found that isomer A is more stable than isomer B, which is also supported by the space-filling model showing the more steric repulsion in isomer B than the isomer A. Our DFT studies also shed light on C-H activation by metal-superoxo species. The ring size of TMC rules the oxidizing power of metal-superoxo species. This is the first computational study on the effect of ring size and metal ion on the electronic structure and catalytic reactivity of metal-superoxo species towards C-H bond activation. Here, we have explored the effect of ring size on the electronic structures and reactivity of these species towards C-H bond activation. From DFT calculations, it is found that 13-TMC ligated metal-superoxo species are more reactive than 14-TMC rings except for iron-superoxo species. C-H activation barrier is small with 13-TMC, and due to smaller ring size metal displaced out of plane along the z-axis compare to the 14-TMC ligand. It is found that iron-superoxo is most reactive, and the vanadium-superoxo species is least reactive. The reactivity pattern for the superoxo is found Fe (14-

TMC) > Mn (13-TMC) > Cr (13-TMC) > Cr (14-TMC) > Fe (13-TMC) > Mn (14-TMC) > Co (13-TMC) > Co (14-TMC) > V (13-TMC) > V (14-TMC).

To this end, our calculations show that the ring size of the TMC ligand plays an important role to control reactivity. By tuning the ring size one can alter the reactivity of metal-superoxo species towards organic substrates.

5.5 References

(1) Nam, W. *Acc. Chem. Res*. **2007**, *40*, 465-634.

(2) Nam, W.; Lee, Y.-M.; Fukuzumi, S. *Acc. Chem. Res.* **2014**, *47*, 1146-1154.

(3) Fukuzumi, S.; Ohkubo, K.; Lee, Y.-M.; Nam, W. *Chem. -Eur. J.* **2015**, *21*, 17548-17559.

(4) Wu, A. J.; Penner-Hahn, J. E.; Pecoraro, V. L. *Chem. Rev.* **2004**, *104*, 903-938.

(5) Yachandra, V. K.; Sauer, K.; Klein, M. P. *Chem. Rev.* **1996**, *96*, 2927-2950.

(6) Tommos, C. G.; Babcock, T. *Acc. Chem. Res.* **1998**, *31*, 18-25.

(7) Tang, X. S.; Randall, D. W.; Force, D. A.; Diner, B. A.; Britt, R. D. *J. Am. Chem. Soc.* **1996**, *118*, 7638-7639.

(8) Gilchrist, M. L., Jr.; Ball, J. A.; Randall, D. W.; Britt, R. D. *Proc. Natl. Acad. Sci. USA.* **1995**, *92*, 9545-9549.

(9) Meunier, B. Ed. Biomimetic Oxidations Catalyzed by Transition metal Complexes; Imperial College Press: London, **1999**.

(10) Wertz, D. L.; Valentine, J. S. *Struct. Bonding (Berlin)* **2000**, *97*, 37-60.

(11) Kovaleva, E. G.; Neibergall, M. B.; Chakrabarty, S.; Lipscomb, J. D. *Acc. Chem. Res.* **2007**, *40*, 475-483.

(12) Wolfe, M. D.; Lipscomb, J. D. *J. Biol. Chem.* **2003**, *278*, 829-835.

(13) Bassan, A.; Blomberg, M. R. A.; Siegbahn, P. E. M. *J. Biol. Inorg. Chem.* **2004**, *9*, 439-452.

(14) Tarasev, M. D.; Ballou, P. *Biochemistry* **2005**, *44*, 6197-6207.

(15) Kim, D.; Cho, J.; Lee, Y.-M.; Sarangi, R.; Nam, W. *Chem. -Eur. J.* **2013**, *19*, 14112-14118.

(16) Cho, J.; Sarangi, R.; Nam, W. *Acc. Chem. Res.* **2012**, *45*, 1321-1330.

(17) Cho, J.; Sarangi, R.; Kang, H. Y.; Lee, J. Y.; Kubo, M.; Ogura, T.; Solomon, E. I.; Nam, W. *J. Am. Chem. Soc.* **2010**, *132*, 16977-16986.

(18) Cho, J.; Kang, H. Y.; Liu, L. V.; Sarangi, R.; Solomon, E. I.; Nam, W. *Chem. Sci.* **2013**, *4*, 1502-1508.

(19) Yokoyama, A.; Han, J. E.; Cho, J.; Kubo, M.; Ogura, T.; Siegler, M. A.; Karlin, K. D.; Nam, W. *J. Am. Chem. Soc.* **2012**, *134*, 15269-15272.

(20) Mandon, D.; Jaafar, H.; Thibon, A. *New J. Chem.* **2011**, *35*, 1986-2000.

(21) Sarangi, R.; Cho, J.; Nam, W.; Solomon, E. I. *Inorg. Chem.* **2011**, *50*, 614-620.

(22) Cho, J.; Woo, J.; Nam, W. *J. Am. Chem. Soc.* **2010**, *132*, 5958-5959.

(23) Cho, J.; Woo, J.; Nam, W. *J. Am. Chem. Soc.* **2012**, *134*, 11112-11115.

(24) Cho, K.-B.; Kang, H.; Woo, J.; Park, Y. J.; Seo, M. S.; Cho, J.; Nam, W. *Inorg. Chem.* **2014**, *53*, 645-652.

(25) Makhlynets, O. V.; Das, P.; Taktak, S.; Flook, M.; Mas-Balleste, R.; Rybak-Akimova, E. V.; Que, L., Jr. *Chem. -Eur. J.* **2009**, *15*, 13171-13180.

(26) Makhlynets, O. V.; Rybak-Akimova, E. V. *Chem. -Eur. J.* **2010**, *16*, 13995-14006.

(27) Chen, K.; Costas, M.; Que, L., Jr. *Dalton Trans.* **2002**, *5*, 672-679.

(28) Maiti, D.; Lee, D.-H.; Gaoutchenova, K.; Wurtele, C.; Holthausen, M. C.; Sarjeant, A. A. N.; Sundermeyer, J.; Schindler, S.; Karlin, K. D. *Angew. Chem., Int. Ed.* **2008**, *47*, 82-85.

(29) Maiti, D.; Fry, H. C.; Woertink, J. S.; Vance, M. A.; Solomon, E. I.; Karlin, K. D. *J. Am. Chem. Soc.* **2007**, *129*, 264-265.

(30) Shetti, V. N.; Rani, M. J.; Srinivas, D.; Ratnasamy, P. *J. Phys. Chem.* **2006**, *110*, 677-679.

(31) Engelmann, X.; Monte-Perez, I.; Ray, K. *Angew. Chem., Int. Ed.* **2016**, *55*, 7632-7649.

(32) Hong, S.; Lee, Y.-M.; Ray, K.; Nam, W. *Coord. Chem. Rev.* **2017**, *334*, 25-42.

(33) Neu, H. M.; Baglia, R. A.; Goldberg, D. P. *Acc. Chem. Res.* **2015**, *48*, 2754-2764.

(34) Puri, M.; Que, L., Jr. *Acc. Chem. Res.* **2015**, *48*, 2443-2452.

(35) Suga, M.; Akita, F.; Hirata, K.; Ueno, G.; Murakami, H.; Nakajima, Y.; Shimizu, T.; Yamashita, K.; Yamamoto, M.; Ago, H.; Shen, J.-R. *Nature* **2015**, *517*, 99-103.

(36) Shaik, S.; Kumar, D.; de Visser, S. P.; Altun, A.; Thiel, W. *Chem. Rev.* **2005**, *105*, 2279-2328.

(37) Jackson, T. A.; Rohde, J.-U.; Seo, M. S.; Sastri, C. V.; DeHont, R.; Stubna, A.; Ohta, T.; Kitagawa, T.; Munck, E.; Nam, W.; Que, L., Jr. *J. Am. Chem. Soc*. **2008**, *130*, 12394-12407.

(38) Chiang, C.-W.; Kleespies, S. T.; Stout, H. D.; Meier, K. K.; Li, P.-Y; Bominaar, E. L.; Que, L., Jr.; Mgnck, E.; Lee, W.-Z. *J. Am Chem. Soc.* **2014**, *136*, 10846-10849.

(39) Lewis, E. A.; Tolman, W. B. *Chem. Rev.* **2004**, *104*, 1047-1076.

(40) Peterson, R. L.; Himes, R. A.; Kotani, H.; Suenobu, T.; Tian, L.; Siegler, M. A.; Solomon, E. I.; Fukuzumi, S.; Karlin, K. D. *J. Am. Chem. Soc.* **2011**, *133*, 1702-1705

(41) Cao, R.; Saracini, C.; Ginsbach, J. W.; Kieber-Emmons, M. T.; Siegler, M. A.; Solomon, E. I.; Fukuzumi, S.; Karlin, K. D. *J. Am. Chem. Soc.* **2016**, *138*, 7055-7066.

(42) Kunishita, A.; Kubo, M.; Sugimoto, H.; Ogura, T.; Sato, K.; Takui, T.; Itoh, S. *J. Am. Chem. Soc.* **2009**, *131*, 2788-2789.

(43) Corcos, A. R.; Villanueva, O.; Walroth, R. C.; Sharma, S. K.; Bacsa, J.; Lancaster, K. M.; MacBeth, C. E.; Berry, J. F. *J. Am. Chem. Soc.* **2016**, *138*, 1796-1799.

(44) Devi, T.; Lee, Y.-M.; Jung, J.; Sankaralingam, M.; Nam, W.; Fukuzumi S. *Angew. Chem., Int. Ed.* **2017**, *56*, 3510-3515.

(45) Solomon, E. I.; Brunold, T. C.; Davis, M. I.; Kemsley, J. N.; Lee, S.-K.; Lehnert, N.; Neese, F.; Skulan, A. J.; Yang, Y.-S.; Zhou, J. *Chem. Rev.* **2000**, *100*, 235-349.

(46) Costas, M.; Mehn, M. P; Jensen, M. P.; Que, L., Jr. *Chem. Rev.* **2004**, *104*, 939-986.

(47) Mirica, L. M.; Ottenwaelder, X.; Stack, T. D. P. *Chem. Rev.* **2004**, *104*, 1013-1045.

(48) Cramer, C. J.; Tolman, W. B. *Acc. Chem. Res.* **2007**, *40*, 601-608.

(49) Suzuki, M. *Acc. Chem. Res.* **2007**, *40*, 609-617.

(50) Himes, R. A.; Karlin, K. D. *Curr. Opin. Chem. Biol.* **2009**, *13*, 119-131.

(51) Yao, S.; Driess, M. *Acc. Chem. Res.* **2012**, *44*, 276-287.

(52) Cramer, C. J.; Tolman, W. B.; Theopold, K. H.; Rheingold, A. L. *Proc. Natl. Acad. Sci. U.S.A.* **2003**, *100*, 3635-3640.

(53) Yano, J.; Yachandra, V. *Chem. Rev.* **2014**, *114*, 4175-4205.

(54) Ogata, H.; Lubitz, W. *Angew. Chem., Int. Ed.* **2014**, *53*, 13007-13008.

(55) Cox, N.; Pantazis, D. A.; Neese, F.; Lubitz, W. *Acc. Chem. Res.* **2013**, *46*, 1588-1596.

(56) Young, K. J.; Brennan, B. J.; Tagore, R.; Brudvig, G. W. *Acc. Chem. Res.* **2015**, *48*, 567-574.

(57) Concepcion, J. J.; Jurss, J. W.; Brennaman, M. K.; Hoertz, P. G.; Patrocinio, A. O. T.; Iha, N. Y. M.; Templeton, J. L.; Meyer, T. J. *Acc. Chem. Res.* **2009**, *42*, 1954-1965.

(58) Lee, Y.-M.; Hong, S.; Morimoto, Y.; Shin, W.; Fukuzumi, S.; Nam, W. *J. Am. Chem. Soc.* **2010**, *132*, 10668-10670.

(59) Li, H.; Li, F.; Zhang, B.; Zhou, X.; Yu, F.; Sun, L. *J. Am. Chem. Soc.* **2015**, *137*, 4332-4335.

(60) Du, P.; Eisenberg, R. *Energy Environ. Sci.* **2012**, *5*, 6012-6021.

(61) Joya, K. S.; Joya, Y. F.; Ocakoglu, K.; de Krol, R. V. *Angew. Chem., Int. Ed.* **2013**, *52*, 10426-10437.

(62) Karkas, M. D.; Verho, O.; Johnston, E. V.; Akermark, B. *Chem. Rev.* **2014**, *114*, 11863-12001.

(63) Kovaleva, E. G.; Lipscomb, J. D. *Science* **2007**, *316*, 453-457.

(64) Denisov, I. G.; Makris, T. M.; Sligar, S. G.; Schlichting, I. *Chem. Rev.* **2005**, *105*, 2253-2278.

(65) Shaik, S.; Hirao, H.; Kumar, D. *Acc. Chem. Res.* **2007**, *40*, 532-542.

(66) Rohde, J.-U.; In, J.-H.; Lim, M. H.; Brennessel, W. W.; Bukowski, M. R.; Stubna, A.; Munck, E.; Nam, W.; Que, L., Jr. *Science* **2003**, *299*, 1037-1039.

(67) Klinker, E. J.; Kaizer, J.; Brennessel, W. W.; Woodrum, N. L.; Cramer, C. J.; Que, L., Jr. *Angew. Chem., Int. Ed.* **2005**, *44*, 3690-3694.

(68) Que, L., Jr.; Tolman, W. B. *Nature* **2008**, *455*, 333-340.

(69) Chen, P.; Solomon, E. I. *Proc. Natl. Acad. Sci. USA* **2004**, *101*, 13105-13110.

(70) MacBeth, C. E.; Golombek, A. P.; Young, V. G., Jr.; Yang, C.; Kuczera, K.; Hendrich, M. P.; Borovik, A. S. *Science* **2000**, *289*, 938-941.

(71) Ansari, A.; Jayapal, P.; Rajaraman, G. *Angew. Chem., Int. Ed.* **2015**, *127*, 574-578.

(72) Prigge, S. T.; Eipper, B. A.; Mains, R. E.; Amze, L. M. *Science* **2004**, *304*, 864-886.

(73) Chen, P.; Solomon, E. I. *Proc. Natl. Acad. Sci. USA* **2004**, *101*, 13105-13110.

(74) Cora, E. M.; Golombek, A. P.; Young, V. G., Jr., Yang, C.; Kuczera, K.; Hendrich, M. P.; Borovik, A. S. *Science* **2000**, *289*, 938-941.

(75) Bathelt, C. M.; Ridder, L.; Mulholland, A. J.; Harvey, J. N. *J. Am. Chem. Soc.* **2003**, *125*, 15004-1500.

(76) Bathelt, C. M.; Ridder, L.; Mulholland, A. J.; Harvey, J. N. *Org. Biomol. Chem.* **2004**, *2*, 2998-3005.

(77) Shetti, V. N.; Rani, M. J.; Srinivas, D.; Ratnasamy, P. *J. Phys. Chem. B* **2006**, *110*, 677-679.

(78) Hong, S.; So, H.; Yoon, H.; Cho, K.-B.; Lee, Y.-M.; Fukuzumi, S.; Nam, W. *Dalton Trans*. **2013**, *42*, 7842-7845.

(79) Cramer, S. A.; Jenkins, D. M. *J. Am. Chem. Soc.* **2011**, *133*, 19342-19345.

(80) Cho, J.; Woo, J.; Han, J. E.; Kubo, M.; T. Ogura, Nam, W. *Chem. Sci.* **2011**, *2*, 2057-2062.

(81) Frisch, M. J.; Trucks, G. W.; Schlegel, H. B.; Scuseria, G. E.; Robb, M. A.; Cheeseman, J. R.; Scalmani, G.; Barone, V.; Petersson, G. A.; Nakatsuji, H.; Li, X.; Caricato, M.; Marenich, A. V.; Bloino, J.; Janesko, B. G.; Gomperts, R.; Mennucci, B.; Hratchian, H. P.; Ortiz, J. V.; Izmaylov, A. F.; Sonnenberg, J. L.; Williams-Young, D.; Ding, F.; Lipparini, F.; Egidi, F.; Goings, J.; Peng, B.; Petrone, A.; Henderson, T.; Ranasinghe, D.; Zakrzewski, V. G.; Gao, J.; Rega, N.; Zheng, G.; Liang, W.; Hada, M.; Ehara, M.; Toyota, K.; Fukuda, R.; Hasegawa, J.; Ishida, M.; Nakajima, T.; Honda, Y.; Kitao, O.; Nakai, H.; Vreven, T.; Throssell, K.; Montgomery, J. A., Jr.; Peralta, J. E.; Ogliaro, F.; Bearpark, M. J.; Heyd, J. J.; Brothers, E. N.; Kudin, K. N.; Staroverov, V. N.; Keith, T. A.; Kobayashi, R.; Normand, J.; Raghavachari, K. A.; Rendell, P.; Burant, J. C.; Iyengar, S. S.; Tomasi, J.; Martin, C. M.; Millam, J. M.; Klene, M.; Adamo, C.; Cammi, R.; Ochterski, J. W.; Morokuma, R. L. K. O.; Farkas, F. J. B.; Fox, D. J. Gaussian, Inc., Wallingford CT, 2016.

(82) Becke, A. D. *J. Chem. Phys*. **1993**, *98*, 5648-5652.

(83) Lee, C.; Yang, W.; Parr, R. G. *Phys. Rev. B: Condens. Matter Mater. Phys*. **1988**, *37*, 785-789.

(84) Grimme, S. *J. Comput. Chem.* **2006**, *27*, 1787-1799.

(85) Chai, J. D.; Head-Gordon, M. *Phys. Chem. Chem. Phys.* **2008**, *10*, 6615-6620.

(86) Zhao, Y.; Truhlar, D. G. *Theor. Chem. Acc.* **2008**, *120*, 215-241.

(87) Tao, J. M.; Perdew, J. P.; Staroverov V. N.; Scuseria, G. E. *Phys. Rev. Lett.* **2003**, *91*, 146401-146404.

(88) Møller, C.; Plesset, M. S. *Phys. Rev.* **1934**, *46*, 618-622.

(89) Ansari, A.; Kaushik, A.; Rajaraman, G. *J. Am. Chem. Soc.* **2013**, *135*, 4235-4249.

(90) Ansari, A.; Ansari, M.; Singha, A.; Rajaraman, G. *Chem. -Eur. J.* **2017**, *23*, 10110-10125.

(91) Monika, Ansari, A. *New J. Chem.* **2020**, *44*, 19103-19112.

(92) Dunning, T. H., Jr.; Hay, P. J. *In Modern Theoretical Chemistry* (Ed: Schaefer, H. F.), Plenum, New York, 1976; Vol. 3.

(93) Hay, P. J.; Wadt, W. R. *J. Chem. Phys.* **1985**, *82*, 270-283.

(94) Hay, P. J.; Wadt, W. R. *J. Chem. Phys.* **1985**, *82*, 299-310.

(95) Wadt, W. R.; Hay, P. J. *J. Chem. Phys.* **1985**, *82*, 284-298.

(96) Kumar, R.; Ansari, A.; Rajaraman, G. *Chem. -Eur. J.* **2018**, *24*, 6660-6860.

(97) Schaefer, A.; Horn, H.; Ahlrichs, R. *J. Chem. Phys.* **1992**, *97*, 2571-2577.

(98) Schaefer, C.; Huber, C.; Ahlrichs, R. *Chem. Phys.* **1994**, *100*, 5829-5835.

(99) Noodleman, L. *J. Chem. Phys.* **1981**, *74*, 5737-5743.

(100) Noodleman, L.; Davidson, E. R. *Chem. Phys*. **1986**, *109*, 131-143.

(101) Mubarak, M. Q. E.; de Visser, S. P. *Dalton Trans*. **2019**, *48*, 16899-16910.

(102) Sessler, J. L.; Tomat, E.; Lynch, V. M. *Chem. Commun.* **2006**, *42*, 4486-4488.

(103) Kandrashkin, Y. E.; Asano, M. S.; van der Est., A. *J. Phys. Chem. A* **2006**, *110*, 9607-9616.

(104) Ghosh, S. K.; Patra, R.; Rath, S. P. *Inorg. Chem.* **2008**, *47*, 9848-9856.

(105) Yamashita, K.-I.; Tazawa, S.; Sugiura, K.-I. *Inorganica Chim. Acta* **2016**, *439*, 173-177.

(106) Chen, W.; Suenobu, T.; Fukuzumi, S. *Chem. -Asian J.* **2011**, *6*, 1416-1422.

(107) Doukkali, A.; Saoiabi, A.; Ferhat, M.; Mugnier, Y.; Vallat, A.; Guilard, R. *New J. Chem.* **2006**, *30*, 997-1009.

(108) Kumar, R.; Chaudhary, N.; Sankar, M.; Maurya, M. R. *Dalton Trans*. **2015**, *44*, 17720-17729.

(109) Dar, T. A.; Uprety, B.; Sankar M.; Maurya, M. R. *Green Chem.* **2019**, *21*, 1757-1768.

(110) Wang, B.; Lee, Y.-M.; Tcho, W.-Y.; Tussupbayev, S.; Kim, S.-T.; Kim, Y.; Seo, M. S.; Cho, K.-B.; Dede, Y.; Keegan, B. C.; Ogura, T.; Kim, S. H.; Ohta, T.; Baik, M.-H.; Ray, K.; Shearer, J.; Nam, W. *Nat. Commun*. **2017**, *24*, 14839-14849.

Chapter 6

Formation of High Valent Metal-oxo Species (Oxo Wall)

6.1 Introduction

High valent metal-oxo species are reactive key intermediates in many processes; such as catalytic oxidation of the organic substrate, water by many enzymes, and biomimetic compounds.[1-8] These species such as iron/manganese-oxo also act as an oxidizing intermediate in many biological oxidation reactions such as respiration, metabolism, and photosynthesis.[9-21] A terminal metal-oxo is often invoked as the primary product of O-O bond cleavage of the ORR (oxygen reducatse reaction) and conversely, O-O bond formation of the OER (oxygen evolving reaction) is often proposed to proceed from a high valent metal-oxo species.[22-23] Manganese-oxo species are involved in the oxygen-evolving complex (OEC) in the photosystem-II, catalase, and manganese superoxide dismutase.[24] Heme iron-oxos are found in P450, cytochrome c oxidase, and the terminal enzyme in respiration. High valent iron(IV)-oxo complexes are the oxidizing agent in the catalytic cycle of tyrosine hydroxylase, and aliphatic halogenase SyrB2.[12] Therefore, the chemistry of high valent terminal metal-oxo species in early transition metals is well known. Early, transition metal forms stable high valent metal-oxo complexes because of the strong π-electron donor nature of terminal oxo ligand and metal have empty *d* orbitals due to which π bond formation takes place by *dπ-pπ* bonding.[25-27] Many terminal metal-oxo species of, chromium,[28] manganese,[29-33,] and iron[34-39] have been synthesized, isolated, and characterized successfully. These species involve in many reactions such as C-H bond activation, and oxygen atom transfer reactions of metalloenzymes, which help to develope oxidizing catalysts.[40-41]

However, synthesis and characterization of high valent terminal metal-oxo species of late transition metals such as cobalt, nickel, and copper remained a long-standing challenge due to an existing strong electronic repulsion between *d* orbital of metals and *p* orbital of oxo due to high *d*-electron count. In oxo species, bond order also decreases due to occupancy of M-O π antibonding orbital due to which late transition metal-oxo species are not stable.[26] Terminal

metal-oxo species are formed by O-O bond cleavage of the ORR (oxygen reductase reaction).[42-48] It may occur either by homolytic or heterolytic cleavage of O-O bond depends upon the electronic environment, i.e. electron-rich environment favors homolytic cleavage, while an electron-deficient environment favors heterolytic cleavage. The formation of terminal oxo is also related to the concept of Oxo wall which is given by Gray and Winkler.[49-50] According to Gray and Winkler, "terminal metal-oxo is not supported by the transition metals beyond eight group metals in tetragonal geometry".

Cr	Mn	Fe	Co	Ni	Cu
Mo	Tc	Ru	Ir	Pd	Ag
W	Re	Os	Rh	Pt	Au

Scheme 6.1. A representation of the "Oxo wall".

Although the metal-oxo species beyond group 8 can be stabilized by using the Lewis acid which can also stabilize the metal-oxo by combining with oxygen.[48]

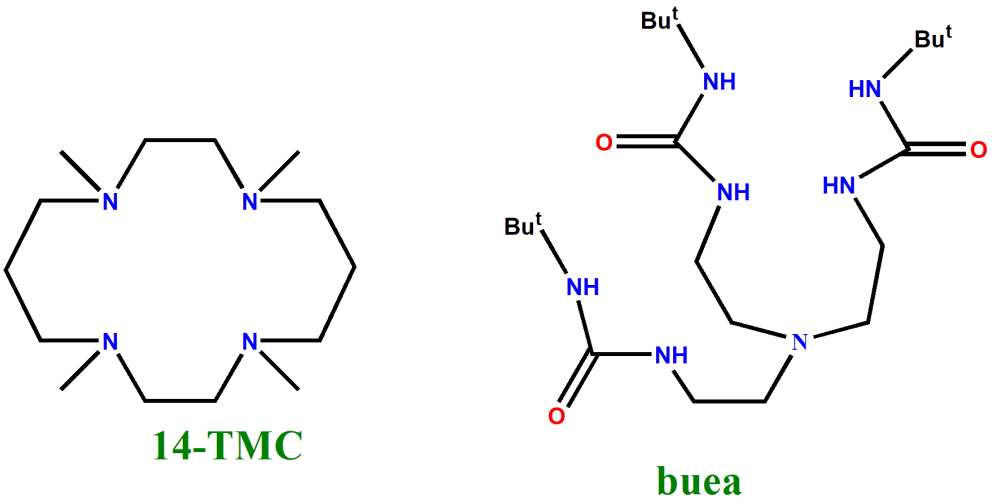

Scheme 6.2. 14-TMC and buea ligand.

Considering all above points, here first time we have undertaken the computational study based on computations of transition states to specifically address the following issues; to find out the reason behind the formation of Oxo wall, by computing and comparing electronic structures of metal hydroperoxo and metal-oxo of first transition series (Cr-Cu) with two different ligands 14-TMC[49] and buea,[50-53] because of the presence of many metal-TMC/buea species, and TMC ligand with octahedral geometry while the buea have trigonal bipyramidal geometry and forms cavity like oxo species. Computing barrier height of O---O bond cleavage and the energetics of the metal-oxo species, followed by a comparative study among them.

6.2 Computational Details

Gaussian16 program is used for all the calculations.[54] Fragment approach is present in Gaussian16, used for all the spin state calculations. Based on previous work, it is predicted that B3LYP,[55-56] B3LYP-D2,[57] wB97XD[58] are advocated to find the correct spin as the ground state of reactant, intermediate, and product. B3LYP-D2 is most appropriate among these.[59-62] So here, we have restricted our calculations only to B3LYP-D2 functional, incorporating dispersion correction of Grimme *et al.*[63-65] The basis set LACVP comprises LanL2DZ-Los Alamos effective core potential for the metals (V, Cr, Mn, Fe, Co, Ni, and Cu)[66-67], and 6-31G/6-31G* basis set is for other atoms (hydrogen, carbon, nitrogen, oxygen, and chlorine) has been used.[68] TZVP basis set is used for all atoms on the optimized geometries for the single point energy calculation.[69-70] Wiberg bond indices are computed by using the natural atomic orbital analysis (NBO). NBO and SNO (spin natural orbital) are performed using G16. Solvation energies are computed by the PCM model using acetonitrile (with TMC ligated species) and n,n-dimethyl amide (with buea ligated species) as a solvent. The transition state is verified by a single negative frequency, animating the corresponding

frequency, and visualized in Gauss View. DFT energies are quoted using B3LYP-D2 solvation including free-energy corrections at 298.15 K temperature. Common notation of $^{mult}MX_{spinstate}$-Y is used throughout, where mult denotes total multiplicity, M represents metal (I=Cr, II=Mn, III=Fe, IV=Co, V=Ni, VI= Cu), and X to ligand (A for the TMC-14, and B for buea), spin state denote the possible spin states and Y represents the transition state and intermediate.

6.3 Results and Discussion

Based on earlier theoretical and experimental studies,[59-61] we have proposed a mechanism for the generation of metal-oxo (such as M^{IV}-oxo and the M^{V}-oxo) from the metal hydroperoxo species is shown in Scheme 6.3. This mechanism is based on O---O bond cleavage, where homolytic cleavage gives the M^{IV}oxo species and the heterolytic cleavage gives M^{V}oxo species. Here, we have computed the structure of 3*d* transition metal hydroperoxo (chromium to copper) species, barrier heights of the O---O bond cleavage, structure, and energetic of the metal-oxo species. We have started calculations with species IA (Cr^{III}-OOH).

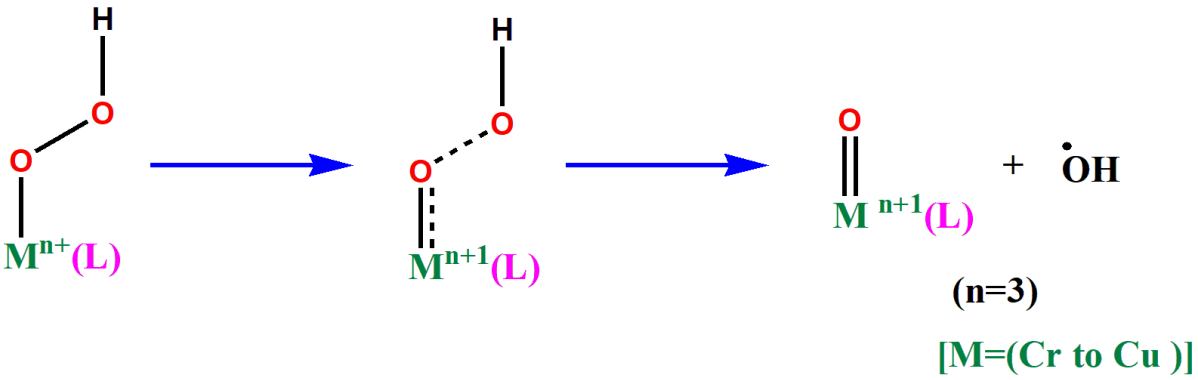

Scheme 6.3. Proposed mechanism for the formation of metal-oxo species.

6.3.1 Metal hydroperoxo species (chromium (IA), manganese (IIA), iron (IIIA), cobalt (IVA), nickel (VA), and copper (VIA))

We have optimized all possible spin states of species IA (Cr^{III}-OOH) and our results show that the $^{4}IA_{hs}$ is found as the ground state and $^{2}IA_{ls}$ is 157.0 kJ/mol higher in energy (see Figure 6.1).[60] Selected bond parameters are shown in Table AX 6.1 of appendix and spin density plots are shown in Table 6.1. Spin density plot and optimized structure of the ground state are shown in Figure 6.1 and Figure 6.2a.

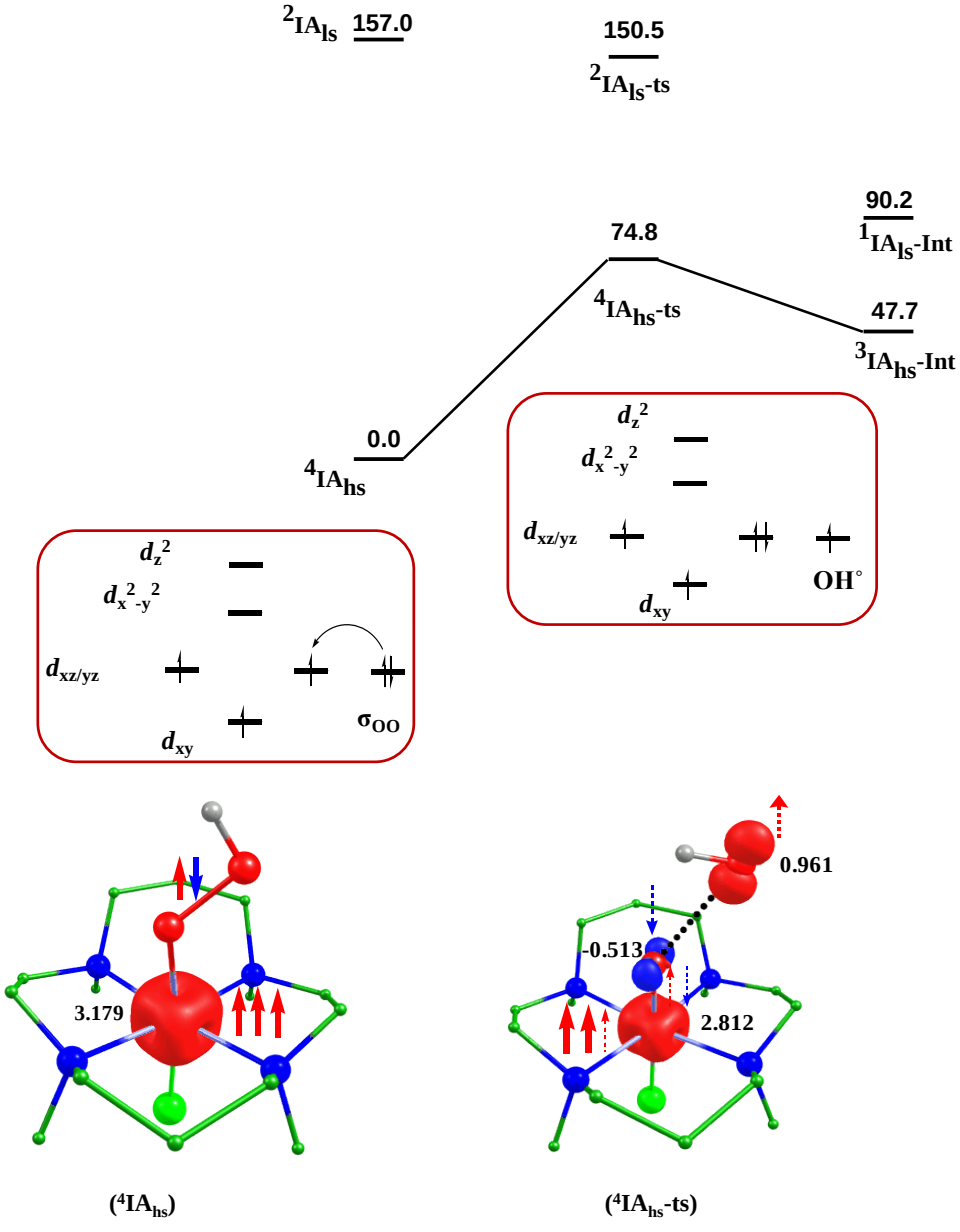

Figure 6.1. B3LYP-D2 computed energy for the O---O bond cleavage of IA species, alongwith schematic involvement of electron and spin density plots of ground state of reactant and transition state.

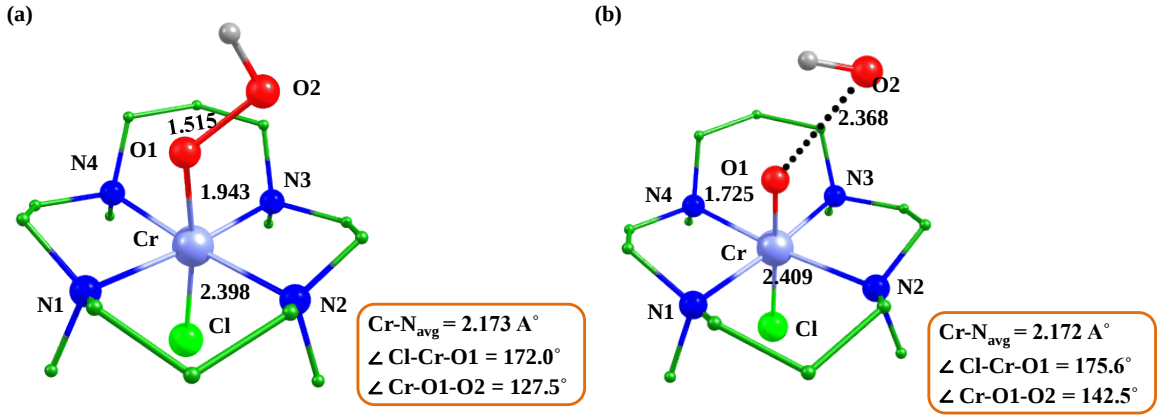

Figure 6.2. B3LYP-D2 optimized structure of ground state a) $^{4}IA_{hs}$, b) $^{4}IA_{hs}$-ts for the O---O bond cleavage of IA species.

Table 6.1. B3LYP-D2 computed selected spin density values of the 14-TMC species (reactants, transition states and products).

Spin state	Metal	O1	O2
[(14-TMC)(Cl)CrOOH, IA]$^{+}$ Species			
$^{4}IA_{hs}$	3.179	-0.001	0.040
$^{2}IA_{ls}$	1.126	-0.045	0.007
$^{4}IA_{hs}$-ts	2.812	-0.513	0.961
$^{2}IA_{ls}$-ts	0.697	-0.281	0.663
$^{3}IA_{hs}$-Int	2.784	-0.569	-
$^{1}IA_{ls}$-Int	0	0	-
[(14-TMC)(Cl)MnOOH]$^{+}$ Species			
$^{5}IIA_{hs}$	3.987	-0.010	0.042
$^{3}IIA_{is}$	2.098	0.042	0.023
$^{1}IIA_{ls}$	0.000	0.000	0.000
$^{5}IIA_{hs}$-ts	3.341	0.269	0.668
$^{3}IIA_{is}$-ts	2.493	0.272	-0.549
$^{4}IIA_{hs}$-Int	2.677	0.545	-
$^{2}IIA_{ls}$-Int	1.165	-0.061	-
[(14-TMC)(Cl)FeOOH]$^{+}$ Species			
$^{6}IIIA_{hs}$	3.980	0.277	0.051
$^{4}IIIA_{is}$	2.896	0.194	0.030

^{2}IIIA$_{ls}$	1.039	0.089	-0.000
^{6}IIIA$_{hs}$-ts	3.275	0.528	0.869
^{4}IIIA$_{is}$-ts	2.352	-0.151	0.0058
^{2}IIIA$_{ls}$-ts	1.309	0.575	-0.775
^{5}IIIA$_{hs}$-Int	3.081	0.632	-
^{3}IIIA$_{is}$-Int	1.313	0.793	-
^{1}IIIA$_{ls}$-Int	0	0	-
[(14-TMC)(Cl)CoOOH]$^{+}$ Species			
^{5}IVA$_{hs}$	2.776	0.437	0.083
^{3}IVA$_{is}$	1.829	0.173	0.013
^{1}IVA$_{ls}$	0.000	0.000	0.000
^{5}IVA$_{hs}$-ts	2.164	0.673	0.798
^{6}IVA$_{hs}$-Int	2.750	1.400	-
^{4}IVA$_{is}$-Int	1.855	0.884	-
^{2}IVA$_{ls}$-Int	-0.026	0.974	-
[(14-TMC)(Cl)NiOOH]$^{+}$ Species			
^{2}VA$_{ls}$	1.277	-0.099	-0.344
^{4}VA$_{hs}$-ts	0.936	0.928	0.853
^{5}VA$_{hs}$-Int	1.545	1.571	-
^{3}VA$_{is}$-Int	0.957	-1.156	-
[(14-TMC)(Cl)CuOOH]$^{+}$ Species			
^{3}VIA$_{hs}$	0.519	0.474	0.123
^{1}VIA$_{hs}$	0.000	0.000	0.000
^{3}VIA$_{hs}$-ts	0.030	1.231	0.796
^{4}VIA$_{hs}$-Int	0.534	1.362	-
^{2}VIA$_{ls}$-Int	-0.165	1.425	-

Computed eigenvalue plot of the ground state is shown in Figure 6.3. The electronic configuration at the metal is found to be $(d_{xy})^1$ $(d_{xz})^1$ $(d_{yz})^1$ $(d_{x^2-y^2})^0$ $(d_{z^2})^0$. Barrier height of O---O bond cleavage of species IA is computed to be 74.8 kJ/mol at high spin state (S=3/2; ^{4}IA$_{hs}$-ts), and 150.5 kJ/mol for low spin state (S=1/2; ^{2}IA$_{ls}$-ts; see Figure 6.1). The optimized structure and spin density plot of the ^{4}IA$_{hs}$ and ^{4}IA$_{hs}$-ts are shown in Figure 6.2. The computed Cr-O and Cr-N$_{avg}$ bond length decreases 1.943/1.725 Å, 2.173/2.172 Å, respectively, while O1-O2 and Cr-Cl bond length increases 1.515/2.368 Å, 2.398/2.409 Å

respectively, and these parameters confirm the transition state of O---O bond cleavage. Computed spin density during the O---O bond cleavage at chromium center ($^4IA_{hs}$-ts) decreases 3.179/2.812 and spin density at O1 and O2 is computed to be -0.513 and 0.961, respectively, (see Figure 6.1) indicates that O---O bond cleaves as homolytically fashion. During O---O bond cleavage, beta (β) electron (see Figure 6.1) is shifted from $^4IA_{hs}$ to $d_{xz/yz}$ of $^4IA_{hs}$-ts to form the π bond which is also supported by the bond angle of 142.5^0 (see Table AX 6.1 of appendix).[62] Bond Parameters and decreasing spin density at chromium center shows the formation of π-bond between the up spin of chromium and the down spin at O1 (see Table 6.1). Spin natural orbital (SNO) analysis shows the transfer of an electron to the metal *d* orbital (see Figure 6.4). This O---O bond cleavage is also supported by computed wiberg bond indices (see Table AX 6.2 of appendix). More, electron-electron (*d*-*d*) exchange interaction decreases electron-electron repulsion and stabilizes the transition state and this may be a reason for the lower barrier at a high spin state (see Figure 6.1).

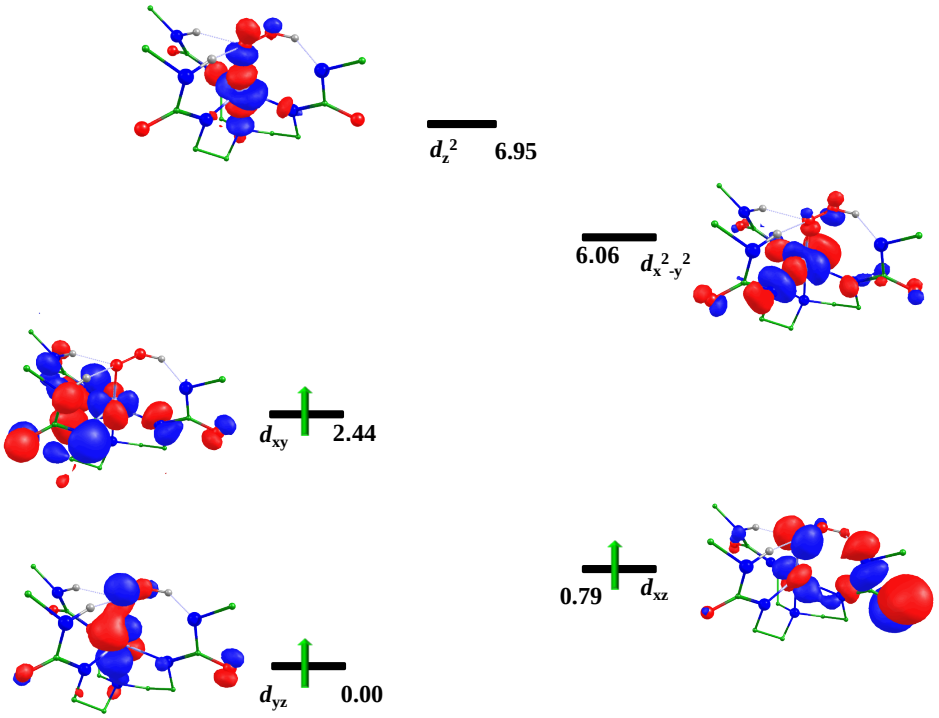

Figure 6.3 Computed eigenvalue plot incorporating energies computed for *d*-based orbitals for alpha corresponding to the ground state $^4IA_{hs}$ of the complex IA (energies are given in eV).

(a)

($^4IA_{hs}$)

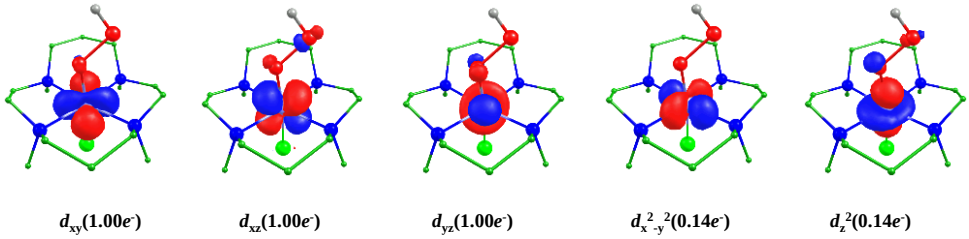

$d_{xy}(1.00e^-)$ $d_{xz}(1.00e^-)$ $d_{yz}(1.00e^-)$ $d_{x^2-y^2}(0.14e^-)$ $d_{z^2}(0.14e^-)$

($^4IA_{hs}$-ts)

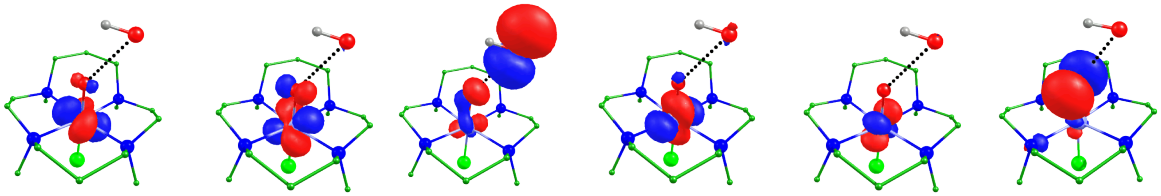

$d_{xy}(1.00e^-)$ $d_{xz}(1.00e^-)$ $d_{yz}(1.00e^-)$ $d_{x^2-y^2}(0.14e^-)$ $d_{z^2}(0.64e^-)$ $d_{yz}(-0.64e^-)$

(b)

$^5IIA_{hs}$

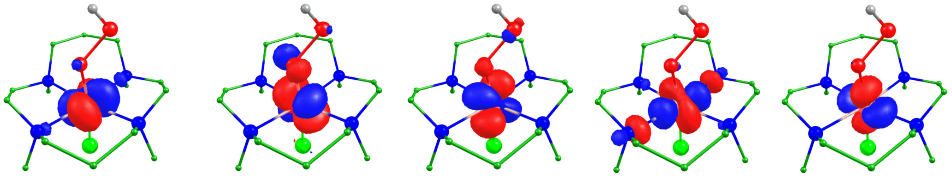

$d_{xy}(1.00e^-)$ $d_{xz}(1.00e^-)$ $d_{yz}(1.00e^-)$ $d_{x^2-y^2}(1.00e^-)$ $d_{z^2}(0.30e^-)$

$^5IIA_{hs}$-ts

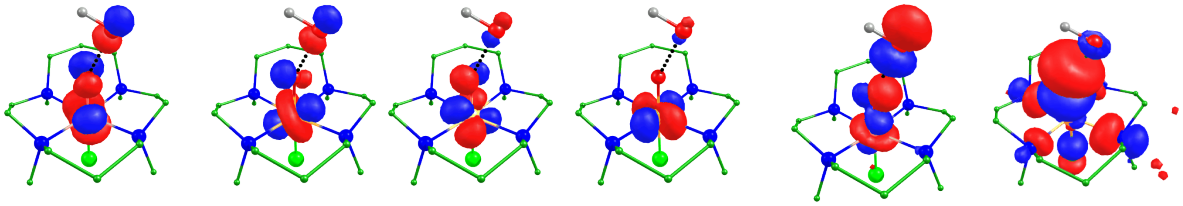

$d_{xy}(1.00e^-)$ $d_{xz}(1.00e^-)$ $d_{yz}(1.00e^-)$ $d_{x^2-y^2}(0.27e^-)$ $d_{z^2}(1.00e^-)$ $d_{xz}(-0.26e^-)$

(c)

$^6IIIA_{hs}$-ts

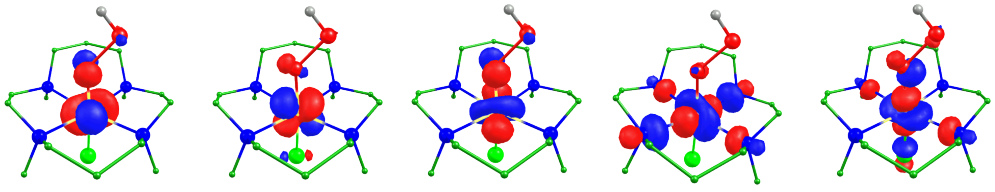

$d_{xy}(1.00e^-)$ $d_{xz}(1.00e^-)$ $d_{yz}(1.00e^-)$ $d_{x^2-y^2}(1.00e^-)$ $d_{z^2}(1.00e^-)$

$^6IIIA_{hs}$-ts

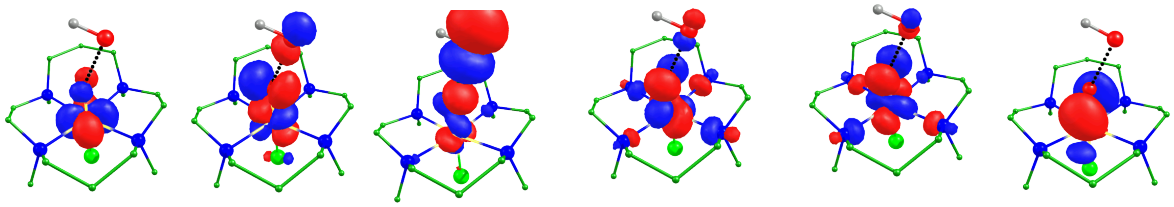

$d_{xy}(1.00e^-)$ $d_{xz}(1.00e^-)$ $d_{yz}(1.00e^-)$ $d_{x^2-y^2}(1.00e^-)$ $d_{z^2}(1.00e^-)$ $d_{xz}(-0.07e^-)$

Figure 6.4. Spin natural orbitals and their occupations (noted in parenthesis) of a) $^{4}IA_{hs}$, $^{4}IA_{hs}$-ts, b) $^{5}IIA_{hs}$, $^{5}IIA_{hs}$-ts, and c) $^{6}IIIA_{hs}$, and $^{6}IIIA_{hs}$-ts.

On moving right in the periodic table from chromium to manganese and iron, one and two extra electrons are added to *d* orbitals, respectively. Similar to chromium species, we have performed the same calculations on manganese and iron species and computed that high spin state (S=2, $^{5}IIA_{hs}$, and S=5/2, $^{6}IIIA_{hs}$) are the ground state in Mn, and Fe species, respectively. The computed spin energetic of other spin states is shown in Figure 6.5 and Figure 6.6.

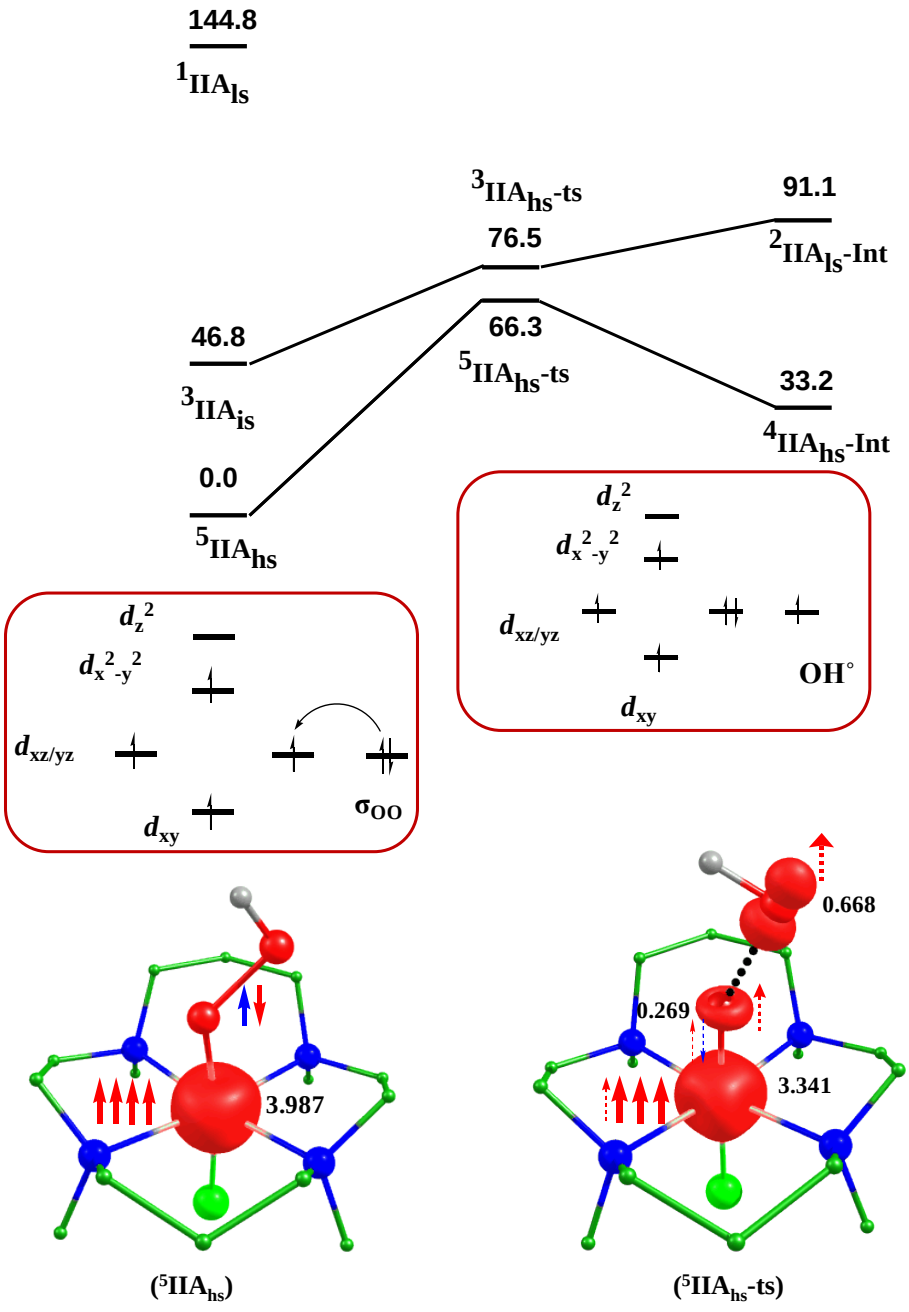

Figure 6.5 B3LYP-D2 computed energy for the O---O bond cleavage of IIA species. The computed barrier height is shown with respect to the reactant (IIA).

The optimized structures of ground state of IIA and IIIA are shown in Figure 6.7a,c. The electronic configuration at the manganese is found to be $(d_{xy})^1$ $(d_{xz})^1$ $(d_{yz})^1$ $(d_{x^2-y^2})^1$ $(d_{z^2})^0$ and at iron center it is found to be $(d_{xy})^1$ $(d_{xz})^1$ $(d_{yz})^1$ $(d_{x^2-y^2})^1$ $(d_{z^2})^1$ (see Figure 6.8). During O---O bond cleavage computed bond parameter shows that Mn-O, Mn-N_{avg}, and Fe-O, Fe-N_{avg} bond length decreased 1.916/1.748 Å, 2.236/2.156 Å, and 1.953/1.677 Å, 2.249/2.221 Å respectively, and O-O, Mn/Fe-Cl bond length increases 1.511/1.854 Å, 2.344/2.433 Å, and 1.495/2.052 Å, 2.378/2.322 Å with Mn and iron species respectively.

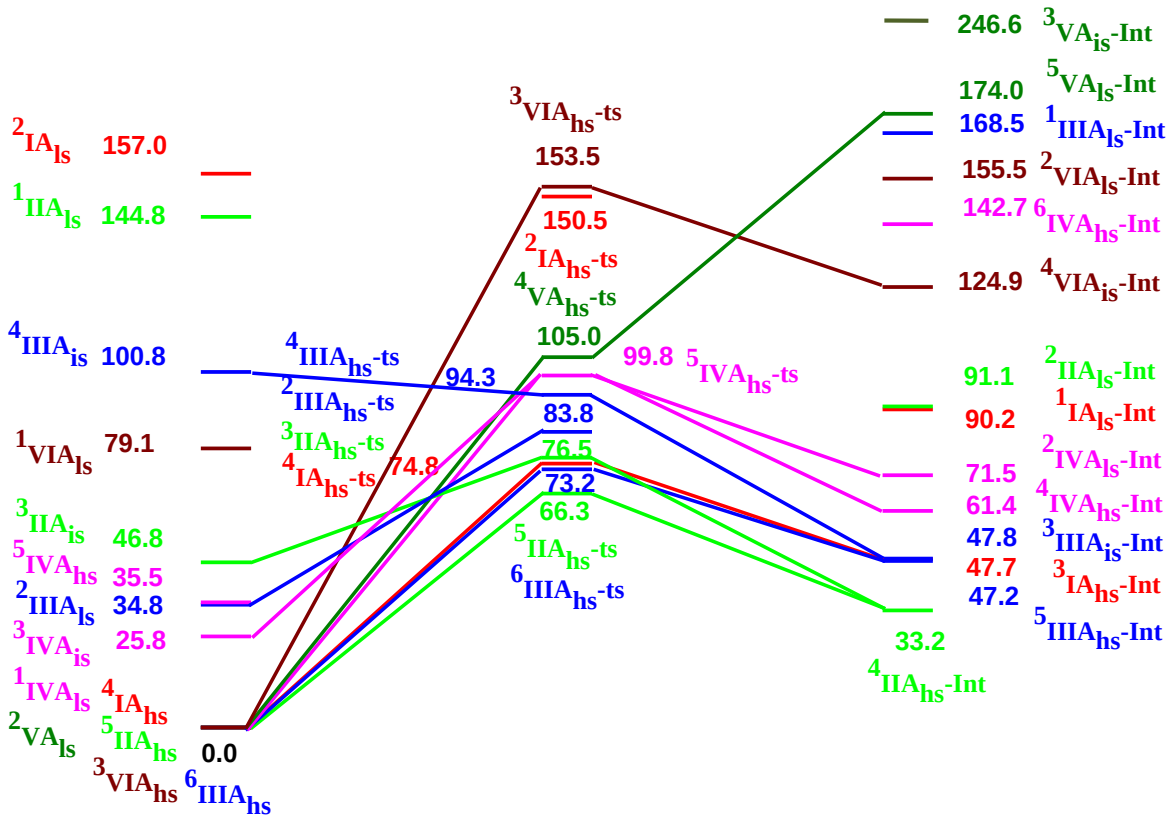

Figure 6.6. B3LYP-D2 computed energy surface for the formation of metal-oxo from metalhydroperoxo with buea ligand chromium (red), manganese (green), iron (blue), cobalt (magneta), nickel (olive), and copper (wine).

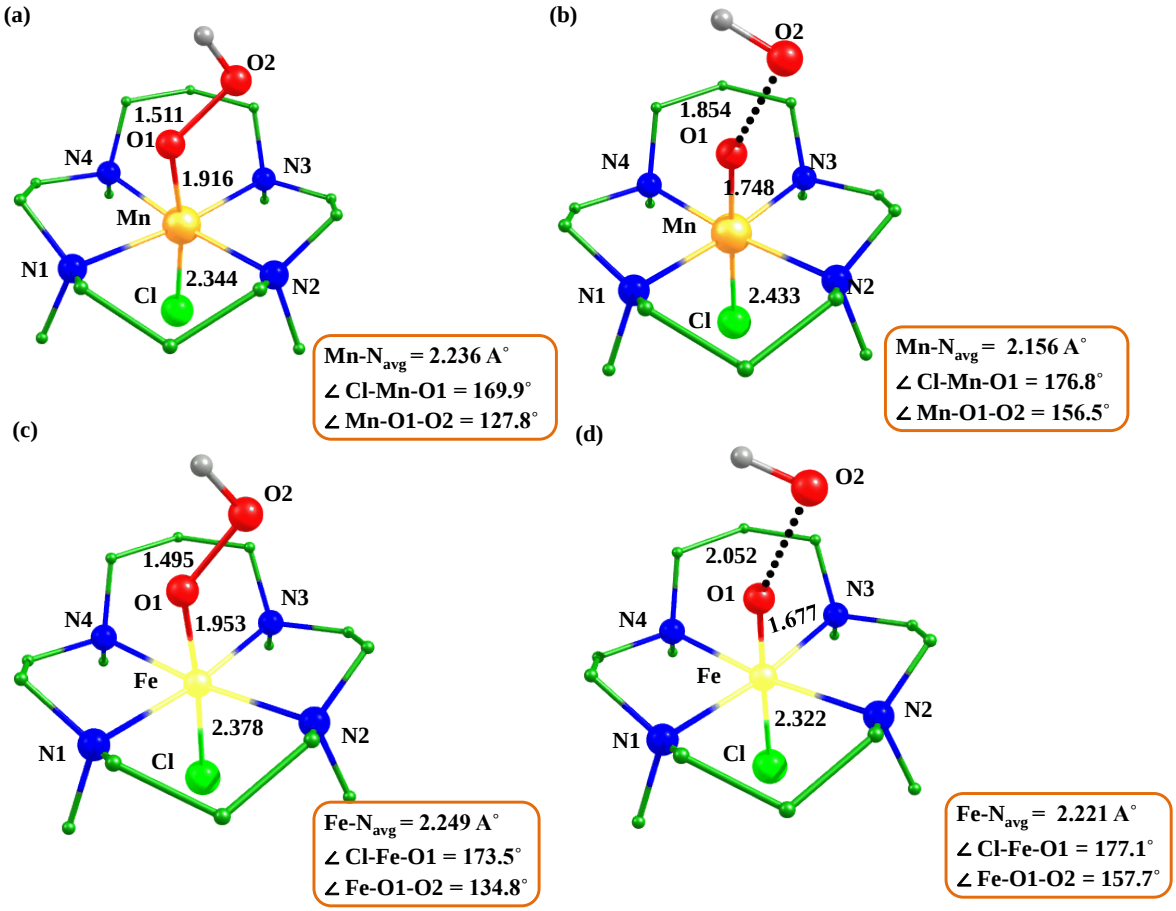

Figure 6.7. B3LYP-D2 a,b) optimized structure (bond length in Å) of ^{5}IIA$_{hs}$, ^{5}IIA$_{hs}$-ts, ^{6}IIIA$_{hs}$and ^{6}IIIA$_{hs}$-ts.

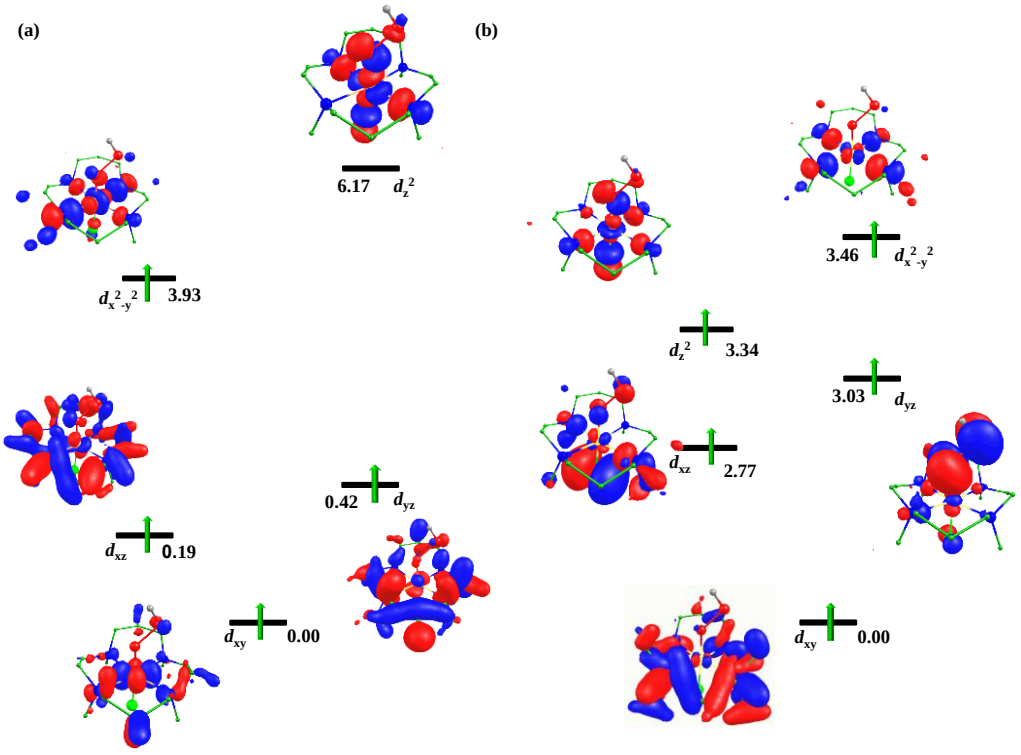

Figure 6.8. Computed eigenvalue plot incorporating energies computed for *d*-based orbitals for alpha corresponding to the ground state $^{5}IIA_{hs}$ of the species IIA, b) $^{6}IIIA_{hs}$ of the species IIIA (energies are given in eV).

Computed spin density at Mn and Fe center decreases 3.987/3.341, 3.980/3.275 respectively, and spin density at O1 and O2 during O---O bond cleavage are found to be 0.269/0.668 and 0.528/0.869 with Mn, Fe species, respectively, these spin density shows that the O---O bond cleavage occurs via homolytic manner. The barrier height of O---O bond cleavage is computed to be 63.3 kJ/mol with manganese and 73.2 kJ/mol with iron (see PES Figure 6.5 and Figure 6.6). Spin natural orbital of ground state of IIA and IIIA species and their transition state during O---O bond cleavage are shown in Figure 6.4, which shows the transfer of electron during O---O bond cleavage.

On moving right in 3*d* series, pairing of electrons starts in cobalt (IVA), nickel (VA), and copper (VIA) species.[25] Computed energetics suggests that $^{5}IVA_{hs}$, $^{2}VA_{ls}$, and $^{3}VIA_{hs}$ spin states are ground states (see Figure 6.6). Computed barrier height of O---O bond cleavage at ground state are 99.8 kJ/mol ($^{5}IVA_{hs}$-ts), 105.1 kJ/mol ($^{4}VA_{hs}$-ts), and 153.5 kJ/mol ($^{3}VIA_{hs}$-ts) with cobalt, nickel and copper species (see Figure 6.6). The optimized structure of ground states of $^{5}IVA_{hs}$, $^{2}VA_{ls}$, and $^{3}VIA_{hs}$ species and their corresponding transition states are shown in Figure 6.9.

M-O1 bond length in metal hydroperoxo species to the transition state decreases 1.934/1.674 Å, 2.013/1.836 Å, 2.291/2.004 Å, with cobalt, nickel and copper species respectively. Electron density at metal center decreases 2.766/2.164, 1.588/0.936, 0.519/0.030, with Co, Ni, and Cu species respectively. Computed significant electron density at oxygen atoms O1 and O2 are 0.673/0.798, 0.928/0.853, and 1.231/0.796, at Co, Ni and Cu species, respectively, confirm the homolytic O---O bond cleavage. The angle during the transition state of the M-O---O bond cleavage are computed to be 156.5˚ ($^{5}IIA_{hs}$-ts), 157.7˚ ($^{6}IIIA_{hs}$-ts),

162.5° ($^{5}IVA_{hs}$-ts), 154.1° ($^{4}VA_{hs}$-ts), and 135.5° ($^{3}VIA_{hs}$-ts) (see Table AX 6.1 of appendix) shows O---O bond cleavage takes place via π-pathway rather than σ-pathway. The barrier heights of O---O bond cleavage in the manganese and iron species is lower at high spin state ($^{5}IIA_{hs}$-ts) and ($^{6}IIIA_{hs}$-ts) than corresponding to their other spin states ($^{3}IIA_{hs}$-ts, $^{4}IIIA_{hs}$-ts, and $^{2}IIIA_{hs}$-ts) because of enhanced exchanged reactivity (see Figure 6.5 and Figure 6.6) and higher barrier height in late transition series because pairing of electron strats in late transition series (see Figure 6.10).

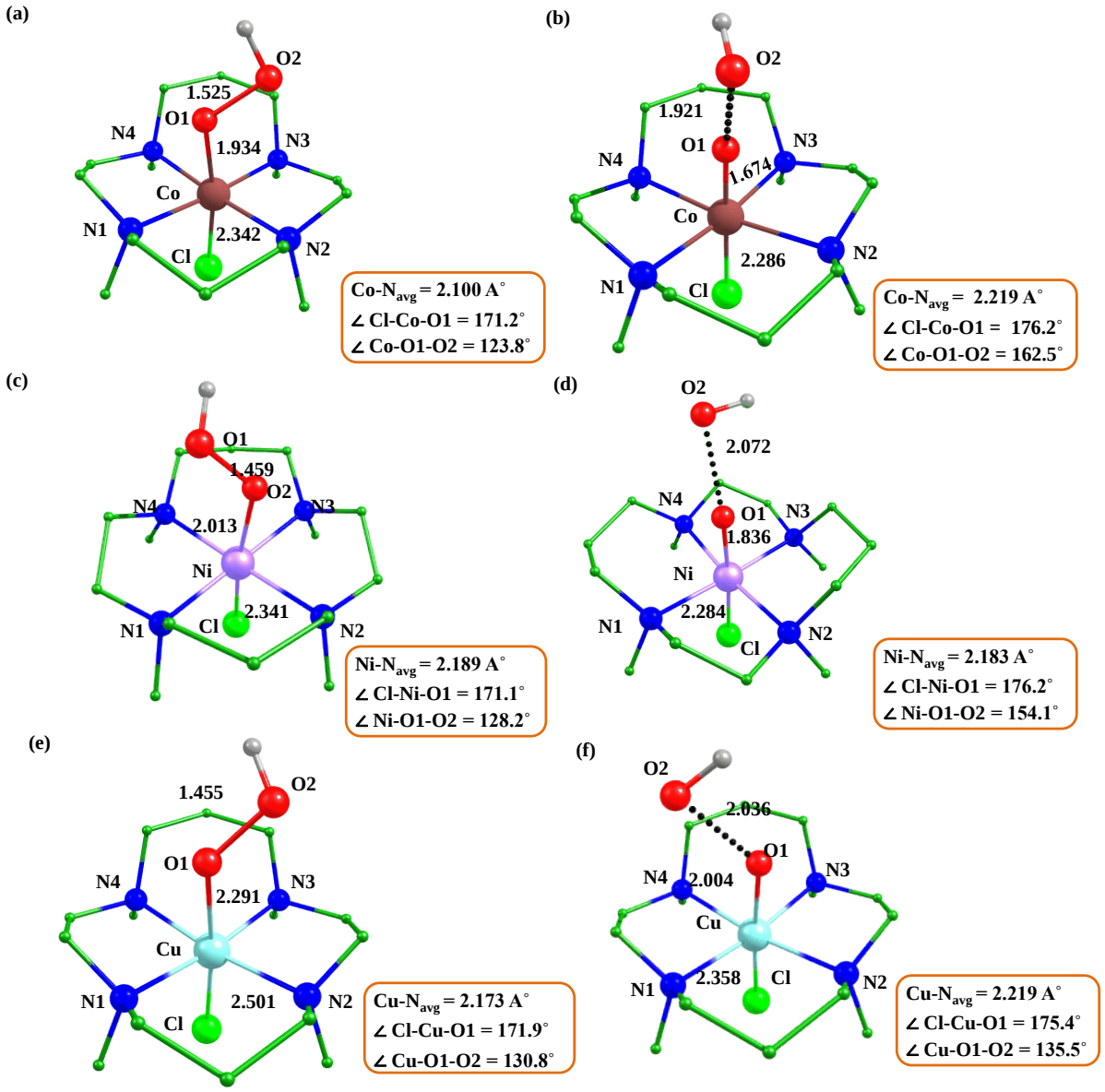

Figure 6.9. B3LYP-D2 optimized structure a) cobalt (^{1}IVA$_{ls}$), b) its transition state ^{5}IVA$_{hs}$-ts), (^{4}VA$_{hs}$-ts), c) optimized structure of nickel (^{2}VA$_{ls}$), d) its corresponding transition state (^{4}VA$_{hs}$-ts), e) optimized structure of ^{3}VIA$_{hs}$ and f) its corresponding transition state(^{3}VIA$_{hs}$-ts).

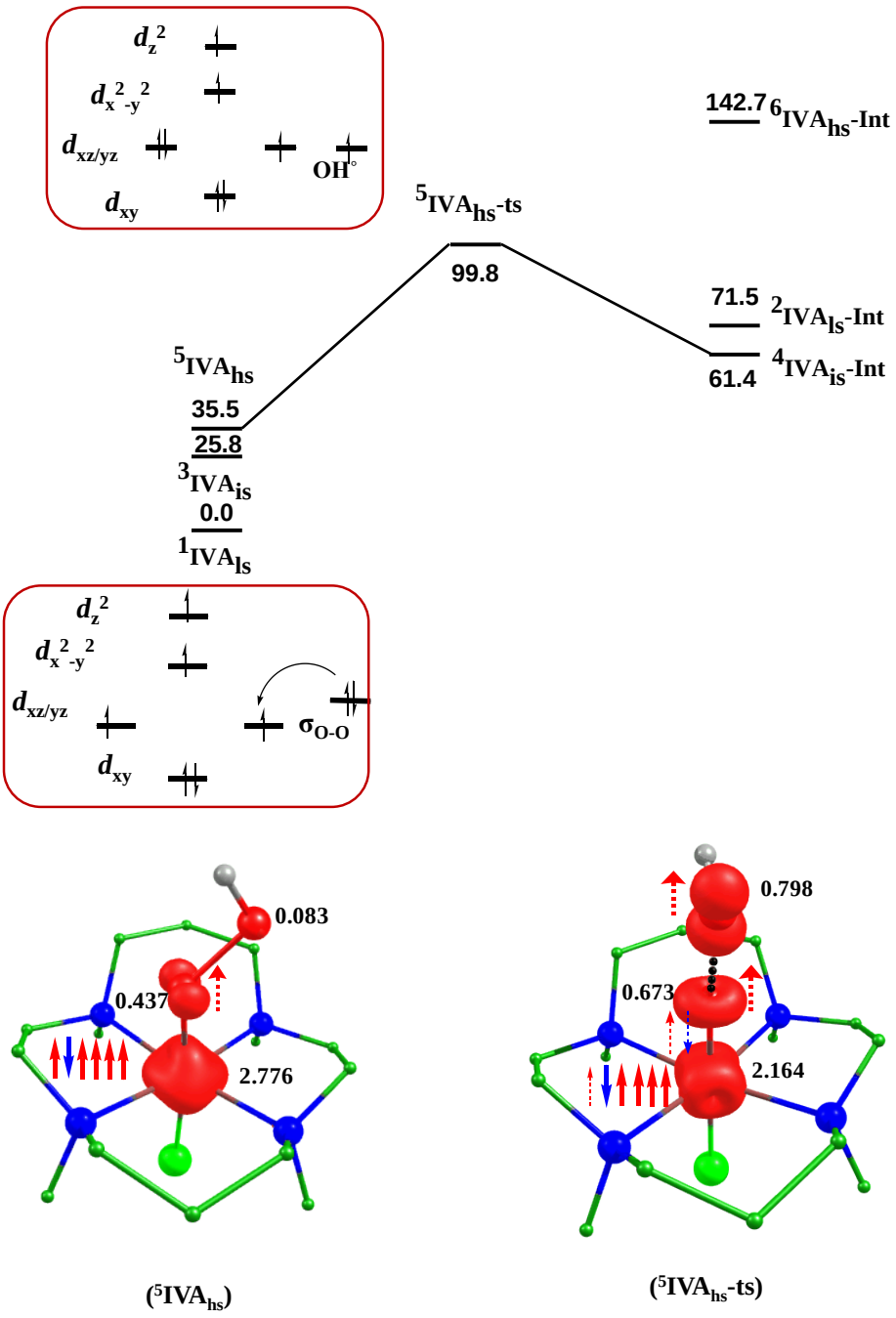

Figure 6.10. B3LYP-D2 computed energy for the O-O bond cleavage of IVA species. The computed barrier height is shown with respect to the reactant (IVA).

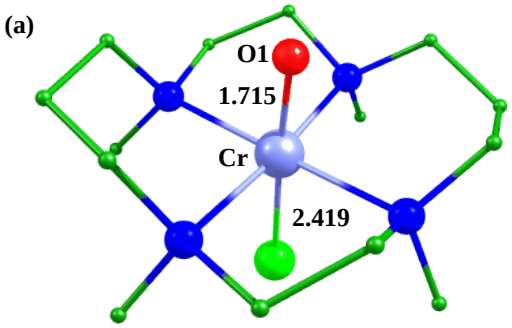

Cr-N_{avg} = 2.171 A°

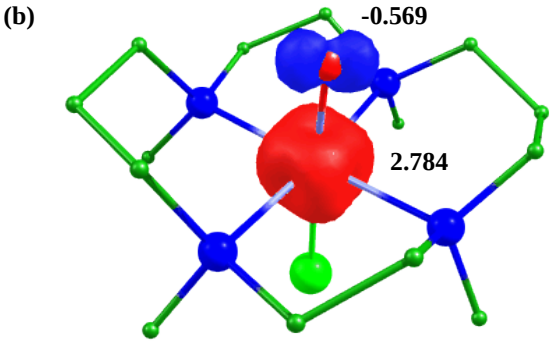

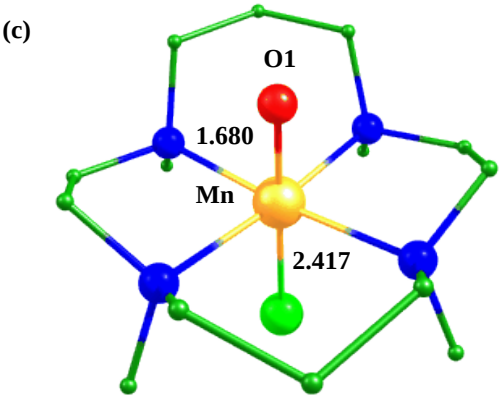

Mn-N_{avg} = 2.145 A°

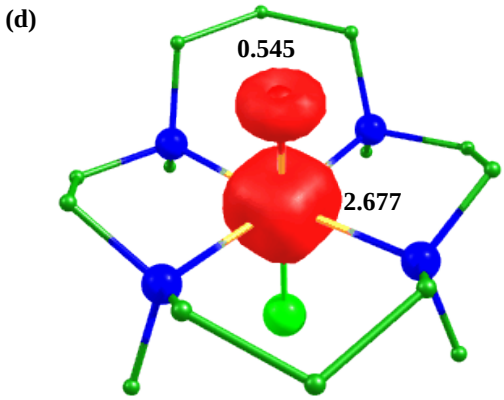

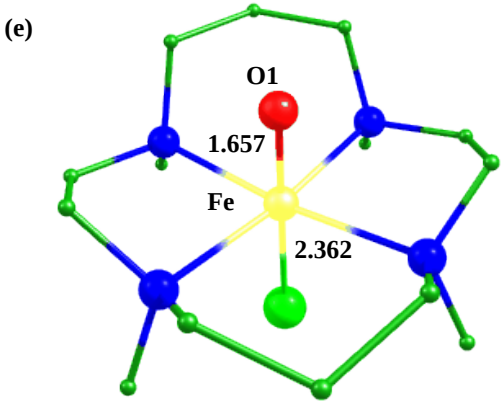

Fe-N_{avg} = 2.219 A°

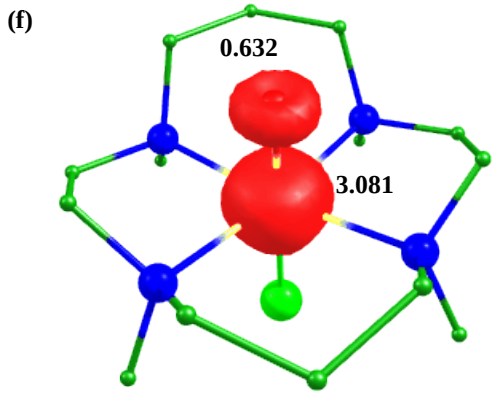

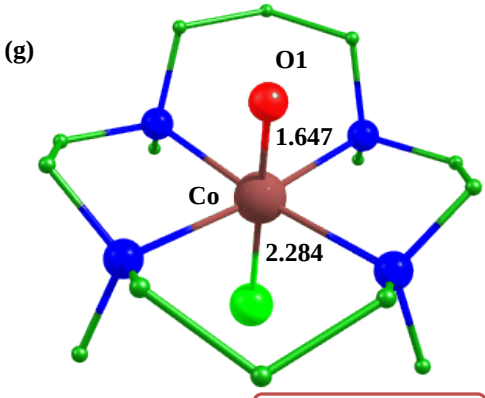

Co-N_{avg} = 2.210 A°

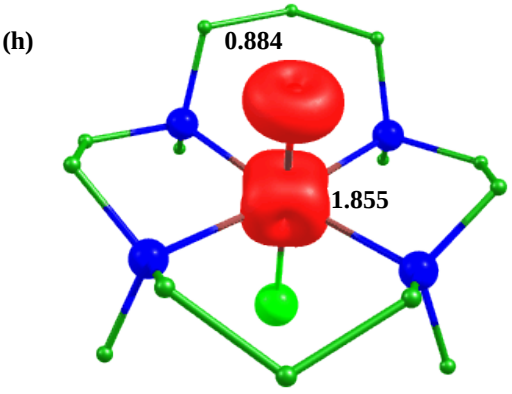

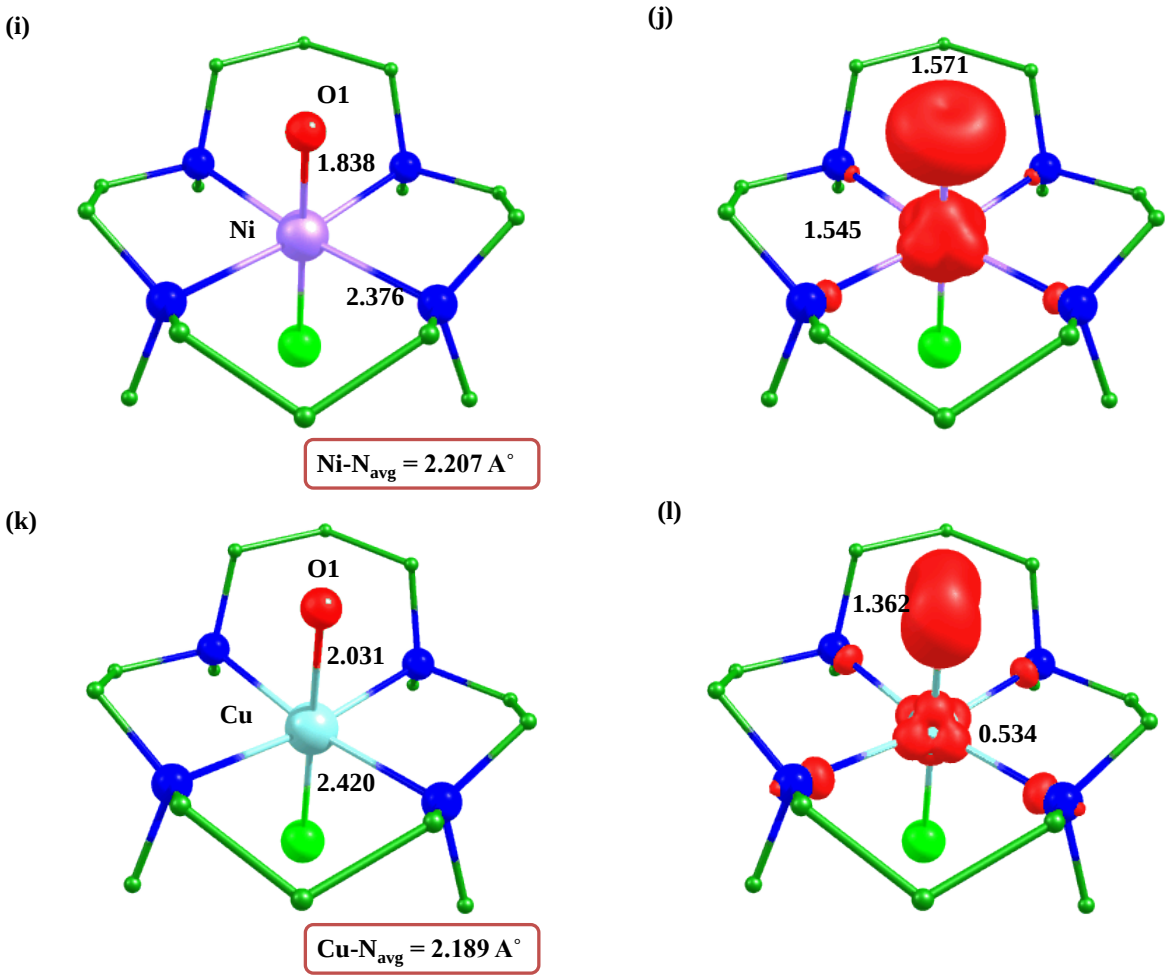

Figure 6.11. B3LYP-D2 a) optimized structure (bond length in Å) b) spin density plot of $^{3}IA_{hs}$-Int; c) optimized structure (bond length in Å) d) spin density plot of $^{4}IIA_{hs}$-Int; e) optimized structure (bond length in Å) f) spin density plot of $^{5}IIIA_{hs}$-Int and $^{5}IIIA_{hs}$-ts; g) optimized structure (bond length in Å) h) spin density plot of $^{4}IVA_{is}$-Int; i) optimized structure (bond length in Å); j) spin density plot of $^{5}VA_{hs}$-Int; k) optimized structure (bond length in Å) and l) spin density plot of $^{4}VIA_{hs}$-Int.

The O---O bond cleavage leads to the formation of metal-oxo species. We have computed all the possible spin states of metal-oxo species. On the basis of their energetics $^{3}IA_{hs}$-Int, $^{4}IIA_{hs}$-Int, $^{5}IIIA_{hs}$-Int, $^{4}IVA_{is}$-Int, $^{5}VA_{hs}$-Int and $^{4}VIA_{hs}$-Int spin states are found to be ground state with IA, IIA, IIIA, IVA, VA and VIA species. Optimized structures and corresponding spin density plots of the ground state of metal-oxo species are shown in Figure 6.11. Selected bond parameters of the studied metal-oxo species are shown in Table AX 6.1 of appendix.

Significant electron density at the oxygen atom may be a witness for the reactive nature of metal-oxo species. We have also computed the M-O stretching frequencies (see Table 6.2).

Table 6.2. Computed stretching frequencies of M-O bond in metal-oxo species.

Metal-oxo	υ (cm^{-1})	Spin State	υ (cm^{-1})
$^{3}IA_{hs}$-Int	558	$^{3}IB_{hs}$-Int	921
$^{4}IIA_{hs}$-Int	869	$^{4}IIB_{hs}$-Int	851
$^{5}IIIA_{hs}$-Int	872	$^{5}IIIB_{hs}$-Int	889
$^{4}IVA_{is}$-Int	849	$^{4}IVB_{is}$-Int	515
$^{5}VA_{hs}$-Int	499	$^{5}VB_{hs}$-Int	390
$^{4}VIA_{hs}$-Int	376	$^{4}VIB_{hs}$-Int	419

6.3.2 Metal hydroperoxo species with buea ligand (IB (chromium), IIB (manganese), IIIB (iron), IVB (cobalt), VB (nickel) and VIB (copper))

We have also enlightened theoretical study from octahedral geometry to trigonal bipyramidal (cavity). So, similar to TMC species, first we have performed optimization on all possible spin surfaces of (buea) Cr-OOH to (buea) Cu-OOH species and also their transition states of O---O bond cleavage. On the basis of energetic it is found that $^{4}IB_{hs}$, $^{5}IIB_{hs,}$ $^{6}IIIB_{hs,}$ $^{4}IVB_{is,}$ $^{4}VB_{hs}$ and $^{4}VIB_{hs}$ spin states are the ground state. Spin energetic at other spin states are also shown in Figure 6.12. Selected bond parameters are shown in Table AX 6.3 of appendix. Selected spin density are shown in Table 6.3. Optimized structures and spin density plots of ground state of metal hydroperoxo IB, IIB, IIIB, IVB, VB and VIB species are shown in Figure 6.13a,c,e,g,i,k. Our DFT calculations show that the computed barrier height of ground state O---O cleavage are 90.2 kJ/mol ($^{2}IB_{hs}$-ts; Cr), 83.6 kJ/mol ($^{5}IIB_{hs}$-ts; Mn), 57.7 kJ/mol

(^{4}IIIB$_{hs}$-ts; Fe), 119.2 kJ/mol (^{5}IVB$_{hs}$-ts; Co), 99.8 kJ/mol (^{4}VB$_{hs}$-ts; Ni) and 154.0 kJ/mol (^{1}VIB$_{hs}$-ts; Cu species) and spin energetics of other spin surfaces (see Figure 6.12).

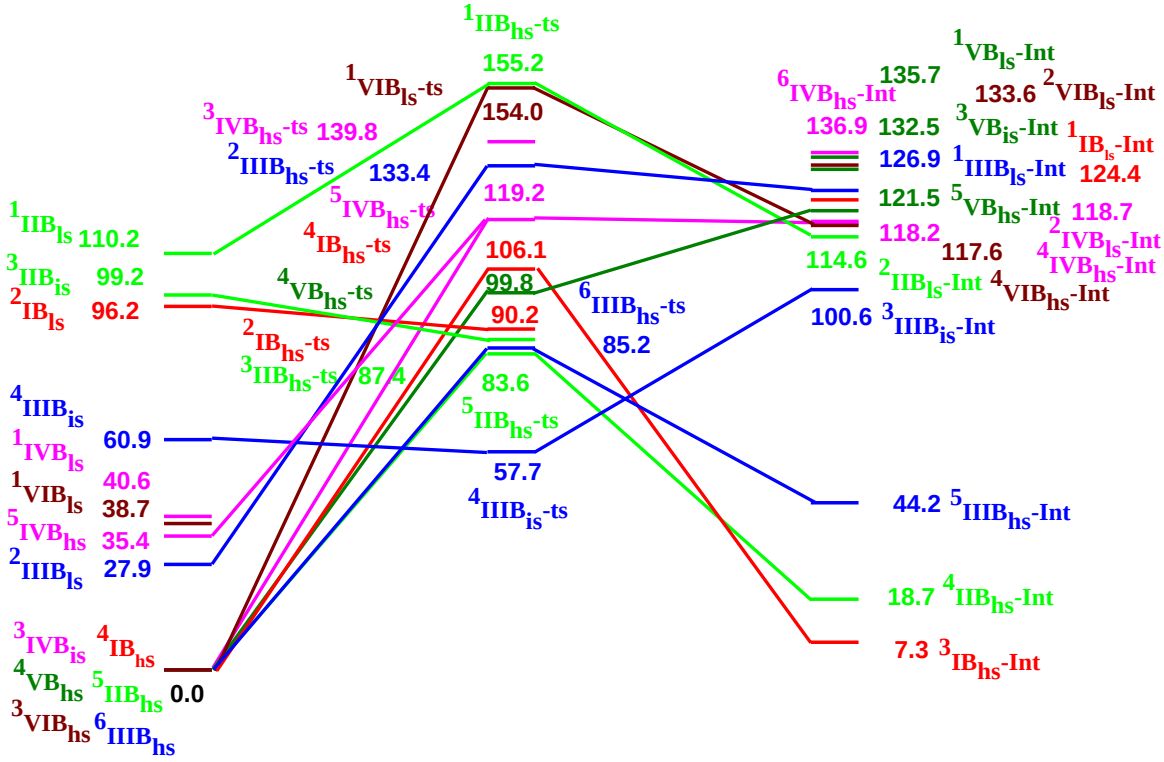

Figure 6.12. B3LYP-D2 computed energy surface for the formation of metal-oxo from metalhydroperoxo with buea ligand Chromium (red), manganese (green), iron (blue), cobalt (magenta), nickel (olive), and copper (wine).

Table 6.3. B3LYP-D2 computed spin density values of the buea species (reactant, transition states, and product).

Spin State	Metal	O_1	O_2
[(buea)CrOOH]$^{-}$			
^{4}IB$_{hs}$	3.005	-0.009	0.012
^{2}IB$_{ls}$	0.991	0.040	-0.009
^{4}IB$_{hs}$-ts	2.549	-0.024	0.545
^{2}IB$_{ls}$-ts	1.089	0.043	-0.111
^{3}IB$_{hs}$-Int	1.930	0.050	-
^{1}IB$_{ls}$-Int	0	0	-
[(buea)MnOOH]$^{-}$			
^{5}IIB$_{hs}$	3.831	-0.038	0.007
^{3}IIB$_{is}$	1.929	0.025	-0.012
^{1}IIB$_{ls}$	0.000	0.00	0.000

$^{5}IIB_{hs}$-ts	3.301	0.056	0.577
$^{3}IIB_{is}$-ts	2.238	0.094	-0.312
$^{1}IIB_{ls}$-ts	0.000	0.000	0.000
$^{4}IIB_{hs}$-Int	2.732	0.256	-
$^{2}IIB_{ls}$-Int	1.004	-0.112	-
[(buea)FeOOH]$^{-}$			
$^{6}IIIB_{hs}$	3.926	0.228	0.026
$^{4}IIIB_{is}$	2.771	-0.017	-0.031
$^{2}IIIB_{ls}$	0.979	0.002	-0.005
$^{6}IIIB_{hs}$-ts	3.381	0.258	0.742
$^{4}IIIB_{is}$-ts	2.826	0.291	-0.631
$^{2}IIIB_{ls}$-ts	1.399	0.080	-0.481
$^{5}IIIB_{hs}$-Int	2.991	0.456	-
$^{3}IIIB_{is}$-Int	1.569	0.375	-
$^{1}IIIB_{ls}$-Int	0	0	-
[(buea)CoOOH]$^{-}$			
$^{5}IVB_{hs}$	2.744	0.206	0.017
$^{3}IVB_{is}$	1.719	-0.117	-0.034
$^{1}IVB_{ls}$	0.000	0.000	0.000
$^{5}IVB_{hs}$-ts	2.107	0.526	0.506
$^{3}IVB_{is}$-ts	1.423	0.279	0.553
$^{6}IVB_{hs}$-Int	2.701	1.044	-
$^{4}IVB_{is}$-Int	1.701	0.664	-
$^{2}IVB_{ls}$-Int	1.562	-0.956	-
[(buea)NiOOH]$^{-}$			
$^{4}VB_{hs}$	1.640	0.229	0.023
$^{2}VB_{ls}$	0.927	-0.135	-0.052
$^{2}VB_{ls}$-ts	0.929	0.336	0.456
$^{5}VB_{hs}$-Int	1.615	1.104	-
$^{3}VB_{is}$-Int	1.634	-0.808	-
$^{1}VB_{ls}$-Int	0	0	-
[(buea)CuOOH]$^{-}$			
$^{3}VIB_{hs}$	0.494	0.344	0.086
$^{1}VIB_{ls}$	0.000	0.000	0.000
$^{1}VIB_{ls}$-ts	0	0	0
$^{4}VIB_{hs}$-Int	0.524	1.169	-
$^{2}VIB_{ls}$-Int	0.493	1.115	-

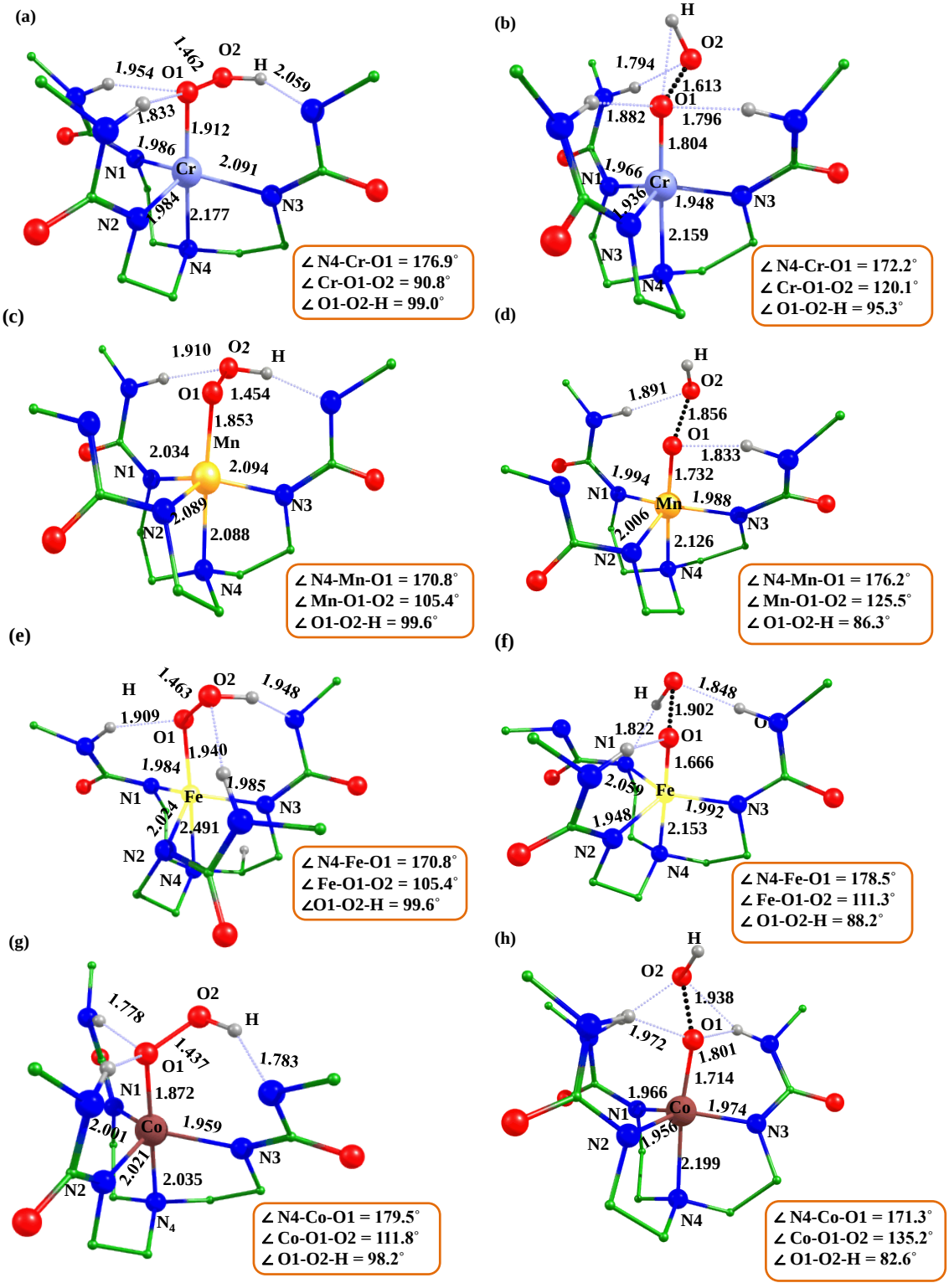
(a)
1.462
O2
H
2.059
1.954
O1
1.833
1.912
1.986
Cr
2.091
N1
N3
1.984
2.177
N2
N4
∠ N4-Cr-O1 = 176.9°
∠ Cr-O1-O2 = 90.8°
∠ O1-O2-H = 99.0°
(b)
H
O2
1.794
1.613
O1
1.882
1.796
1.804
1.966
N1
Cr
1.936
1.948
N3
2.159
N3
N4
∠ N4-Cr-O1 = 172.2°
∠ Cr-O1-O2 = 120.1°
∠ O1-O2-H = 95.3°
(c)
1.910
O2
H
O1
1.454
1.853
Mn
2.034
2.094
N1
N3
2.089
N2
2.088
N4
∠ N4-Mn-O1 = 170.8°
∠ Mn-O1-O2 = 105.4°
∠ O1-O2-H = 99.6°
(d)
H
1.891
O2
1.856
O1
1.833
1.994
1.732
N1
Mn
1.988
N3
2.006
2.126
N2
N4
∠ N4-Mn-O1 = 176.2°
∠ Mn-O1-O2 = 125.5°
∠ O1-O2-H = 86.3°
(e)
H
1.463
O2
1.948
1.909
O1
1.940
1.984
1.985
N1
Fe
N3
2.024
2.491
N2
N4
∠ N4-Fe-O1 = 170.8°
∠ Fe-O1-O2 = 105.4°
∠O1-O2-H = 99.6°
(f)
H
1.848
1.902
O
1.822
N1
O1
1.666
2.039
Fe
1.992
N3
1.948
2.153
N2
N4
∠ N4-Fe-O1 = 178.5°
∠ Fe-O1-O2 = 111.3°
∠ O1-O2-H = 88.2°
(g)
1.778
O2
H
1.437
1.783
O1
N1
1.872
2.001
Co
1.959
N3
2.021
2.035
N2
N4
∠ N4-Co-O1 = 179.5°
∠ Co-O1-O2 = 111.8°
∠ O1-O2-H = 98.2°
(h)
H
O2
1.938
O1
1.972
1.801
1.714
1.966
N1
Co
1.974
N3
1.956
N2
2.199
N4
∠ N4-Co-O1 = 171.3°
∠ Co-O1-O2 = 135.2°
∠ O1-O2-H = 82.6°

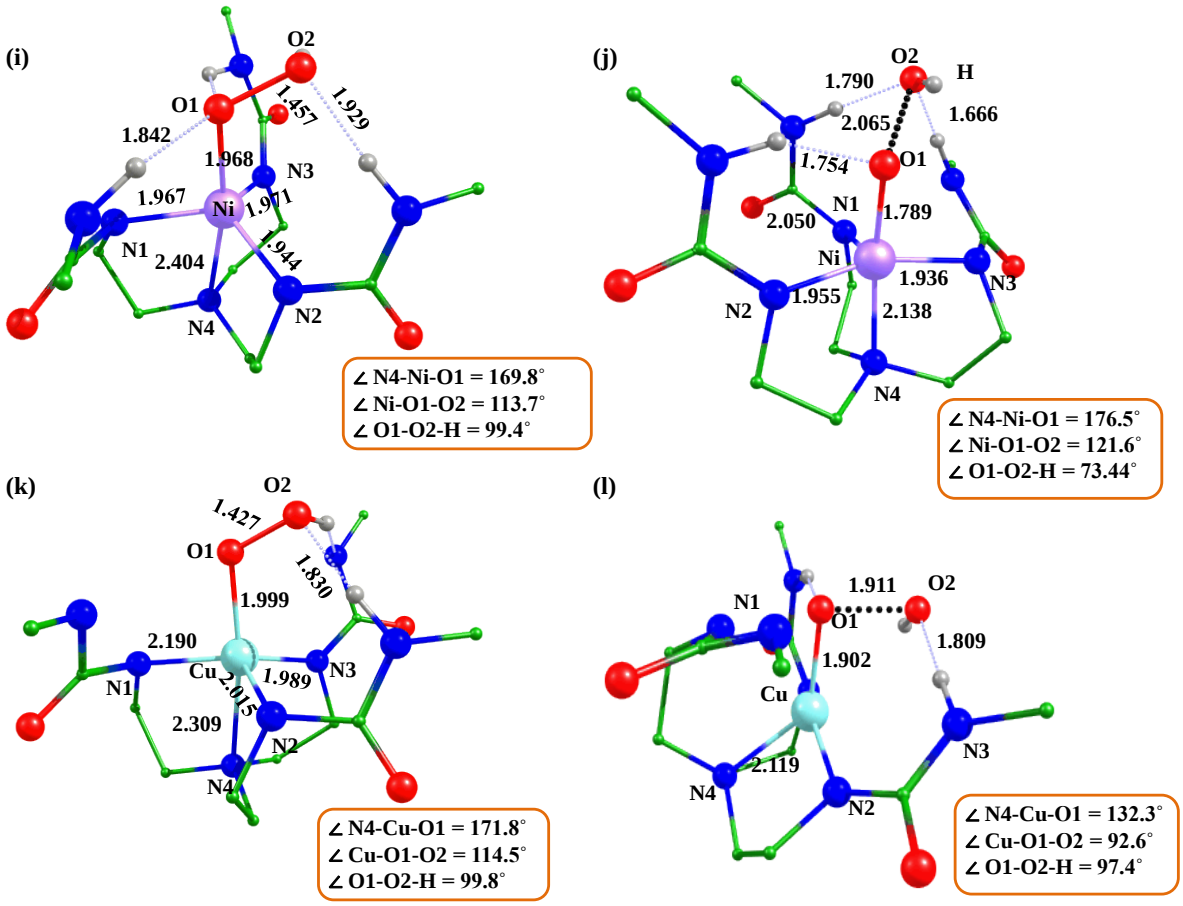

Figure 6.13. B3LYP-D2 optimized structure of ground state $^{4}IB_{hs}$, $^{5}IIB_{hs}$, $^{6}IIIB_{hs}$, $^{3}IVB_{is}$ and $^{4}VB_{hs,}$ and their corresponding transition states $^{2}IB_{ls}$-ts, $^{5}IIB_{hs}$-ts, $^{4}IIIB_{hs}$-ts, $^{5}IVB_{is}$-ts, $^{2}VB_{ls}$-ts.

Optimized structure of ground state of O---O bond cleavage $^{2}IB_{hs}$-ts, $^{5}IIB_{hs}$-ts, $^{4}IIIB_{hs}$-ts, $^{5}IVB_{hs}$-ts, $^{4}VB_{hs}$-ts, and $^{1}VIB_{hs}$-ts are shown in Figure 6.13 b,d,f,h,j,l. Computed M-O bond length decreases during O---O bond cleavage i.e. 1.912/1.804 Å (Cr), 1.853/1.732 Å (Mn), 1.940/1.666 Å (Fe), 1.872/1.714 Å (Co), 1.968/1.789 Å (Ni), 1.999/1.902 Å (Cu) respectively while O1-O2 bond length increases 1.462/1.613 Å (Cr), 1.454/1.856 Å (Mn), 1.463/1.902 Å (Fe), 1.437/1.938 Å (Co), 1.457/2.065 Å (Ni) and 1.427/1.911 Å (Cu) species respectively. These bond parameters support the formation of transition state during O---O bond cleavage. Computed spin density at metal center decreases during O---O bond cleavage i.e. 3.005/1.089 (Cr), 3.831/3.301 (Mn), 3.926/2.826 (Fe), 1.719/2.107 (Co), 1.640/0.929 (Ni), 0.494/0 (Cu). During the O---O bond cleavage with Cu, we have found that buea geometry gets distorted.

As Cu(III) has d^8 electronic configuration with the copper hydroperoxo species,[68] but during O---O bond cleavage electronic configuration at copper center changes i.e. one extra upcoming electron will enter into d_z^2 orbital, which has much higher energy than the d_{xy/x^2-y^2} orbitals due to which during O---O bond cleavage geometry of buea ligand gets distorted. This distortion in geometry may be also due to the John-Teller distortion in Cu d_{xz}/d_{yz} being orthogonal to M-O bond and they can have four electrons in these nonbonding orbitals.

Similar to TMC species, here we have also found that the barrier height of O---O cleavage of Co, Ni, and Cu are relatively higher as compared to corresponding Cr, Mn, and Fe species. This may be due presence of large *d-d* exchange interaction in Cr, Mn, Fe species than the Co, Ni, and Cu species (see Figure 6.14, and 6.15).

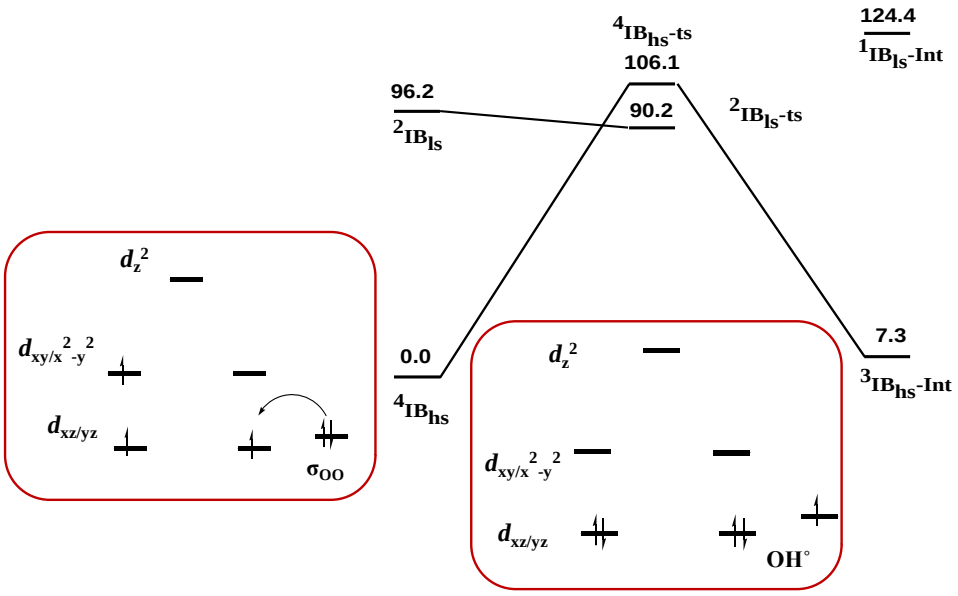

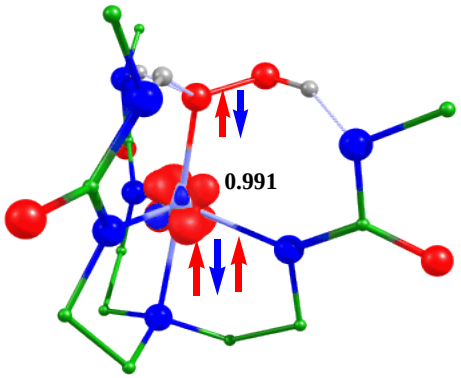

($^2IB_{ls}$)

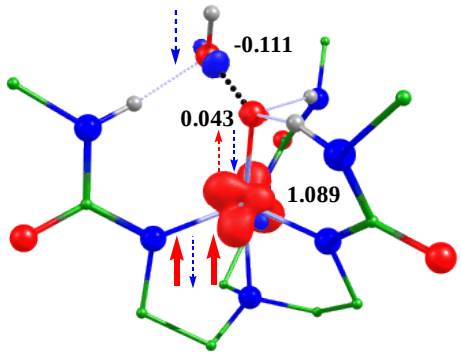

($^2IB_{ls}$-ts)

Figure 6.14. B3LYP-D2 computed energy for the O-O bond cleavage of IB species. The computed barrier height is shown concerning the reactant (IB).

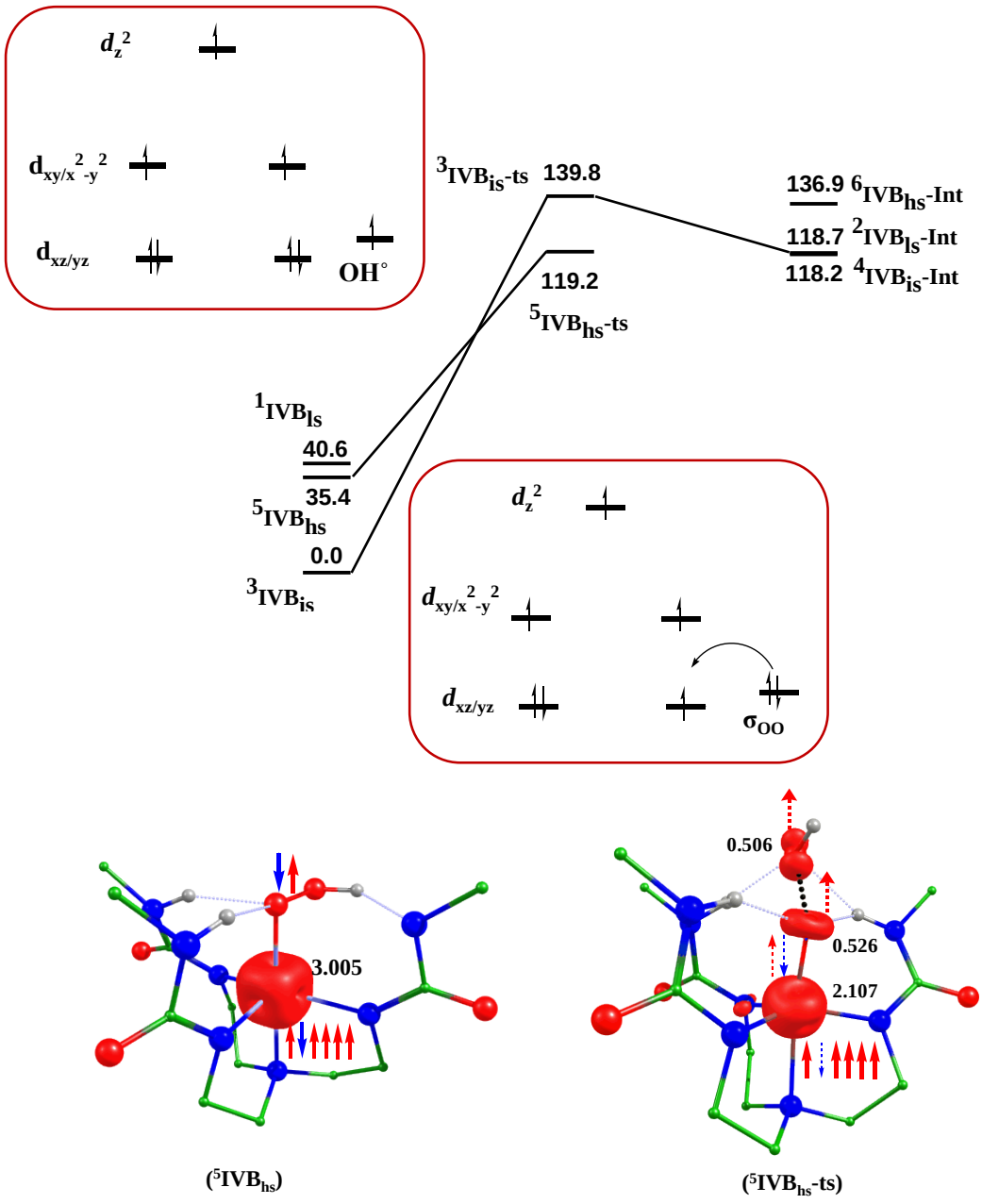

Figure 6.15. B3LYP-D2 computed energy for the O-O bond cleavage of IVB species. The computed barrier height is shown with respect to the reactant (IVB).

The spin natural orbital with occupancies of orbital of ground state of IB, IIB, IIIB, IVB, VB and VIB species and their corresponding O---O bond cleavage transition states are shown in Figure 6.16 these shows the transfer of electron during O---O bond cleavage. Computed wiberg bond index also shows the formation of O---O bond cleavage transition state (see

Table AX 6.4 of appendix). As buea has trigonal bipyramidal geometry and the splitting of *d* orbital is supported by CFT is like $d_{xz} \approx d_{yz} < d_{xy} \approx d_{x^2-y^2} < d_{z^2}$ as shown in Figure 6.17, d_{z^2} orbital have the highest energy and is also supported by Ray (see Figure 6.17). Computed electronic configuration at IB and IIB are found to be $(d_{xz})^1 (d_{yz})^1 (d_{xy})^1 (d_{x^2-y^2})^0 (d_{z^2})^0$ and $(d_{xz})^1 (d_{yz})^1 (d_{xy})^1 (d_{x^2-y^2})^1 (d_{z^2})^0$ (see Figure 6.17). O---O bond cleavage leads to the formation of metal-oxo species. We have performed calculation on all possible electronic configuration of metal-oxo species from the spin energetics it is found that $^3IB_{hs}$-Int, $^4IIB_{hs}$-Int, $^5IIIB_{hs}$-Int, $^5IIIB_{hs}$-ts, $^4IVB_{is}$-Int, $^5VB_{hs}$-Int and $^4VIB_{hs}$-Int are the ground state. Selected bond parameters of metal-oxo species are shown in Table AX 6.3 of appendix. Selected spin density are shown in Table 6.3. Optimized structure and spin density plots of ground state are shown in Figure 6.18. A significant electron densiy at the metal-oxo, oxygen atom indicates its reactive nature.

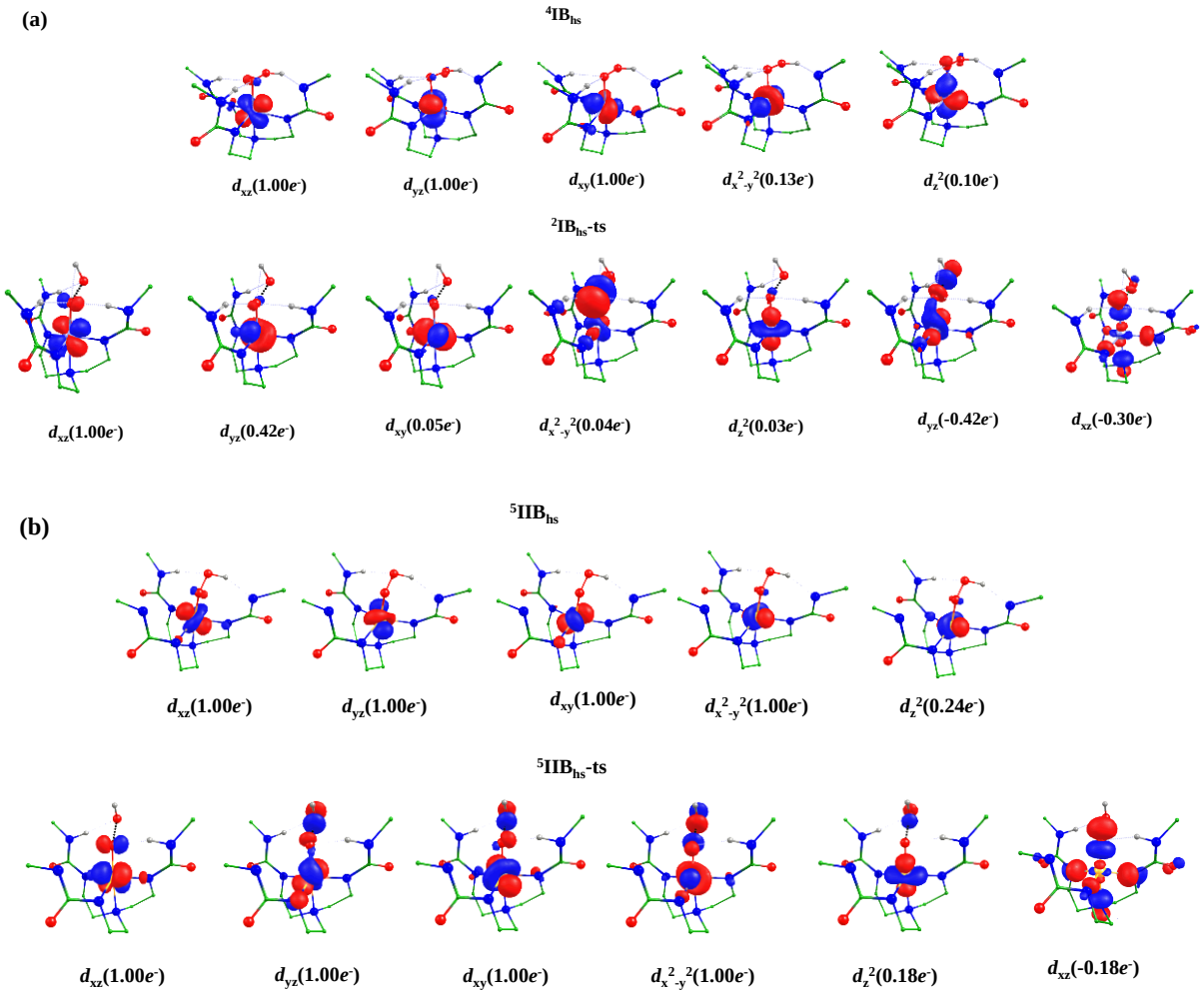

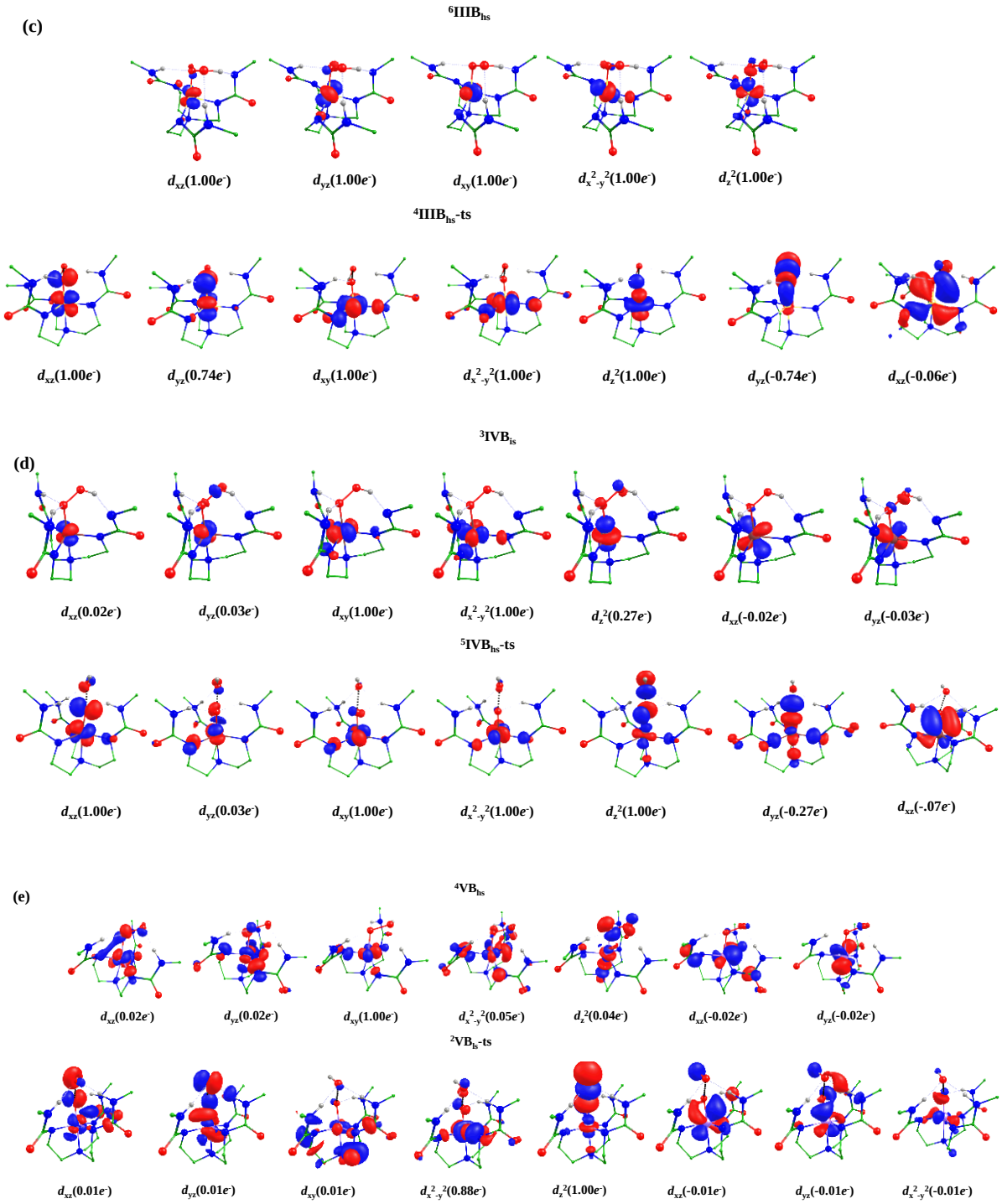

Figure 6.16. Spin natural orbitals and their occupations (noted in parenthesis) of a) ^{2}IB$_{ls}$, ^{2}IB$_{hs}$-ts, b) ^{5}IIB$_{hs}$, ^{5}IIB$_{hs}$-ts, c) ^{6}IIIB$_{hs}$, ^{4}IIIB$_{is}$-ts, d) ^{3}IVB$_{is}$, ^{5}IVB$_{hs}$-ts, e) ^{4}VB$_{hs}$, ^{2}VB$_{ls}$-ts.

Computed stretching frequency of ground state of metal-oxo species are shown in Table 6.2. From literature, only one Co^{IV}=O species with TBP geometry, where oxo is attached to Lewis acid additionally is reported yet.[71] Along with these species, we have also performed

calculation on Ru (VIIB), Os (VIIIB), Rh (IXB), and Ir (XB). We have optimized all the possible electronic configuration of species VIIB, VIIIB, IXB and XB and computed the barrier height of O---O bond cleavage with Ru (VIIB), Os (VIIIB), Rh (IXB), and Ir (XB) with buea ligand. Fom the calculation it is found that $^{2}VIIB_{hs}$, $^{2}VIIIB_{hs}$, $^{1}IXB_{hs}$, and $^{1}XB_{is}$ spin states are the ground state. Selected bond parameters of ground state are shown in Table AX 6.5 of appendix. Optimized structure of ground of species VIIB, VIIIB, IXB and XB are shown in Figure 6.19a,c,e,g. It is found that the O---O bond cleavage barrier is higher with Rh (111.8 kJ/mol; $^{3}IXB_{hs}$-ts) and Ir (77.3 kJ/mol; $^{1}XB_{is}$-ts) species than the corresponding Ru (52.7 kJ/mol; $^{2}VIIB_{ls}$-ts) and Os (21.2 kJ/mol; $^{2}VIIIB_{hs}$-ts) species. We tired to compute transition state of O---O bond cleavage at other spin surfaces of VIIB, VIIIB, IXB and XB species but we were not able to compute all these due to convergence issue. We also tried to compute the barrier height of O---O bond cleavage with 14-TMC and computed the barrier height of O---O bond cleavage with Ru (49.7 kJ/mol) but not be able to compute the barrier with Os, Rh and Ir due to convergence issue. The Optimized ground state structure of VIIB-ts, VIIIB-ts, IXB-ts and XB-ts are shown in Figure 6.19(b,d,f,h).

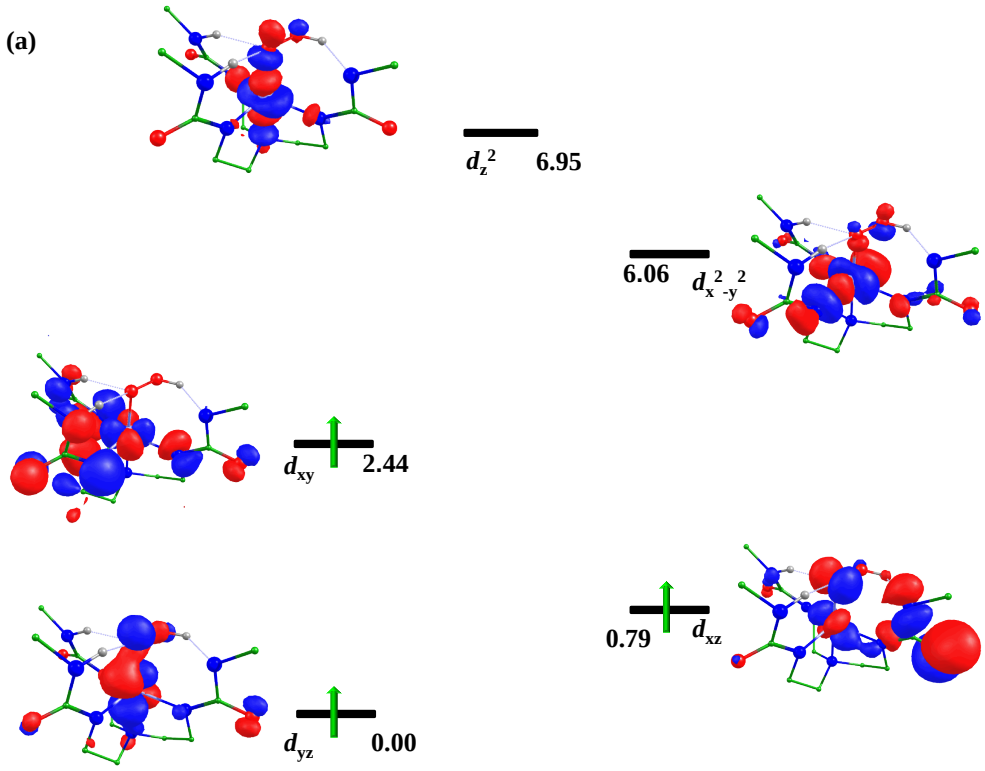

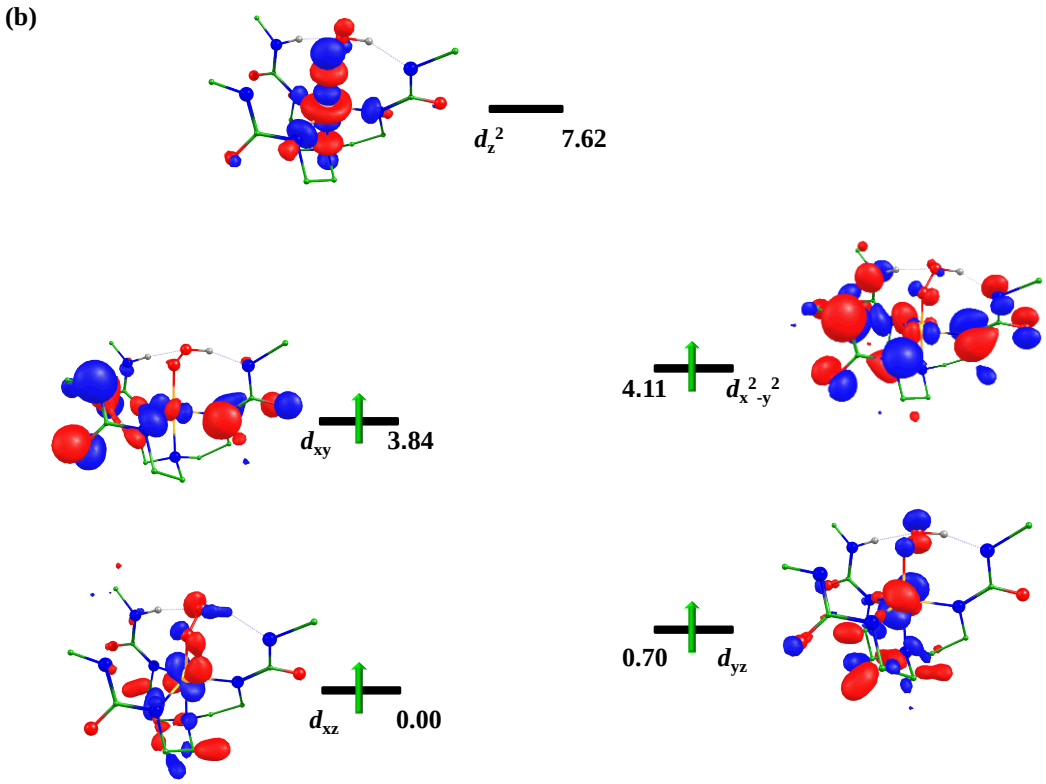

Figure 6.17. Computed eigenvalue plot incorporating energies computed for *d*-based orbitals for alpha and beta spin corresponding to the ground state $^{4}IB_{hs}$, $^{5}IIB_{hs}$ of the complex IIB (energies are given in eV).

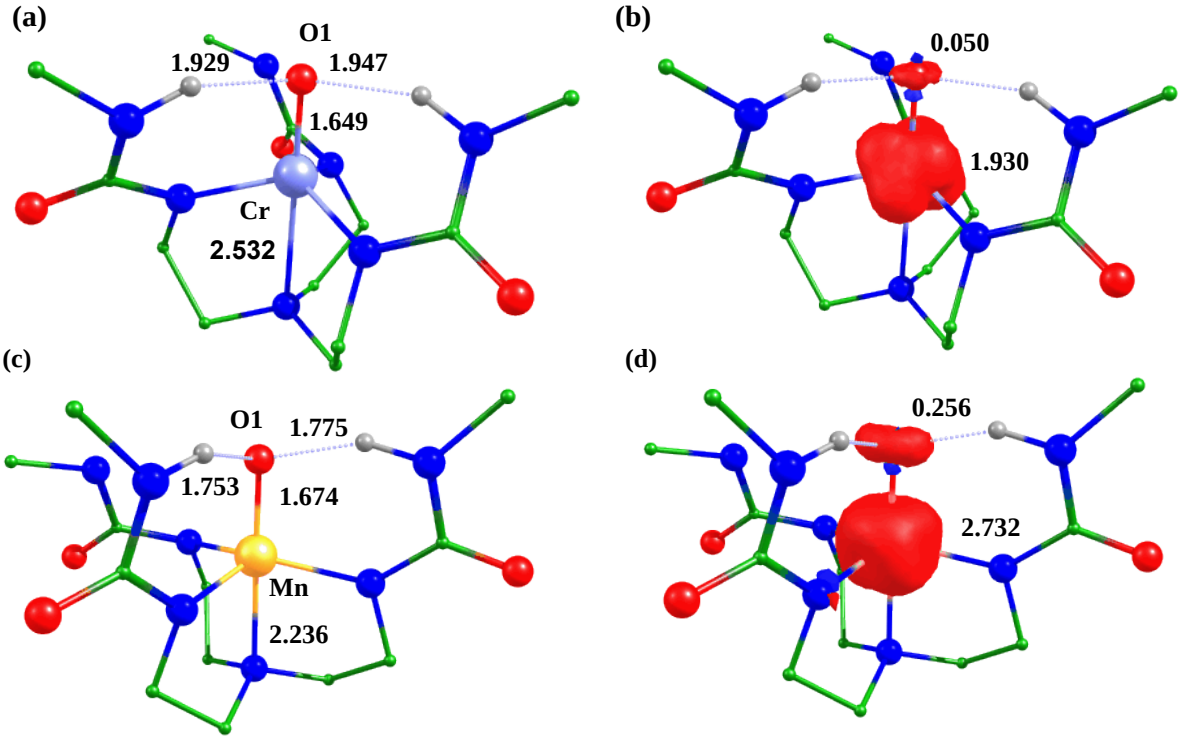

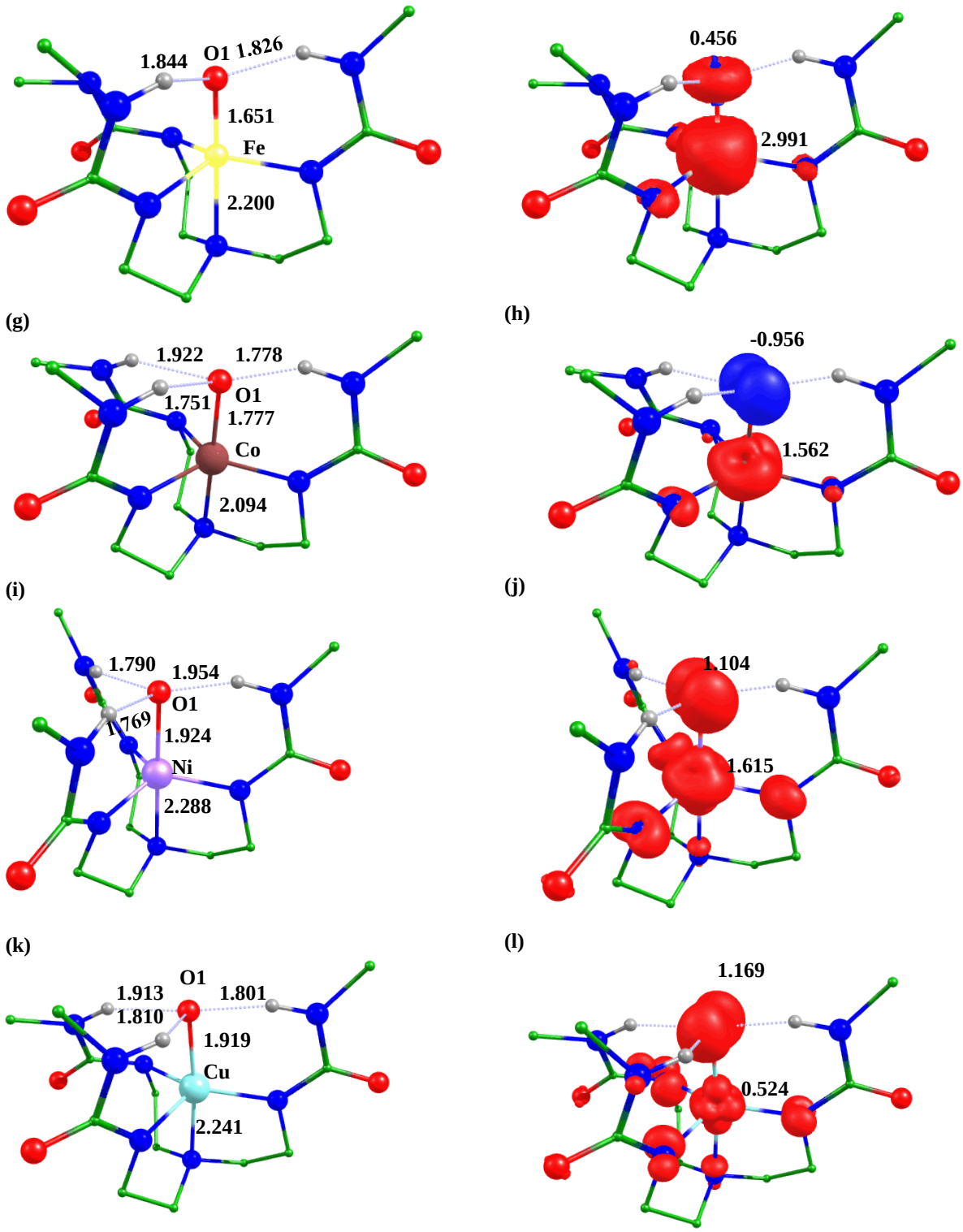

Figure 6.18. B3LYP-D2 a) optimized structure (bond length in Å) b) spin density plot of $^{3}IB_{hs}$-Int; c) optimized structure (bond length in Å) d) spin density plot of $^{4}IIB_{hs}$-Int; e) optimized structure (bond length in Å) f) spin density plot of $^{5}IIIB_{hs}$-Int and $^{5}IIIB_{hs}$-ts; g) optimized structure (bond length in Å) h) spin density plot of $^{4}IVB_{is}$-Int; i) optimized

structure (bond length in Å) j) spin density plot of $^{5}VB_{hs}$-Int; k) optimized structure (bond length in Å) and l) spin density plot of $^{4}VIB_{hs}$-Int.

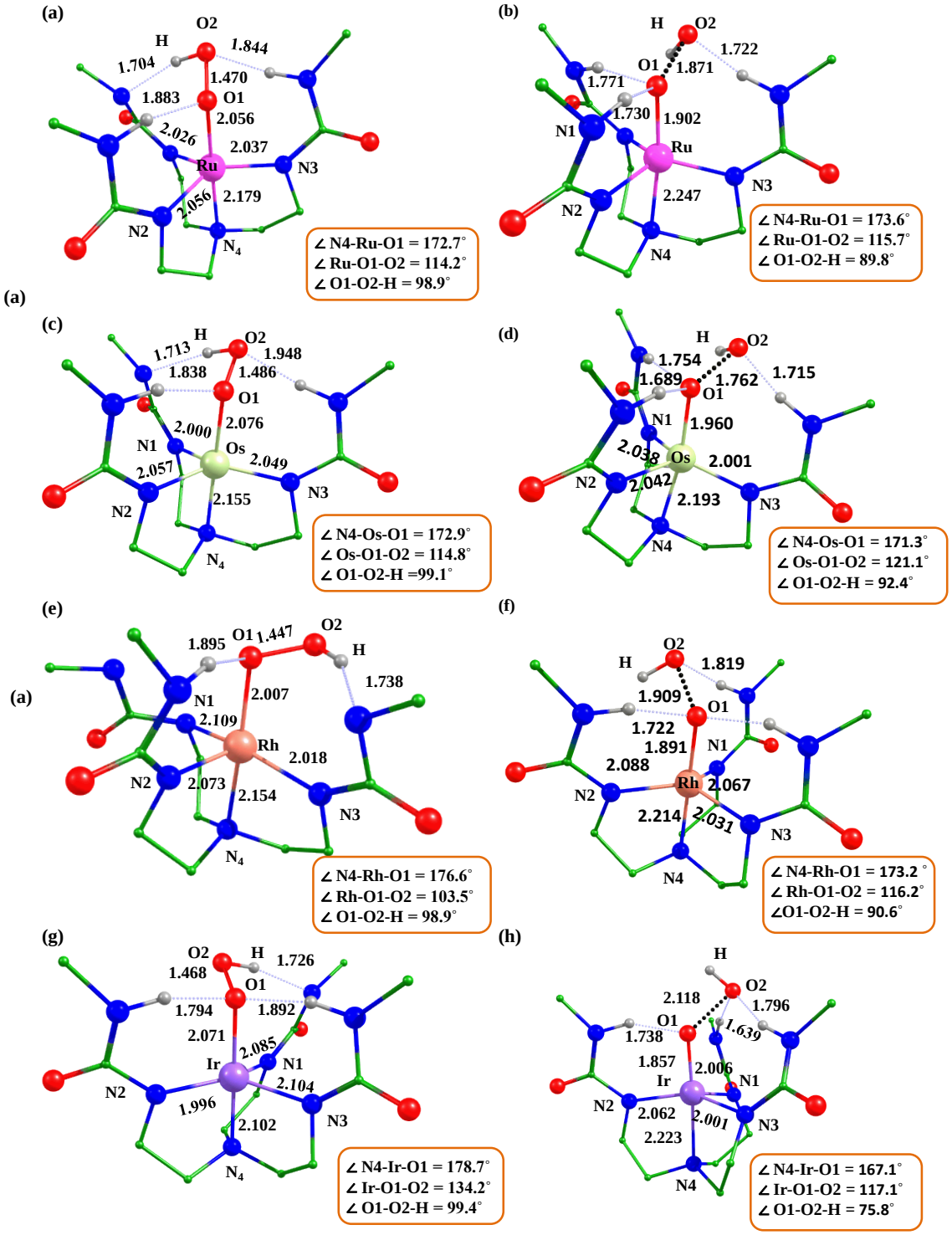

Figure 6.19. B3LYP-D2 optimized structure of ground state $^{2}VIIB_{hs}$, $^{2}VIIIB_{hs}$, $^{1}IXB_{hs}$, $^{1}XB_{is,}$ and $^{4}VB_{hs,}$ and their corresponding transition states $^{2}VIIB_{ls}$-ts, $^{2}VIIIB_{hs}$-ts, $^{3}IXB_{hs}$-ts, $^{1}XB_{is}$-ts.

6.3.3 Comparative study

Computed O---O bond cleavage barrier heights are relatively higher with Co, Ni, and Cu hydroperoxo species than the Cr, Mn, and Fe species. This higher barrier height with (Co, Ni, Cu) species may be due to the pairing of β-electron in the *d*-orbital which decreases the *d*-*d* exchange interaction due to which electronic repulsion increases, which increases the O---O bond cleavage barrier height. Earlier Cr, Mn, Fe species have more number of unpaired electrons as compared to Co, Ni, and Cu species due to which earlier hydroperoxo species (Cr, Mn, Fe) have smaller barrier height of O---O bond cleavage due to enhanced exchange reactivity, which states more the number of unpaired electron more will be the reactivity.[73] Along with this, we saw that filling of an electron in antibonding orbitals starts after d^6 electronic configuration, and due to occupancy of an electron in antibonding orbital decreases bond order which is computed by wiberg bond index, which in turn increases the barrier for O---O bond cleavage. After the O---O bond cleavage metal-oxo species with $OH^{\cdot}/OH^{-}$ are formed, we have computed the energties of these species also. Energy of *d* orbital depends upon the effective nuclear charge on metal, as on going from left to right in periodic table, energy of metal *d* orbitals decreases with increase in the oxidation state of metal. As in early transition metals *d* orbitals are at a higher energy level than the filled O (2*p*) orbital. Due to a decrease in metal *d* orbital energy, this results in incomparable energy of metal *d* orbital and O (2*p*) orbital. From, the computed energies we have found that the energies of metal-oxo (Co-O, Ni-O, and Cu-O) are much higher than that of metal-oxo of Cr-O, Mn-O, and Fe-O with both the 14-TMC and buea ligand (see Figure 6.20). This indicates the instability of late transition metal-oxo species. From, the Computed structural parameters (see Table AX 6.1 and Table AX 6.3 of appendix), we have found that Co-O, Ni-O, and Cu-O bond lengths are longer than the normal metal-oxo bond length with both 14-TMC and buea ligands, and these

long bond lengths are supported by computed smaller metal-oxo (Co-O, Ni-O, and Cu-O) vibrational frequencies (see Table 6.2).

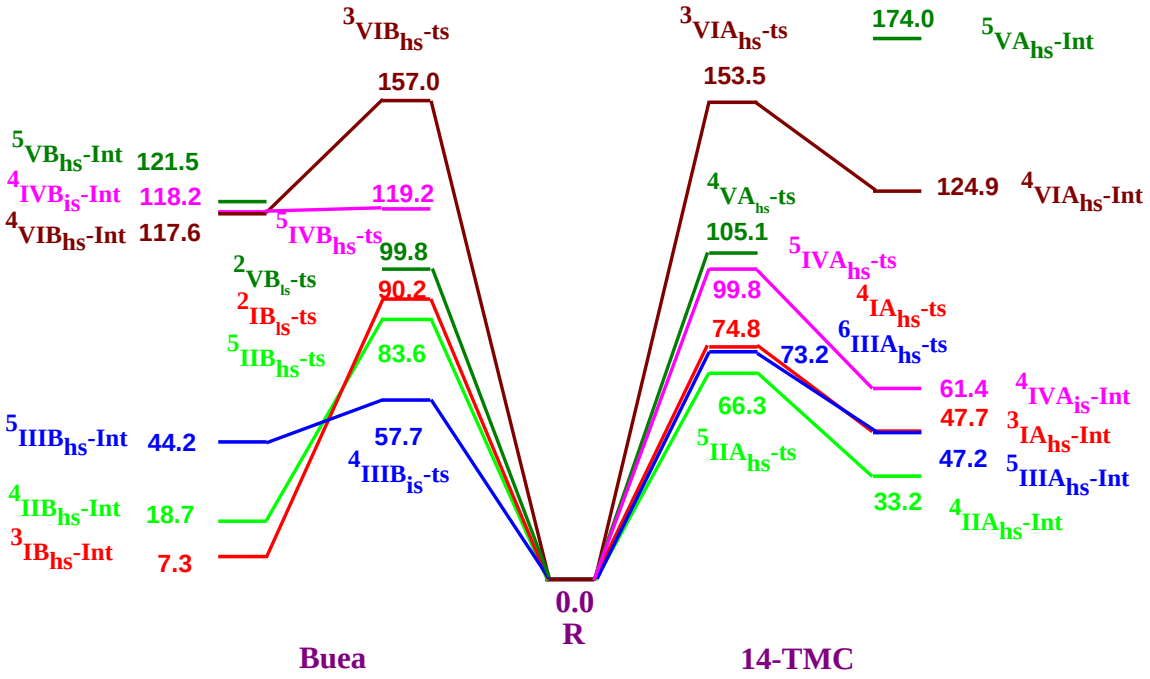

Figure 6.20. B3LYP-D2 computed energy surface for the formation of metal-oxo from metalhydroperoxo with 14-TMC and buea ligand.

Cobalt-oxo bond length is longer also supported by the experiment results.[73-75] These data indicates that the late transition metal-oxo bond has a single bond character. Spin densities at oxygen in metal-oxo (Co, Ni, and Cu) are 0.884/0.664, 1.571/1.104, and 1.362/1.169 with TMC and buea ligand respectively. Metal-oxo bond length and the spin densities at metal and oxygen atoms of metal-oxo show that there exists the valence tautomerism between metal and oxygen.[76] All these support the formation of metal-oxyl and its reactive nature. Intramolecular H-bonding is present in the buea ligand which stabilizes the molecule (see Figure 6.18 and 6.20) that the energy of metal-oxo species formed after O---O bond cleavage with buea ligand has smaller energy as compared to metal-oxo species formed with 14-TMC ligand except for Co^{IV}=O. DFT calculations have been also performed for the formation of terminal metal-oxo species of first the two different ligands.

6.4 Conclusions

From our DFT calculations, we have predicted that O---O bond cleavage in metal hydroperoxo species occurs homolytically and the barrier for O---O cleavage are higher with the late transition metal hydroperoxo species (Co, Ni, Cu) than that of earlier metal-hydroperoxo species (Cr, Mn, Fe) in both the geometries, this higher barrier height of late transition metals (Co, Ni, and Cu) species may be because the pairing of the electron in *d* orbital of metals starts due to which the *d-d* electron exchange interactions decreases due to which the electron-electron repulsion gets dominated which increases the O---O bond cleavage which in turn decreases the stability of metal-oxo. In the earlier transition metal, there are vacant orbital present due to which they can easily accept the electrons donated by oxygen and can easily form the π bond while in the late transition metals there exist the repulsion between the metal filled *d*-orbital electrons and the electron donated by an oxygen atom and thus they do not form the π bond easily. This is also supported in Ru, Rh, Os, and Ir hydroperoxo species. Transition metals from Cr to Cu hydroperoxo species, the computed energies, we have found that metal-oxo of Co, Ni, and Cu are relatively at higher energy than that of Cr, Mn, and Fe oxo species. From, the computed structural parameter of metal-oxo and spin density at metal and oxygen atom suggests that valence tautomerism exists between metal and oxygen in late transition metal-oxo species (Co, Ni, and Cu). Thus, we can say that the metal-oxo of the late transition metal series exists as metal-oxyl. Metal-oxo species acts as a reactive intermediate in the oxidation reaction, along with these are also involved in O-O bond formation. The formation of metal-oxyl seems to be important for O-O coupling.

Their convincing evidence are available for the involvement of these reactive intermediates in many metal-mediated catalytic nucleophilic and electrophilic reactions which are familiar in

biology and chemistry. The study of these species with structure and function relations may lead to a general system that functionalizes the C-H bond or carry group transfer reactions.

6.5 References

(1) Nam, W. *Acc. Chem. Res.* **2007**, *40*, 465-634.

(2) de Montellano, P. R. O. *Chem. Rev.* **2010**, *110*, 932-948.

(3) Krest, C. M.; Onderko, E. L.; Yosca, T. H.; Calixto, J. C.; Karp, R. F.; Livada, J.; Rittle, J.; Green, M. T. *J. Biol.Chem.* **2013**, *288*, 17074-17081.

(4) Nocera, D. G. *Acc. Chem. Res.* **2012**, *45*, 767-776.

(5) Blakemore, J. D.; Crabtree, R. H.; Brudvig, G. W. *Chem. Rev.* **2015**, *115*, 12974-13005.

(6) Comba, P.; Rajaraman, G. *Inorg. Chem.* **2008**, *47*, 78-93.

(7) Bautz, J.; Comba, P.; Laorden, C. L.; Menzel, M.; Rajaraman, G. *Angew. Chem., Int. Ed.* **2007**, *46*, 8067-8070.

(8) Comba, P.; Rajaraman, G.; Rohwer, H. *Inorg. Chem.* **2007**, *46*, 3826-3838.

(9) de Montellano, P. R. O. *Cytochrome P450: Structure, Mechanism and Biochemistry*; Kluwer Academic/Plenum Publishers, 3rd Ed. New York, **2004**.

(10) Rittle, J.; Green, M. T. *Science* **2010**, *330*, 933-937.

(11) Meunier, B. Ed. *Metal-Oxo and Metal-Peroxo Species in Catalytic Oxidations* Springer-Verlag; Berlin, Germany, 2000.

(12) de Montellano, P. R. O. *Cytochrome P450: Structure, Mechanism, and Biochemistry*, Kluwer Academic/Plenum Publishers, 3rd Ed. New York, **2005**.

(13) Sono, M.; Roach, M. P.; Coulter, E. D.; Dawson, J. H. *Chem. Rev.* **1996**, *96*, 2841-2887.

(14) Groves, J. T. *Proc. Natl. Acad. Sci. U.S.A.* **2003**, *100*, 3569-3574.

(15) Denisov, I. G.; Makris, T.M.; Sligar, S. G.; Schlichting, I. *Chem. Rev.* **2005**, *105*, 2253-2277.

(16) Makris, T. M.; Koenig, K. V.; Schlichting, I.; Sligar, S. G. *J. Inorg. Biochem.* **2006**, *100*, 507-518.

(17) Meunier, B.; de Visser, S. P.; Shaik, S. *Chem. Rev.* **2004**, *104*, 3947-3980.

(18) Betley, T. A.; Wu, Q.; Voorhis, T. V.; Nocera, D. G. *Inorg. Chem.* **2008**, *47*, 1849-1861.

(19) Mullins, C. S.; Pecoraro, V. L. *Coord. Chem. Rev.* **2008**, *252*, 416-443.

(20) Cady, C. W.; Crabtree, R. H.; Brudvig, G. W. *Coord. Chem. Rev.* **2008**, *252*, 444-455.

(21) McEvoy, J. P.; Brudvig, G. W. *Chem. Rev.* **2006**, *106*, 4455-4483.

(22) Nocera, D. G. *Inorg. Chem*. **2009**, *48*, 10001-10017.

(23) McEvoy, J.P.; Brudvig, G. W. *Chem. Rev.* **2006**, *106*, 4455-4483.

(24) Lewis, N. S.; Nocera, D. G. *Proc. Natl. Acad. Sci. U.S.A.* **2006**, *103*, 15729-15735.

(25) Winkler, J. R.; Gray, H. B. *Struct. Bond.* **2012**, *142*, 17-28.

(26) Ballhausen, C. J.; Gray, H. B. *Inorg. Chem.* **1962**, *1*, 111-122.

(27) Ray, K.; Heims, F.; Pfaff, F. F. *Inorg. Chem.* **2013**, *22*, 3784-3807.

(28) Cho, J.; Woo, J.; Han J. E.; Kubo, M.; Ogurab, T.; Nam, W. *Chem. Sci.* **2011**, *2*, 2057-2062.

(29) Chen, Z.; Yin, G. *Chem. Soc. Rev.* **2015**, *44*, 1083-1100.

(30) Liu, L. V.; Hong, S.; Cho, J.; Nam, W.; Solomon, E. I. *J. Am. Chem. Soc.* **2013**, *135*, 3286-3299.

(31) Chen, Z.; Yin, G. *Chem. Soc. Rev.* **2015**, *44*, 1083-1100.

(32) Neu, H. M.; Baglia, R. A.; Goldberg, D. P. *Acc. Chem. Res.* **2015**, *48*, 2754-2764.

(33) Swart, M.; Costas, M. *Spin States in Biochemistry and Inorganic Chemistry: Influence on Structure and Reactivity*, Wiley, 2015.

(34) Pattanayak, S.; Jasiewski, A. J.; Rana, A.; Draksharapu, A.; Kundan, K. S.; Wietz, A.; Hendrich, M.; Que, L., Jr.; Dey, A.; Gupta, S. S. *Inorg. Chem.* **2017**, *56*, 6352-6361.

(35) Mukherjee, G.; Calvin, W. Z.; Lee, S. S.; Nag, A. A.; Cantu F. G.; Reinhard, D. K.; Sastri, C. V.; de Visser, S. P. *Dalton Trans*. **2018**, *47*, 14945-14957.

(36) Kleespies, S. T.; Oloo, W. N.; Mukherjee, A.; Que, L., Jr. *Inorg. Chem.* **2015**, *54*, 5053-5064.

(37) Hohenberger, J.; Ray, K.; Meyer, K. *Nat. Commun.* **2012**, *3*, 720-732.

(38) Nam, W.; Lee, Y.-M.; Fukuzumi, S. *Acc. Chem. Res.* **2014**, *47*, 1146-1154.

(39) Ray, K.; Pfaff, F. F.; Wang, B.; Nam, W. *J. Am. Chem. Soc.* **2014**, *136*, 13942-13958.

(40) Gunay, A.; Theopold, K. H. *Chem. Rev.* **2010**, *110*, 1060-1081.

(41) Janardanan, D.; Wang, Y.; Schyman, P.; Que, L., Jr.; Shaik, S. *Angew. Chem., Int. Ed.* **2010**, *49*, 3342-3345.

(42) Mayer, J. M. *Inorg. Chem.* **1988**, *8*, 125-135.

(43) Holm, R. H. *Chem. Rev.* **1987**, *87*, 1401-1449.

(44) Gray, H. B.; Winkler, J. R.; *Acc. Chem. Res.* **2018**, *51*, 1850-1857.

(45) Mukerjee, S.; Skogerson, K.; DeGala, S.; Caradonna, J. P. *Inorg. Chim. Acta*. **2000**, *297*, 313-329.

(46) Gray, H. B.; Hare, C. R. *Inorg. Chem.* **1962**, *1*, 363-368.

(47) OHalloran, K. P.; Zhao, C.; Ando, N. S.; Schultz, A. J.; Koetzle T. F.; Piccoli, P. M. B.; Hedman, B.; Hodgson, K. O.; Bobyr, E.; kirk, M. L.; Knottenbelt, S.; Depperman, E. C.; Stein, B.; Anderson, T. M.; Cao, R.; Geletii, Y. V.; Hardcastle, K. I.; Musaev, D. G.; Neiwert, W. A.; Fang, X.; MoroKuma, K. *Inorg. Chem.* **2012**, *51*, 7025-7031.

(48) Hong, S.; Pfaff, F. F.; Kwon, E.; Wang, Y.; Seo, M.-S.; Bill, E.; Ray, K.; Nam, W. *Angew. Chem., Int. Ed.* **2014**, *53*, 10403-10407.

(49) Grapperhaus, C. A.; Mienert, B.; Bill, E.; Weyhermüller, T.; Wieghardt, K. *Inorg. Chem.* **2000**, *39*, 5306-5317.

(50) Parsell, T. H.; Yang, M. Y.; Borovik, A. S. *J. Am. Chem. Soc.* **2009**, *131*, 2762-2763.

(51) Gupta, R.; Borovik, A. S. *J. Am. Chem. Soc.* **2003**, *125*, 13234-13242.

(52) Gupta, R.; MacBeth, C. E.; Young, V. G.; Borovik, A. S. *J. Am. Chem. Soc.* **2002**, *124*, 1136-1137.

(53) Shirin, Z.; Hammes, B. S.; Young, V. G.; Borovik, A. S. *J. Am. Chem. Soc.* **2000**, *122*, 1836-1837.

(54) Frisch, M. J.; Trucks, G. W.; Schlegel, H. B.; Scuseria, G. E.; Robb, M. A.; Cheeseman, J. R.; Scalmani, G.; Barone, V.; Petersson, G. A.; Nakatsuji, H.; Li, X.; Caricato, M.; Marenich, A. V.; Bloino, J.; Janesko, B. G.; Gomperts, R.; Mennucci, B.; Hratchian, H. P.; Ortiz, J. V.; Izmaylov, A. F.; Sonnenberg, J. L.; Williams-Young, D.; Ding, F.; Lipparini, F.; Egidi, F.; Goings, J.; Peng, B.; Petrone, A.; Henderson, T.; Ranasinghe, D.; Zakrzewski, V. G.; Gao, J.; Rega, N.; Zheng, G.; Liang, W.; Hada, M.; Ehara, M.; Toyota, K.; Fukuda, R.; Hasegawa, J.; Ishida, M.; Nakajima, T.; Honda, Y.; Kitao, O.; Nakai, H.; Vreven, T.; Throssell, K.; Montgomery, J. A., Jr.; Peralta, J. E.; Ogliaro, F.; Bearpark, M. J.; Heyd, J. J.; Brothers, E. N.; Kudin, K. N.; Staroverov, V. N.; Keith, T. A.; Kobayashi, R.; Normand, J.; Raghavachari, K. A.; Rendell, P.; Burant, J. C.; Iyengar, S. S.; Tomasi, J.; Martin, C. M.; Millam, J. M.; Klene, M.; Adamo, C.; Cammi, R.; Ochterski, J. W.; Morokuma, R. L. K. O.; Farkas, F. J. B.; Fox, D. J. Gaussian, Inc., Wallingford CT, 2016.

(55) Becke, A. D. *J. Chem. Phys*. **1993**, *98*, 5648-5652.

(56) Lee, C.; Yang, W.; Parr, R. G. *Phys. Rev. B: Condens. Matter Mater. Phys*. **1988**, *37*, 785-789.

(57) Grimme, S. *J. Comput. Chem.* **2006**, *27*, 1787-1799.

(58) Chai, J. D.; Head-Gordon, M. *Phys. Chem. Chem. Phys.* **2008**, *10*, 6615-6620.

(59) Ansari, A.; Kaushik, A.; Rajaraman, G. *J. Am. Chem. Soc.* **2013**, *135*, 4235-4249.

(60) Ansari, A.; Jayapal, P.; Rajaraman, G. *Angew. Chem., Int. Ed.* **2015**, *127*, 564-568.

(61) Engelmann, X.; Monte-Pérez, I.; Ray, K. *Angew. Chem., Int. Ed.* **2016**, *55*, 7632-7649.

(62) Monika; Ansari, A. *New J. Chem.* **2020**, *44*, 19103-19112.

(63) Ansari, A.; Ansari, M.; Singha A.; Rajaraman, G. *Chem. -Eur. J.* **2017**, *23*, 10110-10125.

(64) Ansari, A.; Jayapal, P.; Rajaraman, G. *Angew. Chem., Int. Ed.* **2015**, *127*, 564-568.

(65) Kumar, R.; Ansari, A.; Rajaraman, G. *Chem. -Eur. J.* **2018**, *24*, 6660-6860.

(66) Dunning, T. H. Jr.; Hay, P. J. *In Modern Theoretical Chemistry* (Ed: Schaefer, H. F.), Plenum, New York, 1976; Vol. 3.

(67) Hay, P. J.; Wadt, W. R. *J. Chem. Phys.* **1985**, *82*, 270-283.

(68) Neisen, B. D.; Gagnon N. L.; Dhar D.; Spaeth A. D.; Tolman B. W. *J. Am. Chem. Soc.* **2017**, *139*, 10220-10223.

(69) Schaefer, A.; Horn, H.; Ahlrichs, R. *J. Chem. Phys.* **1992**, *97*, 2571-2577.

(70) Schaefer, C.; Huber, C.; Ahlrichs, R. *Chem. Phys.* **1994**, *100*, 5829-5835.

(71) Pfaff, F. F.; Kundu, S.; Risch, M.; Pandian, S.; Heims, S.; Ray, P.; Haack, P.; Metzinger, R.; Bill, E.; Dau, H.; Comba, P. *Angew. Chem., Int. Ed.* **2011**, *50*, 1711-1715.

(72) Shaik, S.; Chen, H.; Janardanan, D. *Nat. Chem.* **2011**, *3*, 19-27.

(73) Swart, M. A. *Chem. Commun.* **2013**, *49*, 6650-6652.

(74) Prakash, J.; Rohde T. G.; Meier, K. K.; Jasniewski, A. J.; Heuvelen, K. M. V.; Munck, E.; Que, L., Jr. *J. Am. Chem. Soc.* **2015**, *137*, 3478-3481.

(75) Lacy, D. C.; Park, Y. J.; Ziller, J. W.; Yano, J.; Borovik, A. S. *J. Am. Chem. Soc.* **2012**, *134*, 17526-17535.

(76) Shimoyama, Y.; Kojima, T. *Inorg. Chem.* **2019**, *58*, 9517-9542.

Summary and Conclusions

Summary and Conclusions

The main scope of the present Ph.D. thesis is to understand the electronic structures of metal complexes, formation of high valent metal-oxo and reaction mechanism of the oxygen atom transfer, C-H and O-H bond activation by different high valent metal-oxo/hydroxo/superoxo complexes. The specific problems chosen here are listed below

1. In the first section, we have focused on the exploration of electronic structures of TAML derivate iron monomer and dinuclear species. We have also explored the magnetic exchange coupling constant of μ-oxo and μ-1,2-peroxo diiron TAML derivate species. NBO plots show the ionic and covalent character of the metal-oxygen bond. The nitrogen atom coordinated to the iron matal gains electrons density via the electron delocalization mechanism. The significant spin density at the oxygen atom can be a witness for C-H/O-H/N-H bond activation.
2. In the second section, we have focused on the mechanistic study of allylic oxidation of cyclohex-2-enol to cyclohex-2-enone by using iron(V)-oxo as the oxidant. Here, we have proposed two pathways (***pathway a*** and ***pathway b***), from the computed energy it is found that, barrier height of the C-H bond is small as compare to O-H bond and the second step is barrier-less i.e. C-H bond activation is more favorable than O-H bond activation (***pathway b***). From the computed eigenvalue plot and bond angle it is found that C-H/O-H bond activation occurs via the proton coupled electron transfer mechanism followed by the π pathway. Along with we have also studied the oxygen atom transfer mechanism (epoxidation) that leads to the formation of cyclohexane epoxide, and found that the barrier for oxygen atom transfer is higher than ***pathway a*** and ***pathway b***. This is the first computational study to discuss a comparative study on C-H *vs*. O-H bond activation along with oxygen attack towards cyclohex-2-enol by Fe(V)-oxo species. A significant exchange of metal electrons and

change in structural parameters during transition states can influence reactivity and help to design a potential oxidant for catalytic transformation reactions.

3. In the third section, we have studied the electronic structure of metal-superoxo species with chromium, manganese, iron, and cobalt-superoxo species with two different ring size TMC ligand and also tested their reactivity towards C-H bond activation. From the calculations it is predicted that the 13-TMC ligated superoxo species are more reactive towards C-H bond activation except for iron-superoxo species and first hydrogen abstraction is the rate-determining step in all the studied species, occurs via proton-coupled electron transfer mechanism. The computed bond angles ∠N1-M-N3 and ∠N2-M-N4 show more contraction with 13-TMC species than the 14-TMC which in turn pushes the metal out of the plane and hence increase the reactivity of electrophilic reaction. Our calculations show that the ring size of the TMC ligand plays an important role to control reactivity. By tuning the ring size one can alter the reactivity of metal-superoxo species towards organic substrates.
4. In the fourth section, we have attempted to explore the reason behind the formation of oxo wall in between group 8 and group 9. Metal-oxo species are formed from O---O bond cleavage of metal-hydroperoxo. Here, we have taken the Cr, Mn, Fe, Co, Ni, and Cu with two different geometry octahedral (14-TMC) and trigonal bipyramidal (buea), and it is found that the barrier for O---O bond cleavage is higher with late transition metal hydroperoxo (Co, Ni, and Cu). This is due to enhance exchanged reactivity (EER). As the pairing of electrons starts in the late transition series by which enhance exchange reactivity decreases and the bond order of metal-oxo bond also decreases. This is also supported by 4*d* and 5*d* transition metals (Ru, Rh, Os, and Ir). Computed spin density at oxo and metal-oxo bond distance suggests that the earlier transition metal forms metal-oxo while the late transition metal forms metal-

oxyl. Metal-oxo of the late transition metal series exists as metal-oxyl. Metal-oxo species acts as a reactive intermediate in the oxidation reaction, along with these are also involved in O-O bond formation. The formation of metal-oxyl seems to be important for O-O coupling. These reactive intermediates are involved in many metal-mediated catalytic nucleophilic and electrophilic reactions which are familiar in biology and chemistry. The study of these species with structure and function relations may lead to a general system that functionalizes the C-H bond or carry group transfer reactions.

To this end, our findings on metal complexes and biomimetic catalytic reactions will provide clues to experimentalists to enhance the reactivity/selectivity/efficiency and can be able to predict better high valent non-heme metal catalysts which can be used in several catalytical transformation reactions.

Appendix

Appendix IV

Table AX 4.1. B3LYP computed structural parameters of the $[Fe^{V}(TAML)O]^{-}$ species, intermediates, transition states and product of *Pathway a*.

	Bond lengths (Å)										Bond angle (°)					
	Fe-N1	Fe-N2	Fe-N3	Fe-N4	Fe-O1	O1-H1	O1-H2	H1-O2	H2-C1	C1-O2	Fe-O1-H1	Fe-O1-H2	O1-H1-O2	O1-H2-C1	N1-Fe-N3	N2-Fe-N4
^{4}I	1.880	1.880	1.910	1.910	1.665	-	-	-	-	-	-	-	-	-	156.1	156.1
^{2}I	1.889	1.889	1.894	1.894	1.629	-	-	-	-	-	-	-	-	-	152.3	152.3
$^{4}ts_{a}$-1	1.897	1.902	1.878	1.878	1.720	1.142	-	1.289	-	1.443	117.2	-	174.2	-	154.2	154.4
$^{2}ts_{a}$-1	1.872	1.897	1.895	1.881	1.725	1.116	-	1.326	-	1.430	111.4	-	171.9	-	156.0	152.4
^{6}Int	1.892	1.908	1.910	1.918	1.910	0.979	-	-	-	-	-	-	-	-	154.4	150.3
^{4}Int	1.881	1.881	1.879	1.879	1.806	0.981	-	-	-	-	-	-	-	-	154.7	154.7
^{2} Int							-	-	-	-	-	-	-	-		
$^{6}ts_{a\text{-}hs}$	1.920	1.882	1.887	1.890	2.020	-	1.277	-	1.358	-	-	126.6	-	174.6	158.9	151.5
$^{4}ts_{a\text{-}hs}$	1.887	1.901	1.904	1.890	1.994	-	1.471	-	1.238	-	-	141.3	-	175.7	154.4	155.5
$^{4}ts_{a}$-2_{is}	1.889	1.895	1.885	1.898	1.911	-	1.549	-	1.200	-	-	141.4	-	172.6	156.3	152.7
$^{2}ts_{a}$-2_{is}	1.891	1.892	1.908	1.909	1.966	-	1.307	-	1.327	-	-	140.7	-	175.0	155.3	154.8
$^{2}ts_{a}$-2_{ls}	1.874	1.877	1.886	1.876	1.867	-	1.432	-	1.248	-	-	141.7	-	173.2	159.8	154.1
^{6}P	1.978	1.978	1.909	1.909	-	-	-	-	-	-	-	-	-	-	166.6	166.6
^{4}P	1.863	1.863	1.870	1.870	-	-	-	-	-	-	-	-	-	-	172.0	172.0
^{2}P	1.858	1.870	1.852	1.861	-	-	-	-	-	-	-	-	-	-	171.3	171.3

Table AX 4.2. wB97XD computed structural parameters of the $[Fe^{V}(TAML)O]^{-}$ species, intermediates, transition states and product of *Pathway a*.

	Bond lengths (Å)										Bond angle (°)					
	Fe-N1	Fe-N2	Fe-N3	Fe-N4	Fe-O1	O1-H1	O1-H2	H1-O2	H2-C1	C1-O2	Fe-O1-H1	Fe-O1-H2	O1-H1-O2	O1-H2-C1	N1-Fe-N3	N2-Fe-N4
^{4}I	1.876	1.877	1.883	1.882	1.638	-	-	-	-	-	-	-	-	-	153.9	153.9
^{2}I	1.868	1.870	1.857	1.858	1.667	-	-	-	-	-	-	-	-	-	152.9	153.2
$^{4}ts_{a}$-1	1.860	1.861	1.857	1.870	1.742	1.098	-	1.275	-	1.423	118.7	-	167.1	-	159.0	153.7
$^{2}ts_{a}$-1	1.854	1.868	1.871	1.861	1.760	1.139	-	1.203	-	1.439	119.2	-	119.2	-	153.9	154.9
^{6}Int	1.875	1.890	1.891	1.899	1.889	0.972	-	-	-	-	-	-	-	-	154.6	150.5
^{4}Int	1.867	1.865	1.859	1.859	1.784	0.975	-	-	-	-	-	-	-	-	155.5	155.5
^{2} Int	1.903	1.804	1.913	1.810	1.735	0.977	-	-	-	-	-	-	-	-	163.7	1.810
$^{6}ts_{a\text{-}hs}$	1.872	1.880	1.864	1.844	2.017	-	1.241	-	1.371	-	-	116.2	-	172.2	157.8	156.7
$^{4}ts_{a\text{-}hs}$	1.904	1.890	1.887	1.901	1.994	-	1.471	-	1.238	-	-	141.3	-	175.8	154.4	155.5
$^{4}ts_{a}$-2_{is}	1.885	1.893	1.902	1.877	1.942	-	1.417	-	1.245	-	-	129.3	-	171.2	155.5	155.5
$^{2}ts_{a}$-2_{is}	1.909	1.891	1.892	1.908	1.966	-	1.307	-	1.327	-	-	140.7	-	175.0	155.4	154.8
$^{2}ts_{a}$-2_{ls}	1.900	1.907	1.874	1.879	1.971	-	1.226	-	1.379	-	-	130.9	-	172.4	156.4	154.9
^{6}P	1.959	1.959	1.908	1.908	-	-	-	-	-	-	-	-	-	-	162.3	162.3
^{4}P	1.849	1.858	1.858	1.858	-	-	-	-	-	-	-	-	-	-	172.1	172.1
^{2}P	1.831	1.852	1.833	1.863	-	-	-	-	-	-	-	-	-	-	172.0	172.2

Table AX 4.3. B3LYP computed spin density values of the $[Fe^{V}(TAML)O]^{-}$ species, intermediates , transition states and product of *Pathway a*.

	Fe1	O1	H1	H2	O2	C1
^{4}I	1.274	0.766	-	-	-	-
^{2}I	1.040	0.580	-	-	-	-
$^{4}ts_{a}$-1	1.649	0.251	0.251	-	0.419	-
$^{2}ts_{a}$-1	1.653	0.153	0.012	-	-0.382	-
^{6}Int	3.206	0.381	0.004	-	-	-
^{4}Int	1.804	0.037	0.009	-	-	-
^{2}Int	0	0	0	-	-	-
$^{6}ts_{a}$-2_{hs}	3.217	0.195	-	0.195	0.583	0.151
$^{4}ts_{a}$-2_{hs}	3.154	0.197	-	-0.123	-0.688	0.004
$^{4}ts_{a}$-2_{is}	2.358	0.026	-	0.116	0.757	-0.028
$^{2}ts_{a}$-2_{is}	2.450	0.062	-	-0.115	-0.614	-0.077
$^{2}ts_{a}$-2_{ls}	-0.003	-0.050	-	0.166	-0.031	0.084
^{6}P	3.921	-	-	-	-	-
^{4}P	2.664	-	-	-	-	-
^{2}P	1.228	-	-	-	-	-

Table AX 4.4. wB97XD computed spin density values of the $[Fe^{V}(TAML)O]^{-}$ species and their intermediates and transition states and product of *Pathway a*.

	Fe1	O1	H1	H2	O2	C1
^{4}I	2.312	0.645	-	-	-	-
^{2}I	1.577	-0.708	-	-	-	-
$^{4}ts_{a}$-1	1.500	0.414	-0.033	-	0.496	-
$^{2}ts_{a}$-1	1.866	-0.433	0.052	-	-0.531	-
^{6}Int	3.273	0.381	0.003	-	-	-
^{4}Int	1.804	0.014	0.009	-	-	-
^{2}Int	0.805	-0.601	0.393	-	-	-
$^{6}ts_{a}$-2_{hs}	3.211	0.222	-	0.101	0.560	0.178
$^{4}ts_{a}$-2_{hs}	3.154	0.197	-	-0.123	-0.688	0.004
$^{4}ts_{a}$-2_{is}	2.618	0.124	-	0.108	0.714	0.023
$^{2}ts_{a}$-2_{is}	2.451	0.062	-	0.008	-0.614	-0.077
$^{2}ts_{a}$-2_{ls}	2.628	0.067	-	-0.109	-0.584	-0.137
^{6}P	3.996	-	-	-	-	-
^{4}P	2.744	-	-	-	-	-
^{2}P	0.990	-	-	-	-	-

Table AX 4.5. B3LYP-D2/B3LYP/wB97XD computed structural parameters of the transition states of *Pathway b*.

	Bond lengths (Å)									Bond angle (°)						
	Fe-N1	Fe-N2	Fe-N3	Fe-N4	Fe-O1	O1-H1	O1-H2	H1-O2	H2-C1	C1-O2	Fe-O1-H2	Fe-O1-H1	O1-H2-C1	O1-H1-O2	N1-Fe-N3	N2-Fe-N4
B3LYP-D2																
^4ts_b-1	1.920	1.915	1.890	1.893	1.740	-	1.371	-	1.199	1.445	134.9	-	174.2	-	152.3	153.5
^2ts_b-1	1.877	1.894	1.873	1.892	1.684	-	1.470	-	1.178	1.441	116.0	-	161.3	-	150.8	154.1
^6ts_b-2_{hs}	2.027	2.035	1.973	1.963	1.993	1.807	-	1.009	-	1.343	-	114.8	-	116.7	144.4	145.0
^2ts_b-2_{is}	1.876	1.879	1.891	1.879	1.844	2.220	-	0.983	-	1.377	-	103.5	-	105.6	155.8	158.4
B3LYP																
^4ts_b-1	1.910	1.901	1.904	1.914	1.777	-	1.266	-	1.257	1.444	160.3	-	160.3	-	151.6	152.2
^2ts_b-1	1.874	1.883	1.883	1.883	1.737	-	1.336	-	1.242	1.442	117.5	-	152.3	-	153.6	153.0
^6ts_b-2_{hs}	2.035	1.972	1.962	1.972	1.993	1.807	-	1.008	-	1.343	-	114.8	-	116.7	145.0	144.3
^2ts_b-2_{is}	1.891	1.893	1.898	1.898	2.138	1.554	-	1.058	-	1.342	-	120.8	-	125.3	160.3	158.1
^2ts_b-2_{is}	1.879	1.891	1.878	1.876	1.843	2.220	-	0.982	-	1.377	-	103.5	-	105.5	155.7	158.4
^2ts_b-2_{ls}	1.880	1.884	1.896	1.886	1.882	2.317	-	0.981	-	1.373	-	109.7	-	99.0	158.1	154.5
wB97XD																
^4ts_b-1	1.880	1.895	1.893	1.874	1.739	-	1.452	-	1.162	1.439	134.2	-	174.6	-	152.2	154.2
^2ts_b-1	1.874	1.883	1.883	1.894	1.737	-	1.336	-	1.242	1.442	117.5	-	152.3	-	153.6	153.0
^6ts_b-2_{hs}	2.006	1.964	1.952	1.997	2.008	1.770	-	1.010	-	1.320	-	111.5	-	116.2	147.0	145.6
^2ts_b-2_{is}	1.876	1.885	1.886	1.879	2.124	1.511	-	1.066	-	1.329	-	117.6	-	125.7	160.3	158.7

Table AX 4.6. B3LYP-D2/B3LYP/wB97XD computed spin density values of the transition states of *Pathway b*.

B3LYP-D2	Fe	O1	H1	H2	O2	C1
			B3LYP-D2			
$^{4}ts_{b}$-1	2.853	0.267		0.008		-0.138
$^{2}ts_{b}$-1	1.462	-0.225		0.014		-0.157
$^{6}ts_{b}$-2_{hs}	3.981	0.133	-0.004		0.001	-0.097
$^{2}ts_{b}$-2_{is}	1.386	0.086	-0.006		-0.034	-0.437
			B3LYP			
$^{4}ts_{b}$-1	2.998	0.134		0.026		-0.287
$^{2}ts_{b}$-1	1.668	-0.374		0.035		-0.311
$^{6}ts_{b}$-2_{hs}	3.980	0.133	-0.004		0.001	-0.097
$^{2}ts_{b}$-2_{is}	2.672	0.059	-0.000		0.012	0.015
$^{2}ts_{b}$-2_{is}	1.386	0.086	-0.006		-0.034	-0.437
$^{2}ts_{b}$-2_{ls}	1.277	0.105	-0.004		-0.037	-0.391
			wB97XD			
$^{4}ts_{b}$-1	3.010	0.032		0.000		-0.177
$^{2}ts_{b}$-1	1.668	-0.374		0.035		-0.317
$^{6}ts_{b}$-2_{hs}	4.049	0.107	-0.000		0.004	-0.000
$^{2}ts_{b}$-2_{is}	2.734	0.074	0.004		0.006	0.004

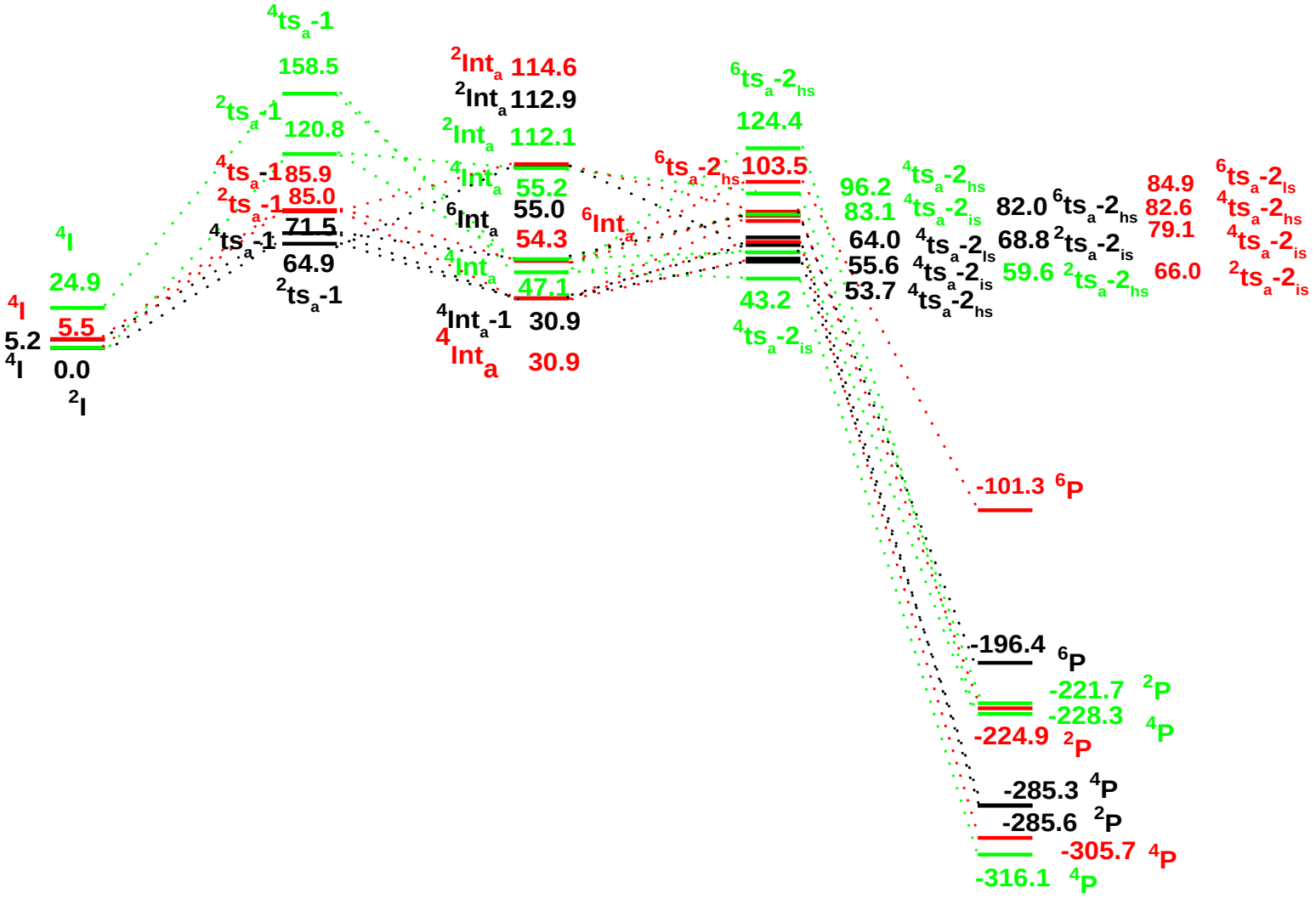

Figure AX 4.1. B3LYP-D2 (black), B3LYP (red) and wB97XD (green) computed energy surface for the ground state of the ***pathway a*** (ΔG in $kJmol^{-1}$).

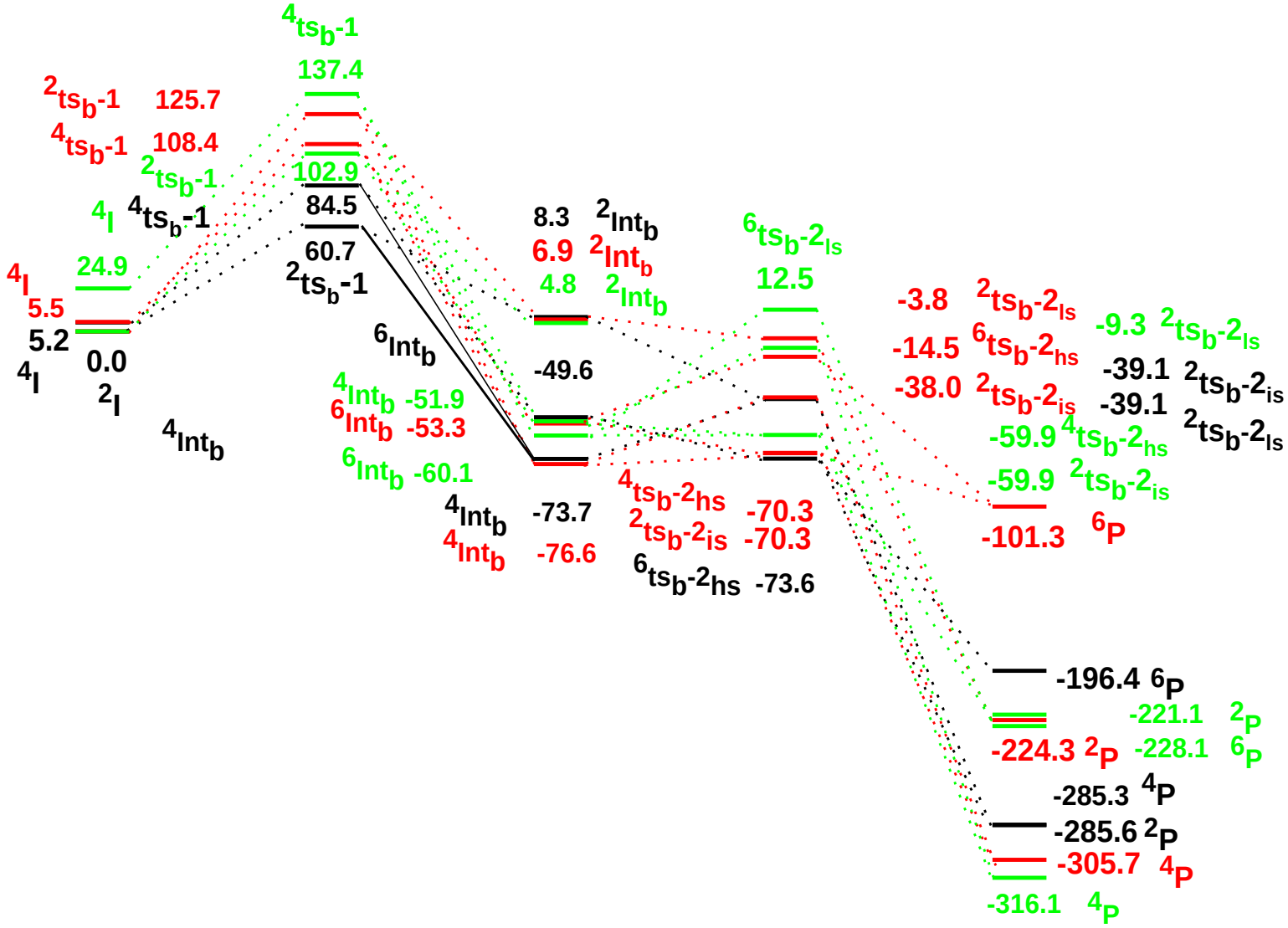

Figure AX 4.2. B3LYP-D2 (black), B3LYP (red) and wB97XD (green) computed energy surface for the ground state of the ***pathway b*** (ΔG in kJmol^{-1}).

Appendix V

Table AX 5.1. B3LYP-D2 computed selective structural parameters of metal-superoxo species, intermediates, transition states and product with 13-TMC ligand.

	Bond length(Å)												Bond angle(˚)					
Spin State	M-O1	O1-O2	M-Cl	M-N1	M-N2	M-N3	M-N4	M-N_{avg}	O2-H1	O2-H2	C-H	O2-C2	MO1O2	O1-M-Cl	O2-H1-C1	O2-H2-C2	N4-M-N5	N6-M-N7
									$[V(13\text{-}TMC)O_2Cl]^+$									
$^4I_{a\text{-}hs}$	1.939	1.369	2.378	2.178	2.145	2.149	2.150	2.155	-	-	-	-	141.1	174.9	-	-	167.9	162.1
$^2I_{a\text{-}hs}$	1.740	1.347	2.369	2.168	2.146	2.156	2.165	2.159	-	-	-	-	176.4	176.3	-	-	167.9	164.4
$^4I_{a\text{-}hs}$-ts1	1.871	1.445	2.416	2.150	2.183	2.155	2.149	2.159	1.407	-	1.221	-	136.2	173.8	175.1	-	165.2	167.8
$^2I_{a\text{-}hs}$-ts1	1.867	1.438	2.415	2.152	2.179	2.155	2.153	2.159	1.364	-	1.246	-	138.9	174.9	177.2	-	167.9	165.0
$^2I_{a\text{-}ls}$-ts1	1.852	1.442	2.408	2.150	2.177	2.152	2.151	8.630	1.355	-	1.253	-	139.9	175.3	177.7	-	165.1	167.9
$^4I_{a\text{-}hs}$-Int	1.874	1.516	2.411	2.146	2.186	2.155	2.143	2.157	-	-	-	-	132.8	172.6	-	-	166.2	167.9
$^2I_{als}$-Int	1.648	1.977	2.437	2.134	2.109	2.164	2.165	2.143	-	-	-	-	131.1	131.1	-	-	161.2	162.2
$^4I_{a\text{-}hs}$-ts2	1.781	1.896	2.461	2.180	2.170	2.125	2.154	2.157	-	1.546	-	1.190	135.9	173.5	-	175.7	165.9	169.5
^2I_a-P	1.621	-	2.451	2.162	2.162	2.139	2.148	2.153	-	-	-	-	-	175.7	-	-	166.7	168.2
Ref[1]	1.568	-	-	-	-	-	-	-	-	-	-	-	-	-	-	-	-	-
									$[Cr(13\text{-}TMC)O_2Cl]^+$									
$^5II_{a\text{-}hs}$	2.039	1.372	2.380	2.154	2.106	2.115	2.123	2.124	-	-	-	-	133.9	171.8	-	-	168.7	163.4
$^3II_{a\text{-}hs}$	1.975	1.365	2.386	2.155	2.112	2.116	2.127	2.127	-	-	-	-	135.6	171.5	-	-	168.6	164.4
$^3II_{a\text{-}ls}$	1.906	1.366	2.366	2.153	2.112	2.114	2.125	2.126	-	-	-	-	139.8	172.4	-	-	168.5	164.6
$^1II_{a\text{-}ls}$	1.925	1.364	2.368	2.153	2.109	2.115	2.127	2.126	-	-	-	-	140.2	172.3	-	-	168.6	164.5
$^5II_{a\text{-}hs}$-ts1	1.951	1.452	2.404	2.122	2.155	2.110	2.112	2.125	1.343	-	1.252	-	131.4	173.1	175.6	-	165.5	169.3
$^3II_{a\text{-}hs}$-ts1	1.946	1.447	2.407	2.130	2.155	2.111	2.111	2.127	1.298	-	1.289	-	132.0	171.0	173.8	-	166.0	168.8
$^3II_{a\text{-}ls}$-ts1	1.906	1.446	2.390	2.130	2.156	2.111	2.110	2.127	1.309	-	1.280	-	134.0	171.7	175.1	-	165.9	168.8
$^1II_{a\text{-}ls}$-ts1	1.906	1.446	2.390	2.130	2.156	2.111	2.110	2.127	1.345	-	1.258	-	134.0	171.7		-	165.9	168.8
$^5II_{a\text{-}hs}$-Int	1.739	2.179	2.397	2.160	2.122	2.111	2.115	2.127	-	-	-	-	136.8	174.2	-	-	166.3	168.5
$^3II_{a\text{-}ls}$-	1.918	1.518	2.384	2.109	2.113	2.154	2.119	2.124	-	-	-	-	129.7	173.1	-	-	168.6	166.5

Int																		
$^{5}II_{a\text{-}hs}$-ts2	1.941	1.749	2.423	2.127	2.139	2.146	2.087	2.125	-	1.557	-	1.192	131.5	172.8	-	177.6	164.7	170.5
$^{3}II_{a\text{-}ls}$-ts2	1.851	1.668	2.414	2.151	2.152	2.086	2.122	2.128	-	1.766	-	1.144	131.5	169.9	-	1.766	166.2	170.1
$^{3}II_{a\text{-}hs}$-P	1.720	-	2.419	2.137	2.134	2.118	2.123	2.128	-	-	-	-	-	177.0	-	-	165.1	168.8
$^{1}II_{a\text{-}ls}$-P	1.584	-	2.392	2.151	2.151	2.105	2.117	2.131	-	-	-	-	-	176.1	-	-	168.0	170.4
$[Mn(13\text{-}TMC)O_2Cl]^+$																		
$^{6}III_{a\text{-}hs}$	2.284	1.379	2.482	2.137	2.075	2.114	2.096	2.105	-	-	-	-	133.7	175.2	-	-	168.9	159.6
$^{4}III_{a\text{-}hs}$	2.078	1.323	2.352	2.231	2.202	2.237	2.161	2.208	-	-	-	-	133.8	170.7	-	-	163.7	158.6
$^{4}III_{a\text{-}is}$	1.967	1.365	2.336	2.136	2.073	2.082	2.102	2.098	-	-	-	-	135.2	170.9	-	-	169.9	163.8
$^{2}III_{a\text{-}is}$	1.910	1.359	2.327	2.135	2.074	2.085	2.103	2.099	-	-	-	-	138.9	173.3	-	-	170.7	164.8
$^{2}III_{a\text{-}ls}$	1.909	1.359	2.326	2.135	2.074	2.085	2.103	2.099	-	-	-	-	138.9	173.3	-	-	170.7	164.8
$^{6}III_{a\text{-}hs}$-ts1	1.931	1.434	2.344	2.238	2.146	2.241	2.183	2.202	1.358	-	1.251	-	131.6	170.5	172.8	-	165.1	162.5
$^{4}III_{a\text{-}hs}$-ts1	1.938	1.426	2.348	2.193	2.232	2.167	2.230	2.205	1.305	-	1.296	-	131.9	169.1	168.5	-	162.3	165.0
$^{4}III_{a\text{-}is}$-ts1	1.901	1.449	2.353	2.095	2.139	2.075	2.079	2.097	1.360	-	1.244	-	132.0	173.3	175.7	-	166.1	171.1
$^{2}III_{a\text{-}is}$-ts1	1.897	1.443	2.357	2.106	2.140	2.075	2.078	2.099	1.315	-	1.279	-	132.5	171.3	173.3	-	166.9	170.5
$^{2}III_{a\text{-}ls}$-ts1	1.886	1.446	2.358	2.105	2.142	2.075	2.078	2.100	1.330	-	1.266	-	132.9	171.7	175.0	-	166.7	170.5
$^{6}III_{a\text{-}hs}$-Int	2.092	1.521	2.493	2.191	2.066	2.159	2.069	2.121	-	-	-	-	129.3	174.6	-	-	168.6	164.8
$^{4}III_{a\text{-}is}$-Int	1.904	1.524	2.358	2.079	2.133	2.083	2.082	2.094	-	-	-	-	127.7	172.6	-	-	170.2	167.0
$^{2}III_{a\text{-}ls}$-Int	2.256	1.320	2.482	2.137	2.075	2.113	2.096	2.105	-	-	-	-	141.1	170.8	-	-	168.9	159.5
$^{4}III_{a\text{-}is}$-ts2	1.811	1.747	2.399	2.088	2.126	2.130	2.051	2.099	-	1.728	-	1.150	130.2	169.2	-	172.3	166.7	170.9
$^{2}III_{a\text{-}ls}$-ts2	1.839	1.653	2.371	2.090	2.133	2.137	2.050	2.102	-	1.765	-	1.145	132.1	170.5	-	173.5	166.8	171.9
$^{4}III_{a\text{-}hs}$-P	1.686	-	2.415	2.103	2.109	2.085	2.099	2.099	-	-	-	-	-	177.1	-	-	166.0	169.0
$^{2}III_{a\text{-}ls}$-P	1.640	-	2.377	2.114	2.115	2.081	2.092	2.100	-	-	-	-	-	176.6	-	-	166.7	170.2
$[Fe(13\text{-}TMC)O_2Cl]^+$																		

$^{7}IV_{a\text{-}hs}$	2.145	1.322	2.364	2.181	2.172	2.209	2.163	2.181	-	-	-	-	155.5	176.4	-	-	163.3	154.3
$^{5}IV_{a\text{-}hs}$	1.983	1.349	2.352	2.181	2.158	2.186	2.186	2.178	-	-	-	-	147.5	176.6	-	-	164.1	158.2
$^{5}IV_{a\text{-}is}$	2.283	1.359	2.443	2.111	2.046	2.078	2.085	2.080	-	-	-	-	134.8	175.3	-	-	158.5	170.3
$^{3}IV_{a\text{-}is}$	2.175	1.369	2.435	2.125	2.048	2.087	2.084	2.086	-	-	-	-	136.0	175.1	-	-	170.8	160.7
$^{3}IV_{a\text{-}ls}$	1.988	1.363	2.338	2.114	2.053	2.059	2.076	2.075	-	-	-	-	131.2	169.6	-	-	170.4	165.4
$^{1}IV_{a\text{-}ls}$	1.956	1.356	2.345	2.061	2.053	2.112	2.073	2.075	-	-	-	-	131.8	171.7	-	-	166.1	171.1
$^{7}IV_{a\text{-}hs}$-ts1	1.970	1.417	2.390	2.183	2.194	2.201	2.167	2.186	1.341	-	1.263	-	143.8	175.9	178.5	-	164.3	160.3
$^{5}IV_{a\text{-}hs}$-ts1	1.941	1.421	2.385	2.198	2.165	2.182	2.194	2.185	1.334	-	1.263	-	142.0	175.5	177.6	-	160.7	164.4
$^{5}IV_{a\text{-}is}$-ts1	1.950	1.426	2.349	2.145	2.188	2.150	2.209	2.173	1.358	-	1.251	-	129.3	169.2	170.9	-	163.0	165.5
$^{3}IV_{a\text{-}is}$-ts1	1.966	1.417	2.364	2.154	2.184	2.157	2.204	2.175	1.295	-	1.305	-	130.3	168.7	169.2	-	165.6	163.0
$^{3}IV_{a\text{-}ls}$-ts1	1.885	1.449	2.355	2.056	2.069	2.116	2.054	2.074	1.370	-	1.239	-	130.0	173.1	176.1	-	167.6	171.4
$^{1}IV_{a\text{-}ls}$-ts1	1.886	1.448	2.357	2.052	2.075	2.118	2.051	2.074	1.337	-	1.262	-	129.8	171.9	174.8	-	171.4	168.0
$^{7}IV_{a\text{-}hs}$-Int	1.970	1.497	2.376	2.157	2.178	2.192	2.207	2.183	-	-	-	-	138.5	164.0	-	-	160.7	164.0
$^{5}IV_{a\text{-}is}$-Int	2.079	1.518	2.463	2.076	2.129	2.050	2.086	2.085	-	-	-	-	130.1	175.4	-	-	164.5	171.3
$^{3}IV_{a\text{-}ls}$-Int	1.878	1.524	2.345	2.056	2.063	2.111	2.059	2.072	-	-	-	-	127.1	172.7	-	-	171.3	168.5
$^{7}IV_{a\text{-}hs}$-ts2	1.967	1.732	2.408	2.202	2.177	2.185	2.151	2.179	-	1.599	-	1.181	133.6	172.7	-	176.8	161.1	167.5
$^{5}IV_{a\text{-}is}$-ts2	1.929	1.639	2.437	2.176	2.210	2.179	2.186	2.187	-	1.592	-	1.183	139.6	172.6	-	175.1	161.9	166.9
$^{3}IV_{a\text{-}ls}$-ts2	1.816	1.714	2.375	2.107	2.112	2.022	2.063	2.076	-	1.701	-	1.156	132.1	171.3	-	172.5	167.9	172.4
$^{5}IV_{a\text{-}hs}$-P	1.663	-	2.322	2.147	2.169	2.183	2.205	2.176	-	-	-	-	-	176.9	-	-	162.3	165.2
$^{3}IV_{a\text{-}is}$-P	1.663	-	2.364	2.093	2.099	2.053	2.071	2.079	-	-	-	-	-	177.3	-	-	171.0	167.1
$^{1}IV_{a\text{-}ls}$-P	1.674	-	2.353	2.090	2.090	2.058	2.070	2.077	-	-	-	-	-	176.7	-	-	170.7	166.7
$^{2}V_{a\text{-}ls}$	1.980	1.354	2.349	2.055	2.093	2.027	2.036	2.053	-	-	-	-	130.8	171.4	-	-	166.9	171.6
Exp.[2]		1.34																
									$[Co(13\text{-}TMC)O_2Cl]^+$									
$^{2}V_{a\text{-}ls}$-	1.953	1.443	2.365	2.026	2.059	2.100	2.024	2.052	1.285	-	1.301	-	128.6	170.3	172.5	-	171.6	168.1

ts1																		
$^{2}V_{a\text{-}ls}$-Int	1.958	1.528	2.340	2.041	2.091	2.023	2.029	2.046	-	-	-	-	124.5	173.1	-	-	168.1	172.4
$^{2}V_{a\text{-}ls}$-ts2	1.901	1.738	2.371	2.135	2.113	2.076	2.087	2.103	-	1.607	-	1.180	128.8	172.5	174.9	-	175.6	175.2
$^{5}V_{a\text{-}hs}$-P	1.921	-	2.334	2.207	2.179	2.183	2.158	2.182	-	-	-	-	175.5	-	-	-	165.4	153.5
$^{3}V_{a\text{-}is}$-P	1.657	-	2.286	2.132	2.193	2.132	2.189	2.161	-	-	-	-	177.1	-	-	-	164.6	168.2
$^{1}V_{a\text{-}ls}$-P	1.853	-	2.351	2.066	2.062	2.024	2.038	2.047	-	-	-	-	178.4	-	-	-	172.1	165.2
Exp.[3]	1.72	-	-	-	-	-	-	2.02	-	-	-	-	-	-	-	-	-	-

Table AX 5.2. B3LYP-D2 computed selective structural parameters of metal-superoxo species, intermediates, transition states and product with 14-TMC ligand.

	Bond Length (Å)								Bond Angel (˚)									
Spin State	M-O1	O1-O2	M-Cl	M-N1	M-N2	M-N3	M-N4	M-N_{avg}	O2-H1	O2-H2	H1-C1	H2-C1	MO1O2	O1-M-Cl	O2-H1-C1	O2-H2-C2	N1-M-N2	N3-M-N4
								[V(14-TMC)O_2Cl]$^+$										
$^4I_{b\text{-}hs}$	1.911	1.370	2.382	2.207	2.188	2.197	2.215	2.202	-	-	-	-	140.0	174.3	-	-	173.1	172.7
$^2I_{b\text{-}hs}$	1.741	1.343	2.371	2.200	2.207	2.200	2.207	2.203	-	-	-	-	173.7	176.1	-	-	173.9	173.9
$^4I_{b\text{-}hs}$-ts1	1.858	1.445	2.419	2.193	2.225	2.213	2.184	2.196	1.407	-	1.216	-	135.3	173.4	176.2	-	174.4	174.6
$^2I_{b\text{-}hs}$-ts1	1.856	1.439	2.418	2.225	2.209	2.186	2.196	2.204	1.364	-	1.239	-	137.5	174.6	178.1	-	174.4	174.5
$^2I_{b\text{-}ls}$-ts1	1.841	1.442	2.412	2.193	2.221	2.206	2.185	2.201	1.355	-	1.244	-	137.5	174.6	178.8	-	174.7	174.4
$^4I_{b\text{-}hs}$-Int	1.859	1.515	2.412	2.180	2.217	2.223	2.192	2.203	-	-	-	-	132.3	172.3	-	-	175.4	175.0
$^2I_{b\text{-}ls}$-Int	1.655	1.912	2.443	2.132	2.216	2.219	2.156	2.181	-	-	-	-	129.7	169.1	-	-	176.6	174.4
$^4I_{b\text{-}hs}$-ts2	1.733	2.074	2.464	2.221	2.196	2.204	2.222	2.211	-	1.550	-	1.211	148.6	178.2	-	173.3	176.2	175.7
$^2I_{b\text{-}hs}$-P	1.616	-	2.451	2.193	2.204	2.192	2.205	2.198		-	-	-	-	176.7	-	-	176.2	176.2
								[Cr(14-TMC)O_2Cl]$^+$										
$^5II_{b\text{-}hs}$	2.021	1.371	2.382	2.179	2.167	2.152	2.177	2.169	-	-	-	-	132.4	172.3	-	-	173.3	172.9
$^3II_{b\text{-}hs}$	1.958	1.363	2.388	2.183	2.167	2.154	2.182	2.171	-	-	-	-	134.7	172.4	-	-	173.8	173.6
$^3II_{b\text{-}ls}$	1.889	1.365	2.368	2.180	2.167	2.154	2.183	2.171	-	-	-	-	139.2	173.2	-	-	174.2	174.0
$^1II_{b\text{-}ls}$	1.909	1.363	2.368	2.180	2.155	2.165	2.177	2.169	-	-	-	-	139.7	173.4	-	-	174.0	173.8
Exp.[4]	1.876	1.231	2.316	-	-	-	-	-		-	-	-	146.3	174.5	-	-	-	-
$^5II_{b\text{-}hs}$-ts1	1.937	1.451	2.406	2.186	2.151	2.161	2.189	2.172	1.343	-	1.250	-	130.7	172.3	172.7	-	174.2	174.3
$^3II_{b\text{-}hs}$-ts1	1.930	1.447	2.409	2.189	2.157	2.168	2.181	2.174	1.298	-	1.286	-	131.9	170.9	170.0	-	174.8	174.7
$^3II_{b\text{-}ls}$-ts1	1.914	1.449	2.390	2.150	2.159	2.187	2.181	2.169	1.309	-	1.247	-	133.1	173.1	173.9	-	174.2	174.3
$^1II_{b\text{-}ls}$-ts1	1.888	1.447	2.390	2.184	2.151	2.162	2.187	2.171	1.345	-	1.258	-	134.2	173.1	-	-	174.6	174.8
$^5II_{b\text{-}hs}$-Int	1.943	1.516	2.397	2.147	2.183	2.196	2.161	2.172	-	-	-	-	127.5	172.0	-	-	175.1	174.6
$^3II_{b\text{-}ls}$-Int	1.894	1.518	2.386	2.161	2.144	2.185	2.196	2.171	-	-	-	-	129.2	171.8	-	-	175.3	174.9
$^5II_{b\text{-}hs}$-ts2	1.911	1.754	2.431	2.159	2.159	2.202	2.202	2.180	-	1.561	-	1.194	127.2	176.7	-	179.6	174.5	174.5
$^3II_{b\text{-}ls}$-ts2	1.867	1.706	2.432	2.156	2.155	2.208	2.208	2.182	-	1.683	-	1.163	125.6	175.1	-	179.0	175.1	175.1
$^3II_{b\text{-}hs}$-P	1.715	-	2.419	2.167	2.167	2.176	2.176	2.171	-	-	-	-	-	176.8	-	-	174.5	174.5
$^1II_{b\text{-}ls}$-P	1.580	-	2.387	2.176	2.182	2.175	2.182	2.179	-	-	-	-	-	176.9	-	-	176.6	176.6
Exp.[5]	1.698	-	2.383											176.8				

									[Mn(14-TMC)O_2Cl]$^+$									
^{6}III$_{b\text{-}hs}$	2.107	1.355	2.393	2.289	2.292	2.122	2.151	2.213	-	-	-	-	133.2	171.8	-	-	170.5	170.2
^{4}III$_{b\text{-}hs}$	2.043	1.322	2.354	2.254	2.273	2.217	2.268	2.253	-	-	-	-	133.1	171.4	-	-	169.6	170.0
^{4}III$_{b\text{-}is}$	1.966	1.365	2.331	2.162	2.137	2.129	2.153	2.145	-	-	-	-	132.8	171.7	-	-	173.7	173.1
^{2}III$_{b\text{-}is}$	1.918	1.357	2.333	2.158	2.161	2.132	2.139	2.147	-	-	-	-	134.5	172.4	-	-	173.8	174.1
^{2}III$_{b\text{-}ls}$	1.884	1.357	2.328	2.157	2.141	2.134	2.158	2.079	-	-	-	-	139.2	173.8	-	-	174.2	174.01
^{6}III$_{b\text{-}hs}$-ts1	1.922	1.430	2.346	2.257	2.265	2.268	2.219	2.252	1.358	-	1.242	-	130.6	171.3	169.6	-	172.7	172.8
^{4}III$_{b\text{-}hs}$-ts1	1.928	1.423	2.353	2.257	2.253	2.276	2.230	2.254	1.305	-	1.296	-	131.3	169.6	167.2	-	173.1	173.2
^{4}III$_{b\text{-}is}$-ts1	1.886	1.447	2.348	2.166	2.134	2.128	2.166	2.148	1.360	-	1.240	-	131.2	172.5	169.7	-	174.8	174.8
^{2}III$_{b\text{-}is}$-ts1	1.881	1.442	2.354	2.140	2.157	2.169	2.133	2.149	1.315	-	1.275	-	132.4	171.2	169.3	-	175.2	175.1
^{2}III$_{b\text{-}ls}$-ts1	1.869	1.444	2.355	2.136	2.158	2.169	2.134	2.149	1.330	-	1.262	-	133.3	171.6	170.9	-	175.1	175.2
^{6}III$_{a\text{-}hs}$-Int	1.916	1.511	2.344	2.132	2.318	2.179	2.313	2.235	-	-	-	-	127.8	169.9	-	-	173.7	173.7
^{4}III$_{a\text{-}is}$-Int	1.885	1.519	2.351	2.117	2.162	2.175	2.130	2.146	-	-	-	-	127.1	171.2	-	-	175.8	175.3
^{2}III$_{a\text{-}ls}$-Int	1.767	1.537	2.343	2.128	2.173	2.184	2.135	2.155	-	-	-	-	130.1	170.8	-	-	176.7	176.3
^{4}III$_{b\text{-}is}$-ts2	1.839	1.654	2.341	2.304	2.209	2.304	2.184	2.250	-	1.769	-	1.146	130.8	168.6	-	173.6	174.8	173.6
^{2}III$_{b\text{-}ls}$-ts2	1.814	1.641	2.369	2.147	2.155	2.147	2.180	2.157	-	1.800	-	1.141	133.9	169.2	-	178.2	175.7	176.7
^{4}III$_{b\text{-}hs}$-P	1.680	-	2.417	2.134	2.157	2.134	2.157	2.145	-	-	-	-	-	2.417	-	-	175.1	175.1
^{2}III$_{b\text{-}ls}$-P	1.637	-	2.370	2.143	2.154	2.143	2.153	2.148	-	-	-	-	-	2.370	-	-	175.6	175.5
									[Fe(14-TMC)O_2Cl]$^+$									
^{7}IV$_{b\text{-}hs}$	2.116	1.327	2.371	2.215	2.223	2.224	2.226	2.222	-	-	-	-	148.1	175.6	-	-	167.6	167.9
^{5}IV$_{b\text{-}hs}$	1.950	1.348	2.355	2.221	2.239	2.213	2.237	2.227	-	-	-	-	145.3	176.0	-	-	170.7	170.2
^{5}IV$_{b\text{-}is}$	2.172	1.364	2.444	2.149	2.135	2.152	2.124	2.140	-	-	-	-	134.9	173.6	-	-	171.3	170.8
^{3}IV$_{b\text{-}is}$	2.160	1.304	2.386	2.232	2.181	2.242	2.215	2.217	-	-	-	-	132.6	173.0	-	-	169.8	170.6
^{3}IV$_{b\text{-}ls}$	1.976	1.363	2.339	2.115	2.130	2.136	2.103	2.121	-	-	-	-	129.5	171.3	-	-	174.6	174.1
^{1}IV$_{b\text{-}ls}$	1.929	1.355	2.346	2.112	2.138	2.136	2.106	2.123	-	-	-	-	130.8	171.7	-	-	174.7	174.9
^{7}IV$_{b\text{-}hs}$-ts1	1.942	1.417	2.395	2.224	2.209	2.241	2.252	2.231	1.341	-	1.258	-	142.3	175.9	178.9	-	171.8	171.8
^{5}IV$_{b\text{-}hs}$-ts1	1.916	1.420	2.391	2.252	2.224	2.210	2.235	2.230	1.334	-	1.259	-	141.1	175.5	177.7	-	172.3	172.1
^{5}IV$_{b\text{-}is}$-ts1	1.947	1.420	2.365	2.263	2.207	2.218	2.190	2.219	1.358	-	1.251	-	128.9	170.5	168.6	-	173.7	173.4
^{3}IV$_{b\text{-}is}$-ts1	1.961	1.412	2.377	2.257	2.213	2.225	2.195	2.222	1.295	-	1.306	-	130.5	169.9	167.0	-	173.5	173.8
^{3}IV$_{b\text{-}ls}$-ts1	1.871	1.447	2.351	2.110	2.150	2.137	2.103	2.125	1.370	-	1.232	-	129.0	172.2	167.0	-	175.7	175.3
^{1}IV$_{b\text{-}ls}$-ts1	1.867	1.447	2.354	2.105	2.111	2.139	2.146	2.125	1.337	-	1.257	-	129.3	171.2	170.5	-	175.9	175.7
^{7}IV$_{b\text{-}hs}$-	1.953	1.495	2.378	2.209	2.229	2.247	2.231	2.229	-	-	-	-	134.8	173.5	-	-	173.0	172.4

Int																		
$^{5}IV_{b\text{-}is}$-Int	2.021	1.514	2.457	2.124	2.166	2.151	2.156	2.149	-	-	-	-	130.6	130.6	-	-	174.5	174.3
$^{3}IV_{b\text{-}ls}$-Int	1.858	1.522	2.344	2.137	2.157	2.106	2.108	2.127	-	-	-	-	126.5	171.4	-	-	176.4	175.9
$^{7}IV_{b\text{-}hs}$-ts2	1.927	1.724	2.403	2.209	2.229	2.260	2.237	2.233	-	1.604	-	1.180	134.4	172.9	-	174.7	173.6	172.6
$^{5}IV_{b\text{-}is}$-ts2	1.802	1.716	2.369	2.100	2.109	2.160	2.142	2.128	-	1.699	-	1.159	130.7	172.0	-	170.8	175.7	176.2
$^{3}IV_{b\text{-}ls}$-ts2	1.802	1.716	2.369	2.100	2.109	2.160	2.142	2.128	-	1.699	-	1.158	130.7	172.0	-	170.7	176.2	175.7
$^{5}IV_{b\text{-}hs}$-P	1.659	-	2.327	2.202	2.202	2.238	2.237	2.219	-	-	-	-	-	177.5	-	-	173.4	173.4
$^{3}IV_{b\text{-}is}$-P	1.657	-	2.362	2.195	2.235	2.207	2.242	2.219	-	-	-	-	-	178.1	-	-	175.4	175.4
$^{1}IV_{b\text{-}ls}$-P	1.669	-	2.347	2.119	2.128	2.119	2.128	2.123	-	-	-	-	-	176.9	-	-	175.3	175.3
Exp.[6]	1.646	-	-	2.067	2.069	2.109	2.117	-	-	-	-	-	-	-	-	-	-	-
								$[Co(14\text{-}TMC)O_2Cl]^+$										
$^{2}V_{b\text{-}ls}$	1.959	1.351	2.348	2.116	2.114	2.116	2.086	2.116	-	-	-	-	129.4	171.6	-	-	174.9	175.1
$^{2}V_{b\text{-}ls}$-ts1	1.939	1.443	2.359	2.089	2.112	2.127	2.083	2.103	1.310	-	1.296	-	127.7	170.4	172.5	-	175.4	175.7
$^{2}V_{b\text{-}ls}$-Int	1.934	1.525	2.342	2.080	2.133	2.114	2.073	2.100	-	-	-	-	123.9	171.2	-	-	176.2	175.7
$^{2}V_{b\text{-}ls}$-ts2	1.926	1.736	2.375	2.073	2.083	2.001	2.044	2.050	-	1.612	-	1.176	130.1	172.4		175.5	167.0	172.9
$^{5}V_{b\text{-}hs}$-P	1.872	-	2.374	2.221	2.225	2.221	2.226	2.223	-	-	-	-	-	174.4	-	-	170.9	170.9
$^{3}V_{b\text{-}is}$-P	1.647	-	2.284	2.199	2.221	2.199	2.221	2.210	-	-	-	-	-	177.5	-	-	173.9	173.8
$^{1}V_{b\text{-}ls}$-P	1.835	-	2.353	2.090	2.098	2.090	2.099	2.094	-	-	-	-	-	177.4	-	-	173.7	173.7

Table AX 5.3. B3LYP-D2 computed spin density values of metal-superoxo species, intermediates, transition states and product with 13-TMC.

Spin State	M	O1	O2	C1
		$[V(13\text{-}TMC)O_2Cl]^+$		
$^4I_{a\text{-}hs}$	2.143	0.236	0.699	-
$^2I_{a\text{-}hs}$	1.960	-0.397	-0.451	-
$^4I_{a\text{-}hs}$-ts1	2.150	-0.011	0.477	0.264
$^2I_{a\text{-}hs}$-ts1	2.162	-0.153	-0.380	-0.283
$^4I_{a\text{-}hs}$-Int	2.121	-0.091	0.076	-
$^2I_{als}$-Int	0	0	0	-
$^4I_{a\text{-}hs}$-ts2	1.985	0.218	0.348	-0.049
^2I_a-P	1.267	-0.195	-	-
		$[Cr(13\text{-}TMC)O_2Cl]^+$		
$^5II_{a\text{-}hs}$	3.219	0.317	0.643	-
$^3II_{a\text{-}hs}$	3.221	-0.397	-0.627	-
$^3II_{a\text{-}ls}$	1.161	0.308	0.606	-
$^1II_{a\text{-}ls}$	1.117	-0.383	-0.648	-
$^5II_{a\text{-}hs}$-ts1	3.170	0.079	0.432	0.301
$^3II_{a\text{-}hs}$-ts1	3.173	-0.106	-0.34	-0.327
$^3II_{a\text{-}ls}$-ts1	1.169	-0.017	0.383	0.319
$^1II_{a\text{-}ls}$-ts1	-1.116	0.102	0.403	0.297
$^5II_{a\text{-}hs}$-Int	1.137	-0.067	0.0136	-
$^3II_{a\text{-}ls}$-Int	1.137	-0.067	0.013	-
$^5II_{a\text{-}hs}$-ts2	3.149	0.376	0.001	-0.118
$^3II_{a\text{-}ls}$-ts2	1.195	0.219	-0.107	-0.115
$^3II_{a\text{-}hs}$-P	2.761	-0.566	-	-
$^1II_{a\text{-}ls}$-P	0	0	-	-
		$[Mn(13\text{-}TMC)O_2Cl]^+$		
$^6III_{a\text{-}hs}$	4.012	0.467	0.637	-
$^4III_{a\text{-}hs}$	4.336	-0.621	-0.765	-
$^4III_{a\text{-}is}$	2.165	0.353	0.613	-
$^2III_{a\text{-}is}$	-0.006	0.353	0.641	-
$^2III_{a\text{-}ls}$	-0.007	0.353	0.641	-
$^6III_{a\text{-}hs}$-ts1	4.100	-0.030	0.371	0.282
$^4III_{a\text{-}hs}$-ts1	4.149	-0.244	-0.384	-0.324
$^4III_{a\text{-}is}$-ts1	2.087	0.1066	0.435	0.288
$^2III_{a\text{-}is}$-ts1	2.092	-0.064	-0.349	-0.316
$^2III_{a\text{-}ls}$-ts1	0.086	0.003	0.392	0.306
$^6III_{a\text{-}hs}$-Int	3.998	0.083	0.027	-

$^{4}III_{a\text{-}is}$-Int	2.093	0.038	0.017	-
$^{2}III_{a\text{-}ls}$-Int	0	-	-	-
$^{4}III_{a\text{-}is}$-ts2	2.194	0.329	-0.160	-0.122
$^{2}III_{a\text{-}ls}$-ts2	0.037	0.297	-0.079	-0.113
$^{4}III_{a\text{-}hs}$-P	2.625	0.555	-	-
$^{2}III_{a\text{-}ls}$-P	1.083	0.012	-	-
$[Fe(13\text{-}TMC)O_2Cl]^+$				
$^{7}IV_{a\text{-}hs}$	3.903	0.687	0.810	-
$^{5}IV_{a\text{-}hs}$	3.938	-0.106	-0.512	-
$^{5}IV_{a\text{-}is}$	2.861	0.542	0.687	-
$^{3}IV_{a\text{-}is}$	3.448	-0.705	-0.842	-
$^{3}IV_{a\text{-}ls}$	1.179	0.329	0.628	-
$^{1}IV_{a\text{-}ls}$	1.233	-0.402	-0.664	-
$^{7}IV_{a\text{-}hs}$-ts1	3.923	0.429	0.502	0.301
$^{5}IV_{a\text{-}hs}$-ts1	3.932	0.232	-0.251	-0.300
$^{5}IV_{a\text{-}is}$-ts1	3.115	-0.040	0.315	0.275
$^{3}IV_{a\text{-}is}$-ts1	3.198	-0.290	-0.433	-0.331
$^{3}IV_{a\text{-}ls}$-ts1	1.028	0.142	0.432	0.282
$^{1}IV_{a\text{-}ls}$-ts1	1.038	-0.014	-0.389	-0.302
$^{7}IV_{a\text{-}hs}$-Int	3.971	0.269	0.052	-
$^{5}IV_{a\text{-}is}$-Int	2.835	0.180	0.023	-
$^{3}IV_{a\text{-}ls}$-Int	1.038	0.078	0.001	-
$^{7}IV_{a\text{-}hs}$-ts2	3.965	0.692	0.008	0.084
$^{5}IV_{a\text{-}is}$-ts2	3.851	0.102	0.025	-0.052
$^{3}IV_{a\text{-}ls}$-ts2	1.045	0.408	-0.086	0.081
$^{5}IV_{a\text{-}hs}$-P	3.052	0.638	-	-
$^{3}IV_{a\text{-}is}$-P	1.288	0.796	-	-
$^{1}IV_{a\text{-}ls}$-P	0	0	-	-
$[Co(13\text{-}TMC)O_2Cl]^+$				
$^{2}V_{a\text{-}ls}$	-0.127	0.449	0.638	-
$^{2}V_{a\text{-}ls}$-ts1	-0.011	0.119	0.349	0.332
$^{2}V_{a\text{-}ls}$-Int	0	0	-	-
$^{2}V_{a\text{-}ls}$-ts2	0.059	0.364	-0.084	-0.122
$^{5}V_{a\text{-}hs}$-P	2.734	1.396	-	-
$^{3}V_{a\text{-}is}$-P	1.831	0.900	-	-
$^{3}V_{a\text{-}ls}$-P	-0.028	0.972	-	-

Table AX 5.4. B3LYP computed spin density values of metal-superoxo species, intermediates, transition states and product with 14-TMC.

Spin State	M	O1	O2	C1
		$[V(14\text{-}TMC)O_2Cl]^+$		
$^4I_{b\text{-}hs}$	2.166	0.203	0.722	-
$^2I_{b\text{-}hs}$	2.014	-0.406	-0.478	-
$^4I_{b\text{-}hs}$-ts1	2.168	-0.020	0.484	0.256
$^2I_{b\text{-}hs}$-ts1	2.181	-0.155	-0.386	-0.272
$^4I_{b\text{-}hs}$-Int	2.1371	0.079	-0.096	-
$^2I_{b\text{-}ls}$-Int	0	0	0	-
$^4I_{b\text{-}hs}$-ts2	1.919	0.175	0.685	-0.029
$^2I_{b\text{-}hs}$-P	1.288	-.2004	-	-
		$[Cr(14\text{-}TMC)O_2Cl]^+$		
$^5II_{b\text{-}hs}$	3.248	0.307	0.650	-
$^3II_{b\text{-}hs}$	3.245	-0.390	-0.633	-
$^3II_{b\text{-}ls}$	1.185	0.299	0.607	-
$^1II_{b\text{-}ls}$	1.132	-0.375	-0.650	-
$^5II_{b\text{-}hs}$-ts1	3.192	0.079	0.432	0.295
$^3II_{b\text{-}hs}$-ts1	3.191	-0.096	-0.346	-0.322
$^3II_{b\text{-}ls}$-ts1	0.945	0.155	0.429	0.291
$^1II_{b\text{-}ls}$-ts1	-1.116	0.101	0.403	0.297
$^5II_{b\text{-}hs}$-Int	3.179	-0.002	0.040	-
$^3II_{b\text{-}ls}$-Int	1.126	-0.044	0.007	-
$^5II_{b\text{-}hs}$-ts2	3.159	0.384	0.014	-0.118
$^3II_{b\text{-}ls}$-ts2	3.099	-0.266	0.099	0.126
$^3II_{b\text{-}hs}$-P	2.784	-0.569	-	-
$^1II_{b\text{-}ls}$-P	0	0	-	-
		$[Mn(14\text{-}TMC)O_2Cl]^+$		
$^6III_{b\text{-}hs}$	4.202	0.287	0.563	-
$^4III_{b\text{-}hs}$	4.344	-0.604	-0.776	-
$^4III_{b\text{-}is}$	2.176	0.331	0.640	-
$^2III_{b\text{-}is}$	2.186	-0.639	-0.377	-
$^2III_{b\text{-}ls}$	-0.012	0.350	0.647	-
$^6III_{b\text{-}hs}$-ts1	4.144	-0.044	0.359	0.266
$^4III_{b\text{-}hs}$-ts1	4.186	-0.248	-0.392	-0.320
$^4III_{b\text{-}is}$-ts1	2.095	0.109	0.441	0.279
$^2III_{b\text{-}is}$-ts1	2.092	-0.051	-0.347	-0.309

$^{2}III_{b\text{-}ls}$-ts1	0.101	-0.014	0.395	0.299
$^{6}III_{b\text{-}hs}$-Int	3.987	-0.010	0.042	-
$^{4}III_{b\text{-}is}$-Int	2.098	0.042	0.023	-
$^{2}III_{b\text{-}ls}$-Int	0	0	0	-
$^{4}III_{b\text{-}is}$-ts2	3.898	-0.214	0.049	0.113
$^{2}III_{b\text{-}ls}$-ts2	0.063	0.251	-0.054	-0.109
$^{4}III_{b\text{-}hs}$-P	2.677	0.545	-	-
$^{2}III_{b\text{-}ls}$-P	1.165	-0.061	-	-
		$[Fe(14\text{-}TMC)O_2Cl]^+$		
$^{7}IV_{b\text{-}hs}$	3.929	0.656	0.799	-
$^{5}IV_{b\text{-}hs}$	3.937	-0.079	-0.521	-
$^{5}IV_{b\text{-}is}$	2.861	0.542	0.687	-
$^{3}IV_{b\text{-}is}$	3.426	-0.834	-0.689	-
$^{3}IV_{b\text{-}ls}$	1.179	0.329	0.628	-
$^{1}IV_{b\text{-}ls}$	1.233	-0.402	-0.664	-
$^{7}IV_{b\text{-}hs}$-ts1	3.930	0.432	0.504	0.292
$^{5}IV_{b\text{-}hs}$-ts1	3.938	0.2473	-0.253	-0.294
$^{5}IV_{b\text{-}is}$-ts1	3.194	-0.076	0.277	0.266
$^{3}IV_{b\text{-}is}$-ts1	3.262	-0.307	-0.447	-0.327
$^{3}IV_{b\text{-}ls}$-ts1	1.031	0.150	0.437	0.269
$^{1}IV_{b\text{-}ls}$-ts1	1.036	0.003	-0.391	-0.295
$^{7}IV_{b\text{-}hs}$-Int	3.980	0.276	0.051	-
$^{5}IV_{b\text{-}is}$-Int	2.896	0.194	0.030	-
$^{3}IV_{b\text{-}ls}$-Int	1.039	0.089	-0.000	-
$^{7}IV_{b\text{-}hs}$-ts2	3.961	0.698	0.0389	-0.118
$^{5}IV_{b\text{-}is}$-ts2	1.049	0.419	-0.080	-0.119
$^{3}IV_{b\text{-}ls}$-ts2	1.049	0.419	-0.080	-0.118
$^{5}IV_{b\text{-}hs}$-P	3.081	0.632	-	-
$^{3}IV_{b\text{-}is}$-P	1.313	0.793	-	-
$^{1}IV_{b\text{-}ls}$-P	0	0	-	-
		$[Co(14\text{-}TMC)O_2Cl]^+$		
$^{2}V_{b\text{-}hs}$	-0.146	0.456	0.642	-
$^{2}V_{b\text{-}hs}$-ts1	0.002	0.107	0.349	-
$^{2}V_{b\text{-}hs}$-Int	0	0	0	-
$^{2}V_{b\text{-}hs}$-ts2	0.061	0.368	-0.077	
$^{5}V_{b\text{-}hs}$-P	2.750	1.400	-	-
$^{3}V_{b\text{-}is}$-P	1.855	0.884	-	-
$^{1}V_{b\text{-}ls}$-P	-0.026	0.974	-	-

Table AX 6.1. B3LYP-D2 computed selected structural parameters of the14-TMC metal-hydroperoxo species, transition states (O---O) and product (metal-oxo).

	Bond length (A˚)							Bond Angel (˚)					
Spin State	M-O	M-N_1	M-N_2	M-N_3	M-N_4	M-N avg	M-Cl	O-O	Cl-M-O	M-O-O	O-O-H	N_1-M-N_3	N_2-M-N_4
						[(14-TMC)(Cl)CrOOH]$^+$ Species							
$^4IA_{hs}$	1.943	2.147	2.183	2.196	2.161	2.173	2.398	1.515	172.0	127.5	99.7	175.0	174.6
$^2IA_{ls}$	1.894	2.161	2.146	2.185	2.197	2.171	2.386	1.518	171.9	129.2	99.6	175.3	174.9
$^4IA_{hs}$-ts	1.725	2.189	2.159	2.164	2.175	2.172	2.409	2.368	175.6	142.5	68.9	174.8	174.8
$^2IA_{ls}$-ts	1.686	2.205	2.163	2.138	2.188	2.173	2.389	1.878	172.8	137.0	89.9	176.6	175.8
$^3IA_{hs}$-Int	1.715	2.167	2.167	2.176	2.176	2.171	2.419	-	176.8	-	-	174.5	174.5
Exp.[4]	1.876	1.231	2.316	-	-	-	-	-		-	-	-	
						[(14-TMC)(Cl)MnOOH]$^+$ Species							
$^5IIA_{hs}$	1.916	2.132	2.318	2.179	2.313	2.236	2.344	1.511	169.9	127.8	99.6	173.7	173.7
$^3IIA_{is}$	1.885	2.117	2.162	2.175	2.130	2.146	2.351	1.519	171.2	127.1	99.3	175.8	175.3
$^1IIA_{ls}$	1.767	2.127	2.173	2.184	2.135	2.155	2.343	1.537	170.8	130.1	99.1	176.7	176.3
$^5IIA_{hs}$-ts	1.748	2.171	2.153	2.140	2.158	2.156	2.433	1.854	176.8	156.5	92.6	174.0	174.2
$^3IIA_{is}$-ts	1.723	2.106	2.160	2.179	2.122	2.142	2.393	1.852	171.6	130.7	89.2	176.6	175.8
$^4IIA_{hs}$-Int	1.680	2.134	2.157	2.134	2.157	2.145	2.417	-	177.7	-	-	175.1	175.1
$^2IIA_{ls}$-Int	1.637	2.143	2.154	2.143	2.153	2.148	2.370	-	177.1	-	-	175.6	175.5
						[(14-TMC)(Cl)FeOOH]$^+$ Species							
$^6IIIA_{hs}$	1.953	2.209	2.229	2.247	2.231	2.249	2.378δ	1.495	173.5	134.8	101.1	173.0	172.4
$^4IIIA_{is}$	2.021	2.124	2.166	2.151	2.156	2.154	2.457	1.514	130.6	130.6	100.8	174.6	174.3
$^2IIIA_{ls}$	1.858	2.137	2.157	2.107	2.109	2.127	2.344	1.522	171.4	126.5	99.3	176.5	175.9
$^6IIIA_{hs}$-ts	1.677	2.242	2.235	2.209	2.197	2.221	2.322	2.052	177.1	157.7	88.2	172.8	172.5
$^4IIIA_{is}$-ts	1.718	2.137	2.150	2.140	2.124	2.139	2.385	1.822	177.1	159.3	93.9	174.9	174.7
$^2IIIA_{ls}$-ts	1.675	2.098	2.138	2.157	2.111	2.126	2.351	2.019	173.8	136.5	83.7	176.7	176.1
$^5IIIA_{hs}$-Int	1.659	2.202	2.202	2.238	2.237	2.219	2.327	-	177.5	-	-	173.4	173.4
$^3IIIA_{is}$-Int	1.657	2.195	2.235	2.207	2.242	2.219	2.362	-	178.1	-	-	175.4	175.4
Exp.[6]	1.646	-	-	2.067	2.069	2.109	2.117	-	-	-	-	-	-
						[(14-TMC)(Cl)CoOOH]$^+$ Species							
$^5IVA_{hs}$	1.984	2.180	2.221	2.216	2.209	2.206	2.415	1.472	171.4	132.1	102.3	174.0	173.3
$^3IVA_{is}$	1.917	2.063	2.243	2.117	2.235	2.164	2.384	1.511	172.0	128.6	100.1	175.6	175.2
$^1IVA_{ls}$	1.934	2.073	2.114	2.133	2.080	2.100	2.342	1.525	171.2	123.8	99.3	176.2	175.7

$^{5}IVA_{hs}$-ts	1.674	2.226	2.226	2.212	2.212	2.219	2.286	1.921	176.2	162.5	92.3	173.1	173.1
$^{6}IVA_{hs}$-Int	1.872	2.221	2.225	2.221	2.226	2.223	2.374	-	174.4	-	-	170.9	170.9
$^{4}IVA_{is}$-Int	1.647	2.199	2.221	2.199	2.221	2.210	2.284	-	177.5	-	-	173.9	173.8
$^{2}IVA_{ls}$-Int	1.835	2.090	2.098	2.090	2.099	2.094	2.353	-	177.4	-	-	173.7	173.7
[(14-TMC)(Cl)NiOOH]$^{+}$ Species													
$^{2}VA_{ls}$	2.013	2.148	2.211	2.198	2.196	2.189	2.341	1.459	171.1	128.2	103.2	173.8	173.7
$^{4}VA_{hs}$-ts	1.836	2.208	2.162	2.192	2.172	2.183	2.284	2.072	176.2	154.1	96.0	171.7	171.8
$^{5}VA_{hs}$-Int	1.838	2.218	2.196	2.197	2.218	2.207	2.376	-	174.8	-	-	172.2	172.2
$^{1}VA_{ls}$-Int	1.853	2.174	2.173	2.184	2.184	2.179	2.289	-	177.1	-	-	171.5	171.5
[(14-TMC)(Cl)CuOOH]$^{+}$ Species													
$^{3}VIA_{hs}$	2.291	2.150	2.181	2.177	2.183	2.173	2.501	1.455	171.9	130.8	104.7	171.1	171.5
$^{1}VIA_{hs}$	1.919	2.207	2.328	2.254	2.326	2.279	2.262	1.475	168.1	125.5	102.8	174.0	174.4
$^{3}VIA_{hs}$-ts	2.004	2.242	2.190	2.228	2.218	2.219	2.358	2.036	175.4	135.5	85.4	171.4	171.4
$^{4}VIA_{hs}$-Int	2.031	2.189	2.190	2.188	2.188	2.189	2.420	-	176.3	-	-	170.5	170.5
$^{2}VIA_{ls}$-Int	2.083	2.183	2.184	2.177	2.178	2.180	2.448	-	176.4	-	-	170.3	170.3

Table 6.2. Computed Wiberg bond indices.

Spin State	M-O	O1-O2
[(14-TMC)(Cl)CrOOH]$^{+}$		
$^{4}IA_{hs}$	0.218	0.246
$^{4}IA_{hs}$-ts	0.374	0.054
$^{3}IA_{hs}$-Int	0.403	-
[(14-TMC)(Cl)MnOOH]$^{+}$		
$^{5}IIA_{hs}$	0.198	0.245
$^{5}IIA_{hs}$-ts	0.443	0.180
$^{4}IIA_{hs}$-Int	0.624	-
[(14-TMC)(Cl)FeOOH]$^{+}$		
$^{6}IIIA_{hs}$	0.260	0.249
$^{4}IIIA_{is}$-ts	0.556	0.107
$^{5}IIIA_{hs}$-Int	0.631	-
[(14-TMC)(Cl)CoOOH]$^{+}$		
$^{1}IVA_{ls}$	0.152	0.244
$^{5}IVA_{hls}$	0.539	0.147
$^{4}IVA_{is}$-Int	0.640	-
[(14-TMC)(Cl)NiOOH]$^{+}$		
$^{2}VA_{ls}$	0.101	0.246
$^{4}VA_{hs}$-ts	0.202	0.143
$^{2}VA_{ls}$	0.423	-
[(14-TMC)(Cl)CuOOH]$^{+}$		
$^{3}VIA_{hs}$	0.106	0.306
$^{3}VIA_{hs}$-ts	0.158	0.088
$^{4}VIA_{hs}$-Int	0.177	-

Table AX 6.3. B3LYP-D2 computed structural parameters of the buea metal-hydroperoxo species (reactant), transition states (O---O) and product (metal-oxo).

	Bond length (Å)									Bond Angle (˚)						
SpinState	M-O	M-N_1	M-N_2	M-N_3	M-N_4	O-O	O-H_1	O-H_2	O-H_3	O_1-M-N_4	M-O1-O2	N_1-M-N_2	N_2-M-N_3	N_1-M-N_3	N_3-M-N_4	O-O-H
							[(buea)CrOOH]$^-$									
$^4IB_{hs}$	1.912	2.177	1.986	1.984	2.091	1.462	1.833	1.955	-	176.9	90.8	143.9	100.7	107.1	83.2	99.0
$^2IB_{ls}$	1.890	2.173	1.975	1.993	2.173	1.470	1.802	1.763	-	177.6	110.6	120.2	103.1	129.1	79.6	97.5
$^4IB_{hs}$-ts	1.762	2.167	1.986	1.974	2.003	1.878	1.797	1.778	-	168.8	116.0	128.7	101.1	119.7	77.9	85.1
$^2IB_{ls}$-ts	1.804	2.159	1.966	1.936	1.948	1.613	1.794	1.796	1.882	172.2	120.1	114.5	115.4	120.5	79.4	95.3
$^3IB_{hs}$-Int	1.649	2.532	1.935	1.943	1.935	-	1.947	1.929	-	179.4	179.4	116.6	115.1	109.6	75.6	-
$^1IB_{ls}$-Int	1.611	2.549	1.934	1.997	1.906	-	1.972	-	-	168.4	-	101.9	131.0	103.6	74.9	-
							[(buea)MnOOH]$^-$									
$^5IIB_{hs}$	1.853	2.094	2.034	2.089	2.088	1.454	1.910	0.994		170.8	105.4	103.8	79.9	81.3	79.1	99.6
$^3IIB_{is}$	1.858	2.129	1.936	1.933	2.008	1.466	1.970	1.918	1.776	177.2	104.4	144.3	102.14	107.7	83.9	98.5
$^1IIB_{ls}$	1.933	2.120	1.896	1.935	1.893	1.429	1.810	1.702	1.884	178.9	110.4	115.7	112.9	125.1	80.8	98.8
$^5IIB_{hs}$-ts	1.732	2.126	1.994	1.988	2.006	1.856	1.833	1.891	-	176.2	125.5	131.1	101.3	118.3	79.2	86.3
$^3IIB_{is}$-ts	1.734	2.101	1.949	1.959	2.101	1.737	1.824	1.923	1.805	172.6	115.7	131.4	100.5	121.5	80.4	91.6
$^1IIB_{ls}$-ts	1.648	2.155	1.857	2.017	1.884	1.900	1.731	1.751	1.955	161.9	127.7	117.4	102.2	128.4	75.7	85.2
$^4IIB_{hs}$-Int	1.674	2.236	1.986	1.952	1.928	-	1.775	1.753	-	175.9	-	137.6	113.7	100.4	82.2	-
$^2IIB_{ls}$-Int	1.658	2.315	1.944	1.927	1.910	-	1.777	1.805	-	176.1	-	127.7	119.1	102.6	79.9	-
							[(buea)FeOOH]$^-$									
$^6IIIB_{hs}$	1.940	2.491	1.984	2.024	1.985	1.463	1.948	1.9092	-	122.8	113.3	118.4	105.8	120.3	77.5	98.2
$^4IIIB_{is}$	1.819	2.174	1.987	2.019	2.035	1.441	1.833	-	1.828	174.2	117.9	128.8	108.5	116.7	81.8	99.0
$^2IIIB_{ls}$	1.844	2.137	1.907	1.966	1.977	1.455	1.719	1.833	-	169.1	117.7	147.5	101.3	105.6	83.1	98.1
$^6IIIB_{hs}$-ts	1.697	2.293	1.999	2.206	1.954	1.929	1.878	-	-	178.7	146.3	123.1	107.4	120.5	79.8	83.4
$^4IIIB_{is}$-ts	1.666	2.153	2.059	1.992	1.948	1.902	1.848	-	1.822	178.5	111.3	119.4	106.1	128.9	82.5	88.2
$^2IIIB_{ls}$-ts	1.678	2.083	1.897	2.007	1.931	1.941	1.745	1.771	1.984	163.3	129.6	119.0	98.6	134.1	98.6	80.8
$^5IIIB_{hs}$-Int	1.651	2.200	1.972	2.005	2.007	-	1.826	1.844	-	178.8	-	123.5	106.8	122.7	81.5	-
$^3IIIB_{is}$-Int	1.661	2.227	1.934	1.960	1.885	-	1.804	1.766	-	172.1	-	141.9	111.0	98.6	81.5	-
$^1IIIB_{ls}$-Int	1.624	2.733	1.871	1.871	1.871	-	-	-	-	179.9	-	111.7	111.6	111.5	72.8	-
							[(buea)CoOOH]$^-$									

$^{5}IVB_{hs}$	1.943	2.008	1.979	1.979	2.322	1.457	1.963	1.794	1.954	176.3	110.2	132.2	104.5	112.9	81.6	99.2
$^{3}IVB_{is}$	1.872	1.959	2.001	2.021	2.035	1.437	1.783	1.778	-	179.5	111.8	121.2	104.3	129.9	84.4	98.5
$^{1}IVB_{ls}$	1.862	1.992	1.916	1.919	2.041	1.445	1.944	1.926	1.772	175.5	99.2	152.8	99.7	103.4	86.3	99.2
$^{5}IVB_{hs}$-ts	1.714	2.199	1.974	1.966	1.956	1.938	1.801	1.972	-	171.3	135.2	111.9	107.1	134.1	81.8	82.6
$^{3}IVB_{is}$-ts	1.724	2.235	1.930	1.928	1.953	2.015	1.751	1.823	-	173.8	137.9	130.9	118.7	103.4	80.6	84.3
$^{6}IVB_{hs}$-nt	1.755	2.466	1.982	1.998	1.987	-	1.861	1.841	-	175.8	-	104.6	117.2	123.0	76.5	-
$^{4}IVB_{is}$-Int	1.714	2.116	1.944	2.018	1.979	-	1.974	1.812	1.786	173.6	-	119.3	128.8	107.3	82.8	-
$^{2}IVB_{ls}$-Int	1.824	2.075	1.965	1.988	1.932	-	1.922	1.778	-	174.2	-	134.9	111.2	110.3	83.7	-
[(buea)NiOOH]$^{-}$																
$^{4}VB_{hs}$	1.969	1.972	1.968	1.945	2.405	1.457	1.929	-	1.944	169.8	113.7	114.3	114.7	121.2	79.8	99.4
$^{2}VB_{ls}$	1.873	1.963	2.079	1.996	2.107	1.425	-	1.842	-	169.6	115.8	108.7	105.8	142.0	83.2	100.2
$^{2}VB_{ls}$-ts	1.789	2.138	2.050	1.955	1.936	2.065	1.666	1.754	1.790	176.5	-	151.5	104.9	98.6	83.4	73.4
$^{5}VB_{hs}$-Int	1.924	2.288	1.960	2.028	1.961	-	1.790	1.769	1.954	172.7	-	124.7	107.4	120.9	81.4	-
$^{3}VB_{is}$-Int	1.972	2.262	2.015	1.954	1.959	-	1.744	1.939	1.771	172.8	-	121.4	125.7	106.7	81.9	-
$^{1}VB_{ls}$-Int	1.745	2.134	1.949	1.936	1.922	-	1.862	1.669	1.892	177.6	-	146.8	100.5	108.9	83.8	-
[(buea)CuOOH]$^{-}$																
$^{3}VIB_{hs}$	1.999	1.989	2.190	2.015	2.309	1.427	-	1.830	-	171.8	114.5	107.4	106.2	138.6	81.9	99.8
$^{1}VIB_{ls}$	1.975	1.947	2.194	1.963	2.337	1.429	-	1.975	1.001	166.6	108.3	105.5	103.7	142.5	78.5	100.3
$^{1}VIB_{ls}$-ts	1.902	2.119	1.899	1.932	2.419	1.911	1.809	-	-	132.3	92.2	112.6	99.1	85.7	83.6	97.3
$^{4}VIB_{hs}$-Int	1.919	2.241	2.001	2.065	2.120	-	1.801	1.913	1.810	175.3	-	122.6	101.2	129.5	82.3	-
$^{2}VIB_{ls}$-Int	1.918	2.276	2.029	2.336	1.986	-	1.756	1.869	-	171.1	-	96.1	112.5	142.3	76.3	-

Table 6.4. Computed Wiberg bond indices.

Spin State	M-O1	O1-O2
	[(buea)CrOOH]$^-$	
$^4IB_{hs}$	0.193	0.244
$^2IB_{ls}$-ts	0.310	0.170
$^3IB_{hs}$-Int	0.507	-
	[(buea)MnOOH]$^-$	
$^5IIB_{hs}$	0.207	0.247
$^5IIB_{hs}$-ts	0.339	0.201
$^4IIB_{hs}$-Int	0.527	-
	[(buea)FeOOH]$^-$	
$^6IIIB_{hs}$	0.235	0.248
$^4IIIB_{is}$-ts	0.528	0.044
$^5IIIB_{hs}$-Int	0.583	-
	[(buea)CoOOH]$^-$	
$^3IVB_{is}$	0.148	0.248
$^5IVB_{hs}$-ts	0.388	0.215
$^4IVB_{is}$-Int	0.583	-
	[(buea)NiOOH]$^-$	
$^4VB_{hs}$	0.191	0.250
$^2VB_{ls}$-ts	0.205	0.158
$^5VB_{hs}$-Int	0.226	-
	[(buea)CuOOH]$^-$	
$^3VIB_{hs}$	0.165	0.272
$^1VIB_{ls}$-ts	0.112	0.116
$^4VIB_{hs}$-Int	0.201	-

Table AX 6.5. Selected B3LYP-D2 computed structural parameters of the buea metal-hydroperoxo species, transition states (O---O) and product (metal-oxo).

	Bond length (Å)									Bond Angle (˚)						
Spin State	M-O	M-N_1	M-N_2	M-N_3	M-N_4	O-O	O-H_1	O-H_2	O-H_3	O_1-M-N_4	M-O1-O2	N_1-M-N_2	N_2-M-N_3	N_1-M-N_3	N_3-M-N_4	O-O-H
								[(buea)RuOOH]$^-$								
^{6}VIIB$_{hs}$	2.135	2.596	2.147	2.157	2.211	1.470	1.964	1.900	-	165.4	105.1	117.4	101.7	117.5	73.9	98.1
^{4}VIIB$_{is}$	1.960	2.239	2.209	2.094	2.108	1.465	1.928	1.770	1.897	174.0	115.3	103.5	145.6	98.3	79.5	100.9
^{2}VIIB$_{ls}$	2.056	2.179	2.026	2.056	2.037	1.470	1.844	1.883	1.704	172.7	114.2	120.3	135.2	97.9	82.1	98.9
^{2}VIIB$_{hs}$-ts	1.902	2.247	2.032	2.010	2.018	1.871	1.722	1.771	1.730	173.6	115.7	125.1	115.9	110.5	80.3	89.8
^{3}VIIB$_{is}$-Int	1.839	2.288	2.065	1.979	2.062	-	1.849	1.859	1.999	172.9	107.3	144.0	96.6	78.4	-	-
								[(buea)OsOOH]$^-$								
^{4}VIIIB$_{is}$	1.939	2.195	2.219	2.075	2.059	1.631	1.814	1.862	1.847	173.6	115.8	147.9	105.2	96.8	80.6	99.8
^{2}VIIIB$_{ls}$	2.076	2.155	2.000	2.057	2.049	1.486	1.838	1.948	1.713	172.9	114.8	132.6	94.6	127.2	83.7	99.1
^{2}VIIIB$_{ls}$-ts	1.960	2.193	2.038	2.042	2.001	1.762	1.689	1.715	1.754	171.3	121.1	122.2	126.2	104.4	80.6	92.4
^{5}VIIIB$_{hs}$-Int	1.832	2.230	2.079	2.069	2.259	-	1.897	1.931	1.984	176.2	-	142.4	104.1	103.6	80.6	-
^{3}VIIIB$_{is}$-Int	1.825	2.272	2.081	2.013	2.064	-	1.989	1.827	-	165.0	-	146.8	95.8	104.9	76.4	-
								[(buea)RhOOH]$^-$								
^{5}IXB$_{hs}$	2.121	2.481	2.155	2.124	2.149	1.444	1.963	1.865	-	172.5	100.2	128.6	111.3	102.1	77.3	100.2
^{3}IXB$_{is}$	2.028	2.133	2.065	2.121	2.155	1.452	1.787	1.849	1.851	177.8	110.6	135.5	101.4	116.0	82.9	98.8
^{1}IXB$_{ls}$	2.007	2.154	2.018	2.109	2.073	1.447	-	1.738	1.895	176.6	103.5	157.5	93.9	99.3	82.9	98.9
^{3}IXB$_{is}$-ts	1.891	2.214	2.067	2.088	2.031	1.909	1.722	1.819	-	173.2	116.2	127.5	123.1	102.2	81.5	90.6
^{4}IXB$_{hs}$-Int	1.884	2.170	2.078	2.135	2.114	-	1.849	1.826	1.836	177.9	114.2	117.9	114.2	120.7	80.9	-
								[(buea)IrOOH]$^-$								
^{5}XB$_{is}$	2.135	2.533	2.132	2.143	2.144	1.460	1.983	1.950	-	173.4	117.9	110.9	125.4	105.5	75.4	100.0
^{3}XB$_{is}$	2.063	2.112	2.038	2.194	2.069	1.470	1.993	1.849	-	178.0	111.6	143.7	104.3	106.4	80.7	99.2
^{1}XB$_{ls}$	2.071	2.102	1.996	2.085	2.104	1.468	1.726	1.794	1.892	178.7	134.2	136.2	84.2	134.2	84.6	99.4
^{1}XB$_{ls}$-ts	1.857	2.223	2.062	2.006	2.001	2.118	1.738	1.796	1.639	167.1	117.1	124.7	88.3	138.5	81.5	75.8
^{6}XB$_{hs}$-Int	1.895	2.568	2.171	2.170	2.171	1.895	1.991	1.990	1.993	179.9	-	113.2	112.1	112.6	73.9	-

$^{4}XB_{is}$-Int	1.899	2.168	2.225	2.054	2.058	1.898	1.816	1.892	1.798	174.9	-	133.7	108.4	111.2	82.2	-
$^{2}XB_{ls}$-Int	1.944	2.194	2.045	2.008	1.974	1.616	1.684	1.735	-	173.9	-	141.8	112.3	99.6	81.8	-

References

(1) Mubarak, M. Q. E.; de Visser, S. P. *Dalton Trans.* **2019**, *48*, 16899-16910.

(2) Gordon, J. B.; Vilbert, A. C.; Siegler, M. A.; Lancaster, K. M.; Moenne-Loccoz, P.; Goldberg, D. P. *J. Am. Chem. Soc.* **2019**, *141*, 3641-3653.

(3) Wang, B.; Lee, Y.-M.; Tcho, W.-Y.; Tussupbayev, S.; Kim, S.-T.; Kim, Y.; Seo, M. S.; Cho, K.-B.; Dede, Y.; Keegan, B. C.; Ogura, T.; Kim, S. H.; Ohta, T.; Baik, M.-H.; Ray, K.; Shearer, J.; Nam, W. *Nat. Commun.* **2017**, *24*, 14839-14849.

(4) Cho, J.; Woo, J.; Nam, W. *J. Am. Chem. Soc.* **2010**, *132*, 5958-5959.

(5) Cho, J.; Woo, J.; Nam, W. *J. Am. Chem. Soc.* **2012**, *134*, 11112-11115.

(6) Rohde, J.-U.; In, J.-H.; Lim, M. H.; Brennessel, W. W.; Bukowski, M. R.; Stubna, A.; Munck, E.; Nam, W.; Que, L., Jr. *Science* **2003**, *299*, 1037-1039.

List of Publications

(1) "*Exploring Catecholase Activity in Dinuclear Mn(II) and Cu(II) Complexes: An Experimental and Theoretical Approach*" Ahmad, M. S.; Khalid, M.; Khan M. S.; Shahid, M.; Ahmad, M.; **Monika**; Ansari, A.; Ashafaq, M. *New J. Chem.* **2020**, *44*, 7998-8009.

(2) "*Mechanistic Insights of Allylic Oxidation of Aliphatic Compound by Tetraamido Iron(V) Species: A C-H vs. O-H Bond Activation*" **Monika**; Ansari, A. *New J. Chem.* **2020**, *44*, 19103-19112.

(3) "*Electronic Structures, Bonding, and Spin State Energetics of Biomimetic Mononuclear and Bridged Dinuclear Iron Complexes: A Computational Examination*" **Monika**; Yadav, O.; Chauhan, H.; Ansari, A. *Struct. Chem.* **2021**, *32*, 1473-1488.

(4) "*How to Identify a Smoker: a Salient Crystallographic Approach to Detect Thiocyanate Content*" Iman, K.; Ahamad M. N.; **Monika**; Ansari, A., Saleh, A .M. H.; Khan, M.S.; Ahmad, M.; Haque, A.R.; Shahid, M. *RSC Adv.* **2021**, *11*, 16881-16891.

(5) "*Novel {Cu4} and {Cu4Cd6} Clusters Derived from Flexible Aminoalcohols: Synthesis, Characterization, Crystal Structures, and Evaluation of Anticancer Properties*" Iman, K.; Raza Md , K.; Ansari, M.; **Monika**; Ansari, A.; Ahmad, M.; Ahamad , M. N.; Qasem, M.A.K.; Hussain, S.; Akhtar M.N.; Shahid, M. *Dalton Trans.* **2021**, *50*, 11941-11953.

(6) "*Effect of Ring Size of TMC Ligands towards C-H Bond Activation by Metal-superoxo: A Theoretical Investigation*" **Monika**; Ansari, A. (Under revision in *Dalton Trans.*)

(7) "*Theoretical Insights for Formation of High Metal Oxo Species: Drives for Oxo-wall"* **Monika**; Ansari, A. (To be submitted)